

Tracking retreat processes at the Falljökull Glacier, SE Iceland

Matthew Tomkins

MSc (By Research) Environmental Science

Supervisors: Dr. Mike James and Dr. Peter Wynn

Lancaster University

2016

Declaration

'I hereby declare that the information on which this dissertation is based has not been plagiarised from any unacknowledged secondary sources.'

Signed Date

Print Name

Abstract

In glacial systems, hydrological forcing of ice velocity may lead to instability and accelerated mass loss. However, recent studies have demonstrated that the relationship between ice melt and ice dynamics is non-linear because subglacial drainage configuration strongly modulates meltwater inputs and results in asynchronicity between surface melt production and ice movement. Furthermore, subglacial drainage undergoes temporal evolution and can vary spatially between and within individual glaciers. As such, the degree of connectivity between ice melt and ice dynamics exhibits spatio-temporal variability. To address this, time-lapse images from Falljökull, SE Iceland, were analysed using Pointcatcher, a feature tracking software. Surface velocities and thinning rates were quantified for the period 2011-2013 and compared to results from energy balance modelling (EBM) to determine the climatic, hydrological and structural controls on glacier dynamics. The results show that melt production at Falljökull is closely linked to energy inputs to the glacier surface, although consistent thinning underestimation by the EBM, equivalent to ~1-3 m, reflects the poor optimisation of the model for thin debris cover. In addition, melt production is strongly modulated by individual events e.g. Grímsvötn eruption, which modify surface conditions and enhance/suppress melt. A clear relationship between ice melt and ice dynamics is also evident in these data although subglacial drainage structure i.e. discrete/distributed, and surface conditions e.g. debris or snow cover, account for periods of de-coupling. Hydrologically induced speed-up events are identified and occur more readily when inefficient distributed systems are present. In contrast, flow variability is markedly reduced when meltwater inputs are suppressed and when efficient discrete drainage is present. Enhanced flow is strongly linked to sliding at the ice-bed interface although this varies spatially and temporally as a function of subglacial drainage configuration. Finally, these data conflict markedly with previous research which inferred that Falljökull was stagnant and wasting away in-situ. Instead, Falljökull is 'active' with movement through ice deformation, basal sliding and subglacial deformation although forward motion is insufficient to offset retreat.

Table of Contents

List of Figures.....	vi
List of Tables.....	xi
Acknowledgements.....	xii
Chapter 1 - Introduction.....	1
1.1 - Glaciers-climate coupling.....	1
1.2 - Ice melt and ice dynamics.....	2
1.3 - Project rationale.....	3
Chapter 2 - Literature Review.....	5
2.1 - Glacier dynamics.....	5
2.1.1 - Internal deformation.....	5
2.1.2 - Basal sliding.....	6
2.1.3 - Subglacial deformation.....	8
2.1.4 - Key methods for measuring ice movement.....	10
2.2 - Energy balance.....	12
2.2.1 - Key variables.....	12
2.2.2 - Controls on energy flux.....	13
2.2.3 - Modelling.....	15
2.3 - Hydrology.....	17
2.3.1 - Supraglacial drainage.....	17
2.3.2 - Englacial drainage.....	18
2.3.3 - Subglacial drainage.....	20
2.3.4 - The theory of hydrodynamic coupling.....	23
2.3.5 - Water storage.....	24
2.4 - Terrestrial time-lapse photography.....	25
2.4.1 - Procedures.....	25
2.4.2 - Recent developments.....	27
2.5 - Meteorological data.....	29
2.6 - Study area: Virkisjökull-Falljökull.....	29
2.6.1 - Regional context.....	29
2.6.2 - Glaciology.....	30
2.6.3 - Meteorology.....	32

2.6.4 - Chronology and previous research	32
Chapter 3 - Methodology.....	36
3.1 - Time-lapse image acquisition and processing.....	36
3.1.1 - Camera specifications and set up.....	36
3.1.2 - Data set.....	36
3.2 - Pointcatcher Analysis.....	38
3.2.1 - Image registration.....	38
3.2.2 - Feature tracking	43
3.2.3 - Geo-referencing	44
3.3 - Data Analysis.....	48
3.3.1 - Spatial groupings.....	48
3.3.2 - Data management.....	48
3.4 - Meteorological data.....	51
3.4.1 - Data processing	51
3.4.2 - Energy balance modelling	51
3.5 - Pointcatcher results	54
3.5.1 - Image registration.....	54
3.5.2 - Glacier feature tracking.....	56
Chapter 4 - Results.....	58
4.1 - Inter-annual variability	58
4.1.1 - Thinning rates.....	58
4.1.2 - Surface velocities	61
4.2 - Energy balance modelling.....	64
4.2.1 - Inter-annual variability in surface melt production	64
4.2.2 - The contribution of radiative and turbulent heat fluxes.....	64
4.2.3 - Intra-annual variability in surface melt production	66
4.3 - Intra-annual variability in thinning and comparison with surface melt	67
4.3.1 - Glacier terminus	67
4.3.2 - Intermediate sector.....	71
4.3.3 - Upper sector.....	74
4.4 - Intra-annual variability in surface velocities and comparison with thinning.....	78
4.4.1 - Glacier terminus	78
4.4.2 - Intermediate sector.....	80
4.4.3 - Upper sector.....	80

4.4.4 - Icefall.....	83
Chapter 5 - Discussion	85
5.1 - Do the results from time-lapse data accurately reflect surface dynamics?.....	85
5.1.1 - Validating time lapse data using GNSS data output.....	85
5.1.2 - How does Falljökull compare to similar glaciers?.....	87
5.2 - Surface melt and thinning rates.....	91
5.2.1 - Inter-annual variability	91
5.2.2 - Glacier terminus 2011-2013	93
5.2.3 - Intermediate sector 2011-2013.....	96
5.2.4 - Upper sector 2011-2013.....	100
5.2.5 - Melt-thinning coupling at Falljökull	101
5.3 - Linking surface dynamics to glacier hydrology	102
5.3.1 - Evidence for hydrodynamic coupling in 2011	103
5.3.2 - Evidence for hydrodynamic coupling in 2012.....	104
5.3.3 - Evidence for hydrodynamic coupling in 2013.....	106
5.3.4 - Potential controls on glacier front dynamics.....	108
5.3.5 - Potential controls on icefall dynamics	109
Chapter 6 - Conclusions.....	111
6.1 - Controls on surface melt production at Falljökull	111
6.2 - Controls on glaciers dynamics at Falljökull.....	112
6.3 - Application of time-lapse data to glacier dynamics	113
6.4 - Achieving project objectives.....	114
6.5 - Further work.....	114
Word Count	115
References	116

List of Figures

Figure 1. The contributions of glaciers and ice caps and the Greenland and Antarctic Ice Sheets to the present-day rate of sea-level rise (s.l.r.), along with their respective volumes and areas. Redrawn from Meier et al., (2007).....	1
Figure 2. Regelation sliding. Redrawn from Benn and Evans (1998)	7
Figure 3. Idealised velocity profiles for an ice mass overlying soft sediments. (a) The ice mass is completely decoupled from its bed, and basal sliding is the only form of basal motion. (b) The ice mass is completely coupled to its bed, and sediment deformation is the only form of basal motion. (c) The ice mass is partially coupled to its bed, and both sliding and sediment deformation occur. Redrawn from Murray (1994).....	9
Figure 4. Albedo variation (A) from Benn and Evans (1998). The clean ice of White Glacier, Axel Heiberg Island, Canada (B) (Photo source: http://tinyurl.com/hk93nm5) and the debris covered Inylchek glacier in Eastern Kyrgyzstan (C) (Photo source: http://tinyurl.com/h9j3ava).....	13
Figure 5. The relationship between debris thickness and mean daily ablation rate. Redrawn from Nicholson and Benn (2006)	16
Figure 6. Supraglacial flow pathways on Solheimajökull, SE Iceland, photo taken by the author.	18
Figure 7. Flow pathways of discrete and distributed subglacial systems.	21
Figure 8. Englacial drainage systems. Upward branching arborescent network (A) formed normal to equipotential contours according to Shreve (1975). However, if the assumption that water (P_w) and ice pressures (P_i) are equal is ignored, then equipotential contours are rotated nearly 90° to the Shreve model (B) which predicts circular conduit cross sections framed by intact glacier ice (C). Redrawn from Gulley et al., (2009)..	22
Figure 9. Forms and timescales of glacier storage. Redrawn from Jansson et al., (2003).....	24
Figure 10. Map of Iceland showing the main glaciers and the Virkis-Falljökull study site (inset). Digital data retrieved from the National Land Survey of Iceland.....	31
Figure 11. Cumulative retreat of the Virkisjökull and Falljökull ice fronts from annual measurements taken by the Icelandic Glaciological Society. From Bradwell et al., (2013).....	33
Figure 12. Structural evolution of Falljökull based on work by Bradwell et al., (2013) and Phillips et al., (2014).	34

Figure 13. Automatic Weather Station 3 and the Falljökull icefall.....	36
Figure 14. Missed days in the glacier front and icefall image sequences (2011-2013) due to cloud cover or precipitation	37
Figure 15. Selecting suitable topographic features for manual tracking (A-D).....	38
Figure 16. Automated tracking and the impact of illumination change (A-F) in images 55-60 from the 2011 AWS1 sequence (05/05/2011 - 07/05/2011) using a correlation threshold of 0.8 and template size of 10 pixels. Red circles indicate location of point observations. The outline of the topography is highlighted (green dotted lines) to demonstrate the impact of illumination.....	39
Figure 17. Manual (A-B) and automatic (C-D) tracking of the AWS1 image sequence in 2015.	40
Figure 18. Manual tracking precision.	41
Figure 19. Rotation around the Omega (X), Phi (Y) and Kappa (Z) axis.	42
Figure 20. Image sensor dimensions.	43
Figure 21. High image resolution of the Solheimajökull dataset enables tracking of distal surface features (inset). Photo credit: James et al., (2016).	44
Figure 22. Manual alignment of LiDAR points and topographic data.....	45
Figure 23. Georeferencing procedure. (A) Image registration throughout the sequence allows the set of feature observations to be represented in one reference camera orientation (grey box). (B) For the observation made closest in time to the first LiDAR survey, 3D coordinates can be calculated by projecting the observation through the perspective centre of the camera, p , onto the DEM surface defined by the LiDAR. (C) Ice direction is estimated based on satellite data to constrain a vertical plane in which the point is assumed to lie at all other times (D) 3D coordinates for all other image observations of that point are then calculated by intersecting their observation rays with the plane.	46
Figure 24. Ice movement at the glacier margin.	47
Figure 25. Map of the Virkis-Falljökull study site, showing the spatial distribution of surface features and camera locations. Data retrieved from the National Land Survey of Iceland.....	49
Figure 26. Horizontal and vertical track length uncertainty for surface feature 6 in the 2011 AWS1 image sequence.	50
Figure 27. The impact of temperature on saturation vapour pressure.....	52

Figure 28. Glacier surface conditions (ice/snow) for EBM (2011-2013).....	53
Figure 29. Topographic feature tracking results.....	54
Figure 30. Results of error analyses for the 2011 AWS1 image sequence. (A) Camera orientation angles. (B) Orientation precision estimates. (C) RMS residuals.	55
Figure 31. Glacier feature tracking results.	56
Figure 32. Glacier feature timelines (interval between the first and last point observation) for the 2011 AWS1 image sequence.....	57
Figure 33. Glacier feature timelines (interval between the first and last point observation) for the 2012 AWS1 image sequence.....	57
Figure 34. Glacier feature timelines (interval between the first and last point observation) for the 2013 AWS1 image sequence.....	57
Figure 35. Retreat and thinning of the Falljökull ice front (10/04/2011 - 31/12/2013).	58
Figure 36. Glacier dynamics at the Falljökull glacier front in 2011.....	59
Figure 37. Glacier dynamics at the Falljökull glacier front in 2012.....	59
Figure 38. Glacier dynamics at the Falljökull glacier front in 2013.....	59
Figure 39. Plotting horizontal velocity magnitudes against Northing for 2011 surface features.	62
Figure 40. Plotting horizontal velocity magnitudes against Northing for 2012 surface features.	62
Figure 41. Plotting horizontal velocity magnitudes against Northing for 2013 surface features.	62
Figure 42. Total melt production and energy totals (mm w.e.) from turbulent and radiative heat fluxes (2011-2013).	65
Figure 43. The relative contribution of energy fluxes to total melt (2011).	66
Figure 44. The relative contribution of energy fluxes to total melt (2012).	66
Figure 45. The relative contribution of energy fluxes to total melt (2013).	66
Figure 46. Cumulative melt (EBM) and cumulative thinning (time-lapse) at the glacier terminus in 2011.....	67

Figure 47. Cumulative melt (EBM) and cumulative thinning (time-lapse) at the glacier terminus in 2012.	68
Figure 48. Cumulative melt (EBM) and cumulative thinning (time-lapse) at the glacier terminus in 2013.	68
Figure 49. Monthly melt (EBM) and average daily thinning (time-lapse) for the glacier terminus in 2011.	70
Figure 50. Monthly melt (EBM) and average daily thinning (time-lapse) for the glacier terminus in 2012.	70
Figure 51. Monthly melt (EBM) and average daily thinning (time-lapse) for the glacier terminus in 2013.	70
Figure 52. Monthly melt (EBM) and average daily thinning (time-lapse) for the intermediate sector in 2011.	71
Figure 53. Monthly melt (EBM) and average daily thinning (time-lapse) for the intermediate sector in 2012.	71
Figure 54. Monthly melt (EBM) and average daily thinning (time-lapse) for the intermediate sector in 2013.	72
Figure 55. Cumulative melt (EBM) and cumulative thinning (time-lapse) at the intermediate sector in 2011.	72
Figure 56. Cumulative melt (EBM) and cumulative thinning (time-lapse) at the intermediate sector in 2012.	73
Figure 57. Cumulative melt (EBM) and cumulative thinning (time-lapse) at the intermediate sector in 2013.	74
Figure 58. Monthly melt (EBM) and average daily thinning (time-lapse) for the upper sector in 2011.	75
Figure 59. Monthly melt (EBM) and average daily thinning (time-lapse) for the upper sector in 2012.	75
Figure 60. Monthly melt (EBM) and average daily thinning (time-lapse) for the upper sector in 2013.	75
Figure 61. Cumulative melt (EBM) and cumulative thinning (time-lapse) at the upper sector in 2011.	76
Figure 62. Cumulative melt (EBM) and cumulative thinning (time-lapse) at the upper sector in 2012.	77

Figure 63. Cumulative melt (EBM) and cumulative thinning (time-lapse) at the upper sector in 2013.....	77
Figure 64. Cumulative displacement graphs for the glacier terminus (A), intermediate (B) and upper sector (C) in 2011.	79
Figure 65. Cumulative displacement graphs for the glacier terminus (A), intermediate (B) and upper sector (C) in 2012.	81
Figure 66. Cumulative displacement graphs for the glacier terminus (A), intermediate (B) and upper sector (C) in 2013.	82
Figure 67. Monthly icefall dynamics (2011).....	83
Figure 68. Monthly icefall dynamics (2012).....	84
Figure 69. Monthly icefall dynamics (2013).....	84
Figure 70. GNSS locations (a) and ice surface velocities between April 2012 and April 2013 (b). Insets show the ice movement vector at each of the four GNSS stations located along the axis of Falljökull with the length of the arrow reflecting ice surface velocity. From Phillips et al., (2014).	85
Figure 71. Flow variability between alpine and marine-terminating glaciers (data from Table 12).	89
Figure 72. Tephra deposition at Falljökull on 23/05/2011 from the Grímsvötn eruption. Tephra was present on the glacier surface throughout 2011.	92
Figure 73. Variation of temperature with depth for the conditions at Colle Gnifetti. Numbers next to curves indicate months (1: Jan, 2: Feb). From Lüthi et al., (2001)..	94
Figure 74. Extension of the debris band across the Falljökull terminus. The terminus is free of thick debris cover in 2012 (A). Debris is present in 2013, with thickness varying with altitude (B).	95
Figure 75. Development of and increased contact with the pro-glacial lake by 26/06/2011.	97
Figure 76. Extended preservation of the seasonal snowpack in 2013, relative to previous years.	99

List of Tables

Table 1. Meteorological variables.	51
Table 2. Energy balance modelling parameters.	53
Table 3. Virkisjokull ablation in 2014 (Flett, unpublished data).....	53
Table 4. Registration results.	56
Table 5. Annual surface velocity and thinning rate data.	58
Table 6. Intra-annual spatial variability in thinning rates: t-test results.....	60
Table 7. Inter-annual temporal variability in thinning rates: t-test results.	60
Table 8. Intra-annual spatial variability in surface velocities: t-test results.....	61
Table 9. Inter-annual temporal variability in surface velocities: t-test results.	63
Table 10. Inter-annual temporal variability in icefall surface velocities: t-test results.	63
Table 11. Energy balance modelling output (2011-2013).....	64
Table 12. Glacier surface velocities recorded at alpine, polythermal, surge-type, arctic and marine-terminating glaciers using time-lapse, GNSS and remote sensing.	88

Acknowledgements

I would like to thank Dr. Mike James and Dr. Peter Wynn for their supervision and support throughout this project. In particular, I am grateful to Mike for guiding me through Pointcatcher and for providing time and advice when I encountered difficulties in data analysis. Peter was a source of encouragement throughout and was instrumental in shaping the aims of this project. His glaciological expertise was also appreciated as I began to understand glacier dynamics at Falljökull. Both supervisors provided constructive comments on this manuscript which enabled me to refine the text and focus closely on the key issues.

I would also like to thank Dr. Jez Everest and the British Geological Survey for generously providing the time-lapse, meteorological and laser scanning data upon which this project was based. I hope that these results are of value to the BGS. Dr. Lee Jones provided assistance with data processing while Dr. Emrys Phillips kindly allowed published figures to be replicated in this thesis.

Finally, I would like to thank my family and friends for their support and guidance throughout the last year. This project would not have been possible without them. Thank you.

Chapter 1 - Introduction

1.1 - Glaciers-climate coupling

Glaciers, ice caps and ice sheets are important components of the global climate system because they respond rapidly to climate forcing (Raper and Braithwaite, 2009; Fountain *et al.*, 2012) and amplify its effects through feedback mechanisms (Flanner *et al.*, 2011). Given the rapidity of anthropogenic climate change (IPCC, 2014), understanding and predicting the response of glacial systems is of paramount importance (McCarroll, 2010).

However, although glaciers undergo adjustment to attain equilibrium with climate (Bahr *et al.*, 2009; Miles *et al.*, 2013), structural and topographic controls condition glaciers to respond individually to secular, decadal or annual climate forcing (Hoelzle *et al.*, 2003). As a result, glaciers can appear to respond asynchronously to regional climate (Patton *et al.*, 2013; Sorg *et al.*, 2015). Spatial variability in glacier-climate response is also evident (Arendt *et al.*, 2002; Zwally *et al.*, 2005). Currently, the greatest contribution to sea level rise is from small ice masses i.e. mountain glaciers and ice caps (Fig. 1), which respond rapidly to climate forcing and have a disproportionate climate feedback effect relative to their size (Raper and Braithwaite, 2006; Hock *et al.*, 2009; Cogley, 2009). These glaciers are expected to remain an important component of eustatic sea level rise for at least another century (Radic and Hock, 2011). Non-climatic factors including glacier size (Kirkbride and Winkler, 2012), geometry (Kuhn, 1989), hypsometry (Oerlemans *et al.*, 2007) and thermal

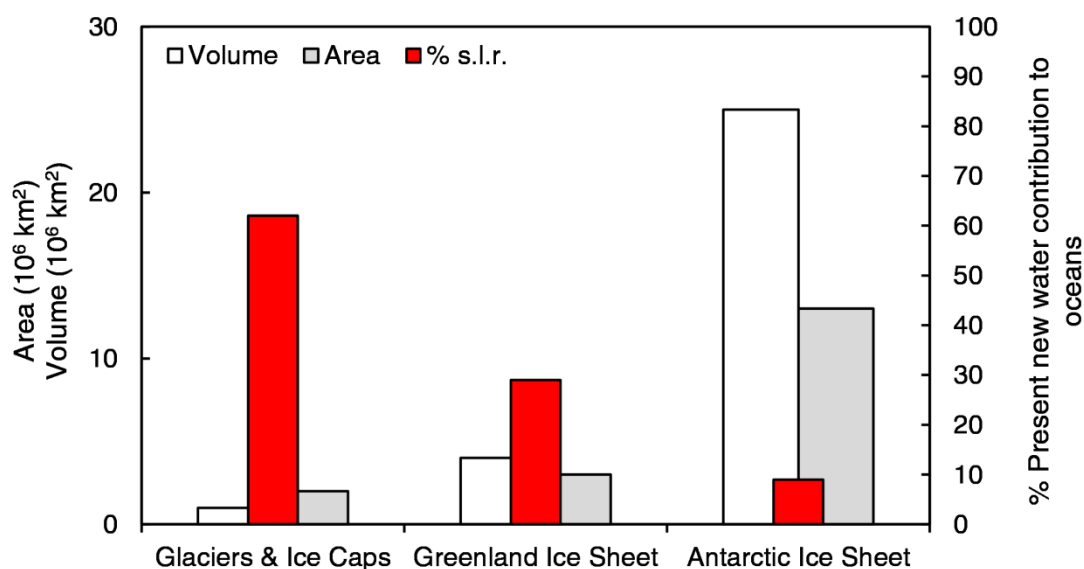


Figure 1. The contributions of glaciers and ice caps and the Greenland and Antarctic Ice Sheets to the present-day rate of sea-level rise (s.l.r.), along with their respective volumes and areas. Redrawn from Meier *et al.*, (2007)

regime (Raper and Braithwaite, 2009) can strongly modulate glacier flow and lead to the virtual decoupling of glacier response from climate (Winkler *et al.*, 2010). Over shorter timescales, surface energy balance (Röthlisberger and Lang, 1987) and glacier hydrology (Copland *et al.*, 2003) also control ice melt and ice dynamics. Further research is clearly necessary to study glacier-climate coupling at a high spatio-temporal resolution to determine the key controls on glacier dynamics.

1.2 - Ice melt and ice dynamics

Glaciers can move through internal deformation, sliding at the ice-bed interface and subglacial deformation. The relative importance of these distinct processes has been linked to surface meltwater input to the glacial system (e.g. Zwally *et al.*, 2002). However, the fundamental process of basal sliding is poorly understood (van Boeckel, 2015). Early research on small alpine glaciers demonstrated that surface meltwater can penetrate to the glacier bed, reduce friction (Bingham *et al.*, 2006) and accelerate flow (Iken *et al.*, 1983; Iken and Bindshadler, 1986). As a result, it was hypothesised that enhanced surface melt production would instigate a positive feedback loop, whereby accelerated glacier flow would increase the transfer of ice to the ablation area where melt and thinning are enhanced (Parizek and Alley, 2004).

However, this direct relationship between meltwater input, subglacial water pressure and basal motion has been challenged by recent research (Sole *et al.*, 2013; Tedstone *et al.*, 2013). Further studies have demonstrated that the relationship between ice melt and ice dynamics is non-local and non-linear (Bartholomaeus *et al.*, 2008; Howat *et al.*, 2008; Minchew *et al.*, 2016). To account for this behaviour, researchers have acknowledged the key role of subglacial drainage structure (location, alignment, interconnection) and morphology (size, shape, roughness) in modulating meltwater inputs and controlling basal water pressures (Hubbard and Nienow, 1997; Hock and Jansson, 2005). In particular, the temporal evolution of subglacial drainage (Flowers and Clarke, 2002) and its shift from steady state conditions (Kamb *et al.*, 1994; Anderson *et al.*, 2004; Bartholomaeus *et al.*, 2008) has proved to be a key control on glacier dynamics (Harbor *et al.*, 1997). Flow variance between distributed (unconnected) and discrete (connected) systems (Arnold *et al.*, 1998) may account for periods of enhanced flow due to basal sliding (Hooke *et al.*, 1990).

Despite this, hydrological forcing of ice velocity can also occur in connected, discrete systems if meltwater inputs are rising faster than the drainage system can adjust to (Bartholomew *et al.*, 2011). Furthermore, subglacial drainage demonstrates significant spatial variability, both between (Irvine-Fynn *et al.*, 2011) and within individual glaciers (Cowton *et al.*, 2013) with structural variation preserved over multiple seasons (Willis *et al.*, 2012). This relationship is further complicated by significant

spatio-temporal variability in surface meltwater production due to glacier surface conditions (Röthlisberger and Lang, 1987). Meltwater inputs to the subglacial system are also modulated by the structure and efficiency of englacial drainage (Flowers, 2008). As a result, the relationship between ice melt and ice dynamics (Iken *et al.*, 1983) is characterised by considerable complexity due to surface energy balance and glacier hydrology. Understanding the controls on glacier dynamics should be a key focus of glaciological research as hydrologically induced glacier speed up may lead to instability and accelerated mass loss (Aðalgeirsdóttir *et al.*, 2011).

1.3 - Project rationale

Small, temperate, mountain glaciers in maritime environments have been shown to be extremely sensitive to climatic perturbations (Shi and Liu, 2000; Dyurgerov, 2003). For this reason, the British Geological Survey (BGS) have been monitoring the Falljökull glacier in SE Iceland. Given the importance of this glacier and similar ice masses in driving eustatic sea level rise (Radic and Hock, 2011), determining the key controls on glacier dynamics will provide a useful insight into the response of similar glaciers to future climate change. Falljökull is undergoing rapid retreat (Bradwell *et al.*, 2013; Phillips *et al.*, 2014) and may have accelerated in the last 5 years.

The BGS have generated large volumes of time-lapse imagery and laser scanning data as well as high temporal resolution meteorological data from three automatic weather stations (AWS). This project will integrate 3D digital elevation models (DEMs) and 2D time-lapse data to derive glacier surface velocities and rates of thinning from which patterns of hydrodynamic coupling i.e. meltwater forcing of ice velocity, can be determined. These data will be generated using Pointcatcher, a feature tracking software previously used on Solheimajökull, SE Iceland (James *et al.*, 2016) and interpreted in the context of structural glacier changes and energy balance modelling. Although time-lapse imagery has been used extensively in glaciological settings, its integration with meteorological data has been limited. The linking of these datasets provides a deeper insight into the mechanics of glacier movement at a high spatio-temporal resolution.

In order to determine the controls on glacier dynamics at Falljökull, this thesis has three main objectives:

1. To generate high spatio-temporal resolution datasets of glacier thinning and ice dynamics at Falljökull using time-lapse imagery.

2. To compare these data with estimates of surface melt production from energy balance modelling to determine the key controls on surface melt.
3. To address the degree of connectivity between ice thinning and ice dynamics in the context of surface melt production and glacier hydrology.

Chapter 2 - Literature Review

2.1 - Glacier dynamics

Glacier flow is a product of stress and strain. Stress is the external force acting upon an object while strain is the response to the applied stress. Stress is expressed by the following equations for normal and shear stress respectively:

$$\sigma = \rho_i gh \quad (1)$$

$$\tau = \rho_i gh \sin a \quad (2)$$

where ρ_i is the weight of the ice, g is gravity, h is ice height and a is slope angle. Normal stress incorporates the vertical forces at work, including the weight of ice and gravity, while shear stress accounts for the forces acting in parallel i.e. slope angle. The response of the glacier to these stresses is expressed as the strain rate which is dependent on the strength of the ice and the contact with and structure of the bed. However, this movement is manifested in three distinct ways incorporating internal, basal and subglacial processes. The relative importance of these processes varies significantly as a result of glacier thermal regime. In cold based glaciers, where ice is frozen to the bed, flow is dominated by internal movement due to a restricted subglacial meltwater flux. In temperate glaciers, where ice is above the pressure melting point throughout, internal, basal and subglacial derived flow are all possible, although the rheology of the bed is a key control. Polythermal glaciers are inherently more complex and flow is a function of the temperature distribution in the ice and at the bed (Irvine-Fynn *et al.*, 2011).

Another key variable to consider is balance velocity, defined as the amount of ice discharged through the equilibrium line i.e. the line of zero net mass loss/gain. Balance velocity variability is crucial to understanding long term changes in glacier velocity and rates of surface elevation change as this determines the amount of ice being transferred to lower elevations where surface melting and runoff are enhanced (Bingham *et al.*, 2006). However, glacier response time i.e. the time it takes for a glacier to respond to an external climate forcing, varies significantly between glaciers. Short steep glaciers, particularly those in maritime environments, may respond in only a few years to climate forcing, while large valley glaciers may take up to a century and ice caps much longer (Kirkbride and Winkler, 2012).

2.1.1 - Internal deformation

Internal movement is a function of ice deformation through the processes of creep and fracture. Creep is described by Glen's flow law:

$$\dot{\epsilon} = A \tau^n \quad (3)$$

where $\dot{\epsilon}$ is defined as the strain rate, A is ice hardness, τ is shear stress and n is the creep exponent, a constant value (~ 3) that refers to the plasticity of the flowing material. Based on the Eqn (3), shear stress increases with ice thickness while the strain rate increases exponentially with depth. However, when ice cannot creep fast enough to adjust its shape for a given stress, brittle failure in the form of ice fracture occurs. Ice fracture is the primary driver of surface crevassing although these features rarely propagate to the glacier bed as an increase in strain rate with depth is offset by an increase in ice strength (Hambrey, 1994).

Traditionally, rates of internal ice deformation were assumed to be constant over short timescales and short term fluctuations in glacier surface motion (e.g. Hooke *et al.*, 1989) were solely attributed to basal or subglacial derived flow. However, numerous studies using inclinometry (Hooke *et al.*, 1992; Harper *et al.*, 1998), englacial tiltmeters (Gudmundsson, 1999; Mair *et al.*, 2003) and differential changes in borehole depths (Sugiyama and Gudmundsson, 2003) have shown that short term changes in ice deformation rates can occur. A notable study on Haut Glacier d'Arolla, Switzerland by Mair *et al.*, (2008) demonstrated daily increases in ice deformation rates due to the occurrence of hydrologically induced, localised basal slippery spots. However, these were not associated with any change in surface velocity. Basal slippery spots are defined as areas where basal drag is low. These features enhance basal motion and result in glacier speed up as shear stresses cannot be supported. This results in the transferral of stress elsewhere over the glacier bed, creating increased ice-bed coupling which accounts for the observed increase in ice deformation rates. This pattern of internal ice deformation (Mair *et al.*, 2008) indicates that basal ice flow can exhibit rapid changes in stress due to small spatial scale variability in bed conditions (Blatter *et al.*, 1998). As such, ice dynamics should be considered in the context of bed rheology.

2.1.2 - Basal sliding

Glaciers can also move due to sliding at the ice-bed interface. However, given that glacier beds are inherently rough, regelation sliding can occur (Weertman, 1957, 1964), with this process initiated due to the variance in pressure between the lee and stoss sides of bedrock obstacles (Fig. 2). Ice melts on the lee side due to enhanced pressure with meltwater flowing over bedrock obstacles and refreezing on the stoss side due to a pressure reduction. The latent heat of this refreezing is advected back through the obstacles to sustain melting although this process cannot be effectively maintained if obstacles are in excess of 1 m in diameter (Kamb, 1970). To accommodate this, enhanced creep occurs where localised ice deformation allows ice

to flow around obstacles. Therefore, the relative importance of enhanced creep or regelation sliding is dependent on obstacle size. However, these processes are largely a function of glacier thickness, surface slope and bed roughness, variables that cannot change over short timescales. Despite this, short term variability in glacier surface velocities are evident (e.g. Nienow *et al.*, 2005). These diurnal fluctuations in surface velocities are fundamentally linked to water pressure and cavitation.

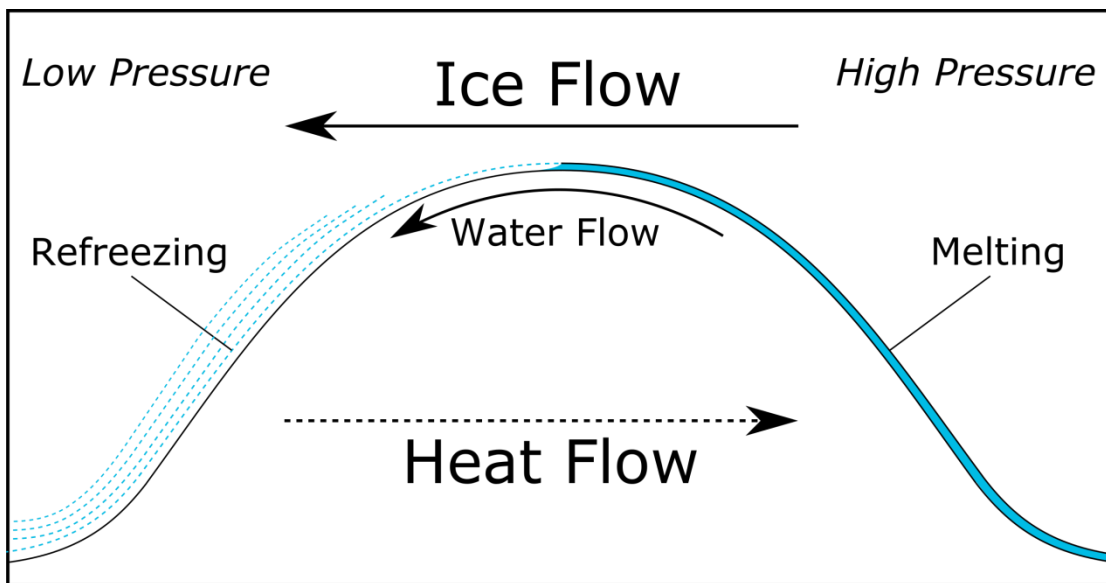


Figure 2. Regelation sliding. Redrawn from Benn and Evans (1998)

The Liboutry-Fowler cavitation sliding law is expressed by the following equation:

$$U_s = \tau^p N^q \quad (4)$$

where U_s is basal sliding, τ is basal shear stress, N is the effective normal pressure (discussed in Chapter 2.3.3) while p and q are empirically determined constants. Although rates of basal sliding increase with basal shear stress, sliding is inversely proportional to the effective pressure. The submergence of minor roughness obstacles (Bingham *et al.*, 2006) promotes enhanced velocities as water cannot support basal shear stress, with pressure concentrated over the remaining portion of the bed in contact with the ice. This accelerates regelation sliding and deformation of the bed due to increased shear stress.

The relationship between surface velocities and subglacial hydrology was studied at John Evans Glacier, Canada (Copland *et al.*, 2003), a predominantly cold-based polythermal glacier. Initial assessments of subglacial hydrology at similar glaciers indicated that penetration of supraglacial meltwater to the bed was limited (Hodgkins, 1997) because water flow along intergranular vein networks is largely absent in cold ice and because crevasses and moulins, features which introduce large scale permeability to ice, are rare due to low rates of ice deformation and refreezing of meltwater. However, seasonal shifts in surface velocity were evident and were

attributed to increased basal sliding as mean horizontal velocities increased from 3.5 cm d⁻¹ in winter to 5.3 cm d⁻¹ in summer, coeval with an enhanced meltwater flux (Copland *et al.*, 2003). However, this seasonal speedup was concentrated during high velocity events which lasted only 2-4 days, while surface velocity fluctuations were not spatially ubiquitous. While the mean velocity of the lower terminus increased by 110% relative to winter levels, upper terminus speedup was limited to 75%, spatial variability that probably accounted for by the increasing prevalence of cold-based ice up-glacier. The key driving force throughout were fluctuations in subglacial water pressure, as the rapid transfer of large meltwater fluxes to the subglacial network led to over pressurisation, uplift of the ice, a reduction in shear stress and increased rates of basal sliding (Copland *et al.*, 2003).

A further study at John Evans Glacier linked basal sliding to subglacial drainage structure (Bingham *et al.*, 2006). Annual dynamics at this glacier are a function of internal deformation and long term average basal motion but significant short term variability can occur as a result of supraglacial hydrological forcing. However, these events are mediated by the efficiency of the subglacial drainage system. Initial forcing occurs during the early melt season as a result of the drainage of large fluxes of supraglacial meltwater, which overcome a threshold to permit englacial drainage through the cold ice. High horizontal surface velocities subsequently propagate down glacier and the glacier exhibits uplift, as high pressure subglacial water overrides the inefficient distributed system. Summer weather conditions are key to determining the timing of this shift from distributed to discrete drainage. Further research using 3D flow modelling was undertaken to determine the spatial distribution of basal sliding (Bingham *et al.*, 2008). However, this study indicated that stress gradient coupling is ineffective at transmitting basal motion anomalies over one part of the bed more widely through the glacier. This is attributed to high drag imposed by the partially frozen bed and friction from the valley walls and topographic pinning points. This study emphasises the dynamic nature of basal motion due to both thermal regime and local topographic and structural controls but also demonstrates that surface velocity variability is more likely to arise directly from local basal forcing i.e. direct surface meltwater input, and not represent stress gradient coupling with non-local basal forcing.

2.1.3 - Subglacial deformation

Glaciers can also move through bed deformation (Boulton *et al.*, 2001). As glaciers are often underlain by a porous layer of till (Boulton and Hindmarsh, 1987), it has been hypothesised that deformation of this till layer will promote glacier movement (Fig. 3; Boulton and Jones, 1979; Clark, 1994; Murray, 1997). At Breidamerkurjökull, Iceland, an early study by Boulton and Jones (1979) concluded that 88% of basal

movement could be attributed to deformable sediment. However, deformation cannot occur until a critical shear stress has been exceeded, described by the following equation:

$$ES = K(\tau - \tau^*)^a N^{-b} \quad (5)$$

where ES is defined as the strain rate, τ is shear stress, τ^* is critical shear stress, N is effective pressure and K , a and b are empirically determined constants.

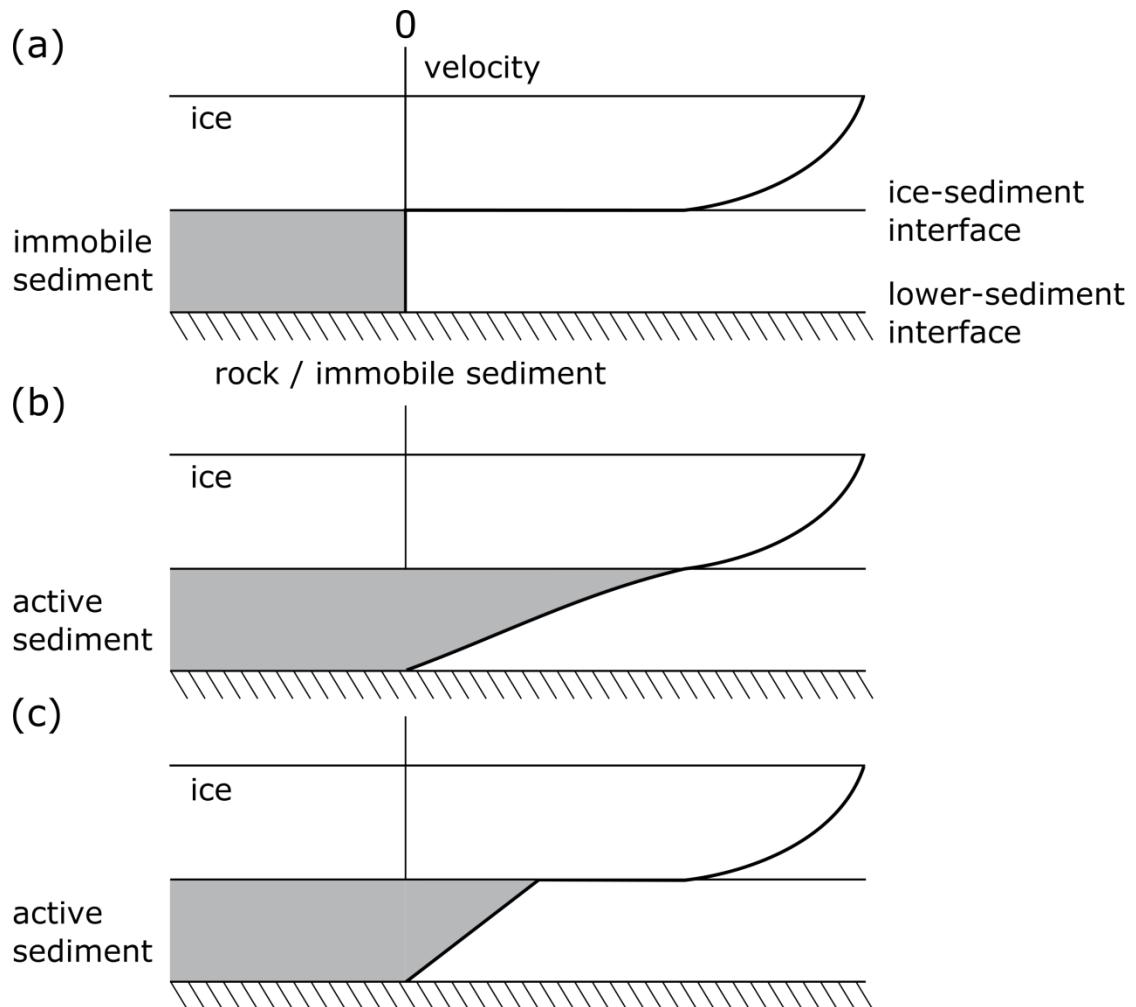


Figure 3. Idealised velocity profiles for an ice mass overlying soft sediments. (a) The ice mass is completely decoupled from its bed, and basal sliding is the only form of basal motion. (b) The ice mass is completely coupled to its bed, and sediment deformation is the only form of basal motion. (c) The ice mass is partially coupled to its bed, and both sliding and sediment deformation occur. Redrawn from Murray (1994).

Critical shear stress is described by the following equation:

$$\tau^* = C + N \tan \phi_i \quad (6)$$

where C is cohesion, ϕ_i is the angle of internal friction based on the arrangement, size and shape of grains and N is normal stress. The structural strength of till and its

propensity for deformation is strongly affected by variation in pore-water pressure. Negative pressure causes grains to be pulled together which increases normal stress and internal friction. In contrast, positive pressure decreases sediment stability as grains are forced apart and internal friction is reduced. As a result, deformation occurs more readily when subglacial drainage is inefficient and when water pressures are high. This is most common during the early melt season when the drainage system has not yet adjusted to higher water flux and through hydraulic jacking, developed more efficient channelized drainage. However, rates of sediment deformation decrease with depth as normal stress and frictional strength increase (Iverson *et al.*, 1995) while water pressures within the sediment layer itself determine its susceptibility to deformation. As such, this process is highly dynamic as water pressures can vary significantly over short timescales due to the varying input of supraglacial meltwater (Clark, 1995).

However, the subglacial deformation hypothesis has been challenged by recent research. Flow modeling indicates that deforming sediment would behave as a nearly perfect plastic and lead to highly unstable behavior (Kamb, 1991). Further work at Storglaciären, Northern Sweden (Iverson *et al.*, 1995) demonstrated that flow acceleration occurred when basal water pressure increased sufficiently to raise the glacier from its bed. Although sediment was undergoing deformation, ice-sediment de-coupling was evident as the rate of deformation decreased during the glaciers most rapid flow and rapidly increased during deceleration. Although unlithified sediment may deform readily if basal water pressures are near the ice overburden pressure, it appears that deformation is not the primary mechanism for movement as it accounted for only 5% of glacier displacement (Iverson *et al.*, 1995). However, deformable beds may be an important control on the timing of periods of fast glacier flow as they provide a smooth surface to support concentrated shear stresses.

2.1.4 - Key methods for measuring ice movement

Glacier surface velocities are primarily measured using satellite remote sensing or in-situ global navigation satellite system (GNSS) data. The recent application of interferometric synthetic aperture radar (InSAR) has allowed researchers to quantify glacier flow over large spatial scales (e.g. Mouginot *et al.*, 2014). Differential interferograms are created based on the difference in phase lengths of multiple SAR images. If the elevation signal can be removed and control points of zero motion identified, then phase length variation must be related to topographic deformation (ice flow) (Rignot *et al.*, 2011). InSAR works effectively independent of cloud cover, solar illumination or surface features (Goldstein *et al.*, 1993) and improves on traditional velocity assessments which are based on oversimplifications, assuming ice

sheet equilibrium and perpendicular ice flow to surface contours (Rignot *et al.*, 2011). Unfortunately, data is typically of low temporal resolution (Quincey and Luckman, 2009). The errors of 16-60 m yr⁻¹ calculated by Mougnot *et al.*, (2014) are closely correlated with the time interval between images. Orbital errors are also possible although are generally smaller than expected (Fattahi and Amelung, 2014). Consistent satellite position between SAR images ensures that phase length variation is solely a function of terrain deformation. InSAR has been applied to the Greenland and Antarctic ice sheets and shown increasing discharge from outlet glaciers (Mougnot *et al.*, 2014) and acceleration into ice sheet interior (Rignot *et al.*, 2011) as well as localised slowdowns, demonstrating significant variation between basins (Thomas *et al.*, 2013). Recent studies have also studied glacier velocities at terrestrial ice caps in Iceland using inSAR (Palmer *et al.*, 2009; Minchew *et al.*, 2016). However, the application of inSAR to small, mountain glaciers has been limited.

In contrast, GNSS data is of higher temporal resolution (e.g. 10s intervals in Sole *et al.*, 2011) and of comparable precision (Manson *et al.*, 2000) and has been applied to mountain glaciers in Iceland (Phillips *et al.*, 2014), New Zealand (Kehrl *et al.*, 2015) and the Himalaya (Copland *et al.*, 2009; Sugiyama *et al.*, 2013). By deploying GNSS receivers along a glacier flow line and linking observations to a stable base station, velocity changes can be quantified. Surface velocity fluctuations have been linked to surface melt-induced changes in subglacial hydrology over short term (Sole *et al.*, 2011) and annual timescales (Sole *et al.*, 2013) in agreement with previous research (Pimental and Flowers, 2011; Sundal *et al.*, 2011; Van de Wal *et al.*, 2008). GNSS data has also been used to demonstrate ice sheet self-regulation (Van de Wal *et al.*, 2015) as well as structural (Phillips *et al.*, 2014) and hydrological controls (Bartholomaeus *et al.*, 2008) on ice dynamics. However, rigorous GNSS data processing is necessary to generate accurate results (King, 2004; Khan *et al.*, 2008). Additionally, GNSS data are typically of low spatial resolution e.g. just 4 GNSS receivers along a 36 km glacier flowline at Kangiata Nunata Sermia in Greenland (Sole *et al.*, 2011).

In contrast, glacier feature tracking through time-lapse image sequences may permit study of small spatial scale variability in glacier flow that is poorly captured by GNSS. Terrestrial time-lapse imagery has the potential to significantly improve our understanding of glacier dynamics by monitoring changes at high spatio-temporal resolutions (Cerney, 2010; Danielson and Sharp, 2013). This technique should provide a practical, cost-efficient alternative (Corripio, 2004; Garvelmann *et al.*, 2013) to in-situ GNSS (Hamilton and Whillans, 2000) or terrestrial laser scanning (Schwalbe *et al.*, 2008) which can be readily applied to many glacial environments with careful planning and choice of site location (Danielson and Sharp, 2013).

2.2 - Energy Balance

2.2.1 - Key variables

Surface energy balance determines the production of meltwater in the supraglacial environment (Röthlisberger and Lang, 1987) but is strongly affected by the characteristics of the glacier surface. When the surface energy budget is positive, energy is available for melt. When the budget is negative, there is a net loss of energy at the glacier surface. Surface energy balance (SEB) is expressed by the following equation:

$$Q_m = Q_{sw} + Q_{lw} + Q_s + Q_l + Q_p + Q_g \quad (7)$$

where m is the energy available for melt, sw is short wave radiation, lw is long wave radiation, s is sensible heat, p is precipitation and g is the heat from conduction. This final variable is often overlooked (Greuell and Oerlemans, 1986; Oerlemans and Klok, 2002) but is important as energy is required to raise the snow or ice surface to 0°C before melting can occur, a process which delays the onset and reduces the total amount of supraglacial melt. The incoming energy from short wave radiation (SWR) is often the primary driver of supraglacial melt (Braithwaite and Olesen, 1990; Munro, 1990) while long wave radiation (LWR) from clouds or surrounding topography often contributes a small net loss of energy (Arnold *et al.*, 1996). At Storbreen, Norway, SWR contributed 76% to surface energy balance (Andreassen *et al.*, 2008), a value supported by previous research (Willis *et al.*, 2002; Hock, 2005). Turbulent heat fluxes of sensible heat, the direct transfer of energy from the atmosphere to the snowpack, and latent heat, the transfer of energy during a change of state i.e. water to ice, contributed the remaining 24% of the surface energy budget. The relative importance of radiative and turbulent heat fluxes is strongly affected by continentality (Engelhardt *et al.*, 2015) as maritime glaciers are subjected to humid air streams and enhanced sensible heat fluxes (Laumann and Reeh, 1993). If all variables are known, a melt rate can be calculated expressed by the following equation:

$$M = Q_m/L \quad (8)$$

where M is the mass of ice melted and L is the latent heat of melting. Determining an accurate melt rate is necessary to understand changes in hydrology and glacier dynamics as a result of variable meltwater flux. Radiative and turbulent energy fluxes are also affected by glacier surface conditions, which can change over hourly (Oerlemans and Klok, 2002), diurnal (Munro, 1990) and seasonal timescales (Sicart *et al.*, 2011) and affect meltwater production and through surface-bed coupling, the patterns of internal, basal and subglacial derived flow.

2.2.2 - Controls on energy flux

Surface melt production due to incoming short wave radiation is strongly dependent on albedo, defined as the reflectivity of the surface (Van de Wal *et al.*, 1992). However, estimating albedo is typically associated with significant errors (Arnold *et al.*, 1996; Klok and Oerlemans, 2002) as spatio-temporal variability is common (Klok and Oerlemans, 2004). Albedo can have a significant impact on melt production as a modelled albedo perturbation of just 0.1 can result in mass balance changes of 0.5 - 1.5 mWE yr⁻¹ (Oerlemans and Hoogendoon, 1989), equivalent to atmospheric warming of 1k (Oerlemans, 1992). Albedo change has a disproportionate effect at the glacier terminus (Munro, 1991) due to the sensitivity of the margin to warming and the increasing prevalence of dust, snow, liquid water and debris cover (Fig. 4). Albedo feedbacks are also key (Greuell and Bohm, 1998) as glaciers with a low ice albedo are more sensitive to change, particularly as a result of climate forcing (Hock *et al.*, 2007; van Pelt *et al.*, 2012). Albedo is affected by snow depth, dust content, debris cover, metamorphism of snow crystals, snow density, water content and the uncovering of superimposed or glacier ice (Paterson, 1994).

A	Surface Characteristics	Albedo Range (%)
	Dry snow	80 - 97
	Melting snow	66 - 88
	Firn	43 - 69
	Clean Ice	34 - 51
	Slightly dirty ice	26 - 33
	Dirty ice	15 - 25
	Debris covered ice	10 - 15

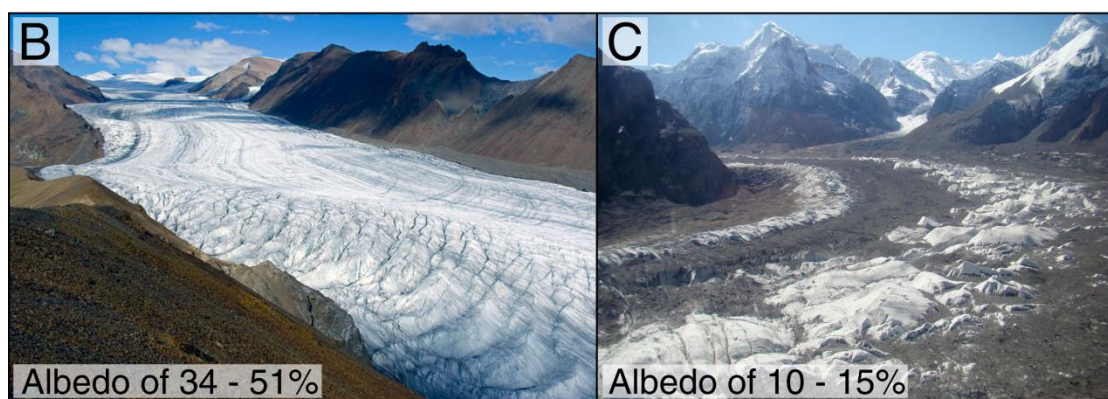


Figure 4. Albedo variation (A) from Benn and Evans (1998). The clean ice of White Glacier, Axel Heiberg Island, Canada (B) (Photo source: <http://tinyurl.com/hk93nm5>) and the debris covered Inylchek glacier in Eastern Kyrgyzstan (C) (Photo source: <http://tinyurl.com/h9j3ava>)

At high latitudes, longwave radiation can provide similar or higher amounts of energy to snow than SWR, typically 10 - 26 MJ m⁻² day⁻¹ (Sicart *et al.*, 2006), as a result of the cosine effect and increased scattering due to long atmospheric path lengths (Muller, 1985; Granger and Gray, 1990; Duguay, 1993). This has been demonstrated for the Greenland Ice Sheet (Ambach, 1974) as high values of net radiation were

correlated with high values of LWR but low values of SWR. However, LWR is also of increasing importance when cloud cover is significant as peak radiation (270 J/cm^2) occurred when cloudiness was ranked 10/10. In contrast, the mean value for net radiation was just 75 J/cm^2 when cloudiness was ranked 0/10 (Ambach, 1974). This trend was also observed at Midtdalsbreen, Norway (Giesen *et al.*, 2008). Although the melt rate was generally higher under clear skies, almost 60% of the melt occurs under cloudy skies as wind speed and humidity were enhanced. In general, melt energy is considerably underestimated on days characterised by dense fog or precipitation (Hock and Holmgren, 1996).

Both SWR and LWR are affected by aspect i.e. the overall flowline direction, as well as local topography. Although energy balance is strongly dependent on incoming net radiation, glacier gradient and orientation are key to determining the spatial distribution of energy (Duguay, 1993), particularly in mountainous terrain (Olyphant, 1986b). Aspect can control diurnal variations in solar radiation incidence, temperature, wind and cloudiness (Evans, 1977). In most regions, the favoured aspect is poleward, which confirms the importance of shade and radiation incidence in affecting surface energy balance, particularly in accumulation areas (Evans, 2006). However, lineated or asymmetric topography can bias glacier aspect. Slope-aspect relationships (Hock, 2005) show that energy balance is latitude dependent and can have positive or negative impacts on the overall irradiance balance depending on the relative angle to solar zenith.

Topography also impacts on LWR by controlling isotropic radiance (Olyphant, 1986a) as a result of atmospheric conditions and surface temperature (Plüss and Ohmura, 1996). This effect is magnified in mountains due to shading. However, LWR is generally more sensitive to sky view factor than the temperature of the emitting terrain surface although terrain emission can be significant when sky irradiance is low, for example during the cold-dry atmosphere of early spring or at high elevations or latitudes. This may enhance snowmelt on opposing facing slopes. The effects of shading, slope and aspect are magnified at high latitudes due to the cosine effect (Duguay, 1993) although this may be tempered by increasing daylight hours. In polar glaciers, the paradoxical role of aspect and slope had no effect on the total amount of incoming radiation but produced cross glacier variations (Arnold *et al.*, 2006). Slope-aspect relations and local topography may be of importance in determining similar variability in melt production at Falljökull, particularly given the steep valley walls and enclosed nature of the basin.

Turbulent heat transfers via sensible and latent heat are strongly controlled by boundary layer conditions including wind, air turbulence and surface roughness (Irvine-Fynn *et al.*, 2014). Under conditions of low wind speed and strong stability, turbulent fluxes may be severely restricted and may reduce to zero (Brock and

Arnold, 2000). Turbulent heat fluxes are assumed to be zero based on the Monin-Obukhov similarity theory (Arnold *et al.*, 2006) when the following conditions are met:

$$u < 2 \text{ m s}^{-1} \text{ and } \frac{u}{T} < 0.3 \quad (9)$$

or

$$u < 1.5 \text{ m s}^{-1} \text{ and } -1.5^\circ\text{C} < T < 1.5^\circ\text{C} \quad (10)$$

where u is wind speed and T is temperature (Brock and Arnold, 2000). Strong stability over melting ice surfaces are best approximated used log-linear air profiles (Braithwaite *et al.*, 1998). However, assumptions about the roughness length profiles for wind and temperature can result in errors, as these parameters can vary over time. While the effect of stability is fairly small, careful model tuning should be undertaken by choosing roughness and albedo values which reduced the error between observed and calculated daily ablation (Braithwaite *et al.*, 1998). Precipitation can also play a key role in turbulent heat fluxes, particularly when the snow/ice surface is $< 0^\circ\text{C}$ as the freezing of rainwater releases latent heat. This process is of particular importance in maritime environments as moist air masses over maritime glaciers increase the transfer of sensible heat and latent heat of condensation (Willis *et al.*, 2002). For these glaciers, net radiation contributes only 10-50% of ablation energy. In contrast, for continental glaciers under clear sky conditions, net radiation has been shown to contribute 66% of ablation energy.

2.2.3 - Modelling

Researchers have attempted to develop energy balance models (EBMs) which incorporate these controls. However, initial models had limited spatial resolution, failed to include turbulent heat fluxes (Munro and Young, 1982) and did not consider the effects of surface albedo variation particularly accurately. As such, the development of a distributed surface energy balance model for Haut Glacier D'Arolla (Arnold *et al.*, 1996) significantly improved on previous studies by incorporating these variables. This study is particularly useful as it emphasises the need for careful consideration of model inputs as radiative fluxes were significantly higher than previous studies. This variability was primarily due to improved albedo parameterization (Oerlemans, 1993; Munro and Young, 1982; Escher-Vetter, 1985) as previous work had overlooked rapid snowline retreat and earlier exposure of bare ice. Energy balance models should incorporate the changing nature of the glacier surface throughout the melt season.

Furthermore, it is preferable if EBMs can be readily adapted to different sites and are flexible enough to enable the integration of additional energy fluxes e.g. Brock and Arnold (2000). However, while the application of these models to Falljökull is straightforward, they may oversimplify complex boundary layer interactions. For example, there is uncertainty over the physics of the surface atmospheric layer in regards to profiles of wind, temperature and humidity and whether these should be derived from physics (Grainger and Lister, 1966; Munro and Davies, 1977; Halberstam and Schieldge, 1981), logarithmic profiles (Munro, 1989; Braithwaite, 1995) or from empirical relationships (Hock and Noetzli, 1997). Further assumptions are involved in determining aerodynamic roughness length (Brock, 1997). The model also assumes no conduction of heat into the snowpack (Brock and Arnold, 2000), although this is assumed to be insignificant except for high alpine and polar glaciers (Price, 1986; Braithwaite, 1995). While the model originally excluded energy contribution from precipitation, as this was deemed important only in exceptional circumstances (Marcus *et al.*, 1985), it was updated by Thompson (2016) to include this energy flux. The impact of debris cover is also not included in this model despite its importance to glacier thermodynamics (Brock *et al.*, 2010). While the updated energy balance model developed by Reid and Brock (2010) does address this issue, it requires accurate data for debris extent, thickness and thermal properties. Results from this updated model corroborate with the Østrem curve (1959) which shows that thin debris cover enhances melt. When debris cover exceeds a critical threshold of 20 - 30 mm (Warren, 1984), melt is suppressed (Fig. 5). Thin debris cover not only reduces albedo but acts as source of retained heat (Carenzo *et al.*, 2016).

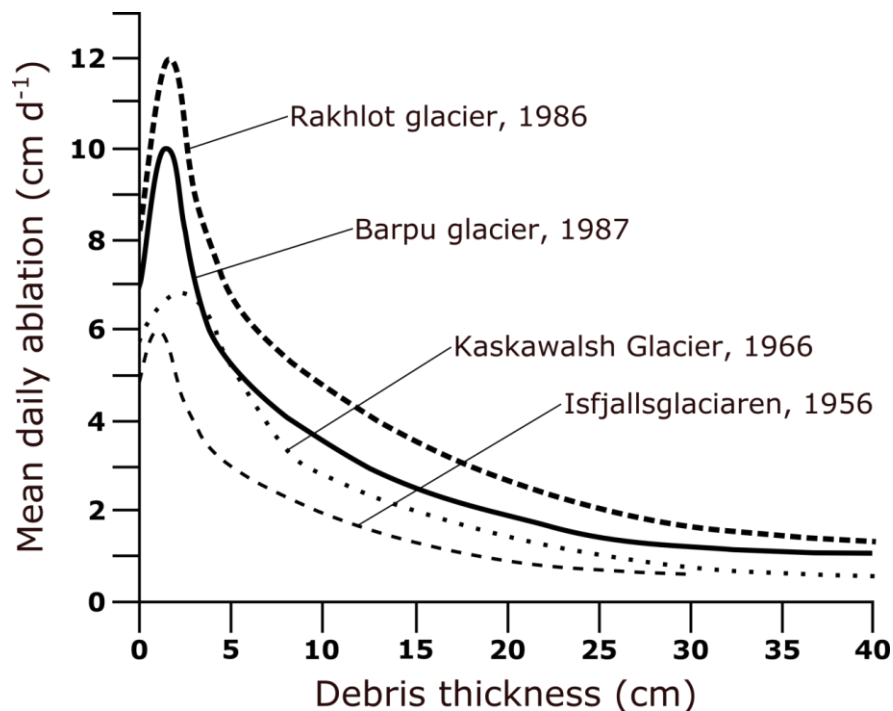


Figure 5. The relationship between debris thickness and mean daily ablation rate. Redrawn from Nicholson and Benn (2006)

2.3 - Hydrology

Glacier hydrology is strongly controlled by surface energy balance as the spatio-temporal variability in supraglacial meltwater production determines the timing and magnitude of water input into the englacial and subglacial environment. See the reviews by Fountain and Walder (1998) and Hubbard and Nienow (1997) for temperate glaciers and Irvine-Flynn *et al.*, (2011) for polythermal glaciers. In cold-based glaciers, it was commonly suggested that the predominance of impermeable ice ensured that supraglacial–subglacial hydrological connections were limited (Bingham *et al.*, 2006). However, researchers now acknowledge that significant transfer does occur (e.g. Boon and Sharp, 2003) and as such, the review of cold based glacier hydrology by Hodgkins (1997) is a useful introduction to the subject. Drainage can effectively be separated into three distinct but interlinked pathways; supraglacial, englacial and subglacial flow.

2.3.1 - Supraglacial drainage

Supraglacial flow is highly dependent on the nature of the glacier surface and is characterised by open stream hydrology (Fig. 6), limited percolation into the ice surface and the rapid transit of water to crevasses and into the englacial system (Fountain, 1992a). This pattern of flow is described by the Manning equation:

$$t_i = nL/R^{2/3}\theta^{1/2} \quad (11)$$

where t_i is water velocity, nL is surface roughness, R is the hydraulic radius of the ice surface and θ is slope angle. In general, an increase in water velocity is associated with an increase in slope angle, a reduction in surface roughness and an increase in the hydraulic radius of the ice surface. In contrast, the presence of snow or the firn layer at the glacier surface introduces complexity to supraglacial runoff (Illangasekare *et al.*, 1990). For example, flow variance between unsaturated wet snow, saturated wet snow and unsaturated dry snow is significant (Colbeck, 1978). For wet snow, which is isothermal at 0°C, storage capacity, snow depth, permeability, water flux, water density, gravity and the viscosity of water interact strongly to augment flow. In contrast, flow through unsaturated dry snow, which is below 0°C, has yet to be robustly described due to the complex interaction between irreducible water content, the freezing and release of latent heat and the presence of ice layers and preferential flow pathways. In general, snow cover leads to significant flow deceleration. In the unsaturated zone, water percolates vertically through the snow before refreezing. The formation of ice layers results in horizontal percolation although layers can disintegrate quickly when subjected to large meltwater fluxes (Male, 1980). Saturated snow leads to direct downslope runoff (Colbeck, 1973).

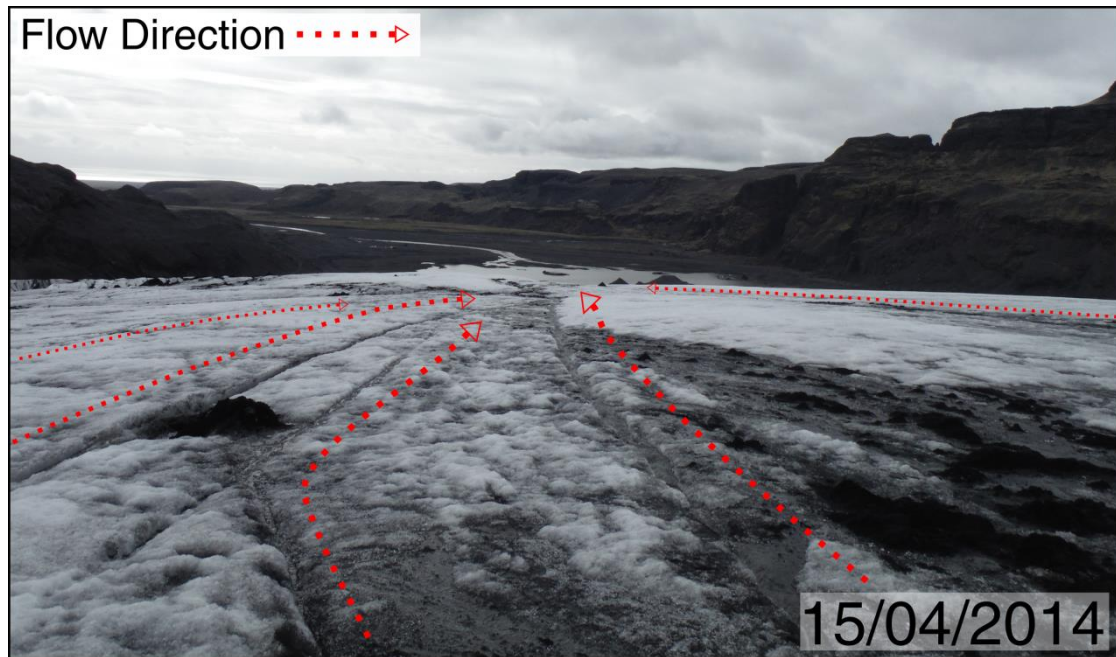


Figure 6. Supraglacial flow pathways on Solheimajökull, SE Iceland, photo taken by the author.

The snow layer can also restrict meltwater input by temporarily storing water in the saturated layer. However, the offset between melt events and discharge into the englacial system varies significantly from spring to mid-summer although there is no clear consensus as to whether this is linked to water storage or an enlarging subglacial hydraulic system (Röthlisberger and Lang, 1987). Another explanation is that the removal of the snowpack leads to the exposure of bare ice and rapid flow into the englacial system (Hannah and Gurnell, 2001). The timing of snowpack removal is key to determining rates of melt and runoff (Willis *et al.*, 2002) while snowpack thickness has been shown to have an effect on the morphology of subglacial drainage systems (Nienow *et al.*, 1998) which in turn controls subglacial water pressures and rates of basal motion (Fischer *et al.*, 1999). Therefore, glacier surface conditions are a key control on ice movement (Willis *et al.*, 2002).

2.3.2 - Englacial drainage

The structure and morphology of englacial drainage varies throughout the year as the change in runoff response time (Munro, 2010) reflects the seasonal development of englacial and subglacial controls (Flowers, 2008). Water flow is distinct between primary permeability i.e. movement of water between ice crystals, and secondary permeability, i.e. water flow through much larger pathways such as channels, moulins and crevasses. The vast majority of meltwater is transferred to the subglacial system through secondary permeability although there is no consensus regarding the structure of englacial flow pathways (Röthlisberger, 1972; Shreve, 1972; Hock *et al.*,

1999). However, englacial drainage is an important control on glacier dynamics as drainage efficiency determines the transfer of water to the bed and the glaciers propensity for basal sliding.

Both Röthlisberger (1972) and Shreve (1972) argued that semi-circular conduits transported the vast majority of water to the bed with their formation and survival dependent on the rate of ice creep and the outward melting of channel walls due to frictional heating. These conduits form an upward branching arborescent network due to the pressure gradient between smaller and larger conduits (Hooke, 1989). The Shreve model is based on the principle that wall melt by dissipation, a process which lowers channel pressure, is enhanced in larger conduits due to greater meltwater discharge and therefore greater heat dissipation per unit wall area (Gulley *et al.*, 2009). This creates areas of low potential which will tap smaller passages in which hydraulic potential is higher and results in an arborescent structure where water is routed into increasingly large channels further down the glacier.

However, despite these models being generally accepted (Fountain *et al.*, 2005a), there are a number of assumptions involved (Gulley *et al.*, 2009). Firstly, they assume steady state conditions, which is clearly not applicable to systems that are fed by supraglacial melt with large diurnal, seasonal and annual fluctuations (Schuler *et al.*, 2004). Secondly, they assume that recharge is distributed evenly across the surface of the glacier. As secondary permeability is the dominant pathway by which supraglacial meltwater is routed into the englacial system, it is clear that this assumption is not valid as the vast majority of meltwater will be concentrated through a limited number of discrete points on the glacier surface leading to significant fluctuations in meltwater input. Additionally, it is assumed that water pressure is always equal to ice pressure and that gradients in ice pressure determine hydraulic gradients (Liboutry, 1996). These theories describe flow in idealised conduit systems which may not reflect the true complexity of englacial flow. The potential for conduit development from vein systems is minimal, even when water content and hydraulic gradients are large. As such, alternative theories have arisen (Hock *et al.*, 1999) which argued that water primarily flows at atmospheric pressure in open channel systems.

Recent research has shown that fractures may be the main pathways of water flow (Fountain *et al.*, 2005a), particularly in temperate glaciers (Gulley *et al.*, 2009). Fractures provide multiple connections between englacial and subglacial systems and are perhaps common on temperate and polythermal glaciers and concentrated in the accumulation area. Fractures are characterised by steep plunges ($\sim 70^\circ$), narrow openings (40 mm) and slow water speeds (10 mm s^{-1}) (Fountain *et al.*, 2005b) and propagate to depths of approximately 130 m. Fractures develop in situ or through the advection of surface crevasses (Pohjola, 1993; Copland *et al.*, 1997) with formation

linked to supraglacial conditions (Fountain and Walder, 1998; Stenborg, 1973) and the density variation between ice and water, which forces the surrounding ice to crack apart. As such, conduits are most likely to develop where concentrated surface water i.e. supraglacial lakes, provides a point source of high water flux which destabilises the fracture flow system. Increased water flux, friction and heat dissipation in larger fractures leads to faster enlargement in these pathways. Recent research has demonstrated that fractures are also present in cold based glaciers (Van der Veen (2007)). These studies demonstrate the complexity of englacial hydrology in transporting meltwater to the subglacial system.

2.3.3 - Subglacial drainage

The structure and morphology of subglacial flow pathways exerts a strong influence on the pressure and velocity at which meltwaters are routed beneath glaciers (Hubbard and Nienow, 1997). This controls rates of basal sliding (Iken, 1981) and subglacial sediment deformation (Clarke, 1987). Drainage is divided into two distinct systems: discrete and distributed (Boulton *et al.*, 2007). The structure of flow pathways within these systems is also strongly controlled by bed rheology (Fig. 7). Discrete systems are characterised by large water fluxes in which there is an inverse relationship between pressure and flux (Clark and Walder, 1994). Although the ice creep can result in channel closure, discrete channels can persist even when water levels fall as rates of ice deformation are much lower than the variability of water levels.

In contrast, distributed systems are characterised by linked cavities, which are formed in lee of bedrock protuberances (Kamb, 1987), as well as canals on soft subglacial sediments (Boulton and Hindmarsh, 1987) with inefficient but high pressure flow. Film flow can also occur at the ice bed interface (Weertman, 1972) through regelation sliding. Pore water flow, in which water moves with sediment, is also associated with distributed drainage. The spatial distribution of discrete or distributed systems is largely a function of pressure as water flows from high to low elevation and high to low pressure (Shreve, 1972). Subglacial drainage structure has been studied using dye tracing (e.g. Sharp *et al.*, 1993), meltwater chemistry (Tranter *et al.*, 1993), mapping of deglaciated bedrock (Sharp *et al.*, 1989), proglacial hydrographs (Covington *et al.*, 2012), borehole water level fluctuations (Iken and Bindshadler, 1986) and electrical conductivity and turbidity at the glacier bed (Hubbard *et al.*, 1995).

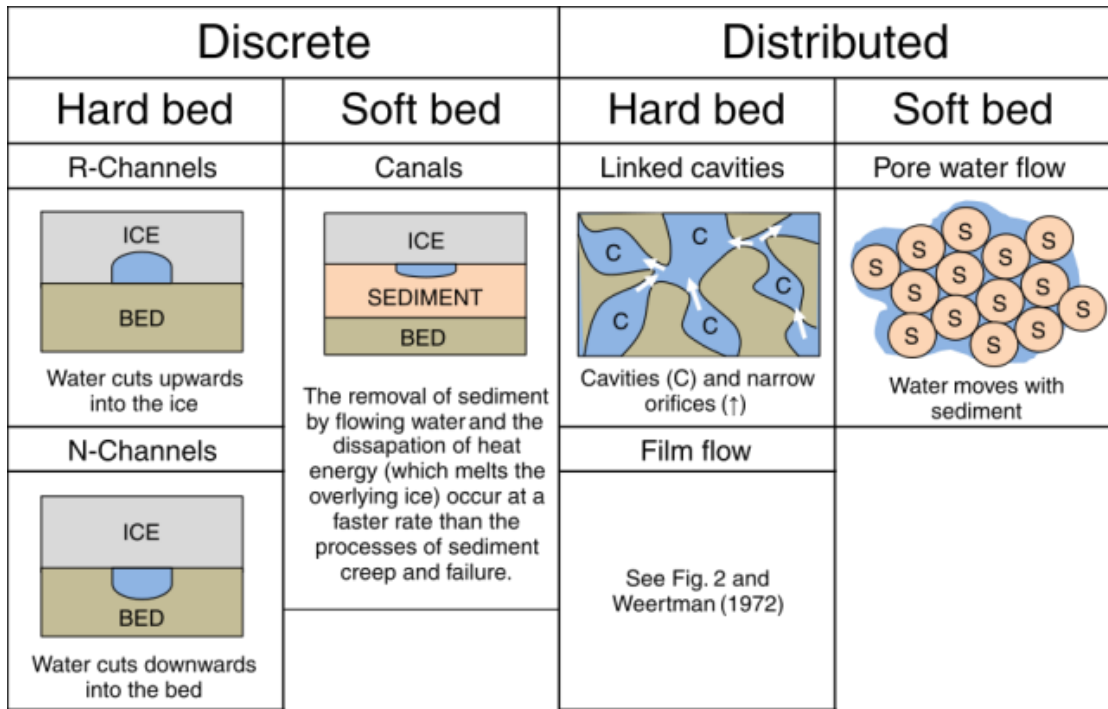


Figure 7. Flow pathways of discrete and distributed subglacial systems.

The varying importance of discrete and distributed drainage is dependent on the pressure-flux relationship which is a key determinant of ice movement. Ice overburden pressure (12) and effective pressure (13) interact strongly and are described as follows:

$$P_i = p_i g (H - z) \quad (12)$$

$$N = P_i - P_w \quad (13)$$

where p_i is ice density, p_w is water pressure, g is gravity, H is surface elevation and z is actual elevation. If ice overburden pressure and water pressure are equal, the effective pressure is 0. In the terrestrial landscape, the hydraulic potential (ϕ) of water is a function of atmospheric pressure and elevation:

$$\phi = p_w g z \quad (14)$$

However, when water is bounded by overlying ice, ice overburden pressure and thus hydraulic potential is described as:

$$\phi = p_w g z + p_i g (H - z) \quad (15)$$

Hydraulic potential is a measure of the available energy of water and governs its direction of flow, with decreasing pressure down glacier. However, these equations involve a number of assumptions. Firstly, they assume that englacial and subglacial channels are always water filled. Given the significant temporal and spatial variability of supraglacial meltwater input, channels will often alternate between

atmospheric and ice-derived flow. Additionally, it is assumed that pressures must be equal and opposite. However, if channels are full and flow is solely controlled by ice overburden pressure, then equipotential contours are a useful indicator of water flow (Fig. 8). Once at the bed, water flows at 90° to these contours.

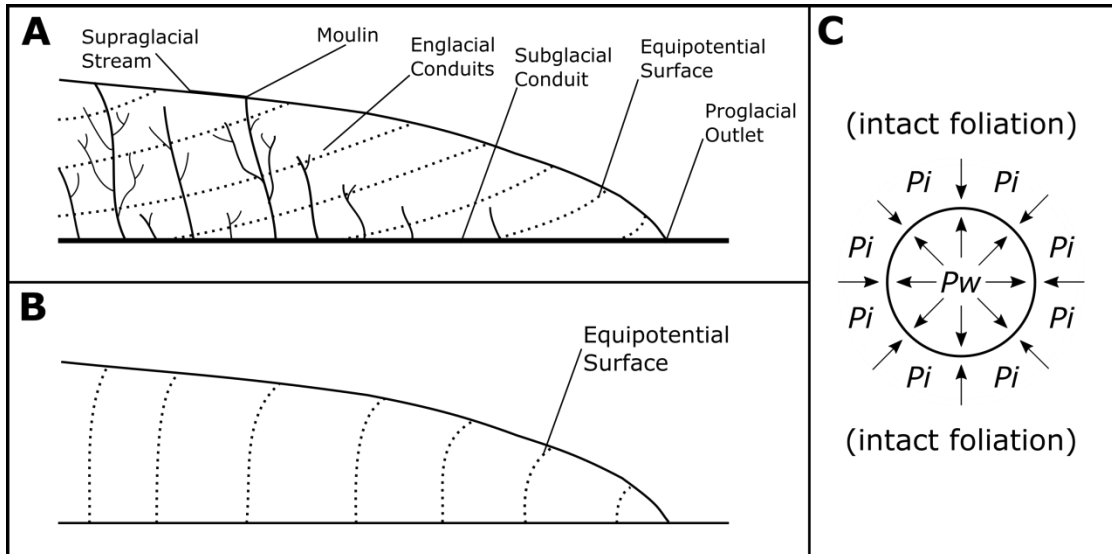


Figure 8. Englacial drainage systems. Upward branching arborescent network (A) formed normal to equipotential contours according to Shreve (1975). However, if the assumption that water (P_w) and ice pressures (P_i) are equal is ignored, then equipotential contours are rotated nearly 90° to the Shreve model (B) which predicts circular conduit cross sections framed by intact glacier ice (C). Redrawn from Gulley *et al.*, (2009).

The subglacial drainage system also undergoes significant temporal evolution. The timing of the seasonal transition from distributed to discrete drainage is an important control on glacier dynamics as demonstrated through theory (Alley, 1989), observation (Harbor *et al.*, 1997) and glaciohydraulic modelling (Arnold *et al.*, 1998). Subglacial drainage structure and morphology strongly modify melt and precipitation inputs (Hock and Jansson, 2005) which in turn, determine the timing and duration of periods of basal sliding. This seasonal transition is predominantly linked to the input of peak meltwater discharges during the melt season into the steady state distributed system. This is dependent on initial snow depth and superimposed ice formation as well as local meteorology (Flowers and Clarke, 2002). The input of peak discharges overwhelms the distributed system which is adjusted to smaller discharges and causes water to back up in englacial voids (Iken *et al.*, 1983). This raises subglacial water pressures and promotes hydraulic jacking, a process which steepens the hydraulic gradient and increases downstream water flow velocity and results in greater frictional melting (Hooke *et al.*, 1990). This in turn causes the system to become more hydraulically efficient with increased coupling between the bed and surface and rapid subglacial transitions from a hydraulically unconnected to a connected state (Flowers and Clarke, 2002). The maintenance of connected, discrete

drainage is dependent on subglacial water pressures. In the summer, higher discharges due to enhanced supraglacial melt increases the frictional heating of channel walls which offsets channel closure by creep. In contrast, meltwater discharges are significantly reduced during winter with frictional melting insufficient to offset channel closure. The transition to this winter state is characterised by deterioration of the basal drainage network, drawdown of subglacial storage reservoirs and a heightened sensitivity to precipitation and surface refreezing (Flowers and Clarke, 2002). Additionally, although subglacial drainage regularly undergoes seasonal reorganisation, it can also vary spatially for individual glaciers (e.g. Cowton *et al.*, 2013) while structural variation can be preserved over multiple seasons (Willis *et al.*, 1990; Willis *et al.*, 2012).

2.3.4 - The theory of hydrodynamic coupling

It has been shown that hydrological forcing of ice velocity through basal sliding (Nienow *et al.*, 2005) and subglacial deformation (Boulton *et al.*, 2001) is dependent on the structure and morphology of subglacial drainage (Iken, 1981; Clarke, 1987). As such, hydrodynamic coupling i.e. meltwater forcing of ice velocity, should occur more readily when distributed subglacial drainage is present as meltwater inputs can rapidly over-pressurise channels, cause hydraulic jacking and lead to periods of basal sliding (Hooke *et al.*, 1990). In contrast, flow variability should be reduced in channelised, discrete systems as meltwater inputs are more efficiently transferred out of the glacial system. Surface dynamics at glaciers underlain by discrete systems should be predominantly controlled by internal deformation.

Therefore, the degree of connectivity between surface meltwater generation and surface velocities could be used as a proxy for subglacial drainage configuration. However, hydrological forcing of ice velocity can occur despite the existence of discrete drainage (Bartholomew *et al.*, 2011). At the Leverett Glacier, Greenland, ice velocity remained high and variable when meltwater inputs were rising faster than the drainage system could adjust to (Cowton *et al.*, 2013). Coeval periods of fast glacier and high surface melt production were evident during the early summer, despite the presence of discrete drainage (Cowton *et al.*, 2013). As such, hydrodynamic coupling can occur throughout the year if surface meltwater or precipitation inputs are sufficient to cause over-pressurisation.

As such, drainage system configuration can hold little influence upon ice dynamics under scenarios of overwhelming meltwater generation (Bartholomew *et al.*, 2011). With the exception of these events, hydrodynamic coupling/de-coupling will be observed as followed:

1. Events which exhibit close coupling between melt production and forward motion i.e. basal sliding due to over-pressurisation of distributed systems (e.g. Iken *et al.*, 1983).
2. Events which demonstrate a clear disconnection between melt production and forward motion, accounted for by the process of hydrodynamic decoupling. This can take the form of (A) the suppression of meltwater input and a return to internal deformation (e.g. Hooke *et al.*, 1989) or (B) when enhanced meltwater input to discrete systems has no impact on glacier dynamics (e.g. Mair *et al.*, 2002).

Determining the degree of connectivity between ice melt and ice dynamics and identifying periods of hydrodynamic coupling at Falljökull may provide an understanding of how similar glaciers will respond i.e. speed up/slowdown, under scenarios of sustained thinning and enhanced meltwater input to the subglacial system.

2.3.5 - Water storage

Water storage also introduces complexity to this model of hydrodynamic coupling but is often overlooked (Killingtreit *et al.*, 2003) and is poorly handled by conceptual or mathematical models (Jansson *et al.*, 2003). Storage occurs at a variety of timescales and in different forms, from the long term storage of water as glacial ice to the hourly storage of water in the englacial and subglacial system (Fig. 9). The long term storage effect of glaciers is ultimately dependent on climate (Fountain and Tangborn, 1985).

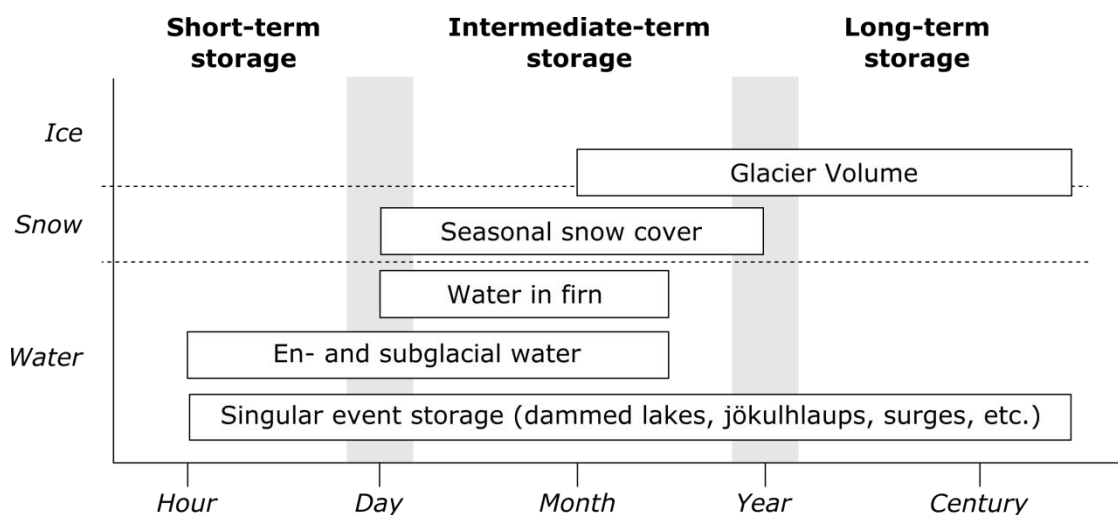


Figure 9. Forms and timescales of glacier storage. Redrawn from Jansson *et al.*, (2003).

Intermediate water storage is an important control on seasonal water flux, as winter accumulation and summer ablation produces a strong seasonality in discharge (Stenborg, 1970; Tangborn *et al.*, 1975). This water is primarily stored in the firn layer (Schneider, 2000) which responds strongly to seasonal changes, with saturation during the winter period and drainage during the summer (Jansson *et al.*, 2003) and is effective at delaying water transport (Dyurgerov, 2002). However, the firn may be reduced or vanish in warming climate, particularly for glaciers with a narrow altitude range (Braun *et al.*, 2000). The impact of the firn layer has been demonstrated at Hofsjökull, Iceland (Woul *et al.*, 2006). For this terrestrial ice cap, meltwater discharge is expected to increase by up to 50% by the end of the century and subsequently decrease as the ice cap area diminishes (Aoalgeirsdottir *et al.*, 2006). Modelling showed that retreat of the firn layer resulted in reduced water retention, redistributed but not reduced discharge, accelerated runoff generation and amplified peak discharges (Hock *et al.*, 2005). Similar changes may occur at other Icelandic ice caps e.g. Öraefajökull, which could lead to flow modification in outlet glaciers e.g. Falljökull.

Water can also be stored over intermediate timescales in the subglacial environment, as indicated by the early melt season uplift of various glaciers (Iken *et al.*, 1983; Jansson and Hooke, 1989; Raymond *et al.*, 1995). However, as Jansson *et al.*, (2003) note, there is still doubt as to where this seasonal water is located in the glacier system. Short-term water storage is also evident. Diurnal variations in discharge are well documented (Lang, 1967) with a significant lag between peak solar input and peak discharge (Munro, 1990). This cycling is attributed to ice melt (Elliston, 1973) and the structure of the englacial and subglacial system as well as the maturity of drainage channels in the snow and firn (Singh *et al.*, 1997). Short term water storage is generally enhanced in distributed systems as flow velocities are significantly reduced.

2.4 - Terrestrial time-lapse photography

2.4.1 - Procedures

Since the earliest applications of time-lapse photography to Mount Rainer, U.S. and Unteraargletscher, Switzerland by Miller and Crandell (1959) and Flotron (1973) respectively, numerous studies have shown ice velocity variation using this technique (Harrison *et al.*, 1986, 1992; Evans, 2000; Ahn and Box, 2010; Schubert *et al.*, 2013). However, there is no standard methodology for generating time-lapse data or interpreting it quantitatively, although the majority of studies follow the same basic procedures of image registration, feature tracking and geo-referencing.

Methodological variation between studies cannot be discounted as a source of variation in ice velocity estimates.

Image registration is a crucial step in all image analysis tasks (Zitová and Flusser 2003) as it defines the relationship between different images and enables camera rotations to be isolated when comparing across a time sequence. Although camera position is generally constant, thermal effects, wind vibration or settling of the camera can result in camera rotation (Dietrich *et al.*, 2007). By locating static points in the image sequence at a high level of precision, camera rotations can be identified and corrected for. This is a necessary process as a “stable step-up seems nearly impossible” (Eiken and Sund, 2012)

Feature tracking, which involves observations of glacial features across an image sequence, is often undertaken using automated algorithms which can generate matching accuracies of potentially up to 0.02 pixels (Maas *et al.*, 2010). However, natural features on the glacier surface often do not form sharply defined targets (Eiken and Sund, 2012) and care should be taken to select features which are representative of surface displacement. Automated feature tracking has been used to study glacier surface motion (e.g. Scambos *et al.*, 1992; Kaab and Vollmer, 2000; Leprince *et al.*, 2007; Amundson *et al.*, 2008) although given the systematic changes in the appearance of natural features, automated matching will eventually fail. However, manual tracking of natural (e.g. Eiken and Sund, 2012) or non-natural features (Harrison *et al.*, 1986) is time-intensive and unlikely to deliver sub-pixel accuracies.

Deciding between automated and manual tracking is largely dependent on the relative magnitude of feature displacements. Rapid and high magnitude changes are perhaps best captured by manual tracking, while longer term and lower magnitude changes can be captured by automatic techniques at a much greater precision (Danielson and Sharp, 2013). Both automated and manual feature tracking are affected by the resolution (pixels) and clarity of the generated image. Image clarity is affected by falling snowflakes and rain droplets, snow and rain on the ground, lens internal reflections and enclosure window optical distortion (Ahn and Box, 2010). The degree of illumination can also result in under or over-exposure which can make feature identification challenging (Eiken and Sund, 2012), particularly for heavily crevassed surfaces which are illuminated differently throughout the day e.g. icefalls. In the study by Ahn and Box, (2010), image loss was 6-10% based on these factors, increasing to 15-20% when fog cover was included. As such, a suitable number of images per day are necessary to ensure a statistically robust dataset.

Finally, geo-referencing involves aligning images to a contemporaneous digital elevation model (DEM) using specific control points. This requires a camera model

i.e. a generalized description of how the camera represents any 3D scene in its 2D image (James *et al.*, 2016), as well as the viewing distance to control points and image geo-referencing parameters to describe the camera position and how it is oriented within the geographic coordinate system. Determining an accurate focal length is necessary (Rasmussen, 1986) in order to balance the field of view, velocities and distance to targets (Eiken and Sund, 2012). Early studies found that generating absolute distances from time-lapse data was challenging (e.g. Harrison *et al.*, 1986; Harrison *et al.*, 1992; Evans, 2000). However, geo-referencing should now be considered an essential step, as the value of time-lapse data is dependent on the ability of the image to be georectified to a meaningful coordinate system (Messerli and Grinsted, 2015), thus permitting comparison with other studies.

2.4.2 - Recent developments

However, technical issues can complicate quantitative data processing for conventional photography (Farinotti *et al.*, 2010). As James *et al.*, (2016) note, the oblique view from terrestrial vantage points means that the effective scale varies across the image while with single-camera (monoscopic) installations, ice motion towards or away from the camera cannot be determined. Additionally, horizontal and vertical movement can only be distinguished for specific camera orientations. Furthermore, classical algorithm based correlation techniques are disadvantaged by dramatically increased computational times with an increase in image size and the number of correlation points (Rosen *et al.*, 2004; Leprince *et al.*, 2007). As a result, some studies do not quantitatively analyse time-lapse data but interpret it qualitatively to support velocity measurements from other sources (e.g. Boon and Sharp, 2003; Andersen *et al.*, 2011).

However, recent studies have addressed these limitations. In particular, the development of the Normalized Cross-Correlation (NCC) algorithm by Vernier *et al.*, (2012) improved on classical algorithm based correlation techniques by optimising memory management to avoid temporary result re-computations (Vernier *et al.*, 2011). This program has been applied to glacier flow for the Argentière glacier, France by combining terrestrial image sequences with high resolution TerraSAR-X data. Using this technique, image registration was twice as fast as conventional approaches. However, this program does not account for the problems associated for monoscopic installations.

ImGRAFT, an automated tracking algorithm (Messerli and Grinstead, 2015) is a more appropriate tool as it is designed for oblique terrestrial images for which there are currently limited post-processing options available. Most software focus on feature tracking or geo-referencing (Corripio, 2004; Harer *et al.*, 2013) but are poorly

optimised for oblique terrestrial images and do not incorporate camera motion and lens distortion efficiently, as they are generally designed for aerial and satellite imagery. Processing using this software can also result in a loss of image quality and detail. In contrast, ImGRAFT directly integrates DEMs for geo-referencing and feature tracking (Messerli and Grinstead, 2015) and is of comparable efficiency to previous studies when handling large images (e.g. Vernier *et al.*, 2012).

However, automated matching of image pairs (Messerli and Grinstead 2015) would have limited success as terrestrial time-lapse images are affected by drift due to an unstable camera, variable weather, illumination, snow cover conditions and an ice surface that evolves rapidly due to melting (James *et al.*, 2016). These variables are not accounted for by Messerli and Grinstead (2015). As such, the use of image tracking software such as Pointcatcher (James *et al.*, 2016) represents an improvement on previous techniques (Vernier *et al.*, 2012; Messerli and Grinstead, 2015) and builds on feature tracking applications used for laboratory and volcanic image sequences (Delcamp *et al.*, 2008; Applegarth *et al.*, 2010; James and Robson, 2014). Procedures for image registration enable the isolation of camera drift and orientation change from glacier surface movement, with Monte Carlo error analysis used to determine the precision of camera orientations. Furthermore, the careful use of automated and manual tracking techniques can limit errors due to variable weather and illumination. Manual procedures i.e. rather than automated matching of image pairs, allows suitable features that are representative of surface movement to be selected and tracked through the image sequence. This limits the impact of rapid surface melting which can obscure the signal of glacier flow, particularly when surface melt is significant relative to ice movement (James *et al.*, 2016). Features representing thrust planes should be rejected as recorded velocities are a function of both surface movement and melt back along the reverse inclined plane (James *et al.*, 2016).

The integration of multi-temporal DEMs allows the direction of glacier surface movement to be calculated for each surface feature. At Sólheimajökull, SE Iceland, James *et al.*, (2016) acquired terrestrial laser scanner (TLS) data at the start and end of a 73 day image sequence using a laser scanner (Riegl LPM-321) which was capable of providing useful data at a distance of 3.5 – 4 km (Schwalbe *et al.*, 2008; James *et al.*, 2009). These high resolution topographic datasets were visually aligned to the image scene to generate accurate 3D geographic point coordinates for point observations at the start and end of feature tracks. Intermediate point observations were assumed to be located on the vertical plane between these points. This software is optimised for challenging oblique glacial image sequences and is suitable for use at similar mountain glaciers e.g. Falljökull. At Sólheimajökull, asynchronous variations of ~10% in surface velocities and rates of thinning were identified over timespans of ~25 days (James *et al.*, 2016) while the average surface velocity (17 cm d^{-1}) is in agreement with

velocities recorded for similar temperate glaciers e.g. velocities of up to $\sim 20 \text{ cm d}^{-1}$ at Eystri-Hagafellsjökull, an outlet glacier of Langjökull, Iceland (Minchew *et al.*, 2016).

2.5 - Meteorological data

Time-lapse data, if correctly registered, tracked and geo-referenced, is a powerful record of glacier change. However, linking this dataset to climatic variables requires data of comparable temporal resolution. As such, the establishment of Automatic Weather Stations (AWS) is clearly beneficial (Abbate *et al.*, 2013). AWS have been increasingly used for process-oriented energy and mass balance measurements (e.g. Oerlemans and Klok, 2002). They are highly automated, provide high temporal resolution data and can be used to study micro-meteorological variables such as air temperature, humidity, wind speed and radiation (Sicart *et al.*, 2011). Unlike data from regional weather stations or from climate modelling, the results from AWS are intimately coupled to the surface energy balance of the proximal glacier.

AWS are becoming more common and increasingly affordable, which encourages researchers to setup multiple AWS at different elevations at the field site (e.g. Virkisjökull Weather Observatory, BGS). This allows researchers to look at changing conditions with altitude and gradients in temperature, humidity and pressure along the glacier flow line. An AWS is typically composed of a data-logger, a power unit and a number of meteorological sensors but a recent advancement has been the inclusion of a communication facility which allows daily data retrieval (Abbate *et al.*, 2013). This removes the need for periodic site visits for data gathering as near-real-time data communication allows timely assessment of the correct functioning of the data logger and enables researchers to quickly identify when site visits are necessary.

Linking AWS measurements to mass balance (e.g. van de Wal *et al.*, 2005), surface energy balance (e.g. van Pelt *et al.*, 2012) and hydrology (e.g. Wagnon *et al.*, 1999) is now routine. However, few studies have effectively linked AWS and time-lapse photography to study glacier dynamics at a high temporal resolution, an approach which could yield a deeper insight into the mechanics of glacier movement.

2.6 - Study area: Virkisjökull-Falljökull

2.6.1 - Regional context

As the studies by Radic and Hock (2011) and Arendt *et al.*, (2002) have shown, mountain glaciers and ice caps are expected to remain an important component of eustatic sea level rise for at least another century. Given that 11% of Iceland is

currently glaciated (Björnsson and Pálsson, 2008), the potential for mass loss is significant. These glaciers are particularly sensitive to climatic fluctuations (Jóhannesson and Sigurðsson, 1998; Sigurðsson *et al.*, 2007) due to their maritime North Atlantic setting, high-mass turnover and steep gradients. The majority of ice volume is accounted for by the 4 main ice caps (Fig. 10) including Vatnajökull (8,100 km³), Langjökull (900 km³), Hofsjökull (890 km³) and Mýrdalsjökull (590 km³) (Björnsson and Pálsson, 2008). These ice caps account for 94% of the ~11,100 km² area of all Icelandic glaciers (Björnsson and Pálsson, 2008). These glaciers are predominantly temperate, dynamic and characterised by high annual mass turnover (Aðalgeirsdóttir *et al.*, 2011) and have responded rapidly to changes in temperature and precipitation during historical times (Björnsson, 1979; Björnsson *et al.*, 2003; Aðalgeirsdóttir *et al.*, 2006; Björnsson and Pálsson, 2008; Gudmundsson *et al.*, 2011). Vatnajökull is the largest temperate ice cap in the world and has lost over 400 km³ of ice since 1890 (Pagli *et al.*, 2007), with this shift to negative mass balance coeval with a mean temperature increase of 1-2°C (Björnsson, 1979). The sensitivity of this ice cap was demonstrated by Björnsson (2002) as mass balance was positive from 1991-1994, close to zero in 1995 but negative from 1996-2001. The 21 km³ mass loss due to balance changes (1991-2001) was closely linked to climatic variability (Pagli *et al.*, 2007).

2.6.2 - Glaciology

Öræfajökull is the southernmost sector of Vatnajökull and is glaciologically distinct and characterised by high-mass turnover (Bradwell *et al.*, 2013). The ice cap has 13 officially named outlets (Sigurðsson & Williams 2008) of which many, including Virkisjökull-Falljökull, terminate close to sea level. These outlet glaciers are all maritime (Bradwell *et al.*, 2013) with the vast proportion of mass loss occurring during the summer (May-September) (Björnsson, 1998). This region is important as average mass balance gradients in Öræfajökull outlet glaciers are the strongest in Iceland (Björnsson, 1998; Björnsson & Pálsson 2008) which combined with steep glacier profiles, makes them some of the highest-mass-turnover glaciers in Europe (Dyurgerov, 2002). From the summit of Öræfajökull at 2000 m above sea level (a.s.l), the ice flows to the west as twin outlet glaciers which split below 1200 m a.s.l into separate glacier arms – Virkisjökull and Falljökull, which are separated by a prominent bedrock ridge named Rauðikambur (Bradwell *et al.*, 2013). These glaciers share an accumulation area of ~5 km², with equilibrium line altitude estimated at 1000 - 1200 m a.s.l. (Björnsson and Pálsson, 2008). Although these glaciers recombine in their terminal zone, which previously extended ~2 km further down-valley (Gudmundsson 1997), a wide supraglacial debris band, sourced from Rauðikambur, marks the distinction between the glaciers at ~300 m a.s.l. These steep glaciers

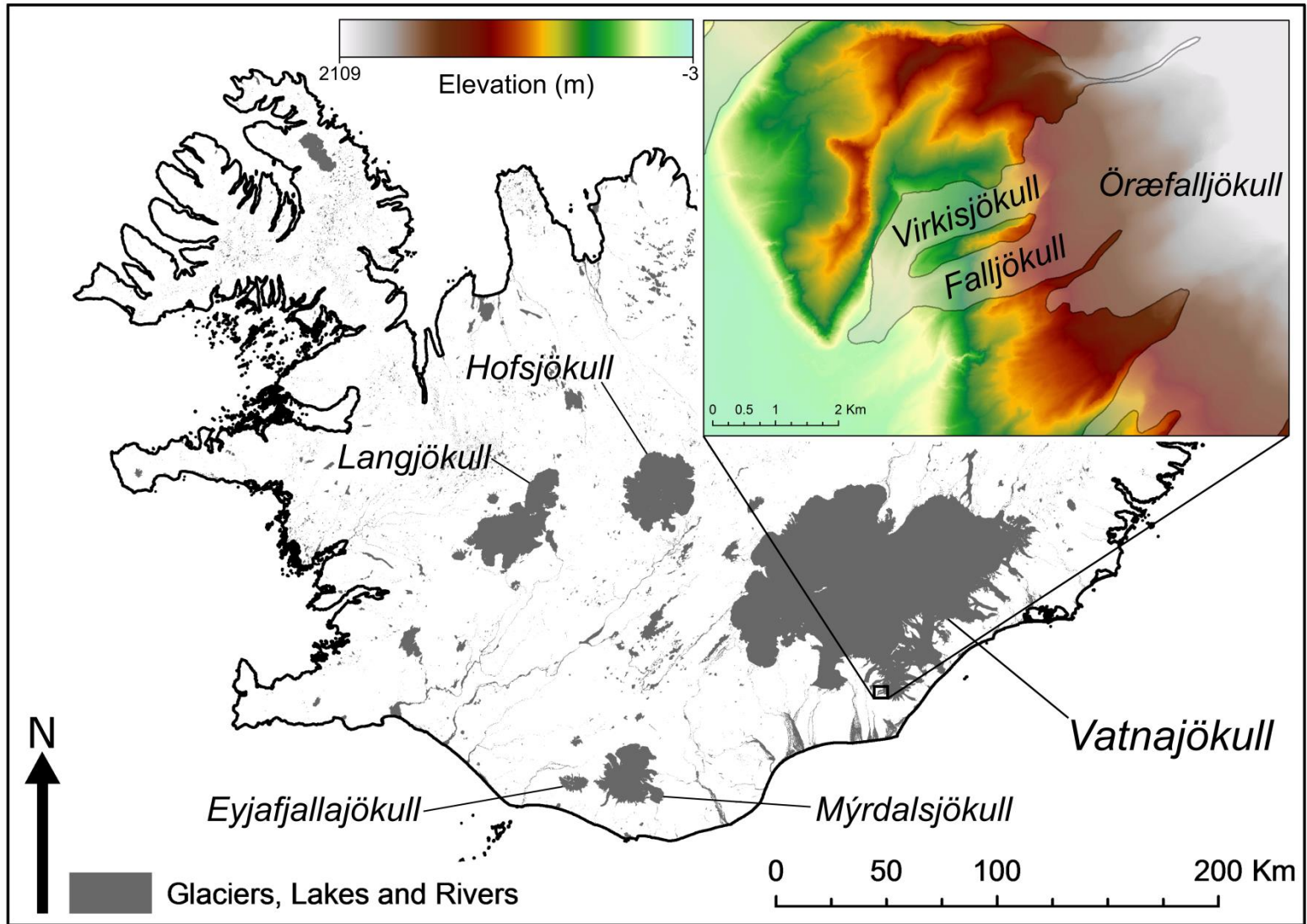


Figure 10. Map of Iceland showing the main glaciers and the Virkis-Falljökull study site (inset). Digital data retrieved from the National Land Survey of Iceland.

descend from the accumulation area to the glacier terminus via steep icefalls, an elevation difference of ~1350 m in just 2-3 km (Phillips *et al.*, 2014). Virkisjökull and Falljökull are both temperate with ice above the pressure melting point throughout, in line with the majority of Icelandic glaciers (Björnsson and Pálsson, 2008). However, determining bed rheology is more challenging (Björnsson *et al.*, 2003). The main outlets of eastern Vatnajökull predominantly rest on impermeable unconsolidated till (Björnsson and Einarsson, 1991) although many glaciers in the southeastern sector of the ice cap rest on impermeable bedrock (Björnsson *et al.*, 2003). However, porous lava beds are evident at Mýrdalsjökull, Langjökull and western Vatnajökull (Björnsson *et al.*, 2003). Field observations at Falljökull indicate that the glacier snout rests on a thin (< 1 m), discontinuous subglacial till which overlies semi-lithified volcanogenic diamicton (Phillips *et al.*, 2013). As such, the glacier front at Falljökull is probably underlain by a porous layer of till and is characterised by soft bed rheology.

2.6.3 - Meteorology

The region is characterised by a mild oceanic climate with ~150 days of precipitation per year (Einarsson 1984). There is no strong seasonal trend in precipitation although October, December and January are typically the wettest months (Bradwell *et al.*, 2013). However, topography exerts a strong control on precipitation values as to the south and west of Öraefajökull, mean annual precipitation is just ~1800 mm, increasing to 3000 mm in the east and exceeding 7000 mm on the summit plateau (Guðmundsson, 2000). The annual range in temperatures is limited (~11°C) although temperatures vary on a seasonal timescale as average temperature falls from 8-12°C in summer to 0-4°C in winter (Bradwell *et al.*, 2013). Summer maxima of 20°C and winter minima of -5°C are possible but rarely exceeded. Given this mild climate, snow is absent on low ground (< 200 m) for much of the year and is generally present for only 3-4 weeks during the winter.

2.6.4 - Chronology and previous research

Annual measurements of the glacier front position at Falljökull by the Iceland Glaciological Society (IGS) date back to 1957. In contrast, measurements at Virkisjökull were started in 1932, were discontinuous in the 1970s and ceased in 2000 (Bradwell *et al.*, 2013). The large-scale stagnation of the debris-covered ice margin meant that determining ice front position was challenging (Sigurðsson, 1998). As such, measurements since 1968 are unlikely to be representative of the glacier front position. Data from Falljökull are more reliable due to negligible debris cover at the terminus (Bradwell *et al.*, 2013). Ice front position data is shown in Fig. 11.

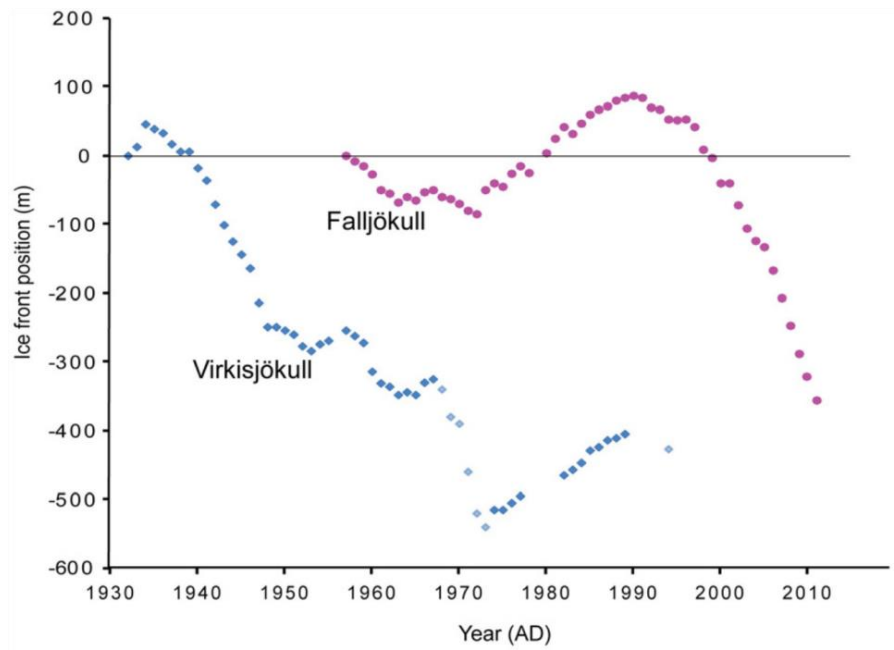


Figure 11. Cumulative retreat of the Virkisjökull and Falljökull ice fronts from annual measurements taken by the Icelandic Glaciological Society. From Bradwell *et al.*, (2013).

Since measurements began, both Virkisjökull and Falljökull have retreated ~1200 m. However, this significant retreat was punctuated by one major readvance (~180 m) between 1970 and 1990 (Sigurðsson, 1998; Bradwell *et al.*, 2013). Considerable mass loss has occurred, demonstrated by the decreasing areal extent and surface elevation of the glaciers, particularly in the ablation area (Phillips *et al.*, 2014). However, contemporary retreat (post-2004) may be distinct compared to previous changes (Bradwell *et al.*, 2013). This study suggests that Virkisjökull-Falljökull was undergoing active (dynamic) retreat before 2004, with some forward motion during the winter and spring (Evans and Twigg, 2002). This pattern of retreat is evident in the landscape with the formation of annual push moraines. Two groups are identified with the older formed between 1935 and 1945 based on lichenometric dating and the younger between 1990 and 2003 based on photographic evidence and field measurements (Bradwell *et al.*, 2013). The spacing between these annual push moraines has increased significantly between 1998 and 2003, perhaps reflecting a progressive increase in the loss of mass relative to changes in forward motion, perhaps as a result of warming summers (Bradwell *et al.*, 2013). The magnitude of these oscillations is inherently a function of mass balance (Phillips *et al.*, 2014) and is therefore partially a function of climate (Björnsson and Pálsson, 2008). This conclusion does support previous research, as a strong relationship has been observed between glacier-front fluctuations and air temperatures since 1930 with summer temperature the primary driver of ice-front recession on a sub-decadal scale (Sigurðsson 2005; Sigurðsson *et al.* 2007).

However, since 2004, the formation of annual push moraines at the margin has ceased. This may indicate that Virkisjökull-Falljökull has crossed a “glaciological threshold” (Bradwell *et al.*, 2013) as the glacier is now retreating at a faster rate in any 5 year period since 1932. However, retreat is no longer active as the glacier is down-wasting and collapsing with negligible forward motion (Schomacker *et al.*, 2014). This retreat was studied on a structural level using terrestrial LiDAR and ground penetrating radar (GPR) which demonstrated that collapse involves intense brittle faulting and fracturing along large-scale, down-ice dipping normal faults (Phillips *et al.*, 2013). GPR shows that a large area of buried ice in the proglacial outwash terrain provides an important control on this down-wasting. Falljökull is not unique in this regard, as ice-cored stagnation topography (Phillips *et al.*, 2014) is evident at a number of Icelandic glaciers including Kötlujökull (Kjær and Krüger, 2001), Bruarjökull (Kjær *et al.*, 2008), and Eyjabakkajökull (Schomacker *et al.*, 2014). A further study proposed a three stage structural glaciological model for retreat (Fig. 12) which expands on the work by Bradwell *et al.*, (2013) with [A] active retreat between 1990-2004, [B] passive down-wasting between 2005-present and [C]

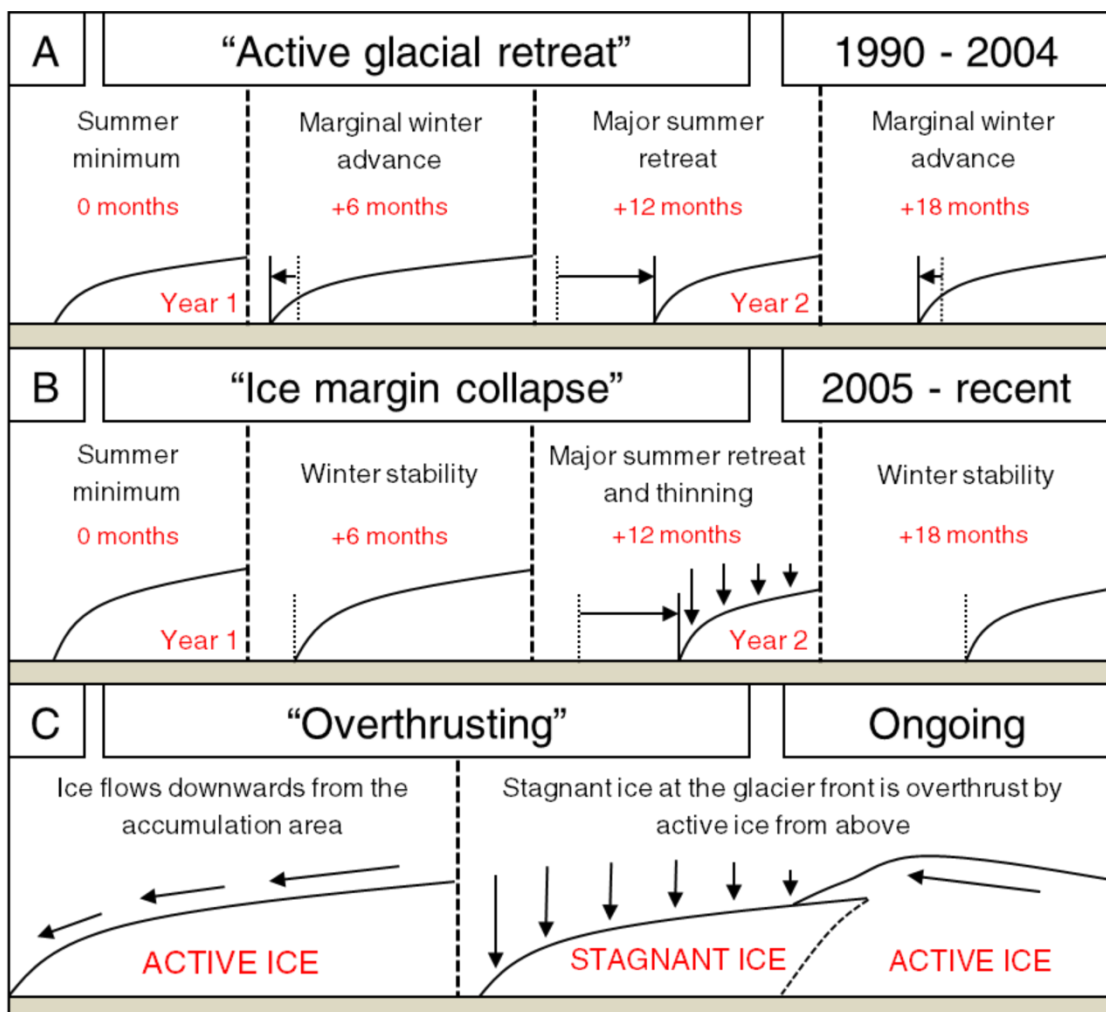


Figure 12. Structural evolution of Falljökull based on work by Bradwell *et al.*, (2013) and Phillips *et al.*, (2014).

continued movement and overthrusting in the upper part of the glacier (Phillips *et al.*, 2014). This crucial third stage is based on GNSS observations, with the lower part of the glacier stagnating while the upper reaches remain active. Significant flow deceleration below a marked topographic bulge is evident, as active ice overrides stagnant ice below. Deformation style varies significantly between active and static ice (Phillips *et al.*, 2014) with this study highlighting the importance of hypsometry, mass turnover and glacier bed topography in controlling glacier velocities.

Chapter 3 - Methodology

3.1 - Time-lapse image acquisition and processing

3.1.1 - Camera specifications and set up

Photographs were obtained from two Vivotek IP7361 Network Bullet Cameras at Falljökull (Fig. 13). These installations provide coverage of the glacier front (AWS1) and icefall (AWS3) and have been operational since 10/04/2011 and 12/04/2011 respectively. Photographs were generated daily at 09:30, 12:30 and 15:30 GMT. Both installations are still operational although this study focuses solely on the period 2011-2013. Given the slow surface velocities previously observed (Phillips *et al.*, 2014) and the large scale stagnation of the terminus (Bradwell *et al.*, 2013), data acquisition at a higher temporal resolution (e.g. hourly) would be an inefficient use of data storage availability. While a progressive increase in surface velocities is evident up glacier, with movement at a rate of 72 m yr^{-1} below the icefall (Phillips *et al.*, 2014), these values are relatively small compared to fast moving maritime glaciers e.g. 40 m d^{-1} at Jakobshavn Isbrae, Greenland (Schwalbe *et al.*, 2008) and do not necessitate more intensive data acquisition. Generating multiple photographs per day minimises the risk of days with no acceptable data.



Figure 13. Automatic Weather Station 3 and the Falljökull icefall.

3.1.2 - Data set

Between time-lapse camera installation and the culmination of the study period on 31/12/2013, 2824 and 2985 images were acquired from AWS1 and AWS3 respectively.

This sequence was down-sampled to 1954 and 2044 acceptable images by removing those in which image quality was compromised by cloud cover or precipitation. Although both datasets provide a satisfactory long term record of glacier dynamics at Falljökull, acceptable images were not available for each day throughout the sequence. At AWS1, the number of missed days accounts for ~10% (102 days) of the total study period while this figure rises to ~12% at AWS3 (122 days). However, AWS1 was not in operation for 65 consecutive days between 19/12/2011 and 23/02/2012, a period which accounts for over 60% of the missed days for this installation. When these dates are excluded, it is evident that missed days due to cloud cover or precipitation are far more likely at AWS3 (122:37), probably reflecting the increase in cloud cover with altitude. The temporal distribution of missed days (Fig. 14) highlights the increase in image loss during the winter months, a trend best explained by more extensive cloud cover and regular precipitation events during this period (Bradwell *et al.*, 2013). Moreover, images acquired in the early morning during winter months were not sufficiently illuminated and were underexposed and unsuitable for image tracking.

Finally, an additional 1929 and 2112 images from AWS1 and AWS3 respectively i.e. the second or third acceptable image for a particular day, are retained in the image sequences. While these could be removed to significantly reduce image processing time without compromising the project timespan, this would prevent the study of any sub-diurnal dynamics at Falljökull.

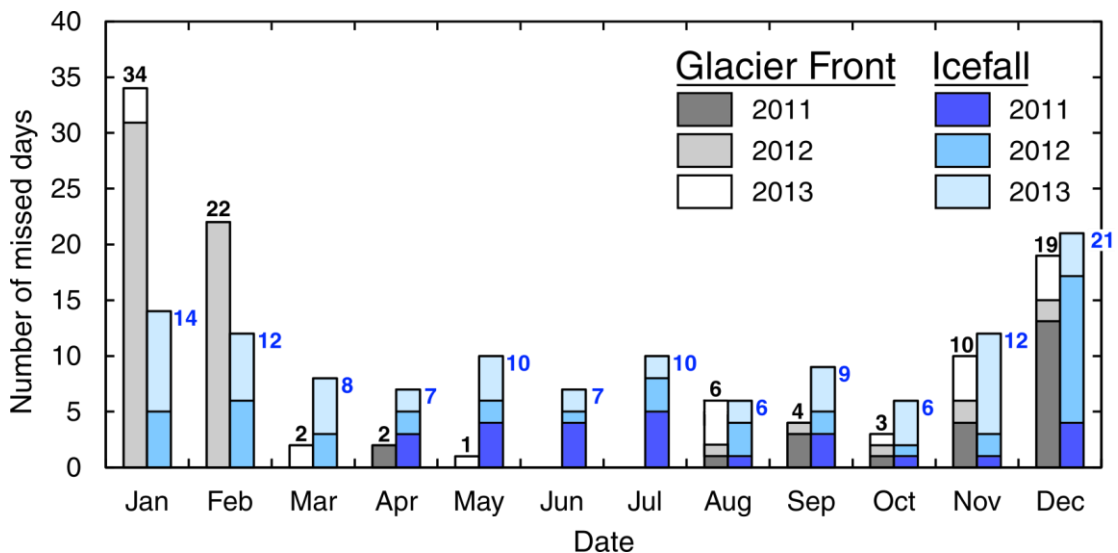


Figure 14. Missed days in the glacier front and icefall image sequences (2011-2013) due to cloud cover or precipitation

3.2 - Pointcatcher analysis

3.2.1 - Image registration

In order to isolate camera movement and facilitate robust glacier surface tracking, image registration was undertaken by tracking stable topographic features through the sequence. Irregular sections of skyline were manually selected, with points covering the width of the image in order to accurately determine camera rotation angles. These features exhibit the best contrast between dark topography and light backgrounds and are therefore the most suitable for tracking (James *et al.*, 2016). A typical feature is shown in Fig. 15. However, static feature tracking was undertaken manually, a time-intensive process. Choosing between automated and manual tracking is largely dependent on the magnitude or speed of the expected change in the sequence. As such, automated tracking of static features would seem to be the most appropriate method (James *et al.*, 2016). If camera position is assumed to be constant, then any camera displacement should be minor, reflecting thermal effects, wind vibration or settling of the installation during periods of ground heave.

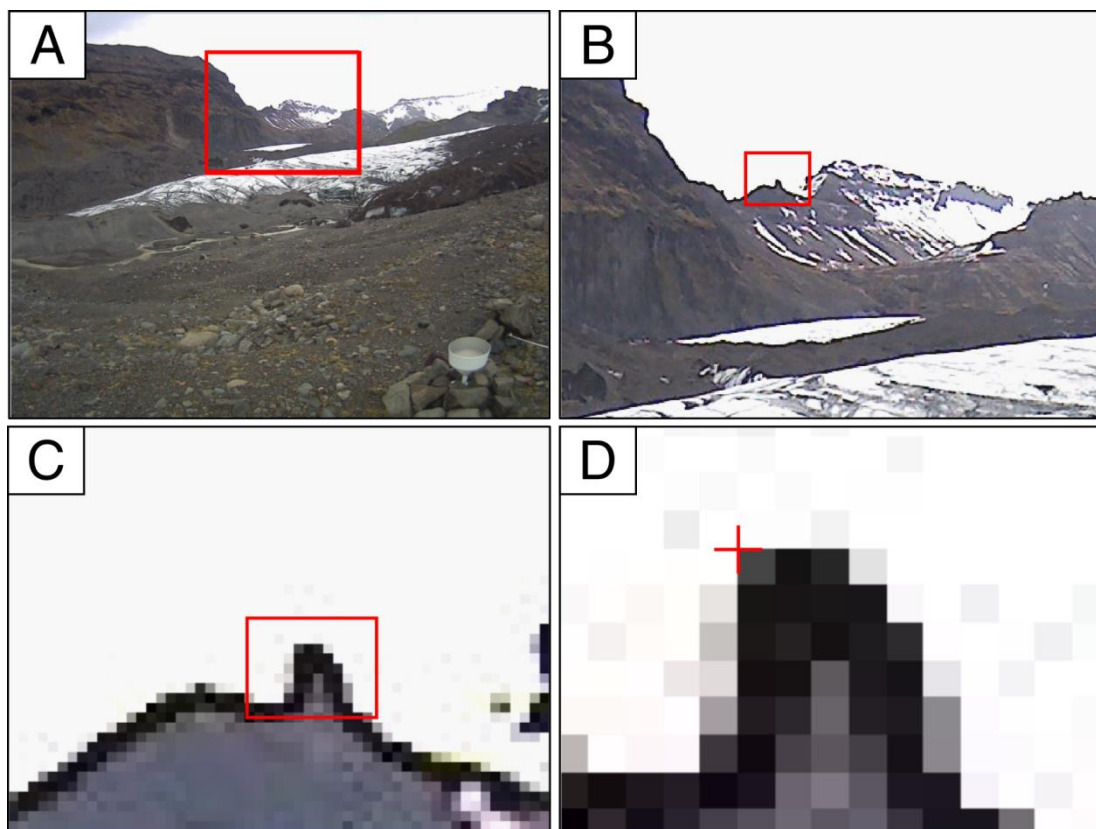


Figure 15. Selecting suitable topographic features for manual tracking (A-D).

However, the magnitude of feature movement is not the only factor to consider. While automated tracking can generate matching accuracies of 0.02 pixels under idealised conditions (Maas *et al.*, 2010), the Falljökull datasets are far from idealised as image quality is strongly affected by cloud and snow cover which leads to

significant errors in automated tracks. Although these can be corrected for by regularly updating the cross-correlation parameters, this is a time-intensive process. Automated tracking also generates a limited number of point observations during the transitional periods (W-S, S-W) when snow cover varies and features change significantly in appearance. This requires further manual interaction. In contrast, fully manual tracking is generally not associated with such significant errors and takes only marginally more time to complete.

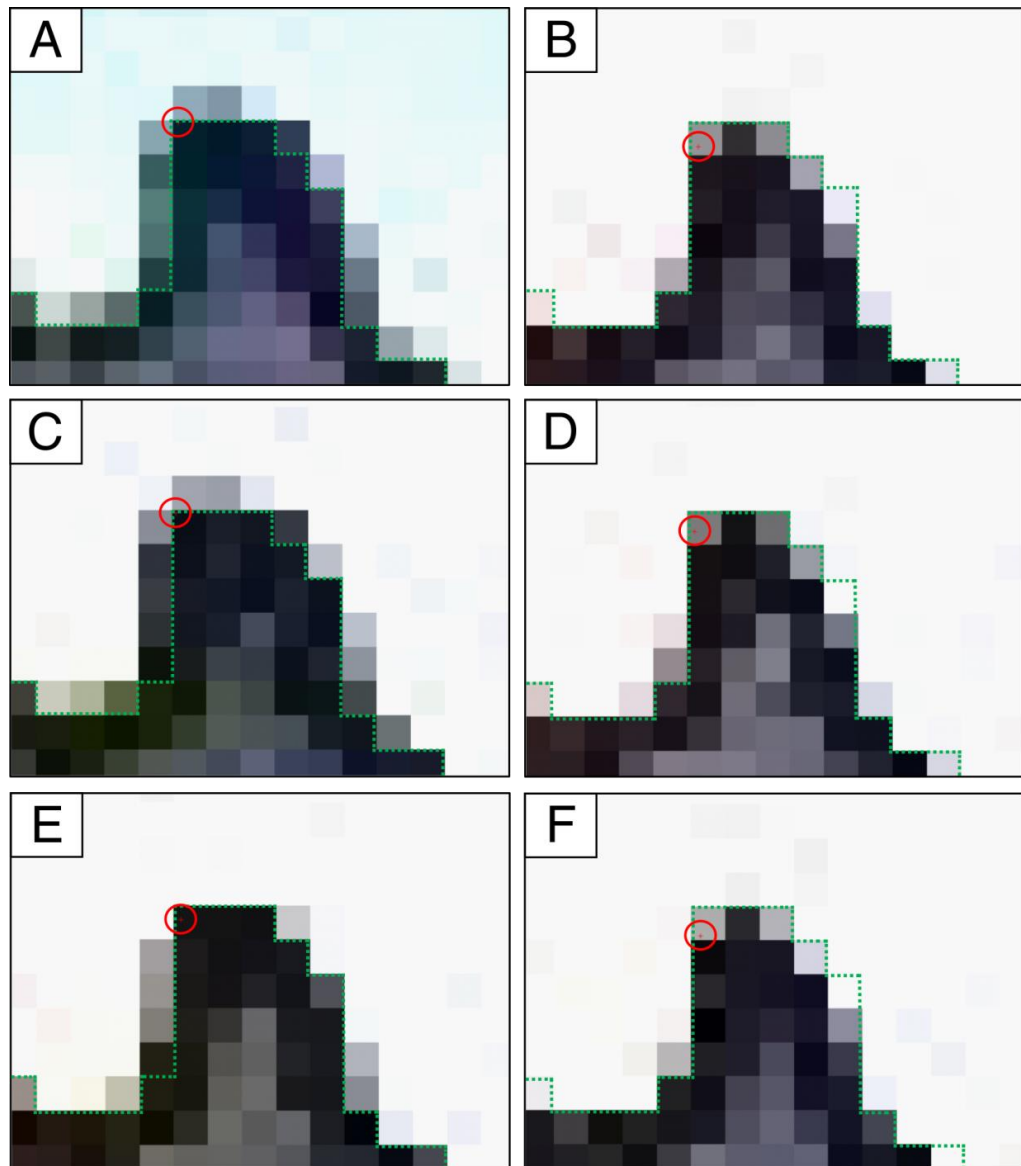


Figure 16. Automated tracking and the impact of illumination change (A-F) in images 55-60 from the 2011 AWS1 sequence (05/05/2011 - 07/05/2011) using a correlation threshold of 0.8 and template size of 10 pixels. Red circles indicate location of point observations. The outline of the topography is highlighted (green dotted lines) to demonstrate the impact of illumination.

Furthermore, illumination variability is difficult to isolate from camera displacement but has a significant impact on the scatter of automated points (Fig. 16). This scatter adds noise to measured point observations, with the magnitude of these

displacements often exceeding displacement due to camera movement. In contrast, careful and rigorous manual tracking would appear to be able to isolate illumination errors. Although solely based on qualitative interpretation, identifying whether changes are consistent across the skyline does seem to provide a useful indicator of whether illumination or camera movement is the primary cause of point displacement. To demonstrate the difference between these techniques, Fig. 17 presents the results of both manual and automated tracking of static features for the AWS1 image sequence in 2015 (time-lapse images were available up to 31/12/2015 but could not be georeferenced and were not included in this project). Although the trends are generally similar, manual tracking is characterised by abrupt shifts in point positions but considerably more stable x-y tracks, as the data is discretised to 1 pixel. As a result, it is not possible to record sub-pixel variation using this method. Manual tracking is most effective when the boundaries between pixels are selected. Although these shifts in point position are abrupt, a displacement of 1 pixel is equivalent to a camera angle change of just 0.052° (Fig. 18).

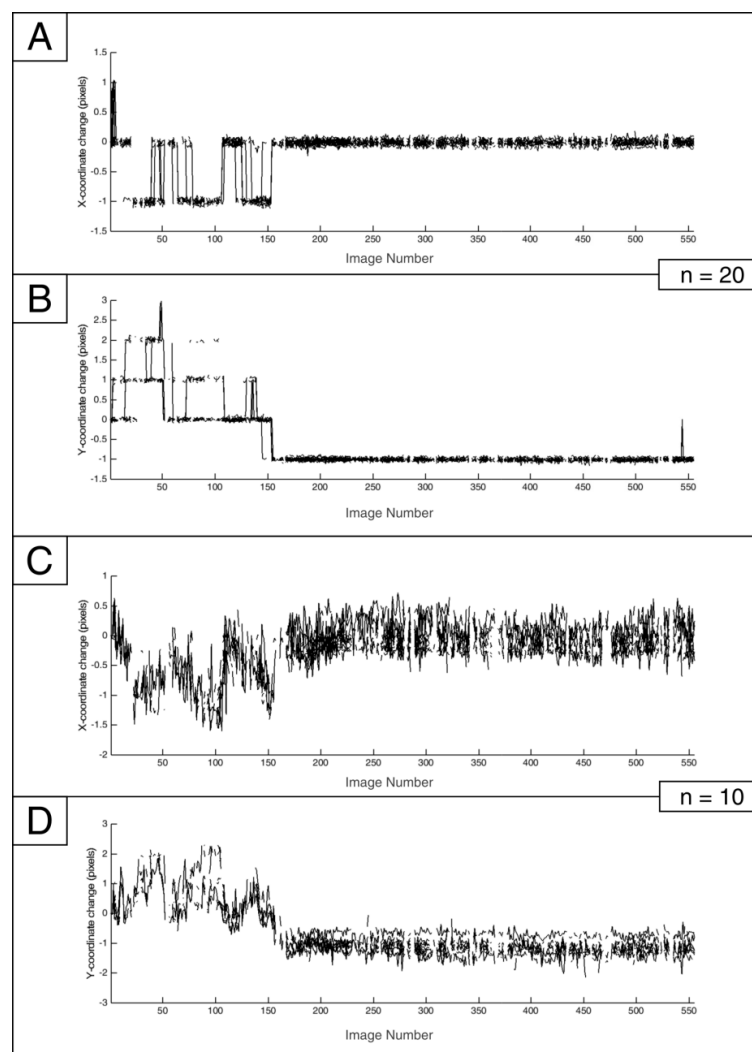


Figure 17. Manual (A-B) and automatic (C-D) tracking of the AWS1 image sequence in 2015.

In contrast, automated tracks exhibit greater variability but are generally coeval with the timing of shifts observed in the manually generated tracks. After image ~160, both techniques indicate a stable camera setup. However, automated tracks are characterised by point scatter of ± 0.5 pixels, variability that is best accounted for by illumination change. While automated tracking may be able to record sub-pixel variation due to camera movements of less than 0.052° in idealised conditions, this relatively small signal is almost certainly obscured by relatively high-magnitude fluctuations ($> 0.052^\circ$) due to illumination change. It is suggested that neither method in their current form can generate results of reliable sub-pixel accuracy. Additionally, manual tracking is more appropriate for glacier surface features. Not only are these features affected by variable snow and cloud cover, illumination variability and camera displacements but they also move due to glacier flow as well as fundamental changes in the features themselves e.g. collapse of debris cones. All these variables would require almost continual updating of the cross correlation parameters. As such, manual tracking of static features will ensure data precision is consistent between these datasets.

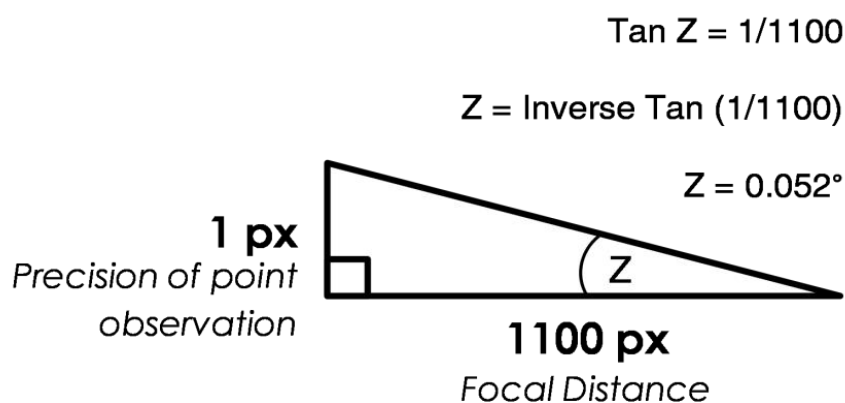


Figure 18. Manual tracking precision.

Another issue to consider is the number of static tracks to generate although 2 is the minimum required to undergo image registration. For this study, 20 static features have been tracked for each year and for each camera installation. This represents the practical maximum number of static features that are trackable in these image sequences, as beyond this number there are few suitable features remaining. Unfortunately, tracking this number of features is time intensive but was undertaken for a number of reasons. Firstly, with more static features tracked, image registration and subsequent error analyses can be more robust. Secondly, it guarantees good spatial coverage of points and satisfactory tracking through the sequence. Generating 20 tracks provides flexibility when snow or cloud cover or a change in illumination obscures parts of the image. The precision of camera rotation angles is highly dependent on the spatial distribution of tracked points across the image scene. As such, tracking only a limited number of points with a restricted spatial distribution

would poorly capture any change in relative camera angles, particularly when parts of the image are obscured.

To register these datasets, the procedures of James *et al.*, (2016) were followed. First, a reference image was selected for each image sequence in which the full 20 static features were observed. Camera angles were determined for all other images relative to this reference image using a robust image-based transform which permits identification and rejection of point outliers. As this process does not account for lens distortion, an additional registration stage was undertaken by defining a registration for each image in terms of a physical camera model which determines camera rotation around the x (omega), y (phi) and optic axes (kappa) (Fig. 19). This camera model required a number of inputs which had to be calculated (sensor size, pixel size, principal point position) or estimated based on integrating the image data with georeferenced LiDAR datasets (focal distance, radial parameters).

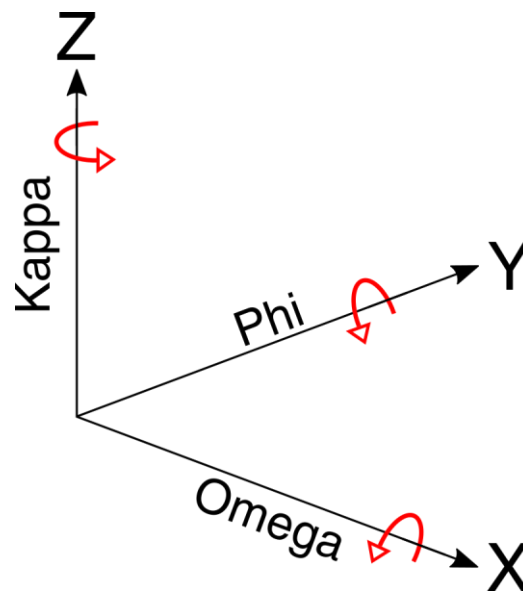


Figure 19. Rotation around the Omega (X), Phi (Y) and Kappa (Z) axis.

In order to determine the precision of the relative camera angles, a Monte Carlo approach was undertaken (James *et al.*, 2016). Camera orientation values were estimated repeatedly with different randomised errors added to the static point's image position. These random offsets are derived from a pseudo-random normal distribution with a standard deviation that reflects the precision of image measurements. The distribution of these random offsets generates standard deviation values for omega, phi and kappa for each image which represents the distribution of likely camera orientation angles. This error analysis also generates a residual RMS value. This is a measure of the quality of image registration based on the distance between static features in a registered image and the equivalent features in the reference image. An estimate of the registration accuracy for each image sequence σ_{mr} is calculated as followed:

$$\sigma_{mr} = (\sigma_r^2 + \sigma_m^2)^{1/2} \quad (16)$$

where σ_r is the image registration error and σ_m is the image registration precision. As features could not be tracked at a sub-pixel precision, registration precision is considered to be ~ 1 pixel.

3.2.2 - Feature tracking

With each image sequence registered, glacier surface features were tracked to determine spatial and temporal variability in surface velocities and rates of thinning. In the study of Sólheimajökull, Iceland by James *et al.*, (2016), the authors tracked ~ 50 individual features although this study focused on a short 73 day sequence comprising just 145 images to test the viability of the site equipment and analysis procedures. Applying the same intensive procedures at Falljökull is not appropriate.

To account for the difficulties of feature tracking in these image sequences, more realistic targets were set to account for the limitations of the camera set up and the deterioration in image quality due to weather and varying illumination. Between 10 and 20 point observations and a minimum of 5 point observations were required in 60% and 80% of images respectively before a sequence was considered sufficiently tracked. Glacier feature tracking results are discussed in Section 3.5.1. As per the recommendation of James *et al.*, (2016), features were selected which were deemed representative of surface displacement. However, due to a small image sensor (Fig. 20) and a restricted image resolution relative to previous studies (e.g. Fig. 21; James *et al.*, 2016), which was exacerbated by the distance from the camera installations to the glacier (< 600 m at AWS1), accurately determining the suitability of each surface

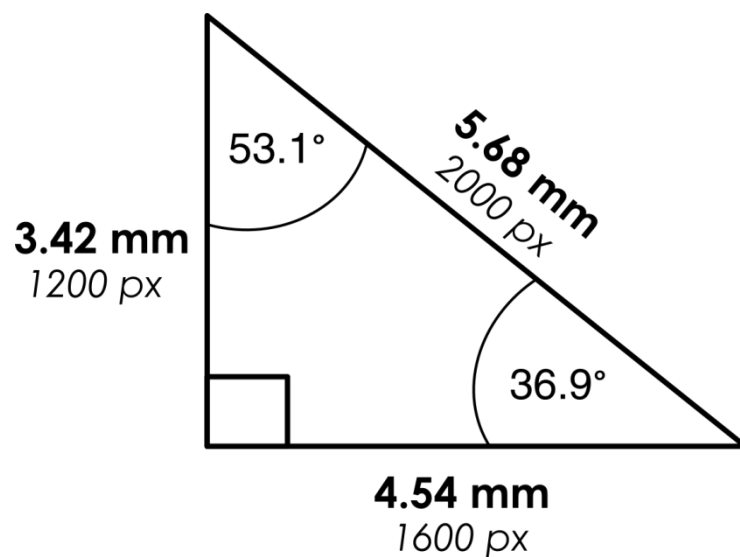


Figure 20. Image sensor dimensions.

feature was challenging. Debris cones and similar supraglacial deposits were deemed the most suitable features for tracking as they exhibited clear contrast between sediment and snow/ice. Due to the project timespan, it was not possible to track features which persisted throughout the entire image sequence. Features which were present in the image sequence for less than ~1 month were not considered for tracking as they are unlikely to be representative of glacier flow. Any movement in these transient features probably reflects the accumulation and rapid collapse of debris structures.

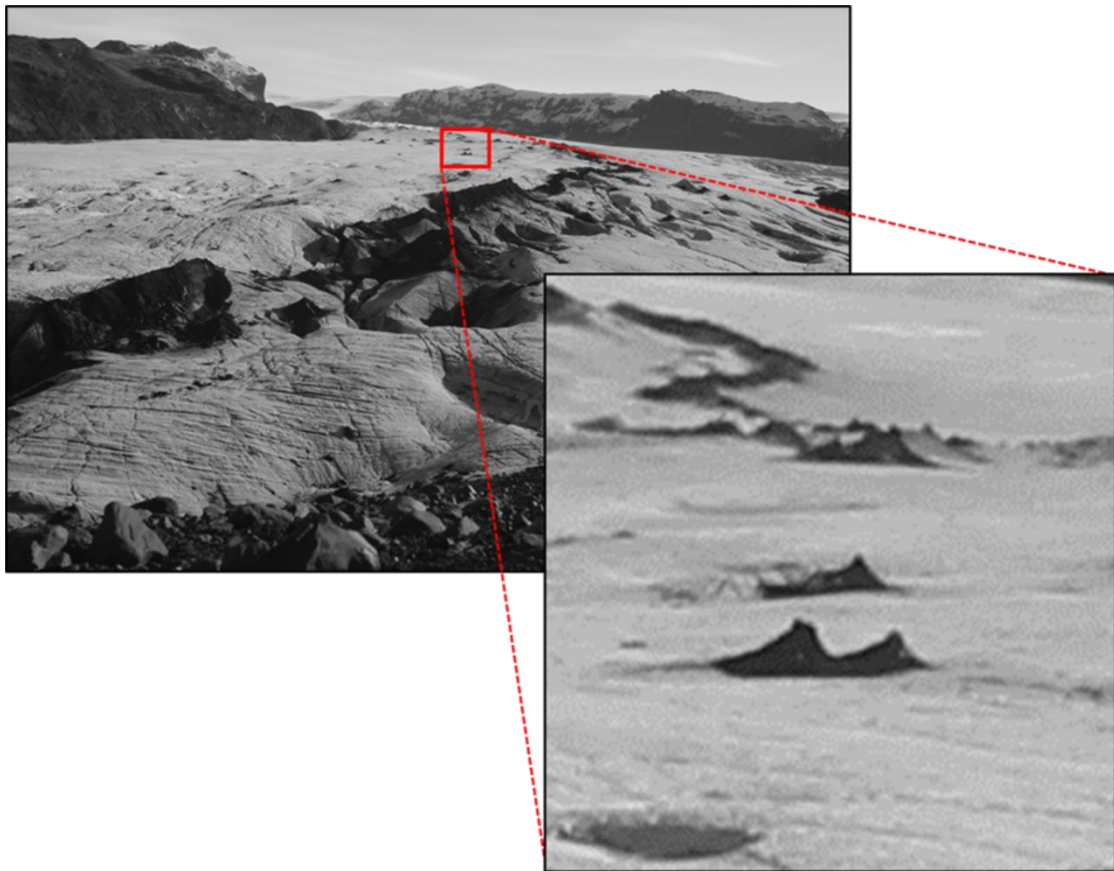


Figure 21. High image resolution of the Solheimajökull dataset enables tracking of distal surface features (inset). Photo credit: James et al., (2016).

3.2.3 - Geo-referencing

By determining camera model information and integrating high resolution DEMs, 3D geographic point coordinates can be derived for individual feature tracks. This involves the manual alignment of the image scene with topographic data from DEMs, a process which describes the position and orientation of the camera within the specific geographic coordinate system. This is then linked to relative camera angles to determine absolute displacement through the sequence. While the down sequence precision of this alignment is based on the precision of the camera

orientations, the initial alignment of the image scene and the DEM is undertaken manually in Pointcatcher (Fig. 22) and is therefore not associated with any formal error analysis. The accuracy of this alignment is strongly affected by a number of parameters including focal distance, camera position and radial distortion.

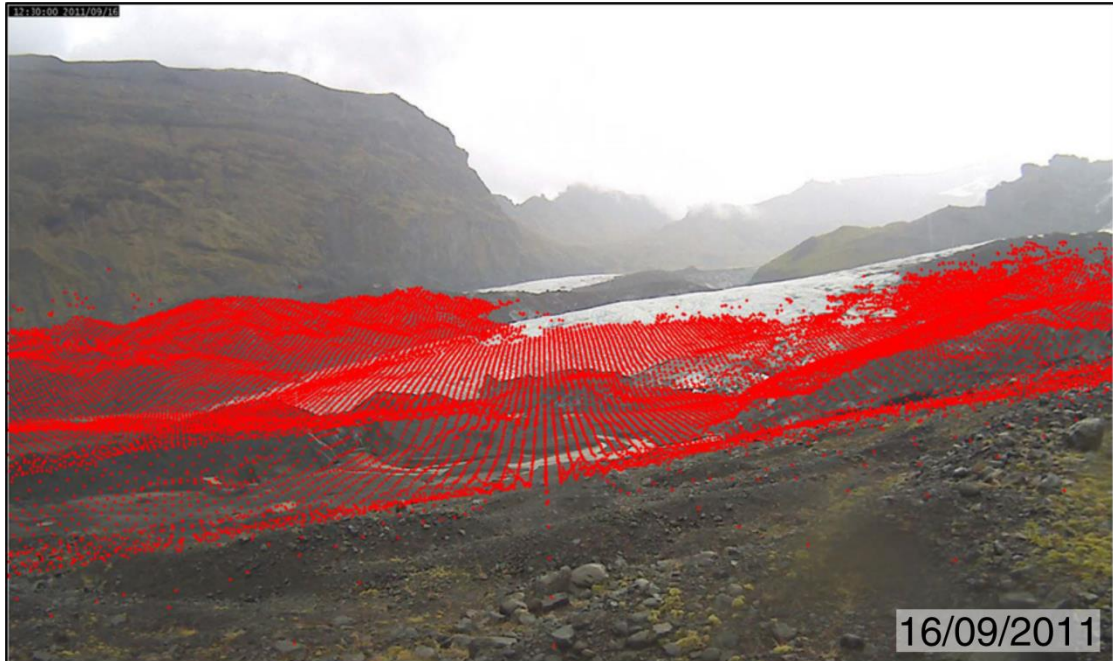


Figure 22. Manual alignment of LiDAR points and topographic data.

Furthermore, with monoscopic installations, movement towards or away from the camera cannot be determined and therefore for most viewing geometries, surface elevation change cannot be isolated from horizontal movement. As discussed in Section 2.4.2, multi-temporal DEMs can be used to address these limitations, with accurate 3D point positions generated for point observations at the start and end of feature tracks (James *et al.*, 2016). The straight line between these points is used to constrain a vertical plane and it is assumed that all intermediate points i.e. those not covered by a DEM, will be located on this plane. This assumption allows 3D coordinates to be calculated for all intermediate points with the signal of surface elevation change isolated throughout the image sequence.

At Falljökull, high resolution LiDAR datasets were collected on an annual basis by the BGS and made available for this project. Unfortunately, with only one DEM available per year, 3D geographic point coordinates can only be generated for one image scene. Without an additional DEM, it is not possible to fully constrain the direction of ice movement and isolate surface elevation change using this method. As such, any horizontal or vertical change in pixel position is treated as movement in XY space (N°, E°). This obscures the signal from surface elevation change as any thinning

or uplift of the glacier, which would be reflected in a change in vertical pixel position, is treated as movement towards or away from the camera.

In order to address this, the direction of ice movement (relative to grid north) can be estimated using satellite data (Glacier front: 220°, Icefall: 245°). This provides the direction of the vertical planes on which all points are situated (Fig. 23). A similar technique has been demonstrated by Schwalbe *et al.*, (2016). While this technique does provide an estimate of the direction of ice movement, it is not practical to generate a unique flow angle (°) and vertical plane for each surface feature as provided by the integration of multi-temporal DEMs. This simple estimate is less robust as it may poorly capture the movement of surface features at the glacier margins (e.g. James *et al.*, 2016), where movement may be almost perpendicular to the glacier flowline (Fig. 24).

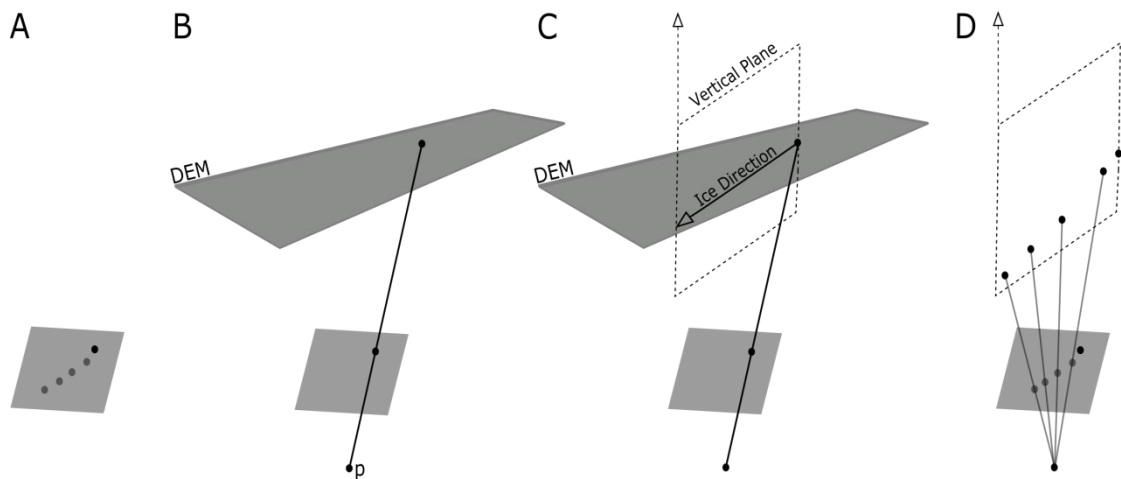


Figure 23. Georeferencing procedure. (A) Image registration throughout the sequence allows the set of feature observations to be represented in one reference camera orientation (grey box). (B) For the observation made closest in time to the first LiDAR survey, 3D coordinates can be calculated by projecting the observation through the perspective centre of the camera, p, onto the DEM surface defined by the LiDAR. (C) Ice direction is estimated based on satellite data to constrain a vertical plane in which the point is assumed to lie at all other times (D) 3D coordinates for all other image observations of that point are then calculated by intersecting their observation rays with the plane.

However, as feature tracks are not continuous through the image sequence, 3D geographic coordinates can only be generated for surface features which are present in the image coincident with the date of DEM generation i.e. feature tracks which end before or start after this image will not be georeferenced. To account for this, 4-5 images were georeferenced for each camera sequence in order to generate 3D geographic coordinates for as many surface features as possible, although not all features could be georeferenced. Given the changing nature of the glacier surface, more regular acquisition of DEMs is necessary in order to accurately georeference the glacier surface. While the approach used in the study is not without uncertainty, as

the changing nature of the ice surface through each year is not reflected in the subsequent georeferenced images, the topographic alignment was consistent throughout and so data should be internally consistent.

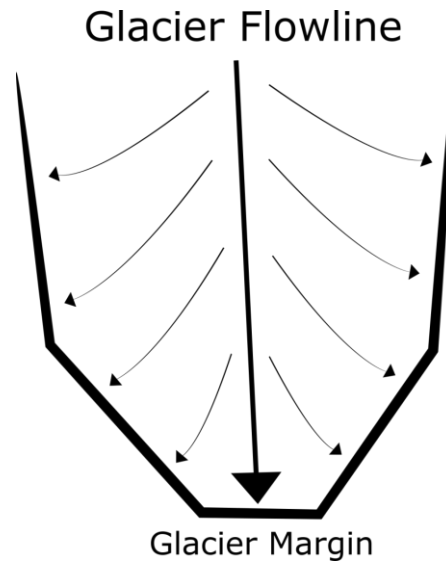


Figure 24. Ice movement at the glacier margin.

Geo-referencing of the icefall dataset was more challenging as DEM coverage of the surrounding topography was severely restricted with LiDAR point distribution limited to just one side of the image scene. As such, although visual alignment of these data could be undertaken, it would be extremely sensitive to a change in camera orientation as well as the adjustment of camera focal distance and radial parameters. To account for this, geographic coordinates were generated from satellite data to provide coverage of the distal topography not scanned using LiDAR. These points were incorporated into the LiDAR dataset and were visually aligned to the surrounding topography to determine camera model information. Visual alignment involved the adjustment of camera model parameters until both sides of the image displayed a satisfactory match. Unfortunately, due to the low spatial resolution of the satellite data, the estimated geographic point coordinates of surrounding topography are of limited precision. Therefore, comparison of the icefall and glacier front datasets should be undertaken cautiously. However, as each icefall dataset (2011-2013) were geo-referenced in this way, these data are internally consistent and comparison between years is possible, although without additional data, the absolute values generated for the icefall cannot be verified.

3.3 - Data analysis

3.3.1 - Spatial groupings

With point observations georeferenced and 3D geographic coordinates generated for each surface feature throughout the image sequences, surface features at the glacier front were allocated to 1 of 3 spatial groupings based on starting point position. This permitted study of spatial variability in surface velocities and rates of thinning. An example of these groupings is shown in Fig. 25. Surface features in the glacier terminus sector were all within 200 m of the terminus position in 2011, although the distribution of points became increasingly restricted by 2013 due to sustained retreat. Intermediate points were generally between 200-400 m upslope from the terminus and generally within ± 100 m of a major fault zone, which was present throughout the 3 year period. Surface features in the upper sector were generally in excess of 500 m from the glacier terminus in 2011. Due to the oblique camera view, it was only possible to track a handful of suitable surface features in the upper sector. As such, error estimates for these data are often significantly higher than for terminus and intermediate sector surface features. Finally, sub-dividing the icefall dataset spatially was challenging due to the complex nature of the ice body and the speed of ice movement. Determining inter/intra-annual spatial variability in surface velocities was not possible for these data.

3.3.2 - Data management

In order to determine the distance travelled for each surface feature, the horizontal and vertical displacement between the first and last point observation were calculated. Daily velocities were calculated by dividing track length by track duration. Mean daily velocities were calculated for each spatial grouping with 1σ uncertainties. T-tests assuming unequal variances were used to calculate whether inter/intra-annual variability between spatial groupings was statistically significant. Annual retreat rates were also calculated for Falljökull over the period 2011-2013 with geographic coordinates of the glacier snout determined at the start and end of each year using georeferenced LiDAR.

To determine the precision of these values, the standard deviations of camera angles (ω , ϕ , κ) at the start and end of each feature track were used to calculate total track length uncertainty (m). By calculating the viewing distance i.e. the distance between the camera position and the georeferenced point observation, straightforward trigonometry allows the precision of the camera angles to be converted to distances. Angular errors i.e. errors due to uncertainty regarding camera rotation, are relatively small, highlighting the consistency of manual tracking of static

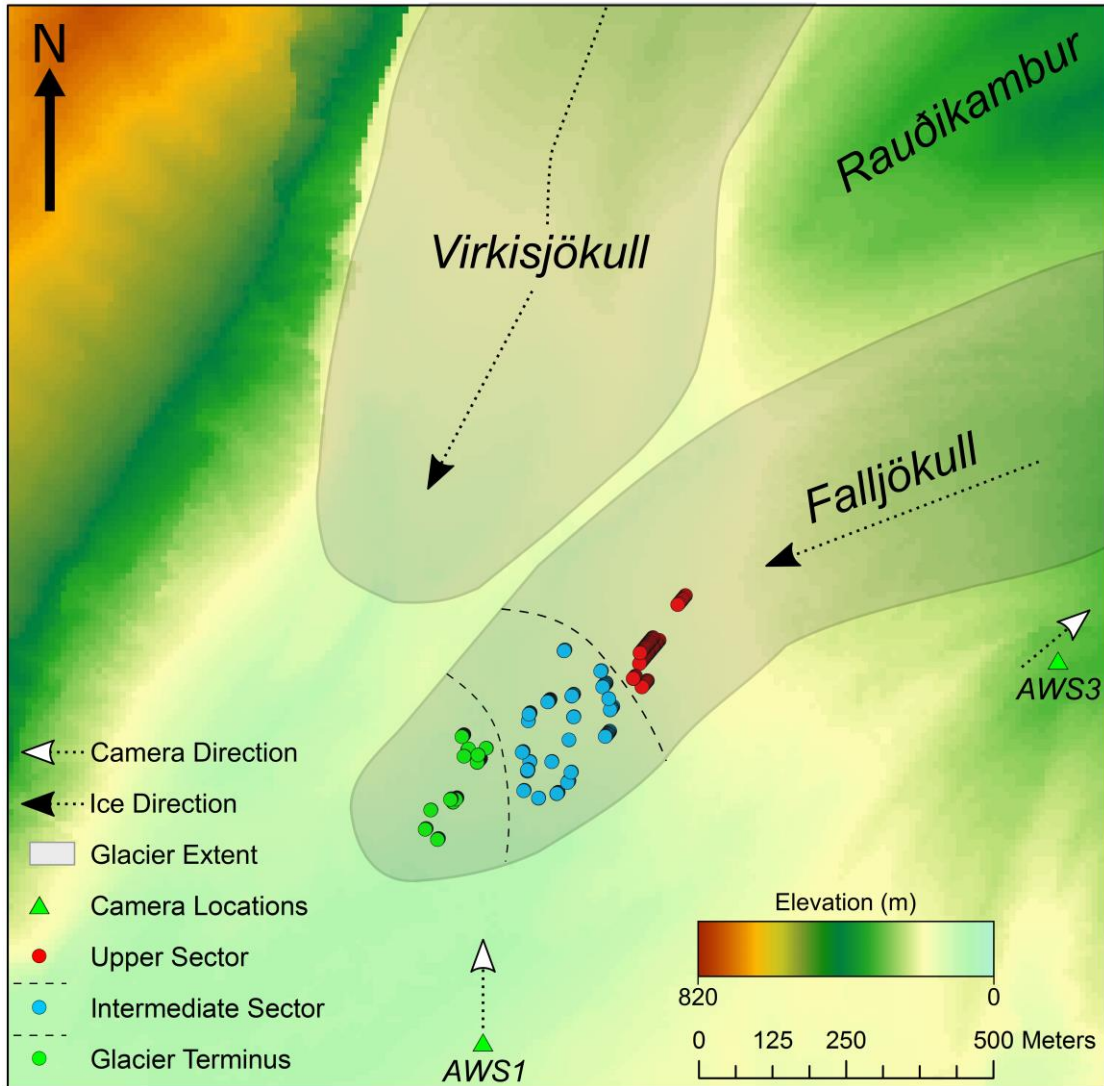


Figure 25. Map of the Virkis-Falljökull study site, showing the spatial distribution of surface features and camera locations. Data retrieved from the National Land Survey of Iceland.

points. However, as the precision of manual tracking is limited to ± 1 pixel, an additional error of 0.052° was added to each uncertainty estimate. Total track length σ_T uncertainty is calculated as follows:

$$\sigma_T^2 = \sigma_\Omega^2 + \sigma_\phi^2 + \sigma_K^2 \quad (17)$$

where σ_Ω is uncertainty around the x axis, σ_ϕ is uncertainty around the y axis and σ_K is uncertainty around the optic axis. An example of this data is shown in Fig. 26.

Surface velocity and thinning rate data were investigated using cumulative displacement analysis which provides a useful insight into glacier dynamics at a high temporal resolution. Firstly, a constant velocity model was generated for each surface feature by dividing the total track length by the track duration. The absolute displacement from that model was calculated for each surface feature at each image interval. An updated constant velocity model was calculated for each spatial

grouping by taking the mean of the horizontal and vertical displacements between subsequent images for each surface feature. Absolute displacements were averaged from the constant velocity position at each interval for images in which at least 2 surface features had been tracked. Based on these data, it was possible to determine whether surface features were moving faster than, on or below the average rate and whether surface features are ahead of or behind the estimated constant velocity position. 1σ uncertainties were calculated for cumulative displacement tracks.

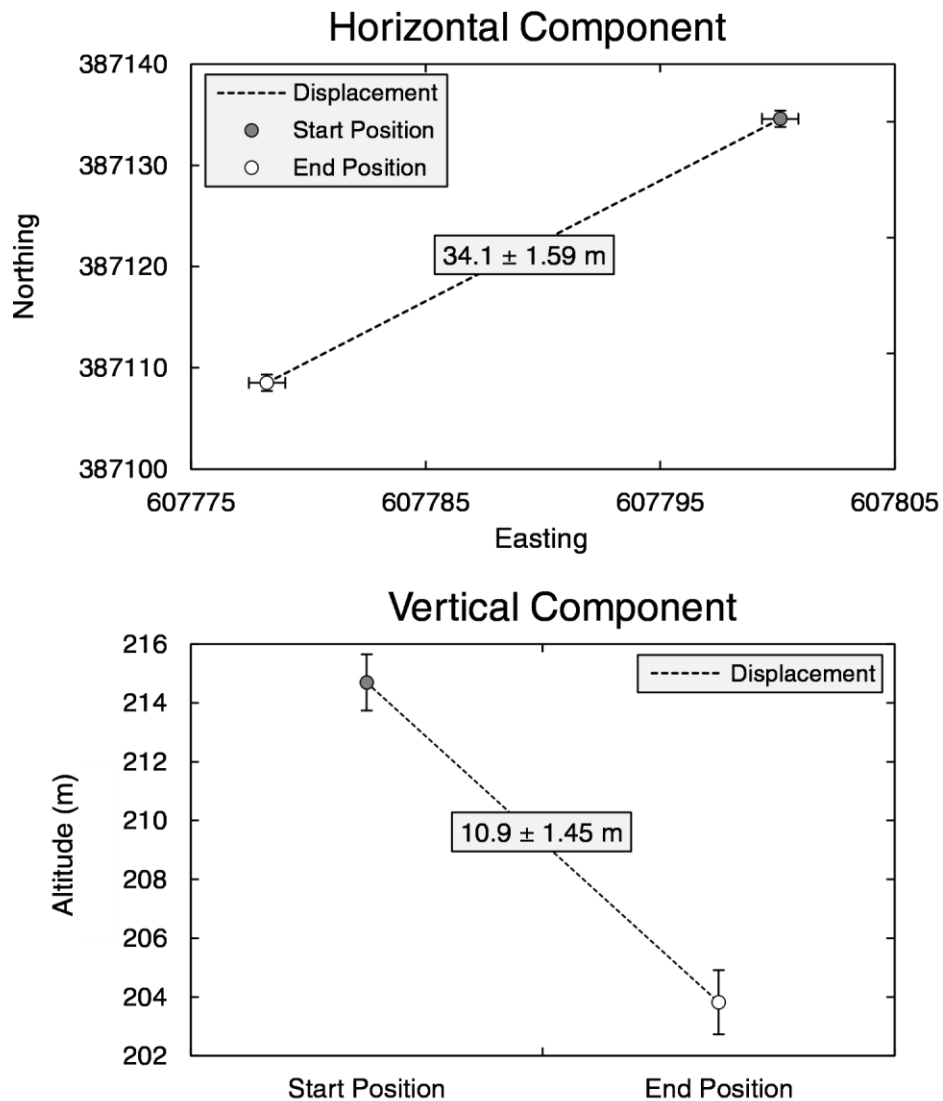


Figure 26. Horizontal and vertical track length uncertainty for surface feature 6 in the 2011 AWS1 image sequence.

3.4 - Meteorological data

3.4.1 - Data processing

In order to determine the climatic controls on glacier dynamics at Falljökull, spatial and temporal variability in surface velocities and rates of thinning were compared to local meteorological data provided by the BGS. Three AWS are currently in operation at Falljökull with data generation since 07/09/2009, 15/09/2010 and 14/09/2011 respectively. The lowest installation (AWS1) is in daily communication with the BGS, permitting daily data retrieval. Each installation records data using a Campbell Scientific CR800 Datalogger and measures each variable every 5 seconds to calculate an hourly average. The measured meteorological variables at each station are shown in Table 1.

Unfortunately, there were significant gaps in the dataset and intensive data processing was required to generate a chronological and sequential data series. Data from AWS1 are predominantly used in this study as the dataset is near continuous, with the exception of a brief period from 16:00 GMT on 06/09/2011 to 11:00 GMT on 10/09/2011. To account for this, temperature, relative humidity and wind speed data from AWS3 and precipitation data from AWS4 were used. This highlights the value of multiple installations which provide redundancy when one or more stations are not operational. While using multiple meteorological datasets would provide a more comprehensive insight into changing conditions with altitude, variability that may have an impact on glacier functioning, it was not feasible to study this within the confines of the project.

Table 1. Meteorological variables.

Variable	AWS1	AWS3	AWS4
Temperature (°C)	✓	✓	✓
Relative humidity (%)	✓	✓	✓
Wind speed (m s ⁻¹)	✓	✓	✓
Wind direction (°)	✓	✓	✓
Precipitation (mm hr ⁻¹)	✓		✓
Solar irradiance (W/m ²)	✓		
Atmospheric pressure (hectopascals)			✓

3.4.2 - Energy balance modelling

As discussed in Section 2.2, meteorological conditions primarily control glacier functioning through surface energy balance, which can be modelled by calculating the inputs of energy to the glacier surface e.g. incoming shortwave radiation, temperature, wind speed and precipitation, in the context of site specific conditions

e.g. latitude, altitude, aspect, hypsometry, surface albedo, surface roughness and temperature lapse rate. A key input to the glacier surface is air vapour pressure which is strongly temperature dependent (Fig. 27). This is calculated by first calculating saturation vapour pressure:

$$ES = A \times EXP(B \times T) \quad (18)$$

where ES is saturation vapour pressure, EXP is the value of the mathematical constant e , raised to the power of the n th value, and T is average air temperature. A (608.19) and B (0.0712) are empirically determined constants. To calculate air vapour pressure, the following equation is used:

$$AVP = (RH/100) \times ES \quad (19)$$

where AVP is air vapour pressure and RH is relative humidity.

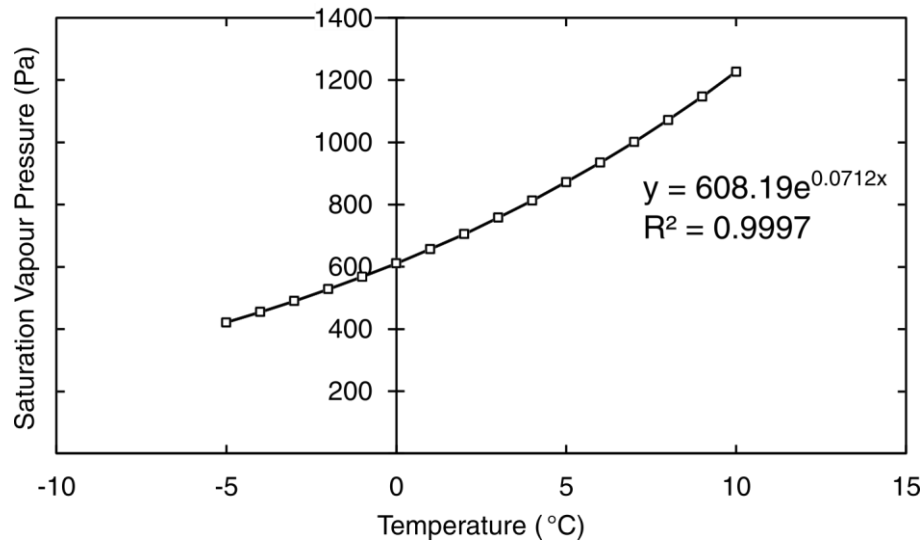


Figure 27. The impact of temperature on saturation vapour pressure.

Surface melt production at Falljökull, incorporating the energy flux related to precipitation (Thompson, 2016), was estimated using energy balance modelling (Brock and Arnold, 2000). Unfortunately, with no ablation data available at Falljökull, it was not possible to adjust the model parameters to ensure that modelled surface melt production was representative of observed surface melt. Ablation stake data were available for Virkisjökull (Flett, unpublished data, Table. 2) and provide a useful comparison with modelled values at Falljökull. However, given that these values are from a unique, albeit proximal glacier, and related to a year not studied in this project, it was not an efficient use of processing time to intensively run the model to achieve a best fit between these datasets.

The model developed by Brock and Arnold (2000) was chosen for its straightforward adaptability to different sites. Model inputs are shown in Table. 3. Periods of

predominantly snow covered or snow free ice were identified and modelled to generate more reliable values for surface melt (Fig. 28). This allowed values for albedo and surface roughness to be tweaked to better capture changing conditions at the glacier surface. This modelling has generated a long term, high temporal resolution dataset (hourly) of glacier surface melt. Variability in surface melt production and the relative contribution of radiative and turbulent fluxes has been demonstrated at inter and intra-annual scales and compared to glacier dynamics.

Table 2. Energy balance modelling parameters.

Site Details	Snow	Ice
Latitude (°)	63.97	63.97
Longitude (°)	-16.8	-16.8
Slope (°)	9.6	9.6
Aspect (°)	40	40
Elevation (m)	150	150
Albedo	0.5	0.1
Roughness (m)	0.00025	0.03
Met St. Elev (m)	156	156
Lapse Rate (°/m)	0.0065	0.0065

Table 3. Virkisjökull ablation in 2014 (Flett, unpublished data).

Elevation (m)	Ablation (mm w.e.) ^a
250	8860
290	7740
300	8870
345	8220
370	7690
400	6730
400	6450
490	4760

^a Based on ablation stake measurements

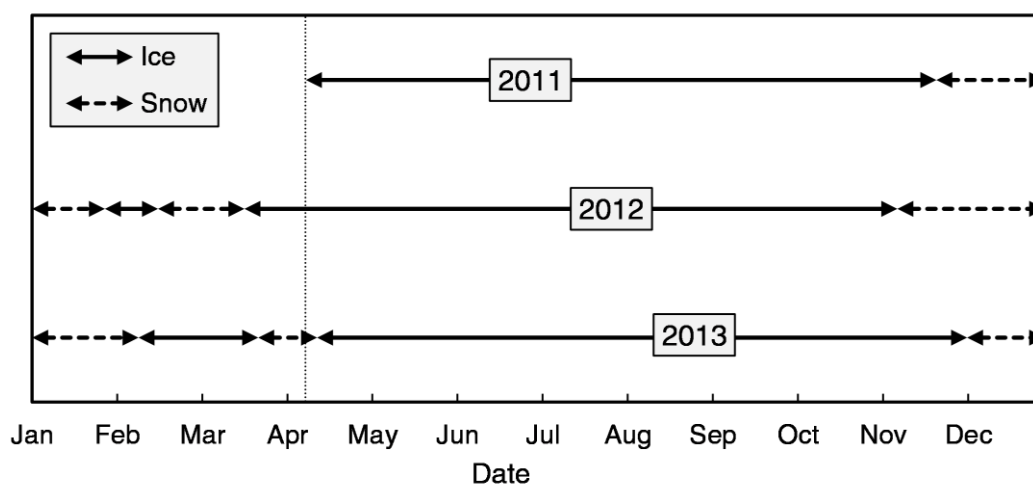


Figure 28. Glacier surface conditions (ice/snow) for EBM (2011-2013).

3.5 - Pointcatcher results

3.5.1 - Image registration

Topographic feature tracking results (Fig. 29) demonstrate that 10 or more features were tracked in > 60% of all images. However, variability between camera installations is evident. These data suggest that tracking 20 topographic features is necessary at AWS1. At this installation, 20 - 40% of images have fewer than 10 point observations. By reducing the target number of tracked features, it is likely that the quality of image registration would be compromised as the majority of images would display a limited spatial coverage of points across the skyline. In contrast, 15 - 20 point observations are evident in over 80% of all images from AWS3 as features are visible more often throughout these image sequences. This is partially due to the reduced distance from the camera installation to the surrounding topography which allows smaller scale topographic features to be tracked. Despite this, using a large number of static points will still generate more reliable results and allows for erroneous data to be easily identified.

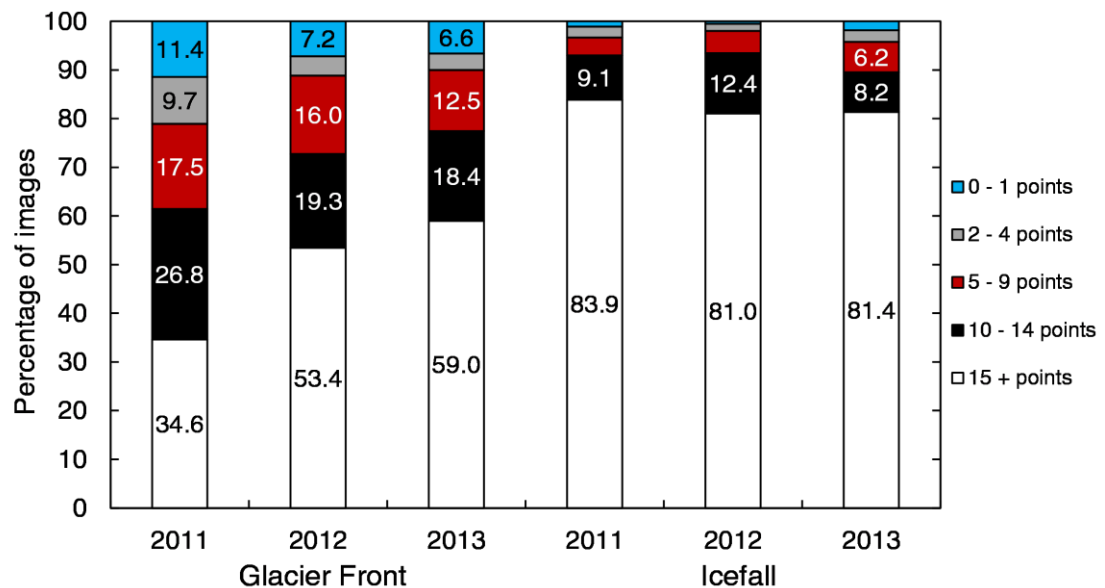


Figure 29. Topographic feature tracking results.

These topographic point observations were used to calculate camera orientation angles, orientation precision estimates and a residual RMS value for each individual image (Fig. 30, A-C). However, given the number of image sequences (6), it was not feasible to present all these data. As such, key data regarding image registration are presented in Table 4. At AWS1, the skyline was obscured by cloud or snow cover in > 50 images. Orientation angles for these images were derived from previous or subsequent images. In contrast, image registration was more successful at AWS3, with only ≤ 20 images with no orientation points (inliers). At AWS3, the mean

number of inliers in successfully registered images is also consistently higher than at AWS1. Camera orientation precision is high throughout, with a maximum mean RMS value of just 0.63 pixels. For 4 image sequences, this decreases to ≤ 0.22 pixels. However, intra-annual variation is evident. In 2011 at AWS1, a change in camera

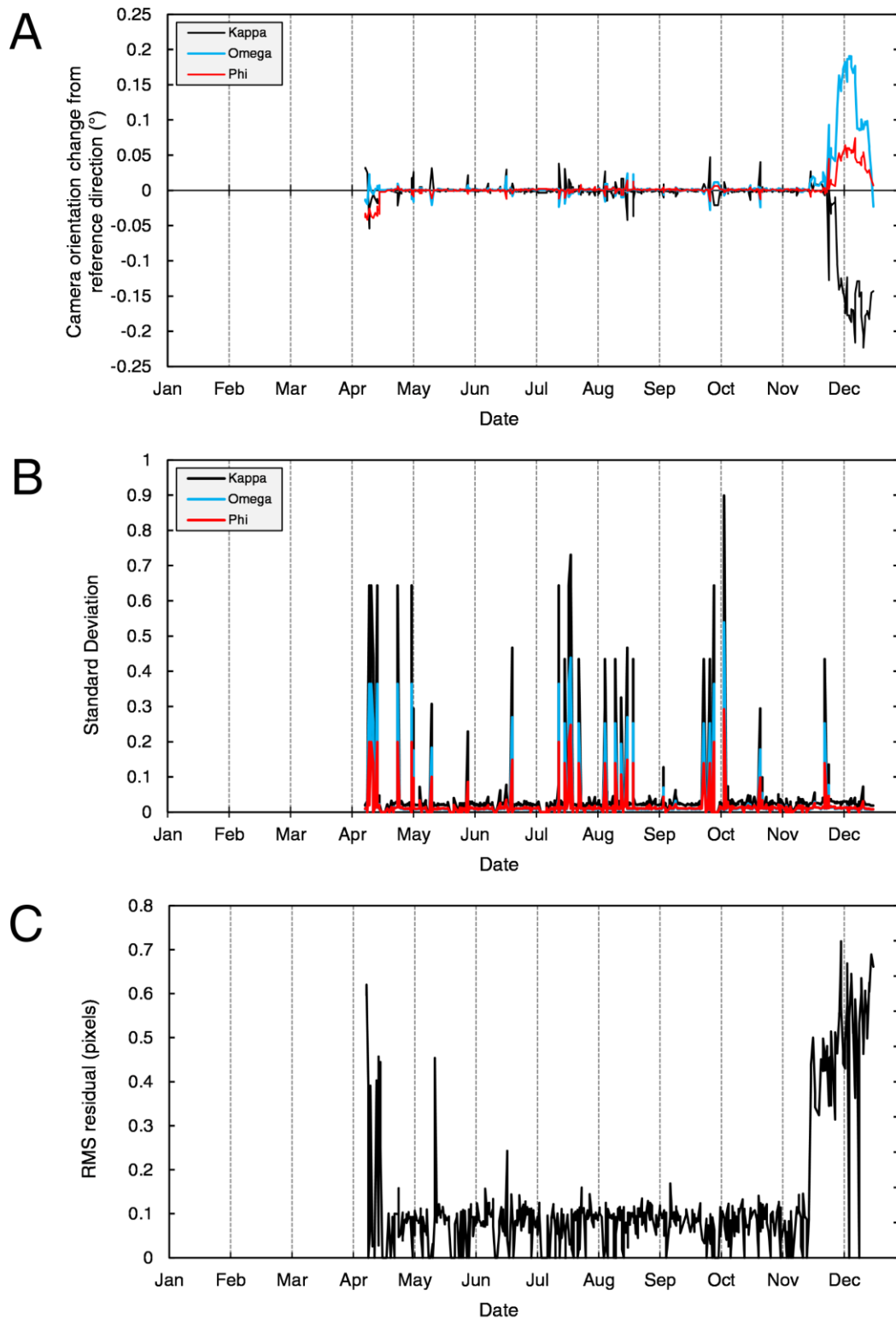


Figure 30. Results of error analyses for the 2011 AWS1 image sequence. (A) Camera orientation angles. (B) Orientation precision estimates. (C) RMS residuals.

orientation from late-November is reflected in an increase in the RMS to 0.5 pixels (Fig. 30, A). This is probably complicated by winter snow cover. However, orientation precision estimates remain low over this period, with mean omega, phi and kappa uncertainties of 0.02° , 0.02° and 0.04° respectively, reflecting the robust manual tracking procedure.

Table 4. Registration results.

Camera	Year	No. registered images	No. images with no inliers	Mean No. inliers ^a	Mean RMS residual	Mean Precision ^b
AWS1	2011	500	78	12	0.14	1.01
	2012	641	57	14	0.11	1.01
	2013	627	51	14	0.45	1.10
AWS3	2011	559	12	18	0.22	1.02
	2012	758	6	17	0.63	1.18
	2013	689	20	18	0.12	1.01

^a in successfully registered images, ^b precision of feature measurement based on Equation (16)

3.5.2 - Glacier feature tracking

Glacial feature tracking statistics are shown in Fig. 31. 10 or more point observations were present in > 60% of images and more than 5 points in > 86.5% of images. However, glacier features could not be tracked through the entirety of each image sequence. Feature timelines for 2011 (Fig. 32), 2012 (Fig. 33) and 2013 (Fig. 34) demonstrate the varying persistence of glacier surface features.

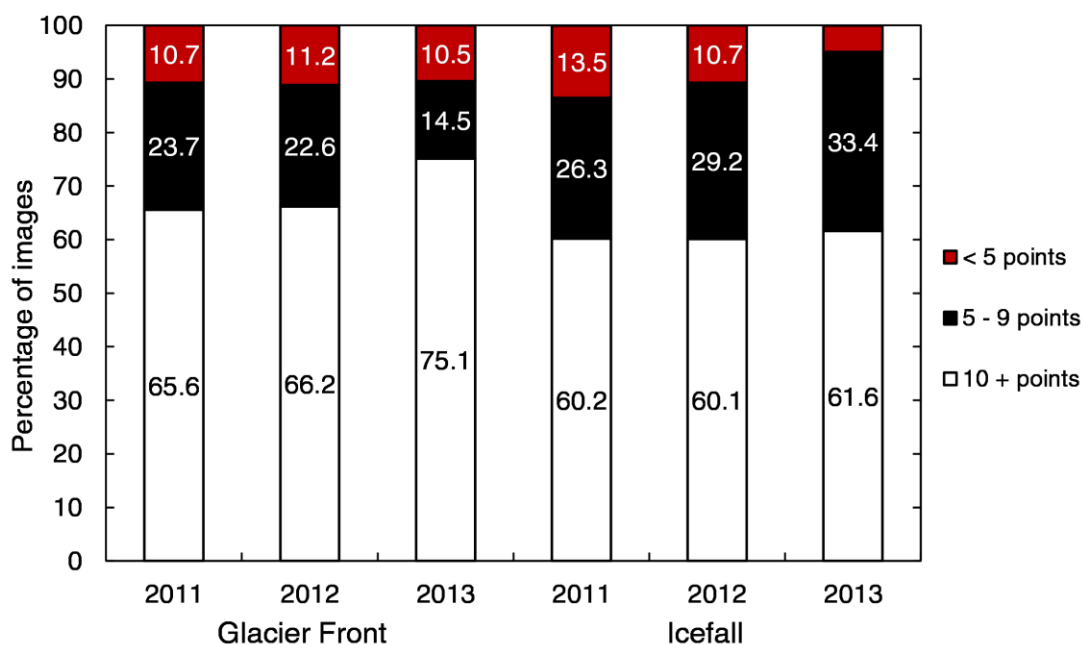


Figure 31. Glacier feature tracking results.

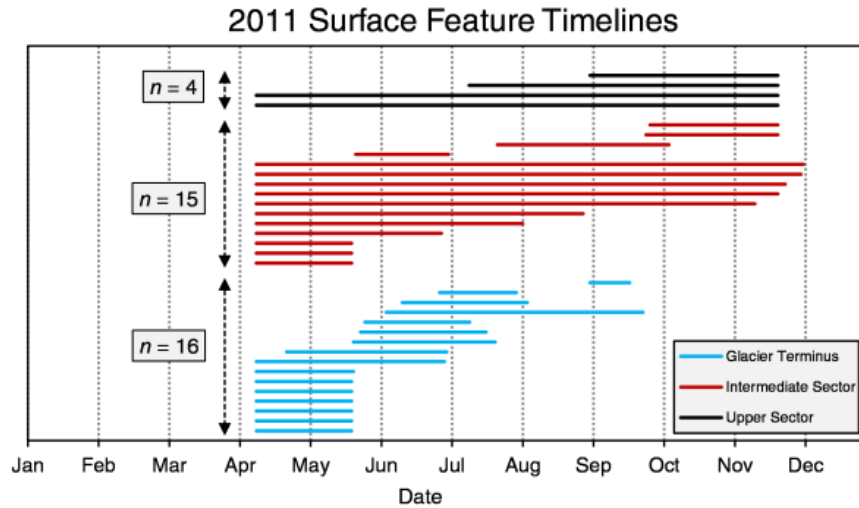


Figure 32. Glacier feature timelines (interval between the first and last point observation) for the 2011 AWS1 image sequence.

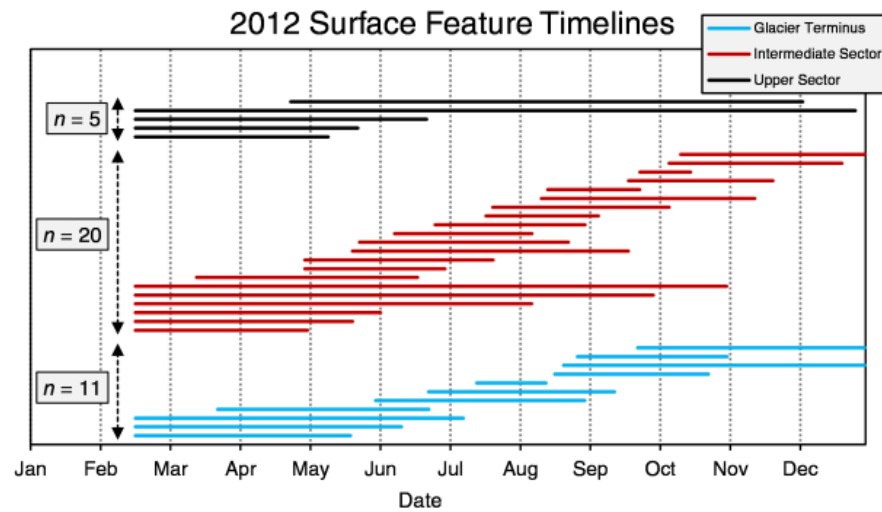


Figure 33. Glacier feature timelines (interval between the first and last point observation) for the 2012 AWS1 image sequence.

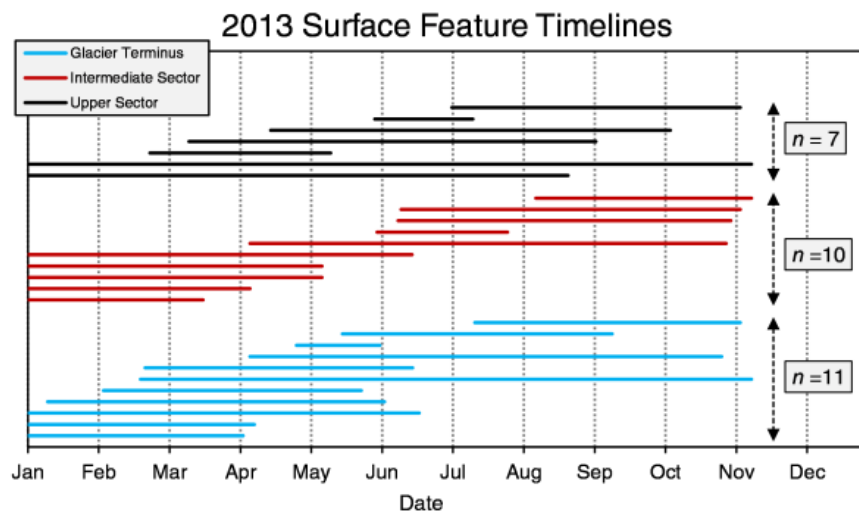


Figure 34. Glacier feature timelines (interval between the first and last point observation) for the 2013 AWS1 image sequence.

Chapter 4 - Results

4.1 - Inter-annual variability

4.1.1 - Thinning rates

Based on the spatial groupings established in Section 3.3.1, spatio-temporal variability in inter-annual rates of surface elevation change are evident (Table 5). However, Falljökull is thinning substantially in all sectors, in excess of 0.029 m d^{-1} throughout the period 2011-2013. Large scale, rapid retreat of the margin and significant surface lowering are clearly evident in Fig. 35. Annual data for glacier dynamics i.e. retreat, forward motion and thinning, are shown for each year in Figures 36-38.

Table 5. Annual surface velocity and thinning rate data.

	Year	Terminus	Spatial Grouping						
			\pm^b	Intermediate	\pm	Upper	\pm	Icefall	\pm
Horizontal Component ^a	2011	0.020	0.005	0.029	0.006	0.077	0.021	1.39	0.05
	2012	0.025	0.006	0.031	0.006	0.141	0.024	1.35	0.05
	2013	0.017	0.005	0.044	0.010	0.158	0.022	1.58	0.08
Vertical Component ^a	2011	-0.060	0.003	-0.052	0.003	-0.044	0.004	-0.68	0.04
	2012	-0.036	0.006	-0.045	0.004	-0.037	0.005	-0.60	0.03
	2013	-0.029	0.006	-0.029	0.006	-0.037	0.007	-0.66	0.04

^a Values are m d^{-1} , ^b 1σ uncertainty

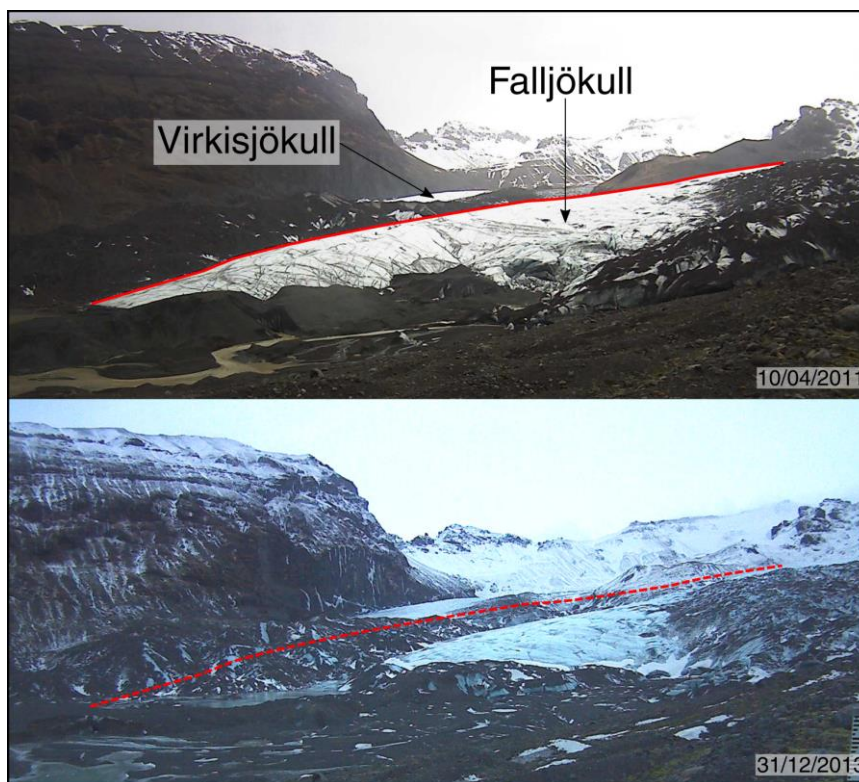


Figure 35. Retreat and thinning of the Falljökull ice front (10/04/2011 - 31/12/2013).

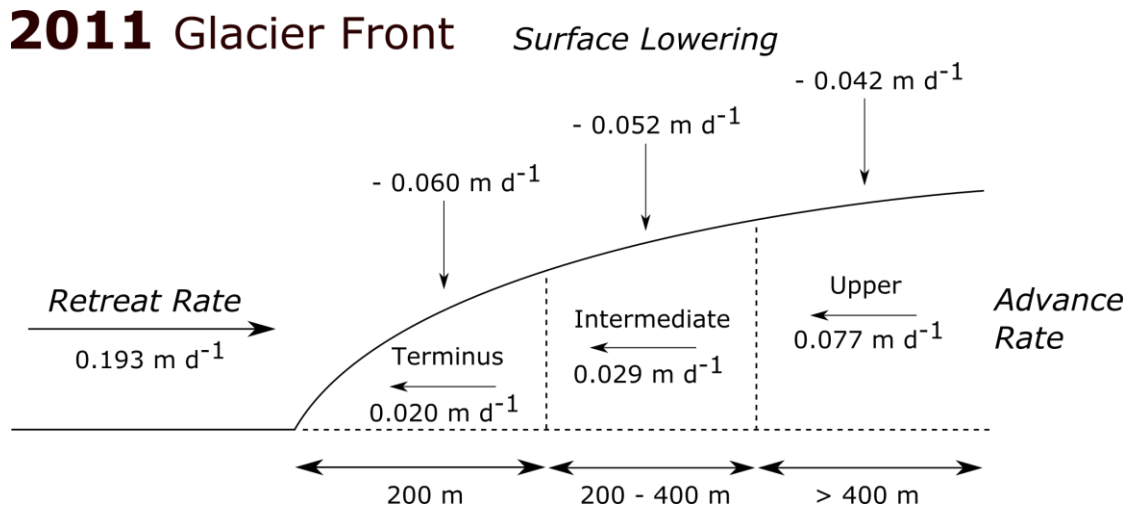


Figure 36. Glacier dynamics at the Falljökull glacier front in 2011.

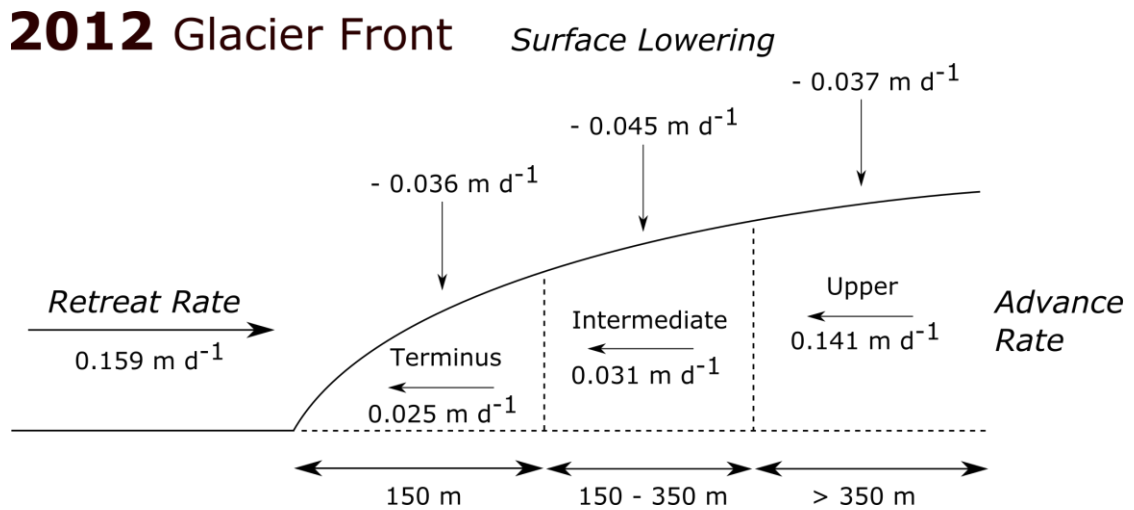


Figure 37. Glacier dynamics at the Falljökull glacier front in 2012.

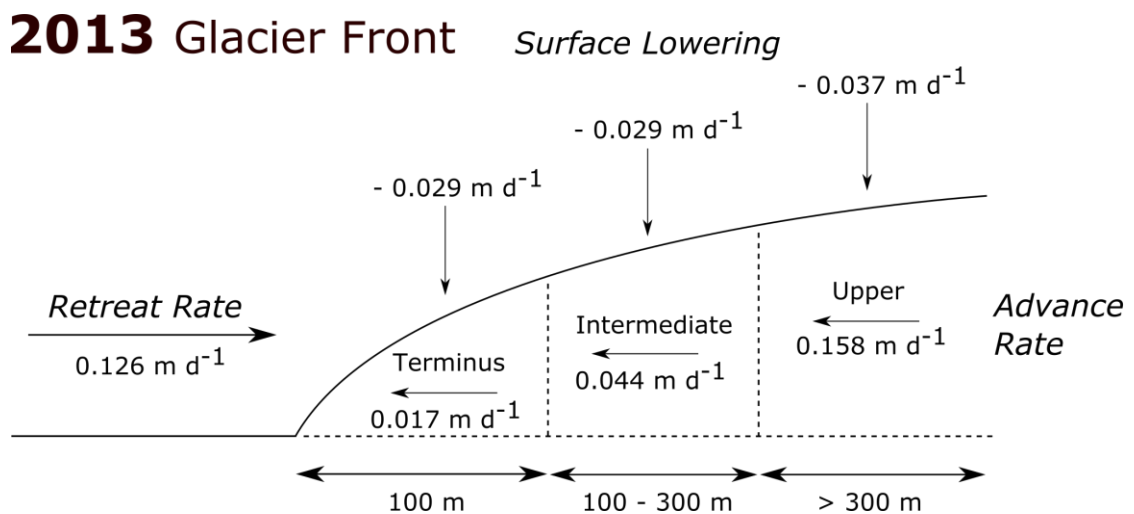


Figure 38. Glacier dynamics at the Falljökull glacier front in 2013.

In 2011, statistically significant spatial variability is evident, as thinning rates decrease from the terminus to the upper sector. While the terminus thins at a rate of $0.06 \pm 0.003 \text{ m d}^{-1}$, the intermediate and upper sectors undergo thinning at $0.052 \pm 0.003 \text{ m d}^{-1}$ and $0.044 \pm 0.004 \text{ m d}^{-1}$ respectively. T-tests show that terminus-intermediate and terminus-upper variability is significant at $p = 0.1$ and $p = 0.5$ respectively. Intermediate-upper variation is not statistically significant ($p = 0.15$). A similar trend is not evident in 2012 and 2013. Thinning rates for each sector in these years are within error ($p = > 0.1$). These results are presented in Table 6.

Table 6. Intra-annual spatial variability in thinning rates: t-test results.

Year	Group 1	Group 2	<i>t</i> Stat	<i>t</i> Critical two-tail	<i>p</i> value	Interpretation ^a
2011	Terminus	Intermediate	-1.94	2.05	0.06	H ₁
	Terminus	Upper	-3.43	2.45	0.01	H ₁
	Intermediate	Upper	-1.58	2.31	0.15	H ₀
2012	Terminus	Intermediate	1.04	2.09	0.31	H ₀
	Terminus	Upper	0.13	2.14	0.90	H ₀
	Intermediate	Upper	-1.13	2.16	0.28	H ₀
2013	Terminus	Intermediate	-0.33	2.10	0.75	H ₀
	Terminus	Upper	0.96	2.14	0.35	H ₀
	Intermediate	Upper	1.16	2.13	0.26	H ₀

^a H₀ - There is no significant difference between the groups, H₁ - There is a significant difference between the groups

Temporal variability is also evident with a statistically significant reduction in thinning rate ($p = < 0.01$) for the glacier terminus and intermediate sector from 2011 to 2013 (Table 7). At the terminus, this is largely accounted for by a statistically significant decrease ($p = < 0.01$) in thinning rate between 2011 and 2012 (- 40%) to just $0.036 \pm 0.006 \text{ m d}^{-1}$. While the intermediate sector also demonstrates a reduction in thinning rate over this interval (- 16%), this is not statistically significant ($p = 0.19$). In contrast, thinning rates fall significantly between 2012 and 2013 for the intermediate sector to just $0.029 \pm 0.006 \text{ m d}^{-1}$ ($p = 0.04$). Both sectors record an average surface lowering of $0.029 \pm 0.006 \text{ m d}^{-1}$ in 2013, which overlaps with the upper sector within

Table 7. Inter-annual temporal variability in thinning rates: t-test results.

Spatial Group	Year 1	Year 2	<i>t</i> Stat	<i>t</i> Critical two-tail	<i>p</i> value	Interpretation ^a
Glacier Terminus	2011	2012	-3.38	2.16	< 0.01	H ₁
	2012	2013	-0.97	2.09	0.34	H ₀
	2011	2013	-4.74	2.16	< 0.01	H ₁
Intermediate	2011	2012	-1.34	2.03	0.19	H ₀
	2012	2013	-2.22	2.13	0.04	H ₁
	2011	2013	-3.18	2.18	< 0.01	H ₁
Upper	2011	2012	-1.06	2.36	0.33	H ₀
	2012	2013	-0.10	2.23	0.92	H ₀
	2011	2013	-0.90	2.26	0.39	H ₀

^a H₀ - There is no significant difference between the years, H₁ - There is a significant difference between the years

error. Rates of surface lowering are stable for the upper sector for the period 2011-2013 with values of $0.044 \pm 0.004 \text{ m d}^{-1}$, $0.037 \pm 0.005 \text{ m d}^{-1}$ and $0.037 \pm 0.007 \text{ m d}^{-1}$ in 2011, 2012 and 2013 respectively.

4.1.2 - Surface velocities

Surface velocities exhibit significant spatio-temporal variability over the period 2011-2013 (Table 8). A consistent inter-annual spatial trend is evident as surface velocities decrease from the upper sector to the terminus. Average surface velocity data plotted against northing (Figs. 39-41) demonstrates a strong correlation between these variables in 2013 ($R^2 = 0.77$, $p = < 0.01$). However, this relationship is more uncertain in 2012 ($R^2 = 0.51$) while these data are poorly correlated in 2011 ($R^2 = 0.35$). In these years, slow surface velocities ($< 0.005 \text{ m d}^{-1}$) are observed higher up the glacier than expected. In 2011, surface velocities of $0.077 \pm 0.02 \text{ m d}^{-1}$ in the upper sector greatly exceeded the values of $0.02 \pm 0.005 \text{ m d}^{-1}$ and $0.029 \pm 0.006 \text{ m d}^{-1}$ recorded for the terminus and intermediate sector respectively. This variability is statistically significant at $p = 0.1$ although relatively large errors for the upper sector ($\pm 0.02 \text{ m d}^{-1}$) account for some overlap of these data. Terminus-intermediate variation is not statistically significant in 2011 and 2012, although more significant variability is evident in 2013 ($p = 0.06$). Variation between all sectors is statistically significant in this year, accounted for by a marked slow-down in the rate of motion of the terminus (-32%) to just $0.017 \pm 0.005 \text{ m d}^{-1}$, an acceleration of the intermediate sector ($+46\%$) to $0.044 \pm 0.01 \text{ m d}^{-1}$ and the maintenance of high surface velocities in the upper sector of $0.158 \pm 0.022 \text{ m d}^{-1}$. These changes in 2013 account for the better relationship between surface velocities and northing in this year (Fig. 41). Throughout the period 2011-2013, the terminus, intermediate and upper sectors flowed at velocity ranges of $1.7 - 2.5 \text{ cm d}^{-1}$, $2.9 - 4.4 \text{ cm d}^{-1}$ and $7.7 - 15.8 \text{ cm d}^{-1}$ respectively.

Table 8. Intra-annual spatial variability in surface velocities: t-test results.

Year	Group 1	Group 2	t Stat	t Critical two-tail	p value	Interpretation ^a
2011	Terminus	Intermediate	-1.08	2.05	0.29	H ₀
	Terminus	Upper	-2.74	3.18	0.07	H ₁
	Intermediate	Upper	-2.31	2.78	0.08	H ₁
2012	Terminus	Intermediate	-0.64	2.05	0.53	H ₀
	Terminus	Upper	-4.69	2.78	< 0.01	H ₁
	Intermediate	Upper	-4.45	2.57	< 0.01	H ₁
2013	Terminus	Intermediate	-2.03	2.18	0.06	H ₁
	Terminus	Upper	-5.89	2.36	< 0.01	H ₁
	Intermediate	Upper	-4.34	2.26	< 0.01	H ₁

^a H₀ - There is no significant difference between the groups, H₁ - There is a significant difference between the groups

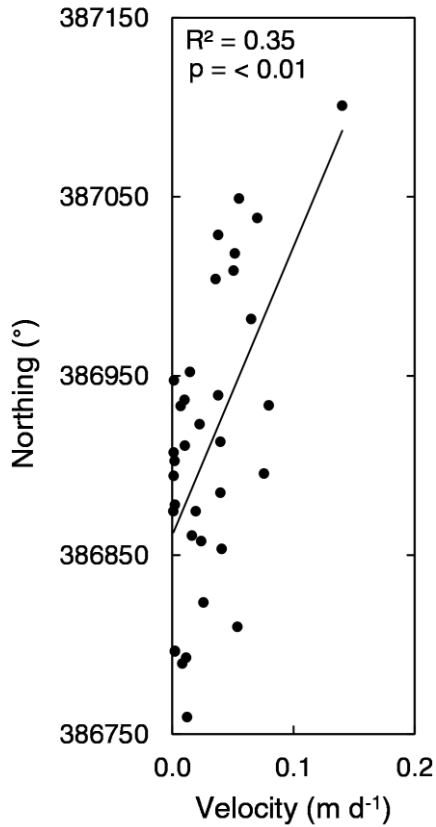


Figure 39. Plotting horizontal velocity magnitudes against Northing for 2011 surface features.

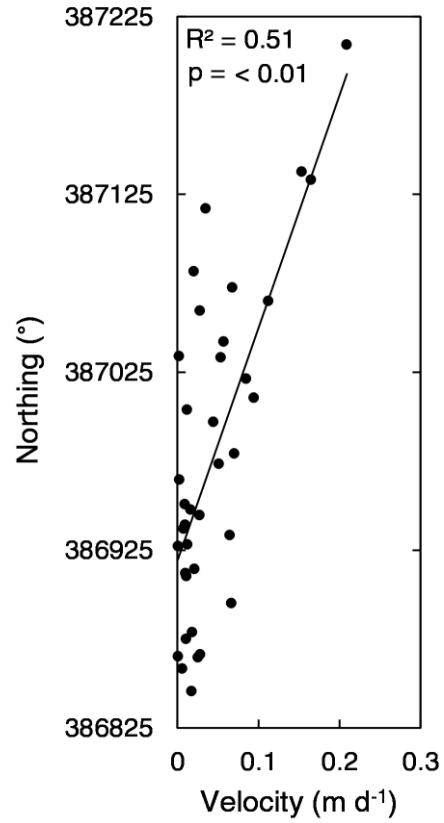


Figure 40. Plotting horizontal velocity magnitudes against Northing for 2012 surface features.

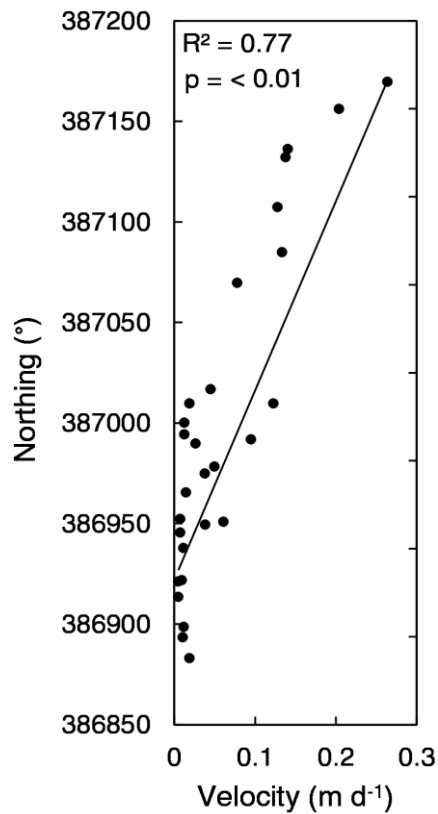


Figure 41. Plotting horizontal velocity magnitudes against Northing for 2013 surface features.

Temporal variability is also evident (Table 9) with a statistically significant increase in surface velocities between 2011 and 2013 for the upper sector ($p = 0.04$). Upper sector variation over this timeframe is largely accounted for by a statistically significant acceleration (+ 83%) in 2012 ($p = 0.09$) to an average annual velocity of $0.141 \pm 0.024 \text{ m d}^{-1}$. In contrast, inter-annual variation is not statistically significant for both the terminus and intermediate sectors at $p = 0.1$. Although changes in motion are apparent, these are not beyond the error of the technique.

Table 9. Inter-annual temporal variability in surface velocities: t-test results.

Spatial Group	Year 1	Year 2	<i>t</i> Stat	<i>t</i> Critical two-tail	<i>p</i> value	Interpretation ^a
Glacier Terminus	2011	2012	-0.63	2.07	0.53	H ₀
	2012	2013	1.02	2.09	0.32	H ₀
	2011	2013	0.39	2.06	0.70	H ₀
Intermediate	2011	2012	-0.21	2.03	0.84	H ₀
	2012	2013	-0.95	2.14	0.36	H ₀
	2011	2013	-1.09	2.14	0.29	H ₀
Upper	2011	2012	-1.96	2.36	0.09	H ₁
	2012	2013	-0.42	2.26	0.69	H ₀
	2011	2013	-2.46	2.31	0.04	H ₁

^a H₀ - There is no significant difference between the years, H₁ - There is a significant difference between the years

At the icefall, surface velocities are stable over the period 2011-2012 ($p = 0.61$). However, a statistically significant acceleration (+ 17%) is evident between 2012 and 2013 ($p = 0.02$) as velocities increase from $1.35 \pm 0.05 \text{ m d}^{-1}$ to $1.58 \pm 0.08 \text{ m d}^{-1}$ (Table 10). In contrast, rates of surface elevation change are within error for the period 2011-2013.

Table 10. Inter-annual temporal variability in icefall surface velocities: t-test results.

Spatial Group	Year 1	Year 2	<i>t</i> Stat	<i>t</i> Critical two-tail	<i>p</i> value	Interpretation ^a
Icefall	2011	2012	0.51	1.98	0.61	H ₀
	2012	2013	-2.47	1.99	0.02	H ₁
	2011	2013	-2.05	1.98	0.04	H ₁

^a H₀ - There is no significant difference between the years, H₁ - There is a significant difference between the years

4.2 - Energy balance modelling

4.2.1 - Inter-annual variability in surface melt production

Surface melt data are available for Falljökull from 10/04/2011 - 31/12/2013 (Table 11). Although meteorological data were available throughout 2011, glacier surface conditions were not known prior to this date. As such, it was not possible to adjust albedo and surface roughness parameters accordingly to achieve a best match between model inputs and the observed glacier surface. When 2012-2013 data were adjusted to cover the same 9 month period to enable comparison between years, significant inter-annual variability in surface melt production was evident (Fig. 42). In 2011, surface melt production was equivalent to 7952 mm w.e. at the glacier front (150 m a.s.l). Total melt exceeded 8700 mm w.e. over the same period in 2012 but was limited to just 6974 mm w.e. in 2013.

Table 11. Energy balance modelling output (2011-2013).

		Year					
		2011	2012	2013	2011	2012	2013
		10/04/2011	01/01/2012	01/01/2013	10/04 - 31/12		
		31/12/2011	31/12/2012	31/12/2013			
Energy Flux Totals in mm w.e.	Shortwave Radiation	5482	7819	6470	5482	7172	5750
	Longwave Radiation	410	2	-188	410	325	150
	Sensible Heat Flux	1664	1818	1362	1664	1430	1029
	Latent Heat Flux	299	-301	-241	299	-288	-50
	Precipitation	98	75	169	98	74	94
	Melt	8468	10072	8544	8468	9267	7556
	Melt Total	7952	9382	7571	7952	8714	6974
Energy Flux Rates in mm w.e. per day	Shortwave Radiation	20.9	24.5	17.8	20.9	27.4	22.0
	Longwave Radiation	1.6	0.0	-0.5	1.6	1.2	0.6
	Sensible Heat Flux	6.4	5.7	3.7	6.4	5.5	3.9
	Latent Heat Flux	1.1	-0.9	-0.7	1.1	-1.1	-0.2
	Precipitation	0.4	0.2	0.5	0.4	0.3	0.4
	Melt	32.4	31.5	23.4	32.4	35.4	28.9
	Melt Total	30.4	29.4	20.8	30.4	33.3	26.7

4.2.2 - The contribution of radiative and turbulent heat fluxes

Surface melt is dominated by shortwave radiative fluxes, which account for 68.9% of total melt in 2011 (Fig. 43), increasing to 82.8% in 2012 (Fig. 44) and 85.5% in 2013 (Fig. 45), equivalent to an energy flux range of 20.9 - 27.4 mm w.e d⁻¹. The smaller contribution of shortwave radiation in 2011 is accounted for by the increased energy flux from longwave radiation (1.6 mm w.e. d⁻¹) and both sensible (6.4 mm w.e. d⁻¹) and latent heat (1.1 mm w.e. d⁻¹) relative to subsequent years. Energy transfer via sensible heat flux contributes 17.6 - 20.9% of total melt over this period demonstrating the important contribution of turbulent heat fluxes in maritime environments. In contrast, longwave radiation demonstrates a negligible (~ 0.0 mm w.e d⁻¹) or even negative contribution (- 0.5 mm w.e d⁻¹) to total melt when the

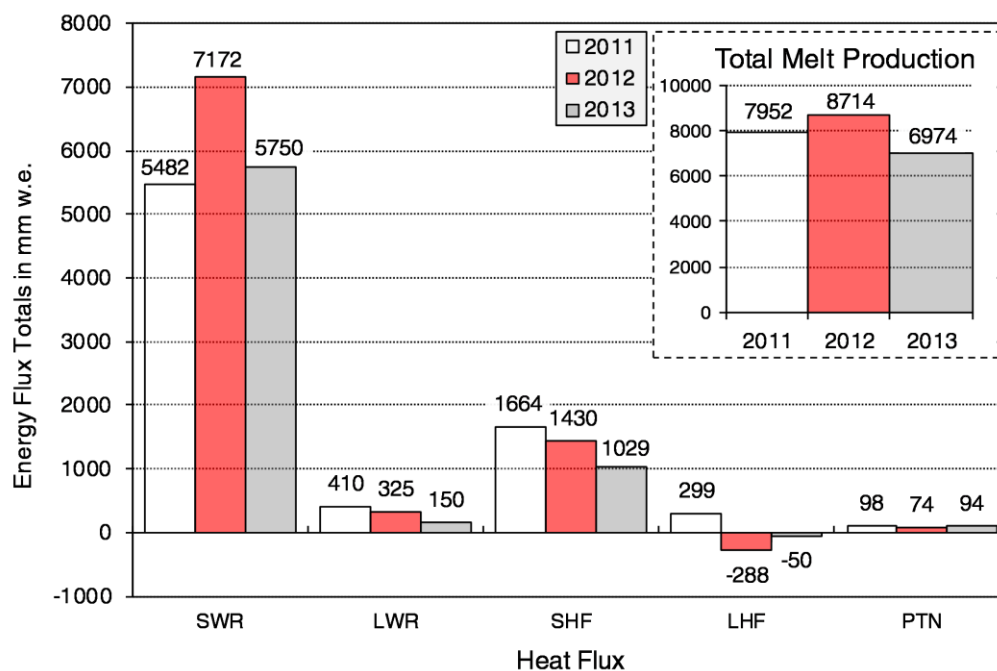


Figure 42. Total melt production and energy totals (mm w.e.) from turbulent and radiative heat fluxes (2011-2013).

entirety of 2012 and 2013 are considered. Latent heat contributes 1.1 mm w.e. d^{-1} to total melt in 2011 but shifts to negative values (- 3.3%) in 2012 (- 1.1 mm w.e. d^{-1}). Its contribution to the surface energy budget is negligible in 2013 at just - 0.2 mm w.e. d^{-1} . Finally, energy inputs from precipitation account for 0.8% - 2.2% of the surface energy budget in each year, equivalent to just 342 mm w.e. from April 2011 to December 2013.

However, the relative importance of radiative and turbulent heat fluxes demonstrates variability over seasonal timescales. In 2012, inputs from shortwave radiation account for > 60% of total melt between February and October. In contrast, the positive energy contribution from longwave radiation is generally small during the summer months (< 10 % of total melt). However, this flux is of increasing importance in the late melt season, accounting for 15% (224 mm w.e.) and 17% (225 mm w.e.) of total melt in July and August 2012 respectively. Furthermore, contributions of sensible and latent heat and the energy flux from precipitation exceed shortwave radiative inputs during the winter. Therefore, although shortwave radiation contributes significantly to total melt throughout each year, additional energy fluxes are of increasing importance as inputs from shortwave radiation decline.

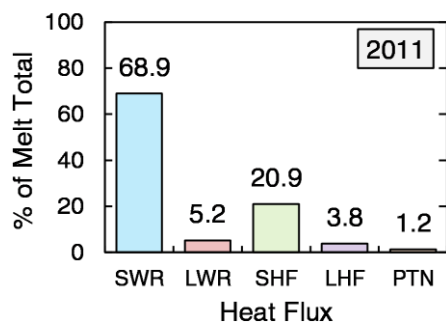


Figure 43. The relative contribution of energy fluxes to total melt (2011).

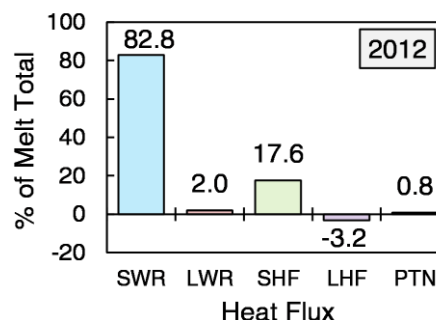


Figure 44. The relative contribution of energy fluxes to total melt (2012).

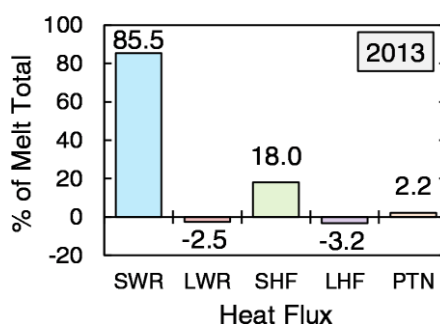


Figure 45. The relative contribution of energy fluxes to total melt (2013).

4.2.3 - Intra-annual variability in surface melt production

Clear seasonal trends in surface melt production are evident in the period 2011-2013. However, although monthly melt totals do vary significantly over this period, the timing of seasonal shifts are consistent in each year. Inter-annual variation is limited with tight coupling for 2011-2012 ($R^2 = 0.84$), 2011-2013 ($R^2 = 0.91$) and 2012-2013 ($R^2 = 0.94$). These data are statistically significant at $p = 0.01$. However, there are some subtle variations between each year.

Firstly, the timing of peak monthly surface melt production varies slightly over this period. In 2011, peak melt occurs in June but this is modelled in May in both 2012 and 2013. Additionally, while peak monthly melt totals in 2011 and 2013 are relatively similar, at 1778 mm w.e. and 1647 mm w.e. respectively, Falljökull is subject to enhanced surface melting in 2012 (2184 mm w.e.). In addition, while melt production exceeds 1000 mm w.e. for just 4 months in 2011 and 2013 (May – August), melt is sustained above 1000 mm w.e. for an extended 6 month period in 2012 (April - September). As such, not only does 2012 exhibit the highest monthly melt total but the peak melt season is sustained for the longest period. In contrast, melt production is severely restricted during the winter months and shifts to a negative surface energy budget in December of each year.

4.3 - Intra-annual variability in thinning and comparison with surface melt

4.3.1 - Glacier terminus

Rates of surface elevation change exhibit seasonal variability at the glacier terminus over the period 2011-2013. These intra-annual variations can be linked to temporal variability in surface melt production. Comparison of cumulative thinning and surface melt data generated through EBM (Figs. 46 - 48) indicates a clear relationship between these variables. Monthly thinning and melt data for the glacier terminus (Fig. 49 - 51) are generally well coupled in both 2012 ($R^2 = 0.64$, $p = 0.006$) and 2013 ($R^2 = 0.76$, $p = 0.001$) although these data are poorly correlated in 2011 ($R^2 = 0.04$, $p = 0.7$). This is probably accounted for by the restricted timeframe of the surface feature tracking data in 2011 (April - September). This makes comparison of cumulative melt and thinning data particularly challenging, as early and late season trends cannot be determined. Despite the poor correlation of this dataset, consistent inter-annual trends are evident.

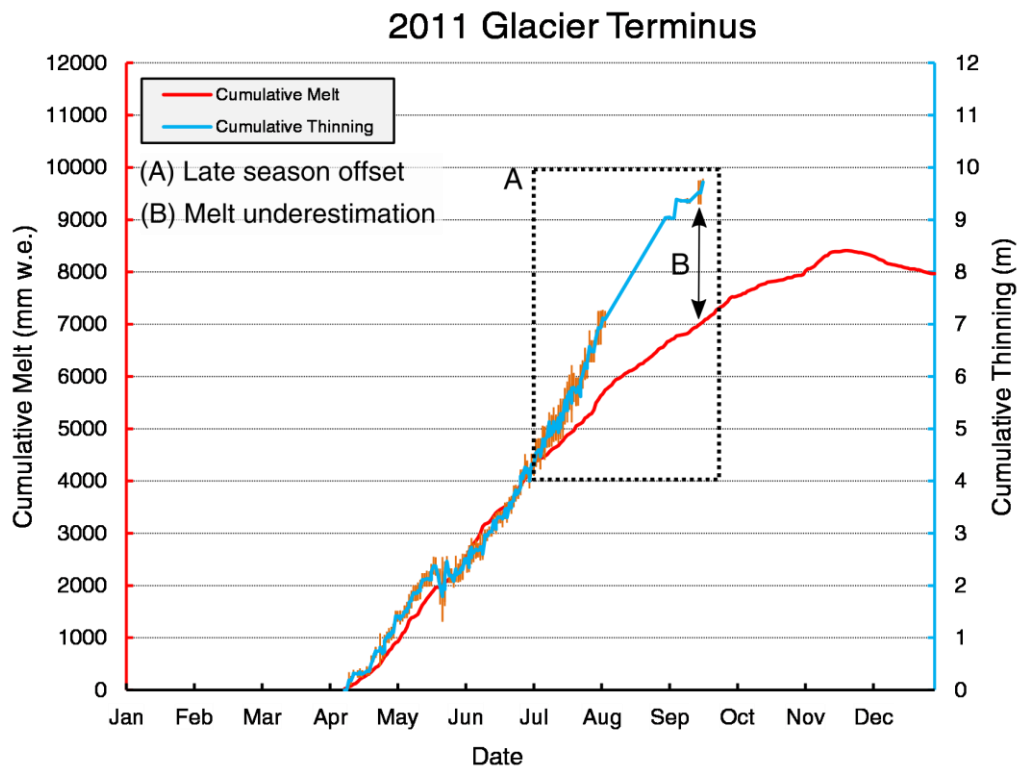


Figure 46. Cumulative melt (EBM) and cumulative thinning (time-lapse) at the glacier terminus in 2011.

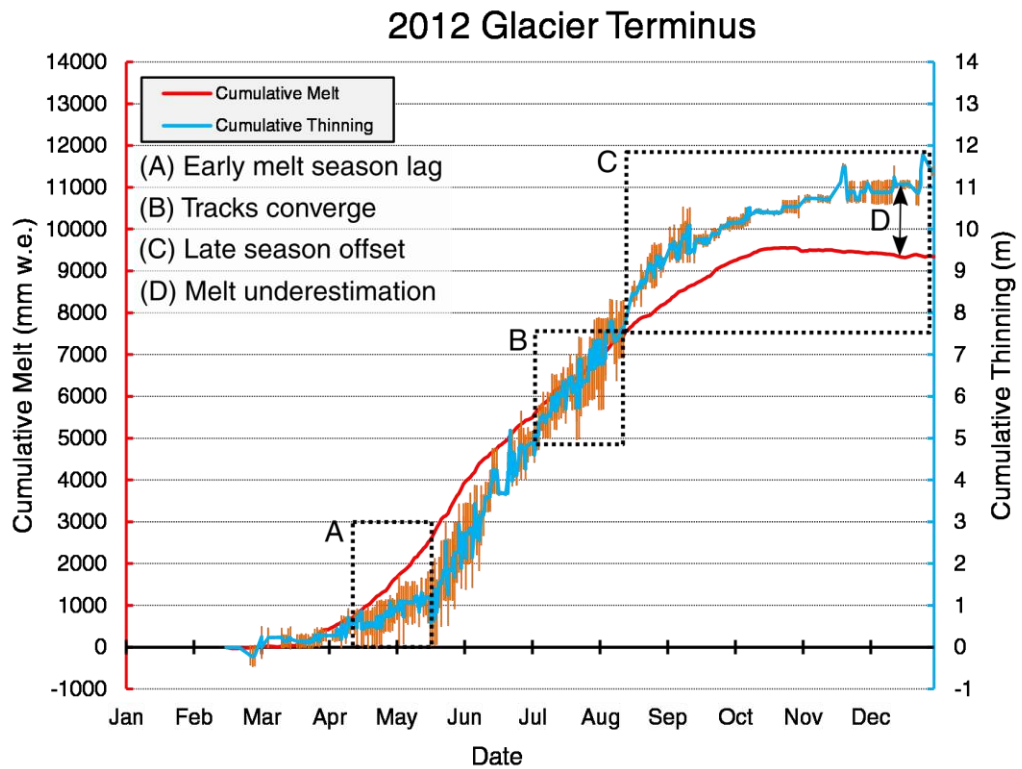


Figure 47. Cumulative melt (EBM) and cumulative thinning (time-lapse) at the glacier terminus in 2012.

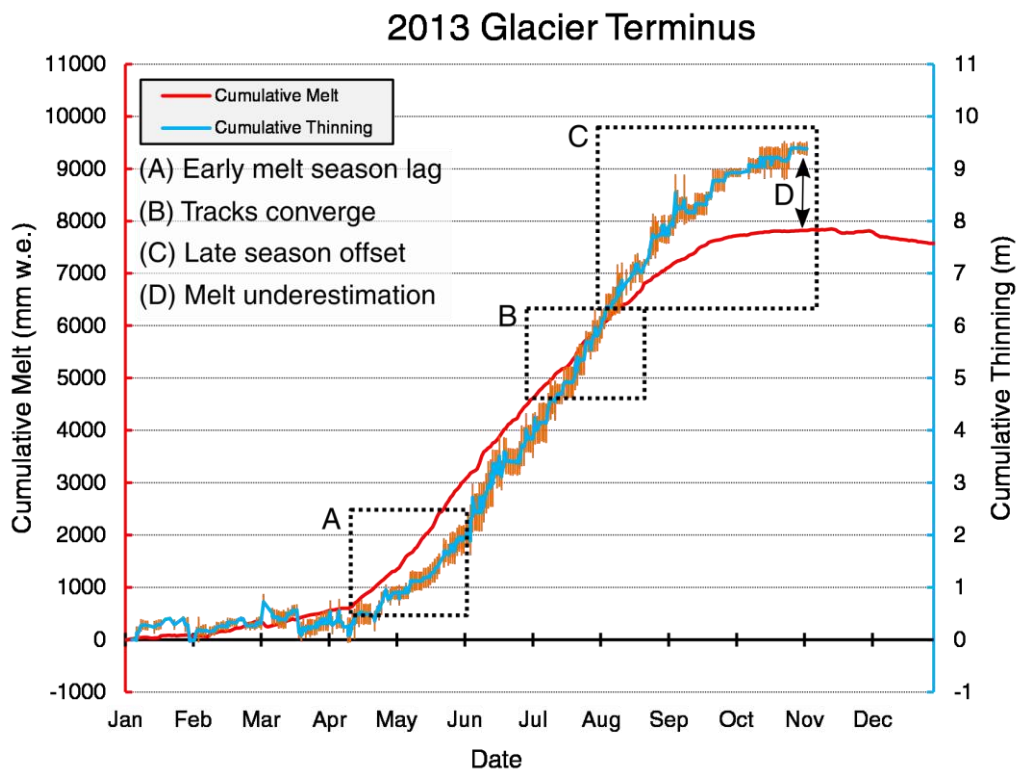


Figure 48. Cumulative melt (EBM) and cumulative thinning (time-lapse) at the glacier terminus in 2013.

Firstly, an early melt season lag is evident between cumulative melt and thinning data in both 2012 (Fig. 47, A) and 2013 (Fig. 48, A). In both years, surface melt production is severely restricted in the first three months (January - March) with cumulative melt production of < 500 mm w.e. Rates of surface elevation change are well correlated at this time with cumulative thinning of < 0.5 m. Surface melt production is significantly enhanced during April with high values for monthly melt modelled through to August in both years. However, there is a clear temporal lag between the onset of enhanced melt and the onset of enhanced thinning. As such, energy balance modelling overestimates glacier terminus thinning early in the melt season.

Secondly, thinning rates during the peak melt season i.e. May - August (2011 and 2013) and April - September (2012), must be higher than predicted by energy balance modelling. The magnitude of the offset between these variables decreases significantly over the peak melt season with convergence of cumulative melt and thinning totals (e.g. Fig. 47, B). For example, on 01/05/2012, 0.88 ± 0.29 m of cumulative thinning is calculated at the terminus. In contrast, cumulative surface melt production is significantly higher and modelled at 1578 mm w.e. However, by 14/07/2012, melt and thinning are within error, with cumulative thinning of 6.08 ± 0.33 m and melt production of 6164 mm w.e. In both 2012 and 2013, cumulative melt and thinning tracks converge in July.

Furthermore, enhanced rates of calculated surface thinning relative to modelled surface melt production are sustained after July, resulting in a clear offset between cumulative melt and thinning which is evident from August in both years (e.g. Fig. 47, C). While the late season trends are well correlated, with a coeval deceleration in melt and thinning from September, energy balance modelling significantly underestimates glacier terminus thinning in the late melt season (e.g. Fig. 47, D). Cumulative thinning of the terminus in December 2012 (11.4 ± 0.12 m) and November 2013 (9.4 ± 0.14 m) greatly exceed the values predicted by EBM at 9346 mm w.e. and 7819 mm w.e. respectively.

Finally, there is a temporal offset between peak melt and peak thinning in each year (e.g. Fig. 51). In 2011, peak monthly thinning of 0.073 ± 0.01 m d⁻¹ occurs in August, two months after modelled peak monthly melt in June. Peak monthly thinning in 2012 (0.074 ± 0.006 m d⁻¹) and 2013 (0.070 ± 0.004 m d⁻¹) also occur after peak melt. While the magnitude of this temporal offset varies between years, its consistency must be accounted for.

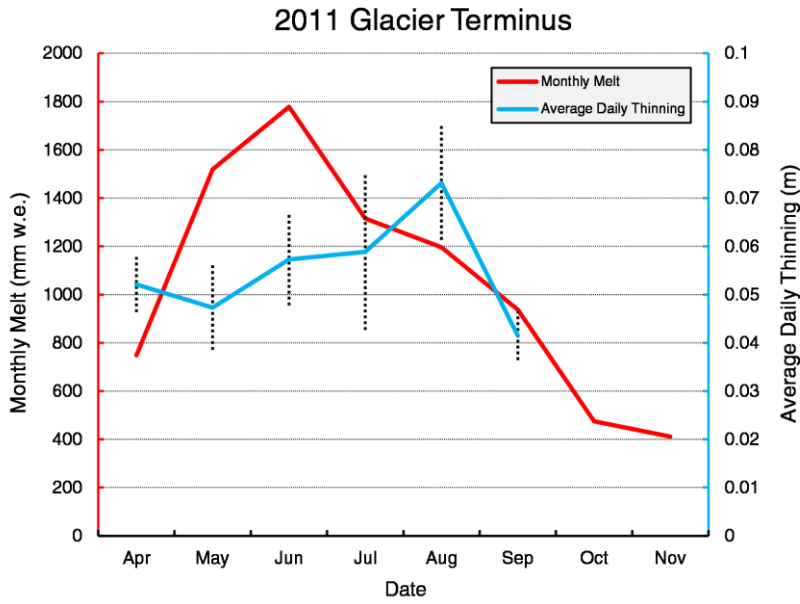


Figure 49. Monthly melt (EBM) and average daily thinning (time-lapse) for the glacier terminus in 2011.

Figure 50. Monthly melt (EBM) and average daily thinning (time-lapse) for the glacier terminus in 2012.

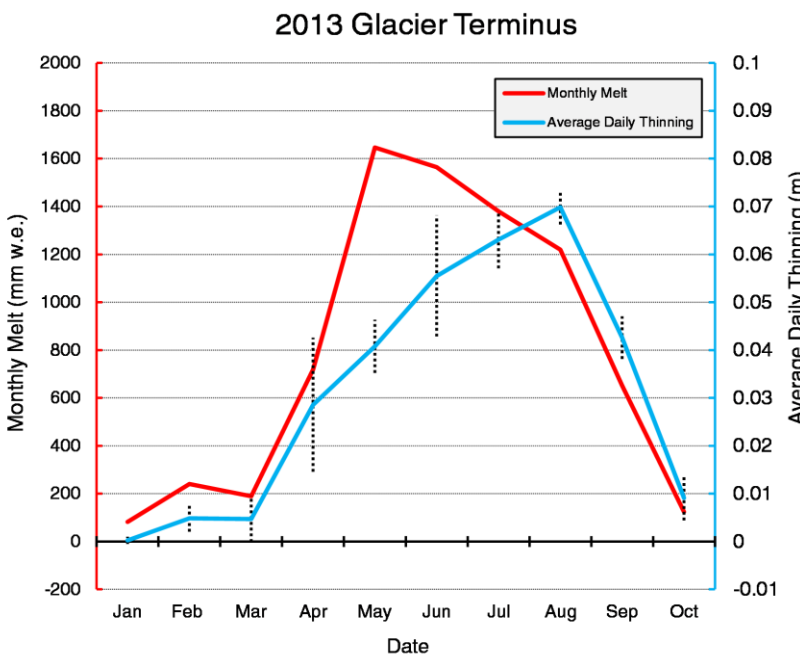
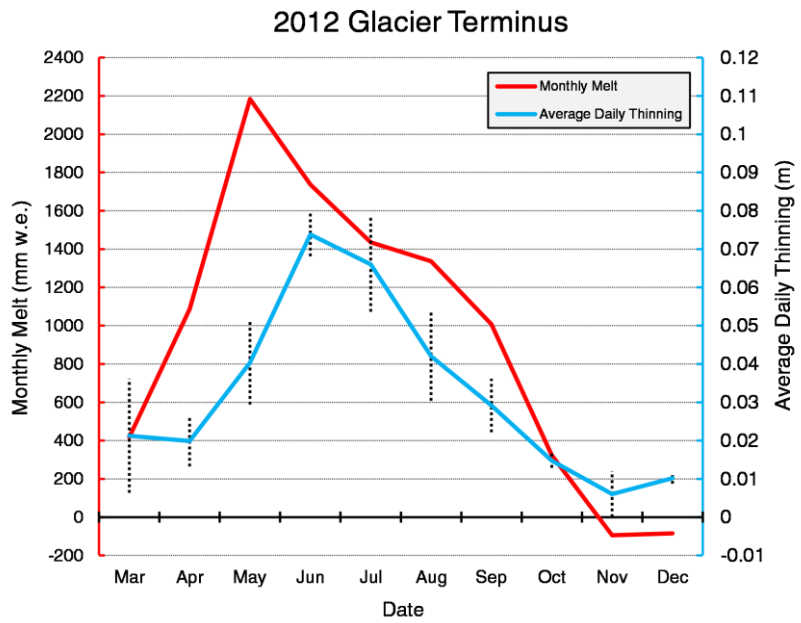


Figure 51. Monthly melt (EBM) and average daily thinning (time-lapse) for the glacier terminus in 2013.

4.3.2 - Intermediate sector

The intermediate sector exhibits greater inter-annual variability. Monthly melt and thinning data demonstrate remarkably tight coupling in 2011 ($R^2 = 0.83$, $p = 0.002$) and close coupling in 2012 ($R^2 = 0.73$, $p = 0.002$). However, the relationship between modelled melt and calculated thinning is more uncertain in 2013 ($R^2 = 0.62$, $p = 0.007$). In 2011, peak monthly melt (1778 mm w.e.) and thinning (0.066 ± 0.006 m d⁻¹) are coeval in June (Fig. 52). Close coupling of these variables is evident from April to October while a marginal increase in thinning rate in November (+ 0.014 m d⁻¹) is the only irregularity. In contrast, a two month offset between peak monthly melt and thinning is evident in 2012 and 2013 (Fig. 53 - 54).

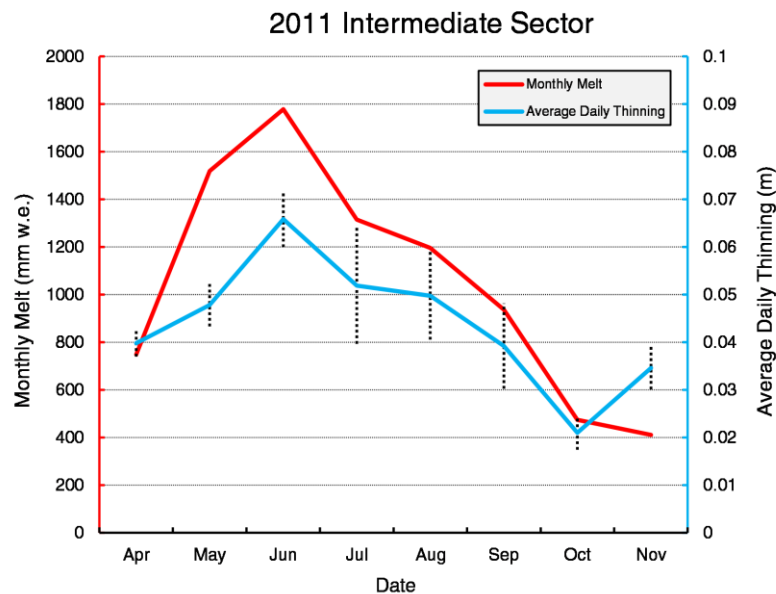


Figure 52. Monthly melt (EBM) and average daily thinning (time-lapse) for the intermediate sector in 2011.

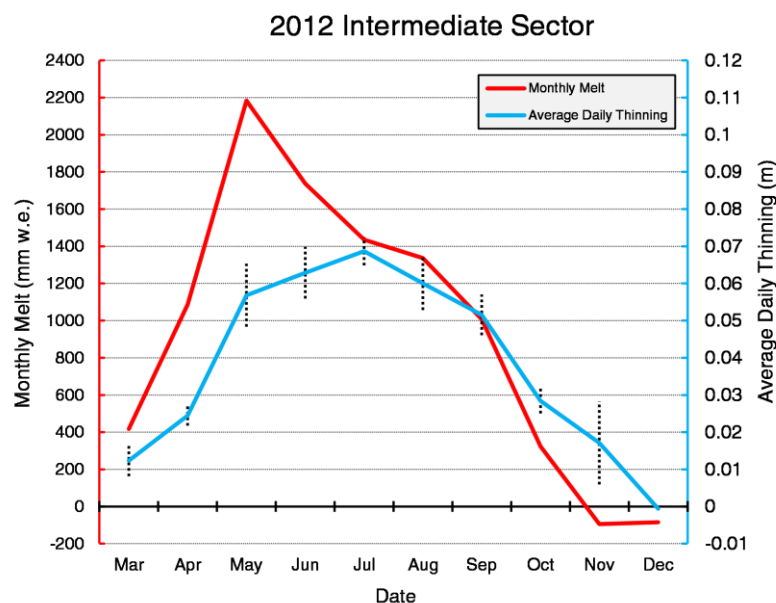


Figure 53. Monthly melt (EBM) and average daily thinning (time-lapse) for the intermediate sector in 2012.

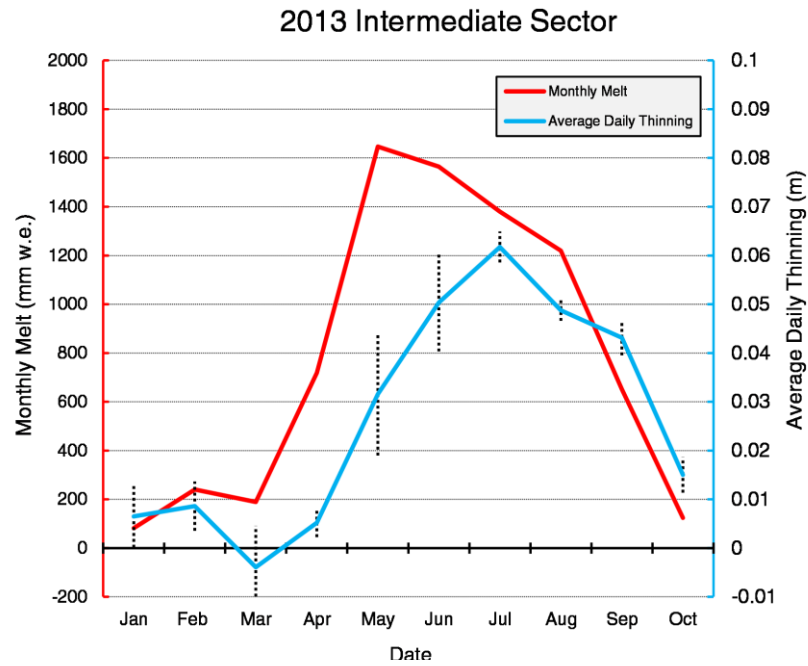


Figure 54. Monthly melt (EBM) and average daily thinning (time-lapse) for the intermediate sector in 2013.

Comparison of cumulative thinning and melt trends reveals further inter-annual variation. Data for 2011 and 2012 are generally well correlated with the trends established at the glacier terminus with an early season lag in 2012 (Fig. 56, A) and a late season offset in both years with thinning underestimated by the EBM after July and August respectively (Fig. 55, B and Fig. 56, D). However, these trends are not

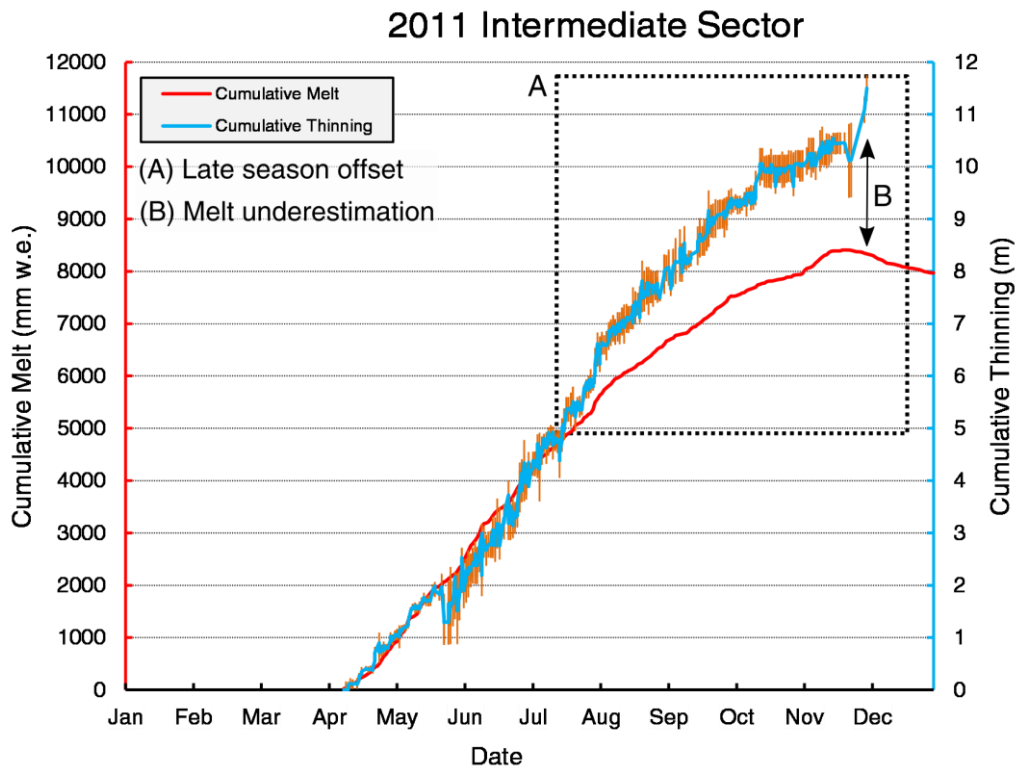


Figure 55. Cumulative melt (EBM) and cumulative thinning (time-lapse) at the intermediate sector in 2011.

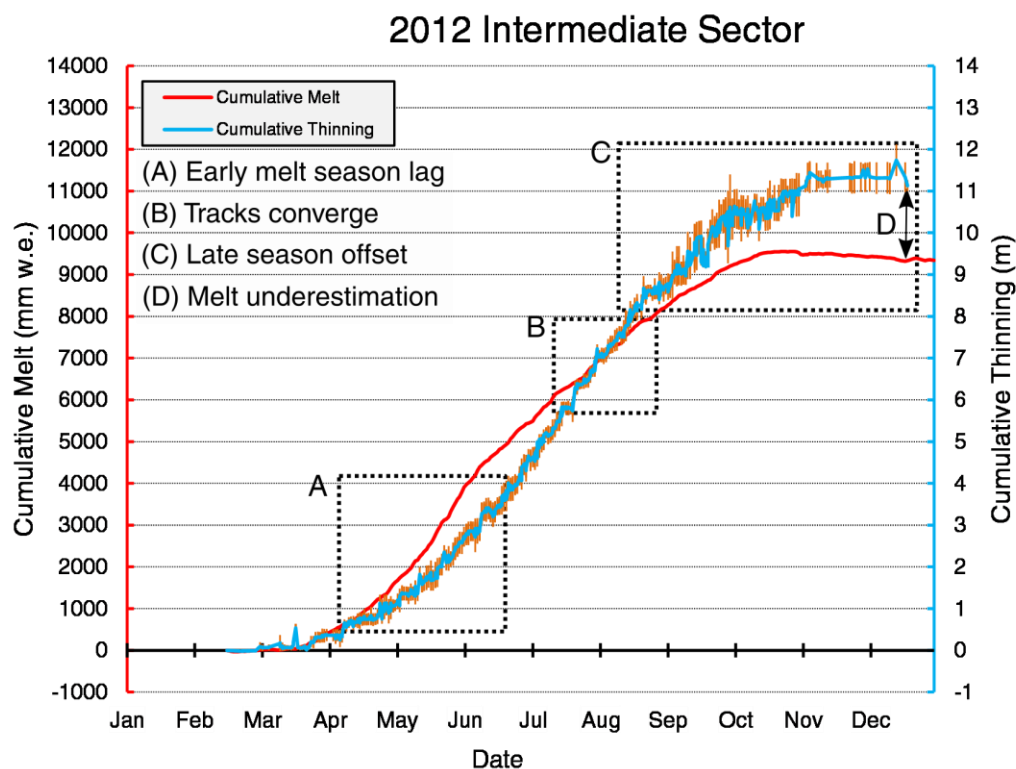


Figure 56. Cumulative melt (EBM) and cumulative thinning (time-lapse) at the intermediate sector in 2012.

evident in 2013. Although cumulative melt and thinning are well correlated in January and February, there is clear separation of these variables in mid-March (Fig. 57, B). The intermediate sector demonstrates a shift from a cumulative surface elevation reduction of -0.64 ± 0.13 m on 17/03/2013 to marginal uplift of $+0.21 \pm 0.13$ m by 21/03/2013. This is sustained throughout April, despite a significant increase in modelled cumulative melt. By the start of May, thinning of the intermediate sector is significantly overestimated by the energy balance model, equivalent to $+1.25$ m. After this date, there is clear shift to above average thinning (Section 4.4.2, Fig. 66, B), leading to the convergence of cumulative thinning and melt in early September. A marginal late season offset is shown, with cumulative thinning of 8.38 ± 0.35 m and cumulative melt of 7819 mm w.e on 04/11/2013. This reduction in the late season offset relative to previous years is accounted for by the suppression of surface lowering in the early melt season.

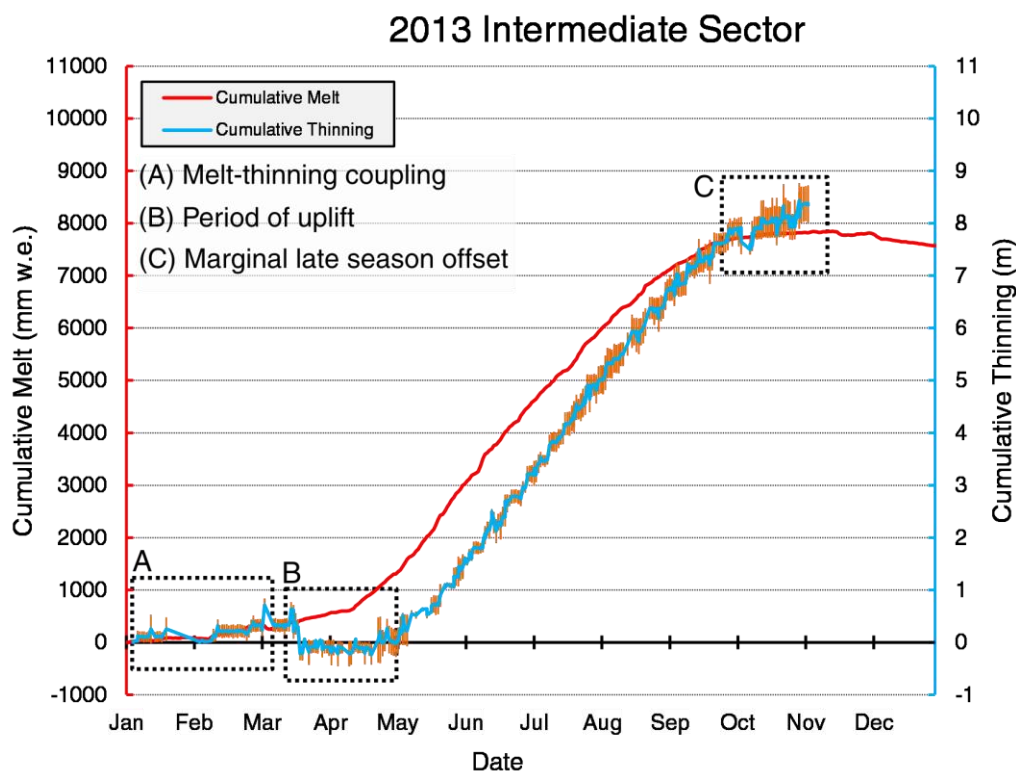


Figure 57. Cumulative melt (EBM) and cumulative thinning (time-lapse) at the intermediate sector in 2013.

4.3.3 - Upper sector

The upper sector also demonstrates reasonable coupling between monthly melt and thinning in 2011 ($R^2 = 0.70$, $p = 0.009$), 2012 ($R^2 = 0.67$, $p = 0.004$) and 2013 ($R^2 = 0.65$, $p = 0.005$). Peak monthly thinning occurs after peak monthly melt throughout this period in agreement with the terminus and intermediate sectors.

However, considerable inter-annual variability is evident at this temporal scale. In 2011, thinning rate variation is marginal between April and September although there is a marked reduction in thinning rate into October (-0.022 m d^{-1}) which is coeval with a fall in melt of 462 mm w.e. (Fig. 58). Despite this coeval melt-thinning reduction, thinning rates in the upper sector in 2011 appear significantly less sensitive to temporal variability in surface melt production. This year exhibits a limited thinning rate range of just 0.027 m d^{-1} . Over the period April - September, this is reduced to just 0.01 m d^{-1} . In contrast, both the terminus and intermediate sectors demonstrate significant variability in 2011. Additionally, enhanced intra-annual variability is evident in the upper sector in both 2012 and 2013 (Fig. 59 - 60) which exhibit thinning rate ranges of 0.07 m d^{-1} and 0.08 m d^{-1} respectively. Clearly, limited intra-annual variability of the 2011 upper dataset must be accounted for.

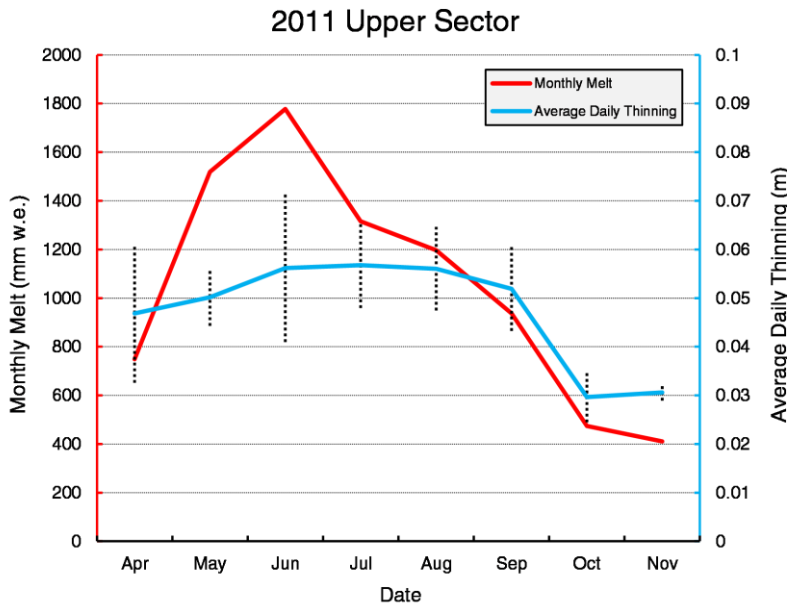


Figure 58. Monthly melt (EBM) and average daily thinning (time-lapse) for the upper sector in 2011.

Figure 59. Monthly melt (EBM) and average daily thinning (time-lapse) for the upper sector in 2012.

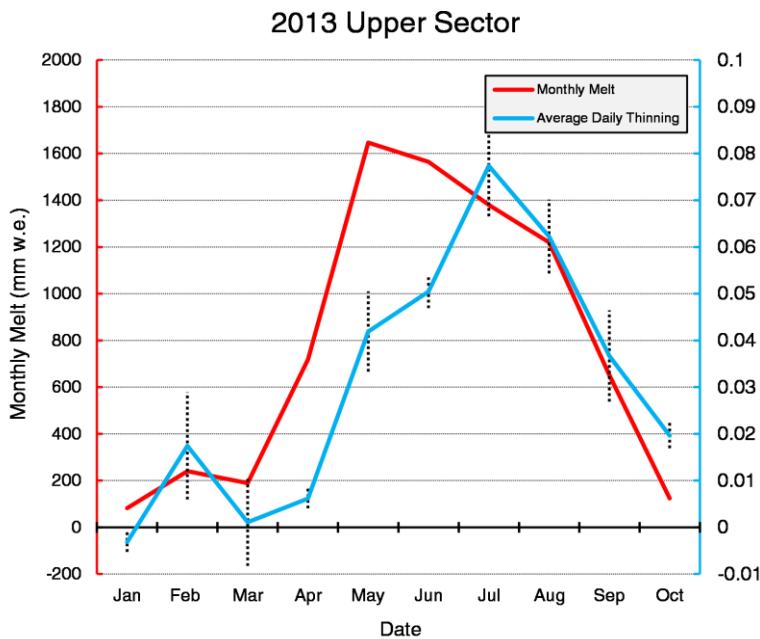
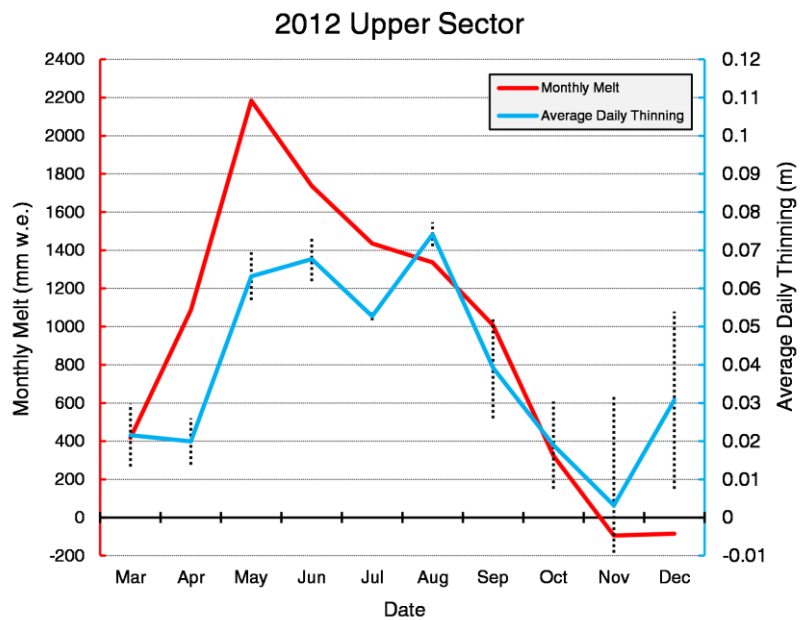


Figure 60. Monthly melt (EBM) and average daily thinning (time-lapse) for the upper sector in 2013.

Furthermore, there is a consistent late season offset between melt and thinning in the upper sector throughout the period 2011-2013 which corroborates with the trends observed at the glacier terminus and intermediate sectors. Thinning underestimation by the EBM is equivalent to - 2.33 m in 2011, - 3.37 m in 2012 and - 1.84 m in 2013 (Fig. 61 - 63). Additionally, an early melt season lag between the onset of enhanced melt and enhanced thinning is evident in 2013. However, this is curiously absent in 2012 with cumulative melt and thinning reasonably well coupled until July. Furthermore, cumulative thinning actually exceeds modelled cumulative melt in early April (Fig. 62, A), as the surface elevation reduction of 1.27 ± 0.22 m by 01/04/2012 greatly exceeds the value predicted by EBM (417 mm w.e.). This period of enhanced thinning is not apparent at the terminus or intermediate sectors in 2012.

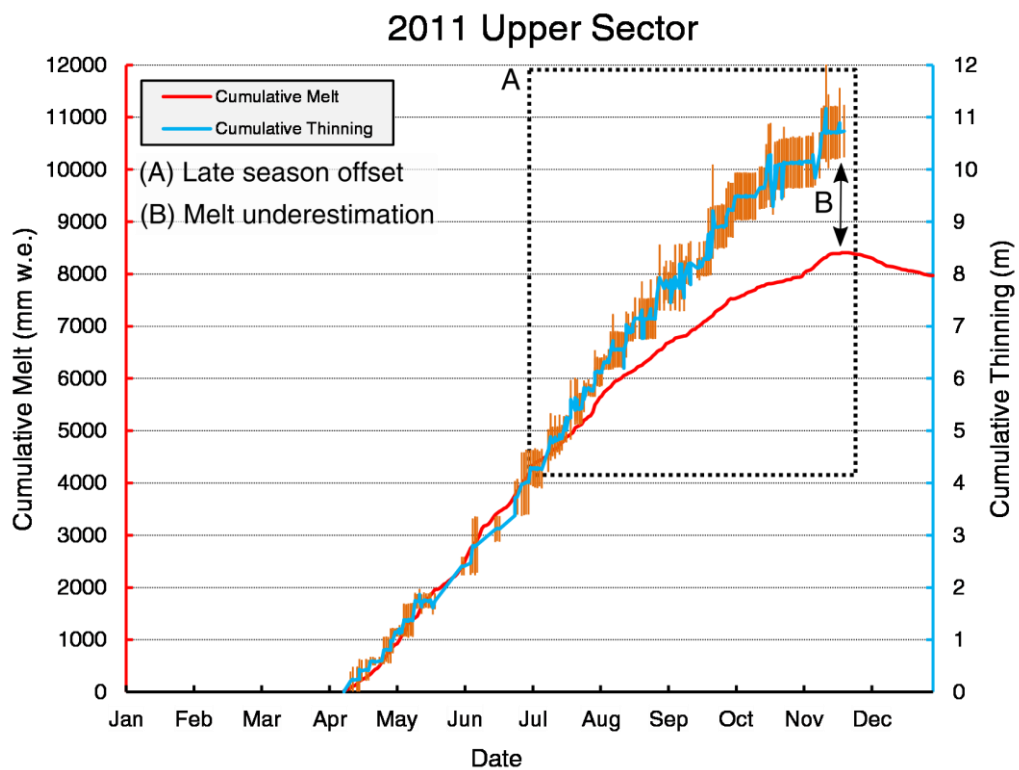


Figure 61. Cumulative melt (EBM) and cumulative thinning (time-lapse) at the upper sector in 2011.

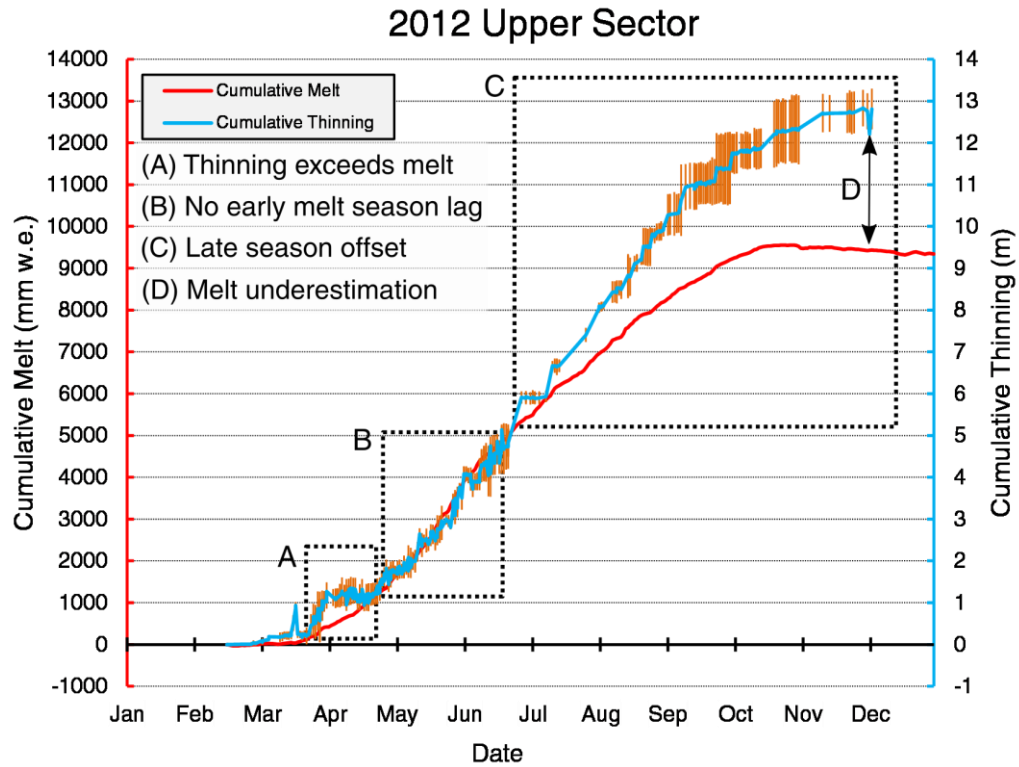


Figure 62. Cumulative melt (EBM) and cumulative thinning (time-lapse) at the upper sector in 2012.

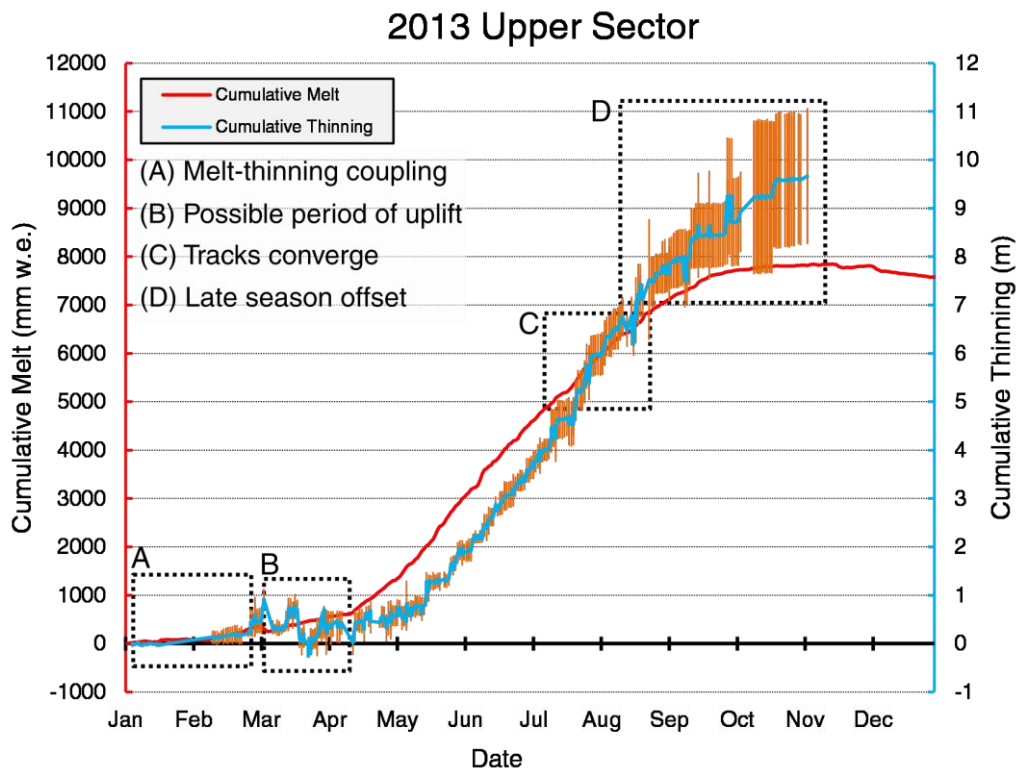


Figure 63. Cumulative melt (EBM) and cumulative thinning (time-lapse) at the upper sector in 2013.

4.4 - Intra-annual variability in surface velocities and comparison with thinning

4.4.1 - Glacier terminus

Intra-annual variability in glacier surface velocities are described based on cumulative displacement graphs (Figs. 64-67) and compared to thinning rate variability to determine periods of hydrodynamic coupling i.e. when periods of fast/slow glacier flow are correlated with periods of high/low rates of surface elevation change. These data exhibit no consistent seasonal trend over the period 2011-2013 although significant inter-annual variability is evident. Hydrodynamic coupling is evident at the glacier terminus in both 2011 and 2012 although the direct relationship between thinning rates and surface velocities is not maintained throughout the entirety of these years. In 2013, these variables are predominantly asynchronous.

In 2011, the glacier terminus exhibits relatively stable flow over the period April to early-June with some minor fluctuations of ± 0.2 m relative to the constant velocity position. However, hydrodynamic de-coupling is evident from early May as thinning rates shift to below average while average surface velocities are maintained. From early June, hydrodynamic coupling is restored as surface velocities and thinning rates shift to above average and remain so until early August. Limited data availability after this date prevents any robust description or interpretation of these data. In 2012, clear periods of fast glacier flow are evident in April and throughout May. Surface velocities are relatively stable after July, within ± 0.5 m of the constant velocity position although an extended period of below average surface velocities is evident from early September. Thinning rates and surface velocities appear well correlated for much of 2012 with coeval peaks and troughs in March and April and after June. However, two clear periods of hydrodynamic de-coupling are identified (Fig. 65, A). A short period of de-coupling is evident in early May as surface velocities shift to above average while thinning is maintained at a below average rate. A much longer period of de-coupling is sustained throughout June as surface velocities decisively shift to below average while thinning is maintained at an above average rate. However, with the exception of these periods, thinning rates and surface velocities are well correlated at the glacier terminus in 2011 and 2012.

In contrast, the glacier terminus exhibits clear hydrodynamic de-coupling in 2013 with asynchronicity between thinning rates and surface velocities from mid-March (Fig. 66, A). A reduction in thinning rate at this time is not reflected in any change in surface velocities which are maintained at an average rate (0.017 m d^{-1}) until mid-May. Furthermore, an increase in thinning rate from mid-April through to September is asynchronous with glacier velocities. However, a short period of fast glacier flow is

event in August and is associated with enhanced thinning. This speed up is quickly curtailed with a return to below average velocities in September. As such, clear inter-annual variability is evident at the glacier terminus. Although periods of hydrodynamic coupling are evident in each year, short intervals of de-coupling in 2011 and 2012 and the extended de-coupling in 2013 must be accounted for.

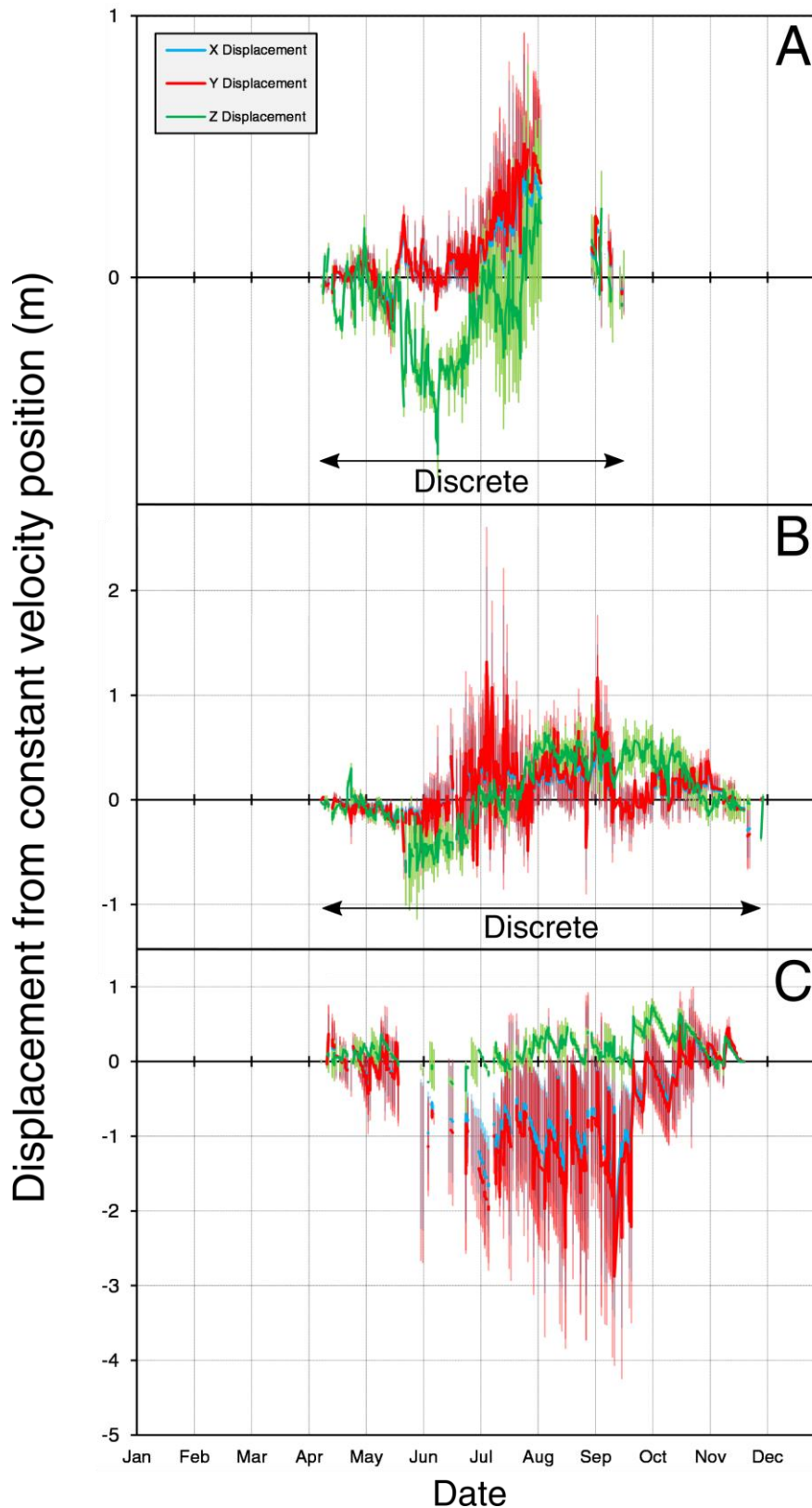


Figure 64. Cumulative displacement graphs for the glacier terminus (A), intermediate (B) and upper sector (C) in 2011.

4.4.2 - Intermediate sector

Hydrodynamic coupling is also evident in the intermediate sector over the period 2011-2013. However, comparison with the glacier terminus reveals spatial variability in the occurrence and duration of periods of hydrodynamic de-coupling. In 2011, the intermediate sector broadly corroborates with the trends identified at the glacier terminus, with average surface velocities through to early-June followed by fast glacier flow through to July (Fig. 64, B). Surface velocities are stable until early September although some relatively high magnitude fluctuations are evident. Furthermore, thinning rates are above average from late-May through to August, reflecting the seasonal increase in surface melt production. A short period of de-coupling is evident in October as thinning rates fall below average, although this has no appreciable impact on ice movement which is maintained at an average rate.

Two periods of hydrodynamic de-coupling are identified in April and June 2012 (Fig. 65, B). In April, surface velocities shift to above average despite a sustained below average thinning rate from early March. In June, this trend is reversed as surface velocities fall while the thinning rate is above average. However, spatio-temporal variability is evident as the timing of the shift from below to above average surface velocities varies between the terminus and intermediate sectors, occurring in late and early-April respectively. In contrast, both sectors demonstrate a synchronous shift to below average surface velocities in early June, with coeval trends in surface velocities and thinning rates after this date.

In 2013, the glacier terminus and intermediate sector demonstrate significant spatial variability (Fig. 66, B). While the terminus is characterised by clear asynchronicity between thinning rates and surface velocities from mid-March, these variables are reasonably correlated until mid-June in the intermediate sector. Hydrodynamic de-coupling is evident from this date as surface velocities fall below average while thinning rates remain high through to late September.

4.4.3 - Upper sector

Determining intra-annual variation in surface velocities in the upper sector is challenging due to a limited number of tracked surface features. This is most apparent in 2011 as tracks are extremely “noisy” and it is difficult to infer anything meaningful from these data (Fig. 64, C). Data from 2012 are more useful as hydrodynamic coupling is evident from March through to June with coeval peaks and troughs in thinning rates and surface velocities. While these variables appear asynchronous after June, surface velocity data are associated with significant errors which make interpretation challenging (Fig. 65, C). This is accounted for by a low

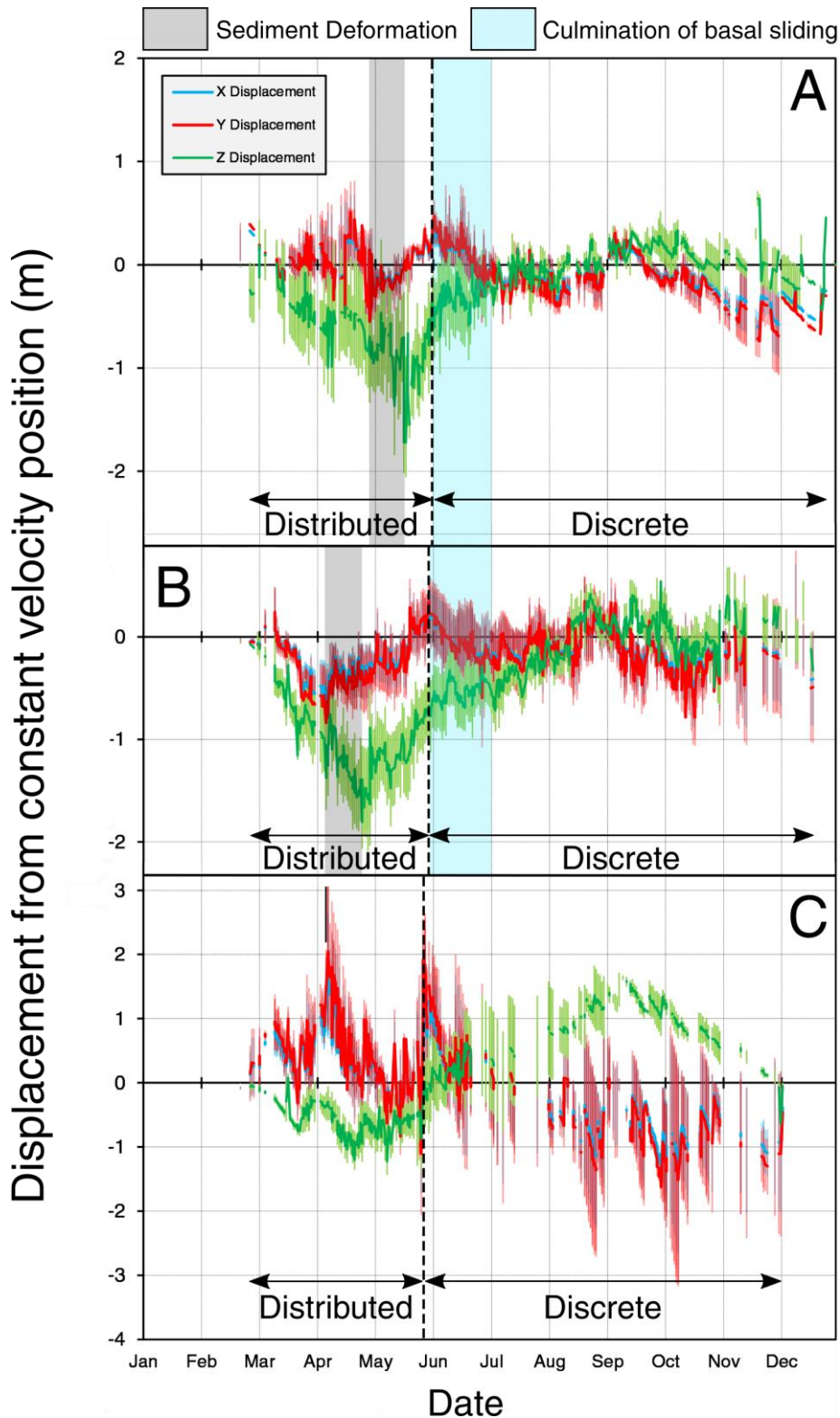


Figure 65. Cumulative displacement graphs for the glacier terminus (A), intermediate (B) and upper sector (C) in 2012.

number of feature tracks from June onwards ($n = 2$). Given the oblique view of this sector, tracking additional surface features was not possible. However, thinning rates are associated with significantly reduced error estimates and corroborate with seasonal trends observed at the terminus and intermediate sectors. As such, it is interpreted that thinning of the upper sector must be spatially consistent to account

for the more robust data. In contrast, surface velocity variability between the two tracked points must be significant to account for greater error values.

In 2013, the upper sector demonstrates an intimate coupling between thinning and surface velocities throughout the year. However, a short period of hydrodynamic decoupling is evident from late-July through to early August as surface velocities fall below average while thinning is maintained at an above average rate (Fig. 66, C).

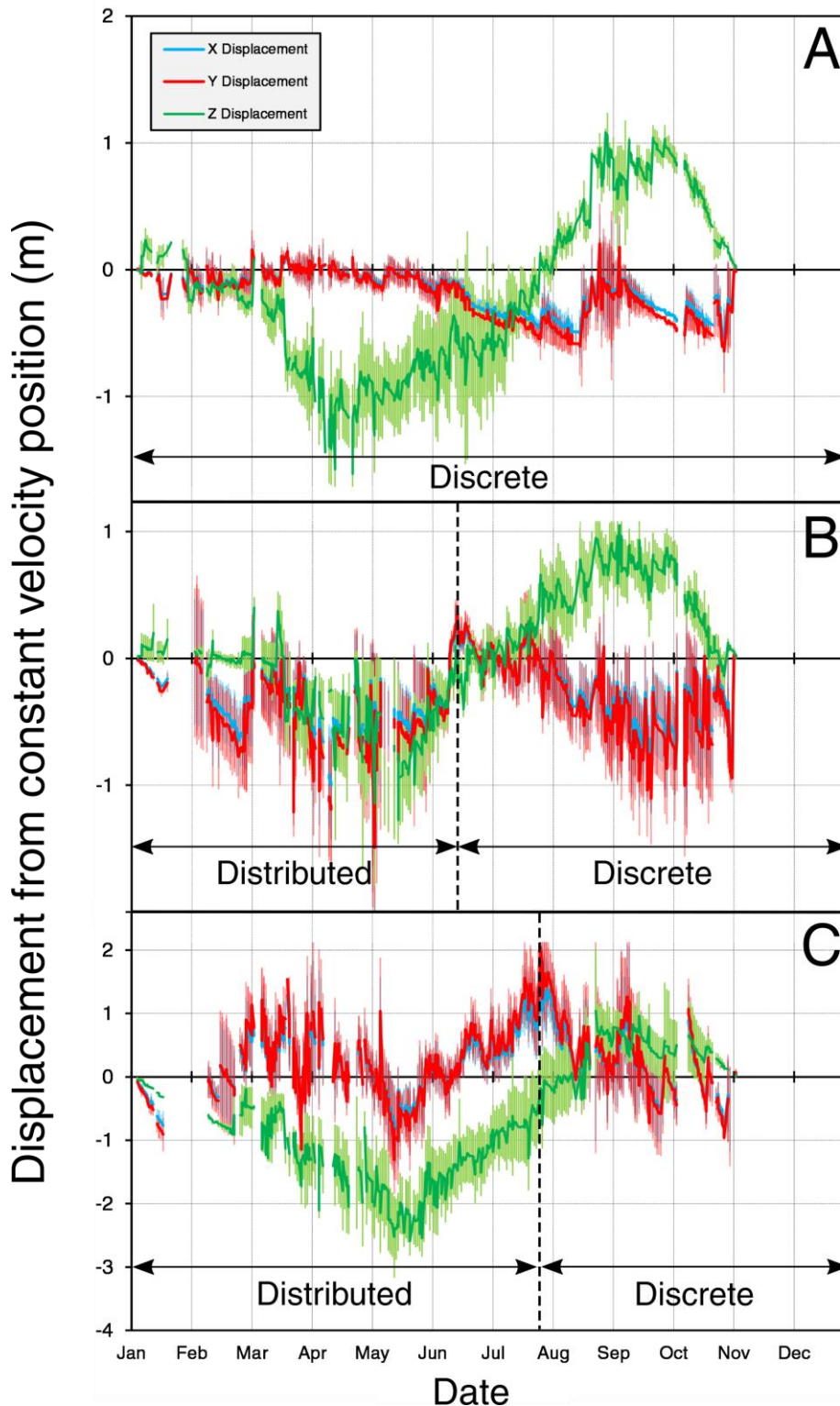


Figure 66. Cumulative displacement graphs for the glacier terminus (A), intermediate (B) and upper sector (C) in 2013.

4.4.4 - Icefall

The icefall dataset is characterised by significantly reduced error values at the monthly scale (Fig. 67-69). In 2011, the icefall exhibits relatively stable flow throughout the tracked period, with a velocity range of just 0.4 m d^{-1} (Fig. 67). However, these data are reasonably correlated with meteorological data as an increase in surface velocity from April to June is coeval with a seasonal increase in surface melt production. Similarly, the steady decrease in surface velocities through to October is in agreement with a reduction in surface melt at this time.

In contrast, both 2012 and 2013 exhibit greater intra-annual surface velocity variability. In 2012, a clear speed up is evident from January through to April before a sustained slowdown into October (Fig. 68). Coupling with melt is reasonable in 2012 although peak velocities occur before peak monthly melt. 2013 exhibits the greatest intra-annual variability with glacier flow of just $0.55 \pm 0.02 \text{ m d}^{-1}$ in January, increasing to $2.11 \pm 0.06 \text{ m d}^{-1}$ in June (Fig. 69). Surface velocities exceed 1.96 m d^{-1} between May and July in line with peak melt. However, while surface velocities decrease through to September ($1.57 \pm 0.09 \text{ m d}^{-1}$), a clear late season speed up appears at odds with decreasing surface melt production at this time. Surface velocities of $1.96 \pm 0.08 \text{ m d}^{-1}$ and $1.88 \pm 0.05 \text{ m d}^{-1}$ are recorded in November and December respectively despite a negative surface energy balance in these months. Clearly, surface melt production is not the only factor which determines icefall movement.

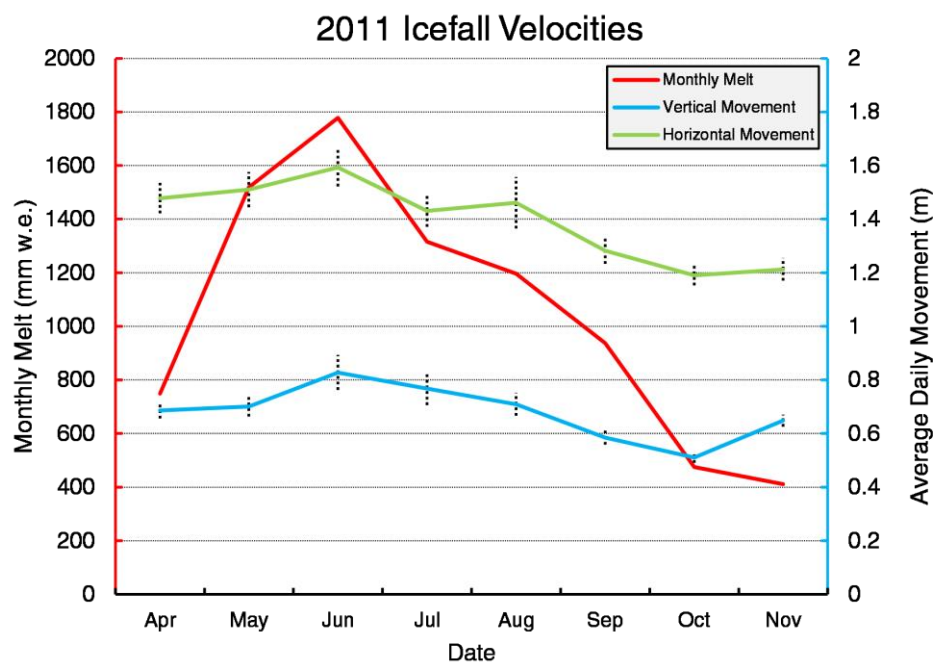


Figure 67. Monthly icefall dynamics (2011)

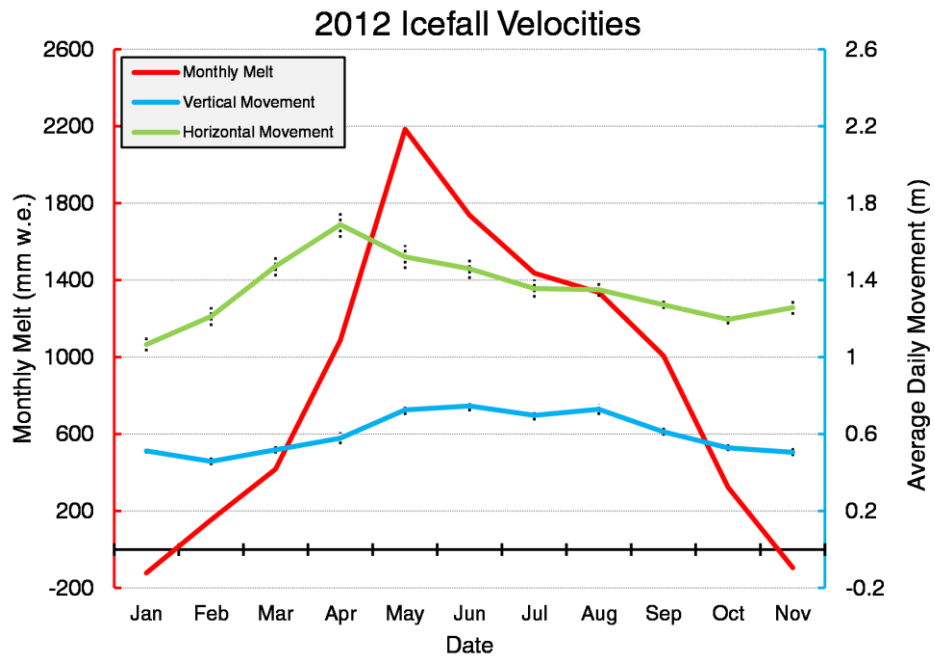


Figure 68. Monthly icefall dynamics (2012)

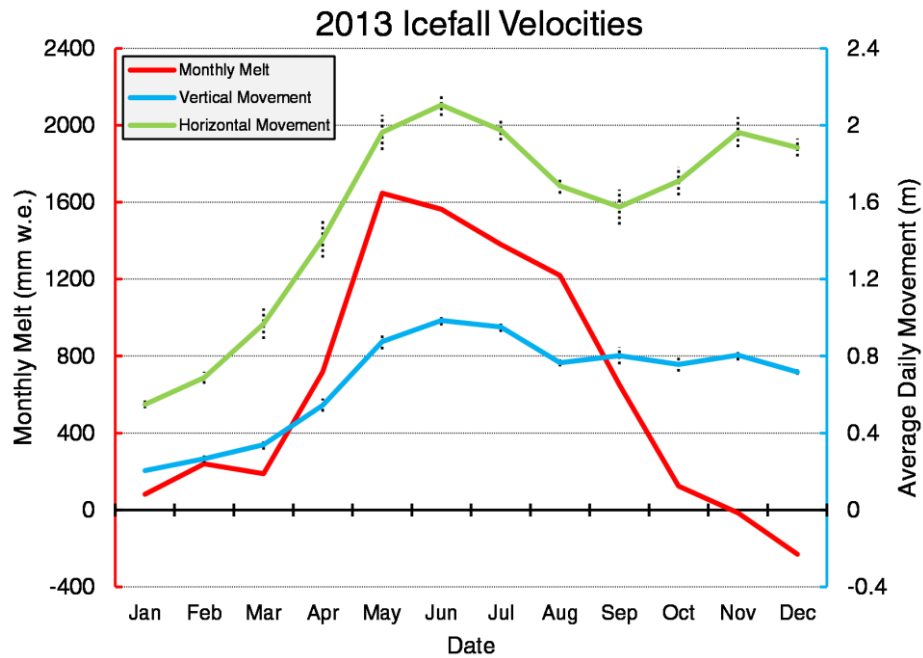


Figure 69. Monthly icefall dynamics (2013)

Chapter 5 - Discussion

5.1 - Do the results from time-lapse data accurately reflect surface dynamics?

5.1.1 - Validating time lapse data using GNSS data output

At Falljökull, GNSS measurements from Phillips *et al.*, (2014) provide a useful comparison for velocities generated using time-lapse photography (Fig. 70). Unfortunately, direct data comparison is challenging as these data cover different time periods. While this project has focused on intra-annual velocity variation, Phillips *et al.*, (2014) report surface velocities from April 2012 to April 2013. This reflects annual movement between the start dates of concurrent melt seasons and is therefore not directly comparable with intra-annual movement i.e. January to December. This is complicated by the limited timespan of glacial feature tracks. The presence of the winter snowpack prevents intensive feature tracking during this period with only a limited number of visible surface features during late-2012 and early-2013. Extrapolating surface velocities derived from the spring-autumn interval is unlikely to generate reliable results given the observed winter slowdown at Falljökull (Phillips *et al.*, 2014). However, the magnitude of this seasonal slowdown decreases towards the glacier front (Fig. 70), with only marginal decrease in surface velocities at the lowest two GNSS stations. Therefore, velocities were calculated over the same 12 month period to enable comparison with GNSS data.

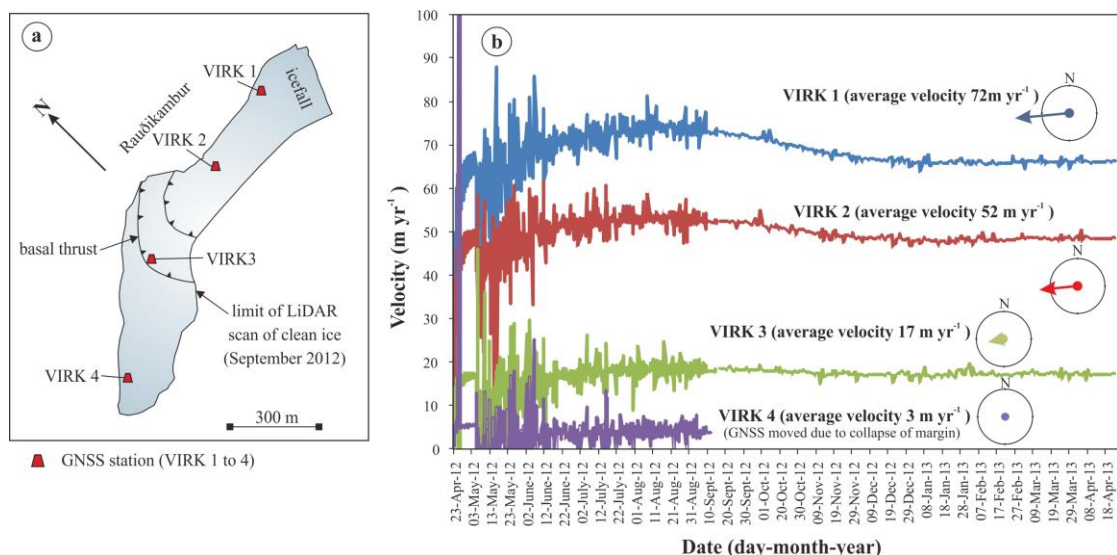


Figure 70. GNSS locations (a) and ice surface velocities between April 2012 and April 2013 (b). Insets show the ice movement vector at each of the four GNSS stations located along the axis of Falljökull with the length of the arrow reflecting ice surface velocity. From Phillips *et al.*, (2014).

Unfortunately, the first 6 months of GNSS data are “noisy” due to the malfunction of the base station (after 28 days). While this was corrected in August 2012, with positional accuracy improved for the remainder of the study period (Phillips *et al.*, 2014), this introduces additional uncertainty to these data. The impact of GNSS malfunction is most pronounced at VIRK4 as surface velocity data from this installation are only available up to September 2012 when it was removed following collapse of the margin. Given that this encompasses the period when base station malfunction had not been corrected, data from VIRK4 should be treated with caution. Data from the remaining GNSS stations (VIRK 1-3) are available through to April 2013 with “noise” significantly reduced for the remaining 6 months of data acquisition. However, these stations are located up/downstream of the glacier front/icefall cameras respectively, further complicating the validation of time-lapse derived velocities with GNSS data.

Between April and September 2012, a surface displacement of 3 m was recorded at VIRK4, equivalent to just 0.008 m d^{-1} . This displacement is solely attributed to displacement on the major normal faults during collapse of the ice front (Phillips *et al.*, 2014) with negligible movement due to ice deformation or sliding at the bed. The lower reaches of Falljökull below VIRK3 are interpreted to be “stagnant”, characterised by limited forward movement and passive downwastage i.e. decay in-situ (Phillips *et al.*, 2014). In contrast, surface velocities from time-lapse imagery indicate displacement of 9.2 m yr^{-1} in the glacier terminus dataset over the same period. However, as this dataset incorporates surface features up to $\sim 200 \text{ m}$ from the glacier front, it is unsurprising that calculated velocities are higher than those generated through GNSS. As intra-group variability over small spatial scales is evident (Fig. 39-41), comparison with the closest tracked surface features to the glacier terminus is more appropriate. In 2012 and 2013, the mean velocity of these closest terminus features is $0.01 - 0.015 \text{ m d}^{-1}$, equivalent to a velocity range of $3.8 - 5.4 \text{ m yr}^{-1}$. This is in better agreement with data from Phillips *et al.*, (2014). However, while this previous study inferred restricted surface velocities for the entire glacier front based on VIRK4 i.e. stagnant ice below GNSS station VIRK3, time-lapse derived surface velocities indicate a progressive increase in surface velocities with altitude in 2012 ($R^2 = 0.51$) and 2013 ($R^2 = 0.77$). In 2011, the mean velocity of the four closest surface features to the terminus was just $0.008 \pm 0.002 \text{ m d}^{-1}$, equivalent to an annual displacement of $2.82 \pm 0.65 \text{ m}$. Both GNSS and time-lapse data confirm extremely restricted surface velocities within $\sim 50 \text{ m}$ of the glacier terminus throughout the period 2011-2013.

However, time-lapse data appears poorly correlated with VIRK3. This GNSS station is $\sim 600 \text{ m}$ from the glacier terminus and recorded a surface displacement of 17 m yr^{-1} , equivalent to 0.047 m d^{-1} . While this is in reasonable agreement with the intermediate

sector, which exhibits a surface velocity of 13.5 m yr^{-1} over the same period, VIRK3 is up glacier of the highest tracked surface features from AWS1. As such, comparison with the upper sector is more appropriate. However, the mean surface velocity of this sector was equivalent to 50.1 m yr^{-1} , nearly three times faster than GNSS derived velocities. While VIRK3 is $\sim 100 \text{ m}$ from the upper sector, it seems unlikely that such a significant flow deceleration would occur within this distance.

High surface velocities generated from time-lapse data at the glacier front appear to contradict the hypothesis of Phillips *et al.*, (2014) as ice is flowing substantially faster than can be accommodated solely by displacement along normal faults. These data indicate that the ice front at Falljökull is still 'active', although forward motion through ice deformation is insufficient to offset retreat. The Falljökull terminus retreated at a rate of 0.193 m d^{-1} , 0.159 m d^{-1} and 0.126 m d^{-1} in 2011, 2012 and 2013 respectively, equivalent to a total retreat of $\sim 155 \text{ m}$ between April 2011 and December 2013. Furthermore, significant intra-annual variability in surface velocities have been demonstrated at Falljökull, variability that is unlikely to be observed in stagnant ice that is wasting away in-situ. Instead, this is perhaps accounted for by basal sliding (Section 2.1.2) or subglacial deformation (Section 2.1.3) as a function of meltwater input. While stagnant ice would exhibit intra-annual variability in thinning rates due to seasonal changes in surface energy balance, surface velocities should be stable as movement would be unaffected by sliding at the bed. Given that periods of hydrodynamic coupling are evident throughout the period 2011-2013, it seems unlikely that the lower reaches of Falljökull are stagnant and "glaciotectonically detached" from the active ice above (Phillips *et al.*, 2014).

Finally, time-lapse data from the icefall confirms that the upper reaches of Falljökull are active with ice transfer from the summit area of Öräfajökull down the mountain flank (Phillips *et al.*, 2014). Unfortunately, due to the relatively slow surface velocities down glacier, it was not possible to study the effect of longitudinal coupling. Fast surface velocities and consistent icefall hypsometry i.e. based on the limited inter-annual variability of surface lowering rates, indicates a close connection between Falljökull and its accumulation area. Additionally, given the acceleration of the icefall in 2013 ($1.58 \pm 0.08 \text{ m d}^{-1}$), a slowdown in the rate of glacier retreat may be observed in subsequent seasons if fast icefall velocities are maintained.

5.1.2 - How does Falljökull compare to similar glaciers?

5.1.2.1 - Surface velocities

Given the conflict between GNSS and time-lapse datasets, it is necessary to compare these data with similar glaciers. Firstly, it is evident that time-lapse derived surface

velocities are reasonable as they are within the range of velocities observed at similar small alpine and polythermal glaciers (Table 12) and are distinct from fast velocities observed at maritime terminating glaciers (Fig. 71). Importantly, while upper sector velocities ($0.077 - 0.158 \text{ m d}^{-1}$) appear significantly faster than expected i.e. relative to GNSS data, these also corroborate with data from similar maritime glaciers. Surface velocities of 0.17 m d^{-1} and 0.20 m d^{-1} have been recorded at distances of $< 1 \text{ km}$ from the terminus of Sólheimajökull, SE Iceland (James *et al.*, 2016) and Variegated Glacier,

Table 12. Glacier surface velocities recorded at alpine, polythermal, surge-type, arctic and marine-terminating glaciers using time-lapse, GNSS and remote sensing.

Publication	Location	Glacier	Type	Details	Method	Velocities (m d^{-1})			
This study	Iceland	Falljökull	Alpine	Terminus	Time-lapse	0.017 - 0.025			
				Intermediate		0.029 - 0.044			
				Upper		0.077- 0.158			
				Icefall		1.35 - 1.58			
Phillips <i>et al.</i> , (2014)	Iceland	Falljökull	Alpine	Terminus	GNSS	0.008			
				Basal thrust		0.046			
				Topographic bulge		0.142			
				Below icefall		0.198			
James <i>et al.</i> , (2016)	Iceland	Sólheimajökull	Alpine	Terminus	Time-lapse	0.17 (Mean) 0.07 - 0.20 (Range)			
Anderson <i>et al.</i> , (2004)	Alaska	Bench Glacier	Alpine	5 GPS antennas at 1 km spacing along the glacier flow line	GNSS	0.025 - 0.038			
Harrison <i>et al.</i> , (1986)	Alaska	Variegated Glacier	Alpine	10 timelapse cameras between 3-9 km from the terminus	Time-lapse	0.2			
Minchew <i>et al.</i> , (2015)	Iceland	Langjökull Hofsjökull	Ice Cap	Velocity estimates for the entire ice cap	InSAR	< 0.20			
						< 0.41			
Whitehead <i>et al.</i> , (2010)	Canada	Fountain Glacier	Polythermal	-	GNSS	0.007 - 0.015			
					Photogrammetry	0.004 - 0.017			
					InSAR	0.008 - 0.015			
Whitehead <i>et al.</i> , (2013)	Canada	Fountain Glacier	Polythermal	Terminus 1 km upstream	Remote Sensing	< 0.005 > 0.022			
Messerli and Grinsted (2015)	Norway	Engabreen	Arctic	-	Time-lapse	0.53			
Harrison <i>et al.</i> , (1992)	Alaska	West Fork Glacier	Surge type	-	Time-lapse	< 12			
						Kronebreen	Outlet		$\sim 1.5 - \sim 3.5$
						Comfortlessbreen	Surge type	-	Time-lapse
van Boeckel (2015)	Iceland	Breiðamerkurjökull	Marine terminating	2 GPS antennas close to the terminus	GNSS	0.73 (Winter)			
							1.15 (Summer)		
Ahn and Box (2010)	Greenland	Rink Isbrae	Marine terminating	Terminus	Time-lapse	14.1			
		Store Gletscher A				13.7			
		Store Gletscher B				13.7			
		Umiamako A				5.7			
		Umiamako B				6			
		Jakobshavn Isbrae				39.7			
Amundson <i>et al.</i> , (2008)	Greenland	Jakobshavn Isbrae	Marine terminating	Terminus	GNSS	28 - 35			
Schwalbe <i>et al.</i> , (2008)	Greenland	Jakobshavn Isbrae	Marine terminating	Terminus	LiDAR	~ 40			
Sole <i>et al.</i> , (2011)	Greenland	Kangiata Nunata Sermia	Marine terminating	4 GPS sensors from 36 - 72 km upstream of the terminus	GNSS	0.271 (Summer)			
Andersen <i>et al.</i> , (2011)	Greenland	Helheim Glacier	Marine terminating	Terminus to $\sim 20\text{km}$ upstream	GNSS	19 - 25			
Maas <i>et al.</i> , (2010)	Chile	Glaciar San Rafael	Marine terminating	-	Time-lapse	< 16			

Alaska (Harrison *et al.*, 1996) respectively. Fast glacier flow in the upper sector, at a distance of ~500 - 800 m from the Falljökull terminus, is not unprecedented.

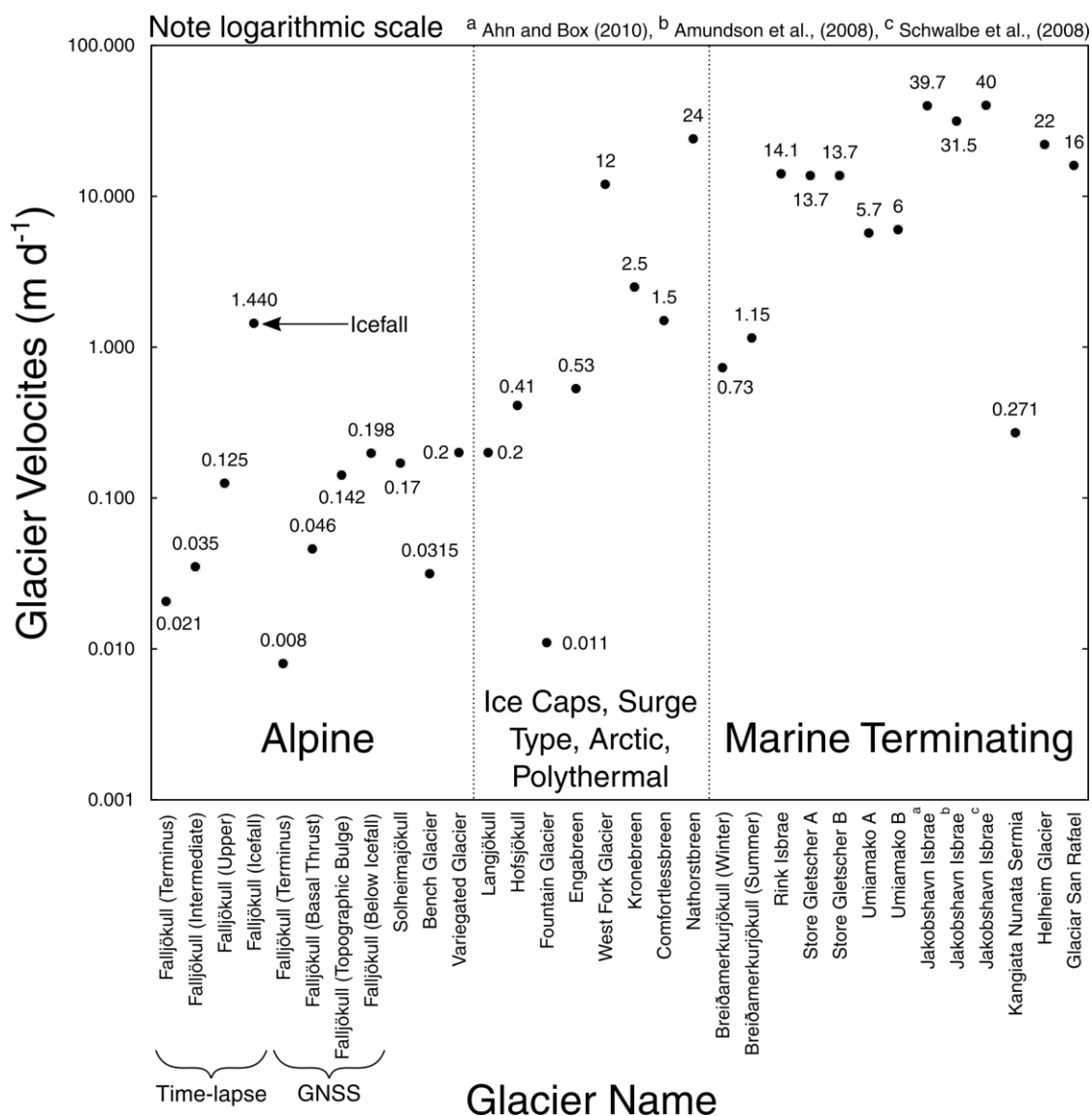


Figure 71. Flow variability between alpine and marine-terminating glaciers (data from Table 12).

However, significantly slower surface velocities have been measured for glacier termini. At Bench glacier, Alaska, GNSS data demonstrated surface velocities of just 0.025 - 0.038 m d⁻¹ (Anderson *et al.*, 2004). At the small, polythermal Fountain Glacier in the Canadian Arctic, restricted terminus velocities have been demonstrated using GNSS (0.007 - 0.015 m d⁻¹), photogrammetry (0.004 - 0.017 m d⁻¹) and inSAR (0.008 - 0.015 m d⁻¹) by Whitehead *et al.*, (2010). Further studies at this glacier have confirmed limited surface movement at the terminus of < 0.005 m d⁻¹ (Whitehead *et al.*, 2013) and 0.006 - 0.012 m d⁻¹ (Whitehead *et al.*, 2014). These data provide a range of velocities which appear well correlated with GNSS data from VIRK4 (0.008 m d⁻¹) and feature

tracking of the closest glacier surface features to the terminus (0.008 - 0.015 m d⁻¹). While terminus sector surface velocities (< 200 m from the glacier front) are slightly faster (0.017 - 0.025 m d⁻¹), they are not unexpected given the temperate thermal regime of Falljökull. As ice is above the pressure melting point throughout, englacial hydrology would be well developed relative to cold-based and polythermal glaciers, leading to enhanced basal sliding as a result of more efficient meltwater input to the subglacial system. Importantly, the studies at Bench Glacier and Fountain Glacier demonstrate that slow surface velocities, often less than 0.01 m d⁻¹, are not necessarily an indication of stagnant ice. Both glaciers are still active with movement at the terminus through ice deformation.

5.1.2.2 - Thinning rates

It is clear that Falljökull is not in equilibrium with climate. The lower reaches of the glacier are thinning substantially with a mean surface lowering of 17 m in 2011 and further thinning of 13.2 m in 2012 and 10.6 m in 2013. However, surface lowering in the terminal zone at Falljökull is estimated at just 2 - 6 m yr⁻¹ (Bradwell *et al.*, 2013) with only ~ 50 m of vertical thinning over the last 15 years (BGS, 2010). As such, the ~40.8 m of surface lowering derived from time-lapse data indicates that either (1) surface lowering was significantly enhanced over the period 2011-2013 or (2) time-lapse data are not representative of glacier front thinning. Unfortunately, comparison with similar glaciers is challenging due to the limited availability of thinning rate data. However, at Sólheimajökull, SE Iceland, a reasonably consistent 3 m vertical change is observed over a 73 day period, equivalent to a mean surface lowering of 0.041 m d⁻¹, although some tracked surface features demonstrate lowering at rates of up to 0.068 m d⁻¹ (James *et al.*, 2016). These data are in agreement with data from Falljökull with mean surface lowering of 0.052 m d⁻¹, 0.039 m d⁻¹ and 0.032 m d⁻¹ in 2011, 2012 and 2013 respectively. Sólheimajökull has experienced thinning of 120 - 150 m (0.023 - 0.029 m d⁻¹) between 1996 and 2010 (Schomacker *et al.*, 2012).

Rapid rates of thinning are also evident at many alpine glaciers. Between 1985 and 1999, extreme thickness losses of up to ~ 80 m were evident for glaciers in the Swiss Alps (Paul and Haeberli, 2008), equivalent to 0.016 m d⁻¹. At Mer de Glace, France, thinning of 4.1 ± 1.7 m yr⁻¹ (0.011 ± 0.005 m d⁻¹) was recorded between 2000 and 2003 (Berthier *et al.*, 2004). Thinning rates in excess of 4 m yr⁻¹ were maintained through to 2008 at this glacier (Berthier and Vincent, 2012). Surface lowering of ~ 4.5 m yr⁻¹ between 1986-1990 (Nuth and Kääb, 2011) and 4.2 ± 1.4 m yr⁻¹ between 1990-2007 (Quincey and Glasser, 2009) have been demonstrated at the Tasman and Murchison glaciers in New Zealand. However, while all these glaciers are experiencing significant surface lowering, thinning rates are markedly lower than at Sólheimajökull and Falljökull. High rates of thinning in these maritime glaciers

perhaps reflects their sensitivity to climate (Sigurðsson *et al.*, 2007; Gudmundsson *et al.*, 2011) and high mass turnover (Aðalgeirsdóttir *et al.*, 2011).

5.2 - Surface melt and thinning rates

5.2.1 - Inter-annual variability

Surface melt production is a function of energy balance and the spatio-temporal variability in inputs to and outputs from the glacier surface. As such, periods of significant surface melt production should be intimately coupled with periods of glacier surface lowering. However, this is not evident at Falljökull at the inter-annual scale as peak annual melt in 2012 (8714 mm w.e.) is not correlated with peak annual thinning which occurs in 2011 (10,065 mm yr⁻¹). Surface melt production increased by 8.7% from 2011 to 2012 but this was coeval with a significant reduction in mean thinning rate (9,204 mm yr⁻¹, April - December). By 2013, both surface melt and thinning rates were suppressed relative to 2012 values, decreasing to 6974 mm w.e. and 7,552 mm yr⁻¹ respectively (April - December). To account for asynchronicity between melt and thinning in 2011-2012, it is necessary to use time-lapse imagery to determine any change in glacier surface conditions.

Surface melt production is strongly modulated by spatio-temporal variability in albedo and surface roughness parameters (Klok and Oerlemans, 2004) due to the presence of debris, snow cover, dust and liquid water (Munro, 1991) which can suppress or enhance melt production relative to modelled values. To represent the predominantly snow free, debris covered environment at Falljökull, energy balance model parameters were chosen to maximise melt production (albedo = 0.1, roughness = 0.03). However, even with these parameters, modelled melt still does not equal thinning rates as determined through time-lapse imagery. It is clear that the EBM (Brock and Arnold, 2000) does not adequately account for all energy fluxes at the glacier surface.

As a result, asynchronicity in 2011-2012 is best explained by the eruption of Grímsvötn in late May 2011 (Petersen *et al.*, 2012) and the deposition of a thin layer of tephra on the glacier surface (Fig. 72). While the energy balance model can account for this through albedo modification, it does not incorporate the spatial distribution or thickness of debris. Several studies have demonstrated the importance of debris thickness in determining melt rates (e.g. Mattson *et al.*, 1993; Kayastha *et al.*, 2000) with a non-linear relationship between these variables as per the Østrem (1959) curve. Thin debris cover acts as a source of retained heat and enhances melt (Carenzo *et al.*, 2016). When debris cover exceeds a critical threshold of 20 - 30 mm (Warren, 1984), melt is suppressed (Brock *et al.*, 2010). This debris was ubiquitous at Falljökull in

2011 although was less extensive towards the end of the melt season, most likely due to supraglacial runoff and aeolian removal of sediment. Despite this, debris cover was still markedly more extensive than in subsequent years and probably accounts for enhanced rates of thinning in 2011. Unfortunately, without information regarding debris thickness or thermal properties (Reid and Brock, 2010), it is difficult to establish this beyond doubt.



Figure 72. Tephra deposition at Falljökull on 23/05/2011 from the Grímsvötn eruption. Tephra was present on the glacier surface throughout 2011.

However, field experiments at Svínafelsjökull, Iceland (Möller *et al.*, 2016), a glacier only ~3 km from Falljökull, demonstrated the impact of supraglacial tephra deposition from the Grímsvötn eruption on ablation rates. Ablation was maximised under tephra layers of 1-2 mm thick, increasing by almost 25% relative to bare ice conditions (Möller *et al.*, 2016) while layers in excess of 100 mm were shown to decrease ablation by ~ 80%. While an albedo reduction was key to increased ablation rates (Warrant and Wiscombe, 1980), the thermal resistance of the particle layer was also important in controlling the heat conduction towards the glacier surface (Nicholson and Benn, 2006; Möller *et al.*, 2016). However, the spatial distribution of volcanic tephra is highly variable (Brown *et al.*, 2012), resulting in high spatio-temporal variability in albedo (Möller *et al.*, 2014). Additionally, while tephra layers are thickest close to the eruption site, distal sites are covered by millimetre to sub-millimetre scale layers (Möller *et al.*, 2016). At a distance of ~58 km from Grímsvötn, it is probable that the tephra layer deposited at Falljökull would be significantly less than 100 mm and is likely to be closer to the optimal 1-2 mm thickness for melt enhancement, although tephra dispersal would be strongly controlled by wind speed and direction (Gudmundsson *et al.*, 2012). Given the spatial ubiquity of this debris layer, all sectors would be expected to exhibit peak thinning in 2011. This is evident at Falljökull with calculated thinning of $0.060 \pm 0.003 \text{ m d}^{-1}$, $0.052 \pm 0.003 \text{ m d}^{-1}$ and $0.044 \pm 0.004 \text{ m d}^{-1}$ for the terminus, intermediate and upper sectors respectively. Higher than expected rates of thinning i.e. relative to modelled surface melt production, are accounted for tephra deposition from Grímsvötn. This demonstrates the importance of glacier surface characteristics in controlling melt and thinning rates but also the value of time-lapse imagery in determining variability in glacier surface conditions at a high temporal resolution.

5.2.2 - Glacier terminus 2011-2013

Over seasonal timescales, surface melt and thinning rates are reasonably well coupled at the glacier terminus. Despite this, a number of consistent inter-annual trends are evident, as discussed in Section 4.3.1.

Firstly, an early melt season lag between modelled melt and calculated thinning is evident in 2012 and 2013. This may be a function of the heat from conduction Q_g i.e. the energy required to raise the ice surface layer to 0°C, which delays the onset and reduces the total amount of supraglacial melt (Greuell and Oerlemans, 1986; Oerlemans and Klok, 2002). This energy flux was not incorporated by Brock and Arnold (2000) but should be added to model calculations for high alpine or polar glaciers (Price, 1986; Braithwaite, 1995) or glaciers characterised by a deep snowpack or firn layer (e.g. Hofsjökull, Iceland, de Woul *et al.*, 2006). However, the consistent

early melt season lag at Falljökull indicates that conduction may also be an important process for glaciers with restricted seasonal snow cover. Temperature profiles at cold-based glaciers (Fig. 73) demonstrate the variation of temperature with depth, with low temperatures ($< -6^{\circ}\text{C}$) present at the glacier surface throughout the year. Ice temperatures at temperate glaciers are significantly higher (Harrison, 1972), although a sub-freezing near-surface layer can occur in the ablation area (Maohuan, 1990). While ice is above the pressure melting point throughout at Falljökull, seasonal freezing of the surface layer may occur and delay the shift to an isothermal ice surface ($\geq 0^{\circ}\text{C}$).

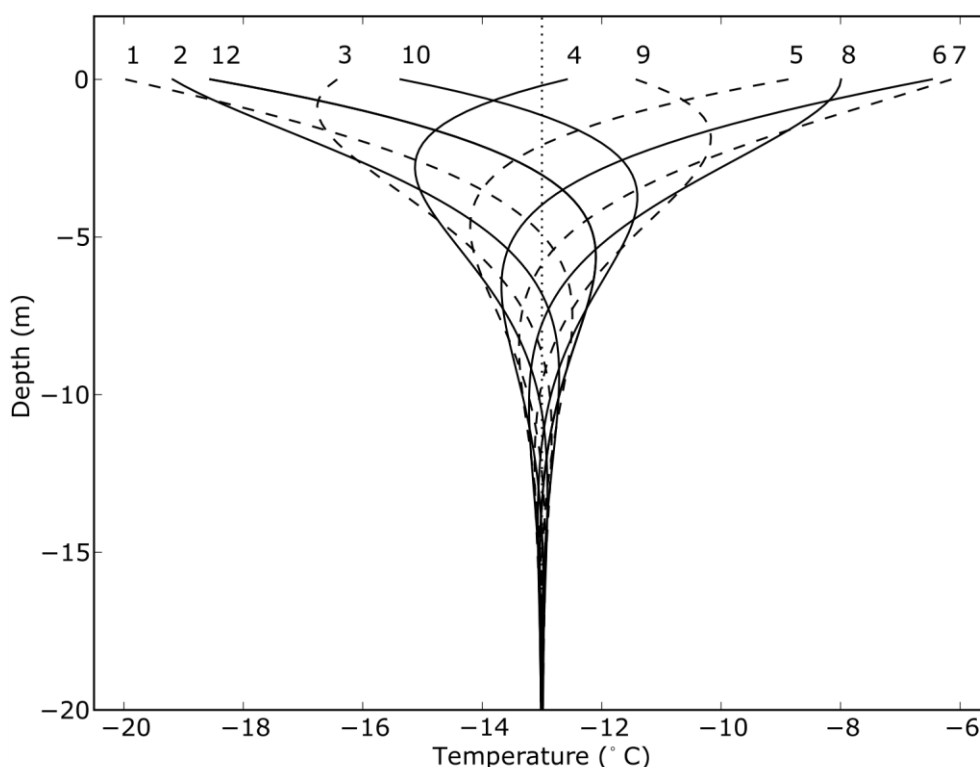


Figure 73. Variation of temperature with depth for the conditions at Colle Gnifetti. Numbers next to curves indicate months (1: Jan, 2: Feb). From Lüthi et al., (2001).

However, the longevity of the early melt season lag is strongly modulated by glacier surface conditions, as thick snow and debris cover can decrease the conduction of heat within the ice (Nicholson and Benn, 2006) and delay the onset of enhanced melt. As such, the magnitude of this temporal offset varies between years with an extended offset in 2013 (Fig. 51) but a much shorter lag in 2012 (Fig. 50). A longer delay between increasing energy inputs to the glacier surface and the onset of enhanced melt in 2013 is accounted for by a fall in surface melt production in 2013 (6974 mm w.e.) which is exacerbated by the perseveration of the winter snowpack and the presence of thick debris cover at the terminus.

In 2013, the winter snowpack was significantly more extensive than in previous years but was also present on the glacier surface until mid-April with numerous snow events observed in May. The extended preservation of the snowpack would suppress total melt, as radiative fluxes would be reduced due to albedo, but also delay the onset of peak thinning as greater surface energy inputs would be required to raise the snowpack to 0°C and initiate melting. However, this is further complicated by the extension of a thick debris band across the glacier terminus in 2013, sourced from the medial moraines between Virkisjökull and Falljökull. Without any supplementary data, it is difficult to estimate the thickness or thermal properties of this debris. However, based on time-lapse imagery, it appears that debris cover is substantially thicker and more extensive than in previous years (Fig. 74). Furthermore, debris is markedly less extensive in the intermediate and upper sectors. If it is assumed that this debris layer is > 20 - 30 mm thick (Warren, 1984), it would insulate the ice and suppress melt (Østrem, 1959). As such, the extended preservation of the seasonal

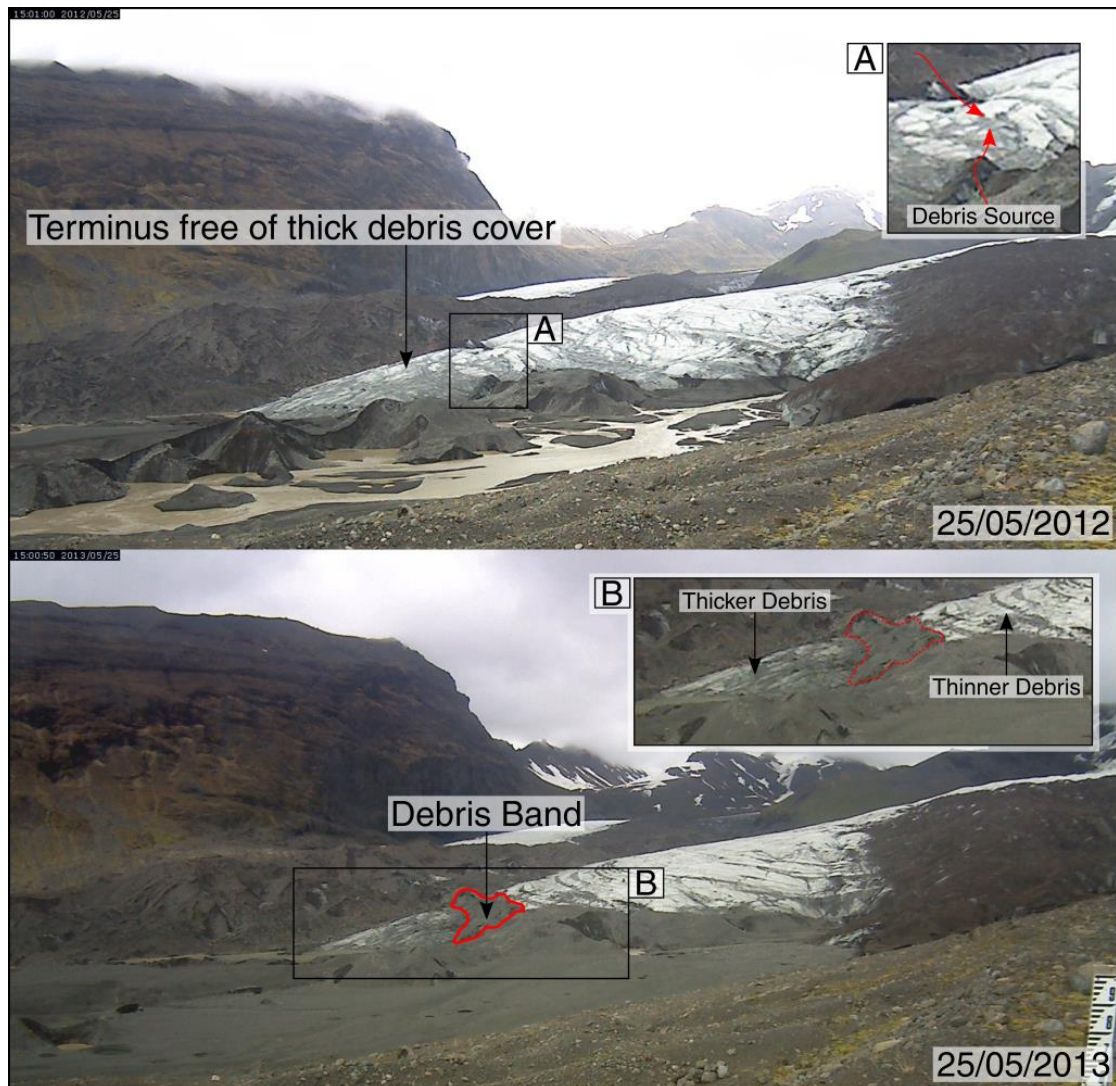


Figure 74. Extension of the debris band across the Falljökull terminus. The terminus is free of thick debris cover in 2012 (A). Debris is present in 2013, with thickness varying with altitude (B).

snowpack and the presence of thicker debris cover at the glacier terminus, in combination with restricted surface melt production in 2013, account for melt suppression and an increased offset between peak modelled melt and calculated thinning. These factors lead to a reduction in energy inputs to the glacier surface, due to the higher albedo of snow and the insulating properties of thick debris cover, and thus delay the shift to an isothermal snowpack (Oerlemans and Klok, 2002).

The glacier terminus also experiences elevated thinning rates during the melt season relative to the values generated via EBM. This leads to a late season offset between modelled melt and calculated thinning which is consistent throughout the period 2012-2013. Modelled melt is significantly underestimated by the EBM, despite the use of maxima/minima albedo and surface roughness parameters to account for surface debris cover. This underestimation is equivalent to ~2.1 m in 2012 and ~1.6 m in 2013 and corroborates with data from Virkisjökull (Thompson, 2016). Poor model optimisation of thin debris cover may explain the consistent thinning underestimation at low elevations and could also be linked to the temporal offset between peak melt and peak thinning throughout the period 2011-2013. Thin debris cover has been shown to act as a source of retained heat (Carenzo *et al.*, 2016) and may lead to melt enhancement even when surface energy inputs decline. For energy balance modelling of glaciers characterised by thin surface debris, the new model by Reid and Brock (2010) may be able to reproduce observed changes in melt rates below debris layers of variable thickness.

5.2.3 - Intermediate sector 2011-2013

The intermediate sector exhibits reasonable coupling between surface melt production and thinning rates throughout the period 2011-2013. However, although many of the trends observed at the glacier terminus are also evident at this higher elevation, asynchronous behaviour is evident with clear spatial variability in calculated thinning rates.

In 2011, the intermediate sector demonstrates intimate coupling between melt and thinning ($R^2 = 0.83$, $p = 0.002$). In contrast, there is a two month offset between peak melt and peak thinning at the glacier terminus. However, variability in surface conditions between these sectors is negligible, with extensive coverage of volcanic tephra from Grímsvötn. Tephra deposits may account for the tight coupling between modelled melt and calculated thinning at the intermediate sector in 2011 as this debris would condition the glacier to respond more rapidly to surface energy inputs. By acting as a source of retained heat, tephra may accelerate the shift to an isothermal snowpack and result in the earlier onset of melt.

However, tephra coverage is also extensive at the glacier terminus and is unlikely to vary in thickness over such small spatial scales. As such, surface energy balance variability cannot fully explain the asynchronicity between these sectors. Instead, the offset between melt and thinning at the terminus may be accounted for by the expansion of the proglacial-lake at Falljökull and increased contact with the glacier snout from late-May 2011. Based on time-lapse imagery, there is limited contact between the glacier snout and the pro-glacial lake prior to this date as the snout is buttressed by a thick layer of debris (Fig. 75). During this time, retreat of the glacier front is marginal. However, from June onwards, this debris layer is not observed and there is direct contact between the snout and the pro-glacial lake. Retreat of the glacier front and rates of thinning are enhanced from June onwards.

It is suggested that higher rates of thinning at the glacier terminus after June, briefly exceeding 0.07 m d^{-1} in August, are accounted for by increased basal heating. This energy flux is unlikely to be important at higher elevations as water-ice contact is limited to the terminus. This spatial variability is not captured by the EBM. Proglacial lakes have been shown to accelerate terminus retreat (Funk and Röthlisberger, 1989; Warren and Aniya, 1999) and increase thinning rates (Naruse and Skvarca, 2000; Tsutaki *et al.*, 2011; 2013). The absence or presence of pro-glacial lakes can account for within-mountain range variability in glacier-climate response (Salinger *et*



Figure 75. Development of and increased contact with the pro-glacial lake by 26/06/2011.

al., 2008) with their importance demonstrated for alpine glaciers in New Zealand (e.g. Quincey and Glasser, 2009; Robertson *et al.*, 2013), the Himalaya (e.g. Thompson *et al.*, 2012) and the European Alps (e.g. Haeberli *et al.*, 2001).

Further spatial variability is evident in the intermediate sector in 2013, as thinning rates are suppressed in March and April. This could reflect early melt season uplift at Falljökull. Glacier uplift has been observed at many alpine glaciers (Iken *et al.*, 1983; Humphrey *et al.*, 1986; Jansson and Hooke, 1989; Raymond *et al.*, 1995) as high water pressures in cavities and subglacial channels result in hydraulic jacking (Iken *et al.*, 1996; Jansson *et al.*, 2003). Alternatively, this period of “uplift” could simply be accounted for by the growth of the snowpack at this time (Fig. 76). However, this is unlikely as surface features were selected which were observable throughout this period i.e. extensive/tall debris structures. These structures are unlikely to be uplifted by the snowpack. In contrast, snowpack growth would obscure low lying surface features. Therefore, meltwater-induced uplift is a plausible explanation as the magnitude and duration of the early melt season uplift at Falljökull, at +0.85 m and ~36 days respectively, is in agreement with observations at Unteraargletscher, Switzerland (+0.6 m, 21 days, Iken *et al.*, 1983). However, similar patterns of uplift are not observed in previous years while spatial variability is evident in 2013. Given this asynchronicity in early melt season behaviour, it is necessary to determine the key drivers of uplift.

Firstly, the occurrence of uplift would be strongly controlled by the structure of the subglacial network (Section 2.3.3) and the presence of discrete or distributed drainage. Based on the spatial distribution of uplift at Falljökull, with no evidence of uplift at the terminus, it is interpreted that this sector is underlain by a channelised, discrete system at this time with the intermediate sector characterised by inefficient, distributed drainage. In the latter, increased meltwater input would over-pressurize the distributed system and lead to glacier uplift as basal shear stress is reduced. In contrast, meltwater input to the glacier terminus would be transferred more efficiently out of the glacier via channels. This interpretation conforms to the arborescent structure of subglacial networks (Hooke, 1987) with channel size decreasing up glacier.

However, a similar pattern of glacier uplift is not evident in 2012, despite the presence of distributed drainage at Falljökull throughout the early melt season. Therefore, subglacial drainage structure is not the only control on early melt season uplift. Instead, uplift may be dependent on the preservation and size of the winter snowpack. Snowpack thickness is an important control on subglacial drainage morphology (Nienow *et al.*, 1998) and thus rates of basal motion (Fischer *et al.*, 1999) while the timing of snowpack removal is also key to surface energy balance (Willis *et al.*, 2002; Hock *et al.*, 2005). Snow generally retards the flow of water into the englacial



Figure 76. Extended preservation of the seasonal snowpack in 2013, relative to previous years.

system through water storage (Schneider, 2000) and by decreasing surface melt production due to albedo (Willis *et al.*, 2002). As such, the seasonal snowpack suppresses total meltwater generation but also delays the movement of meltwater to the subglacial system. As a result, distributed subglacial drainage is more likely under a substantial snowpack as over-pressurization is unlikely. In contrast, the presence of discrete drainage at the glacier terminus indicates that the snowpack may be thinner at lower elevations. A thinner snowpack would have a smaller negative impact on surface melt production with a shorter lag between meltwater generation and input to the glacier. Channelization due to over pressurisation is more likely at this lower elevation.

Therefore, the varying thickness of the snowpack with elevation explains the spatial distribution of subglacial drainage. However, the snowpack not only provides the conditions for uplift i.e. by reducing meltwater inputs and preserving distributed drainage, but is also a key driver of uplift by acting as a source of water. This layer can undergo rapid melt relative to the underlying ice and lead to large meltwater inputs to the englacial system. In 2013, this is supplemented by numerous precipitation events in March and April. Early melt season uplift at Falljökull is strongly controlled by glacier surface conditions (presence of the snowpack), weather (precipitation events) and spatial variability in subglacial hydrology (discrete/distributed).

5.2.4 - Upper sector 2011-2013

Surface melt and thinning rates exhibit reasonable coupling in the upper sector from 2011-2013 while intra-annual trends are generally consistent with those observed at the terminus and intermediate sectors. Firstly, there is a consistent late season underestimation of thinning by the energy balance model, which reflects the poor parameterisation of thin surface debris by the EBM. This may also account for the offset between peak melt and peak thinning in each year. Glacier uplift may also be evident in March 2013, in agreement with observations at the intermediate sector. However, cumulative thinning values fluctuate over this period and it is not possible to confirm this beyond error. If this does reflect meltwater induced uplift, the upper sector is likely underlain by distributed subglacial drainage to accommodate this.

Thinning rates exhibit limited intra-annual variability in 2011, a trend which is poorly correlated with data from subsequent years. Significant seasonal shifts in thinning rate are evident for the upper sector in 2012-2013 (Fig. 59 - 60). Despite this, melt and thinning are reasonably coupled in 2011 ($R^2 = 0.70$, $p = 0.009$), with thinning in excess of 0.05 m d^{-1} from May to September, decreasing to $\sim 0.03 \text{ m d}^{-1}$ in October-November coeval with a significant reduction in surface melt production. This extended

period of high thinning rates may be accounted for by the eruption of Grímsvötn, with melt and thinning enhanced from May and sustained through the melt season. The tailing off of thinning rates from September may reflect the decreasing spatial coverage of the debris layer as well as the late season reduction in surface melt generation.

Further spatial variability is evident in 2012, as an early melt season lag between modelled melt and calculated thinning is not evident in the upper sector. Clear asynchronicity between the upper and terminus-intermediate sectors is also evident in early April as calculated thinning actually exceeds modelled melt at this time (Fig. 62, A). Unfortunately, time-lapse imagery cannot provide a satisfactory explanation for this variability as glacier surface conditions appear similar in each sector. One possible explanation is that faster surface velocities in the upper sector at this time (Fig. 65, C), generally in excess of 0.16 m d^{-1} , may have resulted in more rapid collapse of surface features i.e. debris cones. This glacier surface evolution may have been poorly captured by feature tracking due to the distance to these features ($> 600 \text{ m}$) and the restricted image resolution. Despite this currently unexplained variability, these data are important as they demonstrate small spatial scale variability in thinning rates.

5.2.5 - Melt-thinning coupling at Falljökull

Based on these data, reasonable coupling between surface energy balance and time-lapse derived thinning rates is evident at Falljökull from 2011-2013. However, thinning rates are strongly modulated by spatio-temporal variability in glacier conditions which are not fully accounted for by the energy balance model of Brock and Arnold (2000).

Although trends for surface melt production and thinning are generally coeval, an early melt season lag is evident in many datasets (e.g. Fig. 47). This delay in the onset of increased rates of thinning relative to surface melt production is accounted for by a delayed shift to an isothermal ice surface. Conversely, the energy balance model appears poorly optimised for thin debris cover with consistent late season offset, with thinning consistently underestimated by the EBM. The use of more innovative models which better parameterise surface melt under thin debris cover (e.g. Reid and Brock, 2010) and include the heat from conduction may generate more accurate data on surface energy balance. Despite this, these data clearly show that time-lapse imagery can be used to generate consistent and accurate data on thinning rates which generally corroborate with energy balance modelling and fit a pattern established at similar glaciers (e.g. Schomacker *et al.*, 2012).

Time-lapse imagery can also be used to account for intra-annual variability in thinning rates. In 2011, the Grímsvötn eruption and the deposition of tephra significantly enhanced surface melt, in excess of modelled values. In the same year, the expansion of the pro-glacial lake and its increased contact with the Falljökull glacier snout resulted in asynchronous behaviour of the terminus compared to the intermediate and upper sectors. In 2013, the extended preservation of the winter snowpack may account for the offset between peak melt and peak thinning, although this offset increased at the terminus due to the extension of a thick debris band across the glacier snout. Finally, early melt season uplift of Falljökull may be evident in the intermediate and upper sectors in March and April 2013. Glacier uplift is strongly dependent on the preservation of the snowpack, regular precipitation events and the structure of the subglacial hydrological system. Thinning rates at Falljökull are strongly modulated by individual events i.e. volcanic eruption, pro-glacial lake development, debris band extension, early melt season uplift. However, these events do not obscure the seasonal pattern of thinning as a function of surface energy balance. High temporal resolution time-lapse imagery can be used to identify the form and timing of these events to better understand perceived anomalous thinning rate behaviour.

5.3 - Linking surface dynamics to glacier hydrology

Time-lapse derived thinning rates and modelled surface melt production are well coupled when spatio-temporal variability in glacier surface conditions and individual events are taken into consideration. As such, thinning rate data at Falljökull can be considered to be representative of the input of supraglacial meltwater to the englacial and subglacial system. Given the importance of basal sliding and subglacial deformation in temperate glaciers (Section 2.1), variability in meltwater input should have a significant impact on surface dynamics (Jansson *et al.*, 2003). While intermediate water storage does introduce complexity to this relationship (Jansson *et al.*, 2003), this should have a limited impact at Falljökull due to the absence of a firn layer (de Woul *et al.*, 2006). While short term storage in englacial and subglacial channels may also occur, it was not impossible to detect this signal using time-lapse imagery of limited temporal resolution i.e. maximum 3 photographs per day.

Periods of hydrodynamic coupling/de-coupling are identified as discussed in Section 2.3.4. However, as hydrological forcing of ice velocity can still occur despite the existence of channels (Bartholomew *et al.*, 2011), the following interpretations of subglacial drainage configuration must be validated by other techniques (e.g. Iken and Bindenschadler, 1986; Sharp *et al.*, 1993; Tranter *et al.*, 1993; Hubbard *et al.*, 1995).

Note hydrodynamic de-coupling in this section is distinct from the sedimentary de-coupling process (Iverson *et al.*, 1995) and refers to periods in which high basal water pressures are not associated with enhanced forward motion.

5.3.1 - Evidence for hydrodynamic coupling in 2011

Interpreting the controls on surface velocities in 2011 is challenging due to the limited timespan of surface feature tracks which prevents study of early and late melt season trends. Furthermore, “noise” in the upper sector prevents any interpretation of these data. However, both the glacier terminus and intermediate sectors demonstrate clear periods of hydrodynamic coupling.

At both these sectors, surface velocities and thinning rates are correlated from April to early-May. Glacier flow and thinning are relatively stable over this period, probably reflecting movement through internal deformation when meltwater inputs to the subglacial system are limited. Further coupling is evident later in the melt season from early-June until August at both sectors, as thinning and surface velocities shift to above average rates. This is broadly supportive of a forcing model whereby over-pressurisation of the inefficient subglacial drainage system by surface meltwater leads to basal sliding and increases in forward motion.

However, throughout this model of a coupled hydrological system, there are short-lived periods where surface melt and ice velocity become de-coupled. At the glacier terminus, hydrodynamic de-coupling is evident in May and June (Fig. 64, A) as thinning rates fall below average while average surface velocities are maintained. This demonstrates the importance of variable meltwater input in determining the relative importance of internal and basal derived movement. When surface melt production is restricted and water flux to the subglacial system is limited, surface velocities are primarily a function of internal deformation. Limited surface velocity variability is evident at this time, relative to the peak melt season. Further de-coupling is evident at the intermediate sector in October (Fig. 64, B) and reflects a similar process. A reduction in thinning rate over this period is not correlated with ice dynamics, reflecting the seasonal reduction in surface melt production and a return to movement through internal deformation. Therefore, when meltwater inputs are high or rising faster than the drainage system can adjust to e.g. June - August, basal sliding and enhanced glacier flow can occur. However, when meltwater inputs are suppressed during the early and late melt season e.g. April or September - November, flow variability is limited. Restricted meltwater fluxes during the early-melt season would be insufficient to over-pressurise the immature subglacial drainage system while declining meltwater inputs in the late melt season would be rapidly transferred out of the glacier via efficient, discrete drainage. As such, these

data demonstrate the impact of variable meltwater input in determining the relative importance of internal or basal derived flow (Copland *et al.*, 2003).

Determining the timing of drainage system evolution i.e. distributed to discrete, is challenging as long periods of hydrodynamic coupling are evident throughout 2011 at both the terminus and intermediate sectors. Coupling between thinning and surface velocities during the peak melt season i.e. late-June to August, could indicate the presence of distributed drainage at this time. However, this interpretation contrasts markedly with the paradigm of arborescent subglacial networks (Hooke *et al.*, 1987). A more plausible explanation is that discrete drainage was present throughout 2011 at Falljökull at a distance of < 400 m from the glacier front. As substantial surface lowering is evident in 2011 due to the Grímsvötn eruption (0.052 m d⁻¹), it seems likely that significant meltwater inputs would be transferred to the subglacial system during the peak melt season. This input of meltwater may have occurred faster than the drainage system could adjust to, resulting in flow variability and hydrodynamic coupling in a discrete system (Bartholomew *et al.*, 2011).

5.3.2 - Evidence for hydrodynamic coupling in 2012

Extended periods of hydrodynamic coupling are evident at the terminus, intermediate and upper sectors in 2012. This reflects a coupled hydrological system as inputs of meltwater to the subglacial system during the early melt season (April to May) are correlated with increased surface velocities. Glacier flow variability is generally enhanced during the first half of the year in all sectors and probably reflects temporal variability in meltwater input and periods of basal sliding. In contrast, flow variability is markedly reduced after June in all sectors. This demonstrates the temporal evolution of the subglacial system as enhanced surface meltwater input from May are responsible for increasing channel efficiency and a shift to discrete drainage. Despite these consistent trends, spatio-temporal variability is evident as two clear periods of hydrodynamic de-coupling are identified at the terminus and intermediate sectors (Fig. 65). However, rather than two distinct events, it is interpreted that they are intimately coupled and reflect the commencement and culmination of a period of sedimentary deformation. Subglacial derived flow (Section 2.1.3) is interpreted as a key control on Falljökull surface velocities in 2012.

At the terminus, hydrodynamic de-coupling is evident in late April as a distinct shift to above average velocities is poorly correlated with sustained below average thinning. This contrasts markedly with the coupled hydrological model proposed above as the onset of flow acceleration cannot be directly linked to over-pressurisation of the subglacial system. The transition to above average surface velocities occurs ~3 weeks before thinning rates increase. As such, basal sliding is

probably limited at this time as meltwater inputs are unlikely to be rising quickly enough to over-pressurise the subglacial system. Therefore, a more plausible explanation is that asynchronous flow acceleration from late-April reflects the saturation and deformation of subglacial sediment. Although thinning rates are below average in April, this still accounts for surface lowering of 0.02 m d^{-1} , sufficient to transfer a significant meltwater flux to the subglacial system. This is enhanced by a number of large precipitation events at this time which may have accelerated sediment saturation and deformation. Although sediment deformation rates probably decrease during May (Kamb, 1991; Iverson *et al.*, 1995), basal sliding is maintained by significant melt (2184 mm w.e.) and above average thinning from mid-May. Accelerated rates of sediment deformation during late April are likely to be an important control on glacier instability and act as a catalyst for sustained basal sliding.

In contrast, the extended period of hydrodynamic de-coupling throughout June reflects the culmination of this process. Fast velocities, instigated by rapidly deforming sediment and maintained by high basal water pressures, are curtailed at the end of May with a shift to below average surface velocities. The timing of this slowdown appears to be coeval with a reduction in thinning rate in late-May and early-June, which would decrease the meltwater flux to the base which in turn would lower the ice, increase the applied shear stress and increase the strength of the subglacial sediment due to an increase in intergranular friction (Iverson *et al.*, 1995). Additionally, subglacial channels are likely to have undergone adjustment in response to enhanced meltwater fluxes, with increasing network efficiency and channel size due to enhanced frictional melting as a result of consistently high water pressures. The maintenance of sedimentary deformation requires basal water pressures to remain high to prevent intergranular friction from increasing. Therefore, a reduction in subglacial water pressure in June, due to a slowdown in thinning rate and more developed and efficient subglacial channels, accounts for glacier slowdown in this month.

A similar pattern of hydrodynamic de-coupling is evident at the intermediate sector, reflecting the sedimentary deformation process described above. However, the transition to above average surface velocities occurs in early April, 2 - 3 weeks before the glacier terminus. This offset indicates that the saturation and deformation of sediment varies spatially and is propagated down glacier. In contrast, the switching off of this mechanism is a rapid and spatially ubiquitous process as the shift from above to below average velocities occurs towards the end of May for the intermediate sector and within a few days at the terminus. This implies that a reduction in basal water pressure is rapidly propagated down glacier. This is attributed to a slowdown in thinning rate and an increase in channel efficiency at this time. In contrast, there is

no evidence of hydrodynamic de-coupling in the upper sector during the first half of the year, with coeval peaks and troughs in surface velocities and thinning rates (Fig. 65, C). This implies that sediment deformation was largely restricted to within ~ 350 m of the glacier front. However, clear hydrodynamic de-coupling occurs from June, although this is complicated by considerable data “noise” for surface velocity tracks.

Based on these data, it is interpreted that the glacier front was characterised by distributed subglacial drainage in the early part of 2012. Although the glacier front was underlain by discrete drainage in late 2011, deterioration of the basal drainage network during winter is likely (Flowers and Clarke, 2002) due to limited meltwater inputs, restricted subglacial flow and channel closure via ice creep due to reduced frictional melting (Hooke *et al.*, 1990). The existence of distributed drainage in 2012 is reflected in the tight hydrodynamic coupling evident in all sectors during March. However, as meltwater inputs increase and channels become over-pressurised through April and May, the subglacial system shifts from a hydrologically unconnected to a connected state (Flowers and Clarke, 2002). This is characterised by channelised, discrete drainage which is present by early June, as all sectors demonstrate hydrodynamic de-coupling at this time. Although surface velocities and thinning rates are well coupled at both the terminus and intermediate sectors after this date, this perhaps reflects hydrodynamic coupling in a discrete system (Bartholomew *et al.*, 2011).

5.3.3 - Evidence for hydrodynamic coupling in 2013

Similar shifts from distributed to discrete drainage are interpreted in 2013 although spatial variability is evident. Asynchronous trends for surface velocities and thinning are evident from mid-March at the glacier terminus and are sustained throughout the year. However, although hydrodynamic coupling is evident prior to this date, this is unlikely to reflect the presence of distributed drainage and movement through basal sliding. Surface meltwater production is extremely restricted during these months and would be insufficient to over pressurise the subglacial system (Iken *et al.*, 1983) and promote hydraulic jacking (Hooke *et al.*, 1990). Below average thinning rates until early April reflects restricted energy inputs to the glacier surface. This is exacerbated by the survival and replenishment of the glacier snowpack, which is present much later in the season relative to previous years, as well as the extension of a debris band across the glacier snout. This debris, combined with extensive snow cover and favourable meteorological conditions, would have suppressed melt and led to a reduction in thinning rate. As such, the maintenance of average surface velocities during March and April reflects movement via internal deformation as the

restricted meltwater flux would be insufficient to promote sliding at the bed, irrespective of subglacial drainage structure.

However, surface velocities remain stable from late April to early May, when thinning rates shift from below to above average and meltwater fluxes to the subglacial system are enhanced. If a distributed network was present at the time, hydrodynamic coupling would be evident as rising subglacial water pressures would promote basal sliding. As coupling is not evident, it is likely that the terminus is characterised by discrete drainage, with subglacial channels maintained over the winter period. Extremely restricted glacier velocities in early 2013 (February: $0.008 \pm 0.003 \text{ m d}^{-1}$), reflecting movement via ice creep, may be insufficient to force channel closure. Limited flow variability is evident throughout 2013, reflecting the rapid transit of meltwater out of the glacial system via efficient subglacial channels. Surface velocities at the terminus are therefore predominantly controlled by internal deformation rates. However, there is a marked acceleration at the terminus in mid-August which is coeval with peak monthly thinning ($0.070 \pm 0.004 \text{ m d}^{-1}$). This further demonstrates the potential for hydrodynamic coupling in discrete systems. This acceleration is short lived as thinning rates fall in September (Fig. 66, A), perhaps reflecting a reduction in subglacial water pressure and the curtailment of basal sliding.

In contrast, the intermediate sector demonstrates hydrodynamic coupling until mid-June, with asynchronous trends for surface velocities and thinning rates after this date reflecting a shift to discrete drainage. Early-melt season coupling (January to June) reflects the presence of distributed drainage. Variability in subglacial drainage structure between the terminus and intermediate sector over the early melt season is attributed to spatial variability in basal water pressure. As all meltwater which reaches the subglacial network is routed through the terminus, this sector will be subject to higher water pressures, increased frictional melting and channel growth. This also explains the preservation of discrete drainage through the winter as water fluxes, although reduced relative to summer discharge, will have a disproportionate impact on terminus drainage with enhanced frictional melting and the suppression of channel closure via ice creep. In contrast, given the arborescent structure of subglacial networks, the same meltwater flux at higher elevations will equate to lower basal water pressures, as water is distributed in a greater number of channels. As a result, the terminus is characterised by a heightened sensitivity to meltwater input. By comparison, the meltwater flux required to instigate reorganisation of the subglacial network will increase exponentially up glacier. This interpretation is supported by melt data as the inferred shift to discrete drainage at the intermediate sector occurs in early June after peak melt of 1647 mm w.e. In contrast, channels are

maintained at the terminus throughout early 2013, when surface melt production is significantly reduced.

This trend is also evident in the upper sector which exhibits intimate hydrodynamic coupling throughout much of 2013, with the exception of a late melt season de-coupling in late-July through to mid-August (Fig. 66, C). Prior to this, surface velocities are well correlated with thinning rates with periods of fast glacier flow closely linked to glacier thinning and meltwater input. Basal sliding due to over-pressurisation of the subglacial system is a key driver of glacier flow in the upper sector. However, the late-melt season de-coupling reflects a shift to discrete drainage. Peak thinning (0.077 m d^{-1}) occurs prior to this date and probably accounts for enhanced basal sliding and peak surface velocities in July (0.22 m d^{-1}). A marked glacier slowdown from late July is correlated with sustained above average thinning and is indicative of increasing channel efficiency due to high basal water pressures and a shift to discrete drainage. As such, the extended preservation of distributed drainage i.e. relative to the terminus and intermediate sectors, is a function of arborescent subglacial drainage structure. The temporal evolution of subglacial drainage is strongly dependent on subglacial water pressure but this varies spatially with decreasing sensitivity to meltwater input with elevation.

5.3.4 - Potential controls on glacier front dynamics

Based on time-lapse imagery, periods of internal, basal and subglacial derived glacier flow have been identified throughout the period 2011-2013, although significant spatial variability is evident. Surface velocities at Falljökull are strongly controlled by surface meltwater production. When surface energy inputs are restricted and meltwater inputs to the englacial and subglacial system are limited, glacier flow is predominantly controlled by internal deformation.

However, when meltwater inputs are enhanced, basal sliding and subglacial deformation can occur although this is highly dependent on the structure of the subglacial network (Bingham *et al.*, 2006). This undergoes significant temporal evolution at Falljökull with a melt season shift from discrete to distributed drainage (Alley, 1989; Harbor *et al.*, 1997; Arnold *et al.*, 1998). However, the timing of this shift varies spatially. This is most apparent in 2013 as discrete drainage is maintained at the terminus throughout the year, while the intermediate and upper sectors demonstrate hydrological adjustment in June and late-July respectively. In contrast, channel closure by ice creep occurs during the winter due to the seasonal reduction in energy inputs to the glacier surface and restricted meltwater production. This results in the reestablishment of distributed drainage by the early months of both 2012 and 2013. The timing of hydrological adjustments is strongly dependent on

meltwater input (Flowers and Clarke, 2002) and this varies spatially, with the terminus exhibiting a heightened sensitivity to meltwater input due to higher basal water pressures and increased frictional heating.

However, although periods of discrete drainage are identified at Falljökull throughout 2011-2013, hydrodynamic coupling is still evident in these efficient systems when meltwater inputs increase faster than the drainage system can adjust to (Bartholomew *et al.*, 2011). As such, while fast glacier flow predominantly occurs when the lower reaches of Falljökull are underlain by distributed drainage (e.g. Upper, May-August 2013), short term flow accelerations (e.g. Terminus, August 2013) can occur when meltwater inputs are significant. While it is interpreted that fast glacier flow at Falljökull is predominately attributed to basal sliding as a function of high basal water pressures, it is suggested that subglacial deformation may be an important control on flow variability. However, while deformation may not be the primary driver of fast glacier flow (Iverson *et al.*, 1995), the presence of saturated and deforming sediment may be important to the timing of these events by providing a smooth surface to support concentrated shear stresses and higher basal water pressures.

5.3.5 - Potential controls on icefall dynamics

Few studies have focused on icefall dynamics due to the difficulties of data collection. Icefalls are characterised by intense brittle fracturing and heavily crevassed surfaces as glacier flow is faster than can be accommodated by ice creep (Hambrey, 1994). Feature tracking, although made challenging by the complexity of the terrain, is one of only a few feasible methods for determining icefall velocities. Advancements in terrestrial radar interferometry may also be of value in dynamic, inaccessible locations (Allstadt *et al.*, 2015). However, understanding icefall dynamics at Falljökull is important, as variability in balance velocity over longer timescales (Bingham *et al.*, 2006) determines the transfer of ice from the accumulation to the ablation areas (Quincey and Glasser, 2009). Acceleration or deceleration of the icefall will determine the transfer of ice from Öräfajökull which may have an impact in subsequent seasons and enhance or suppress glacier front retreat.

Unfortunately, it is not within the scope of this project to determine all of the driving controls on icefall dynamics, as no data are available on the structure of the icefall basin or the underlying topography. Furthermore, georeferencing strategies for these data were less robust due to limited data availability (Section 3.2.3). Despite these limitations, surface velocities at the Falljökull icefall (1.35 - 1.58 m d⁻¹) are in good agreement with velocities observed at icefalls at the Nisqually and Emmons glaciers, USA, at 1.0 - 1.5 m d⁻¹ (Allstadt *et al.*, 2015). However, significant intra-annual flow

variability is evident at Falljökull in 2012 and 2013, although variability was limited in 2011. In contrast, the main Nisqually icefall showed limited seasonal variability, with a slight increase in surface velocities from July through to the winter, indicating that this icefall may be relatively well drained throughout the year and is unaffected by seasonal changes in subglacial hydrology (Allstadt *et al.*, 2015). In contrast, similar ice cliffs at the Nisqually glacier, which were characterised by steep surface slopes and high crevasse density, did exhibit intra-annual variability. These seasonal shifts in icefall velocity corroborate with trends observed at the main Nisqually glacier, with periods of glacier sliding due to evolving subglacial hydrology (Fountain and Walder, 1998). This may reflect a heightened sensitivity to meltwater input in these ice cliffs (Allstadt *et al.*, 2015). Based on these data, it is suggested that the Falljökull icefall may be well lubricated by subglacial water during the melt season which promotes fast glacier flow. In contrast, restricted surface melt production during the winter may account for icefall slowdown. However, inter-annual variability is evident. Icefall velocities are generally stable throughout 2011, probably reflecting surface melt enhancement and increased basal lubrication due to Grímsvötn in the late melt season. In contrast, enhanced seasonal variability in 2013 is probably accounted for by the preservation of the winter snowpack which restricts surface energy inputs and basal sliding during the early part of the year but significantly enhances glacier flow during the peak season by acting as a source of surface meltwater. Although additional asynchronous behaviour is evident in 2013, this cannot be explained by surface melt data. Although subglacial hydrology may be an important driver of icefall dynamics, topographic and structural factors, which cannot be determined here, are likely to be of importance.

Chapter 6 - Conclusions

6.1 - Controls on surface melt production at Falljökull

High temporal resolution datasets of surface melt production have been generated at Falljökull through EBM (Brock and Arnold, 2000). These data corroborate with trends established at similar Icelandic glaciers as melt production is dominated by shortwave radiative inputs (Jóhannesson and Sigurðsson, 1998; Sigurðsson *et al.*, 2007). However, due to its maritime setting, melt production at Falljökull is significantly enhanced by turbulent heat fluxes (Laumann and Reeh, 1993). Energy inputs from precipitation are generally marginal although are of increasing importance when shortwave radiative inputs decline (Thompson, 2016). While inter-annual variability in total melt production is evident, seasonal trends are relatively consistent between years.

Comparison of modelled melt data with calculated thinning rates derived from time-lapse imagery has demonstrated some variability between these techniques. Rates of thinning and melt production are generally well correlated at the intra-annual scale, with enhancement of melt and thinning during the peak melt season and suppression during the winter. However, thinning is consistently underestimated by the EBM, despite the use of maxima/minima albedo and surface roughness parameters to maximise melt production in the predominantly snow-free, debris-covered environment at Falljökull. An early season lag and a late season offset between modelled melt and calculated thinning are evident in many datasets. Enhanced rates of thinning, relative to the values predicted by EBM, are maintained throughout the peak melt season and result in significant melt underestimation by ~1-3 m. This inconsistency may be addressed by the use of models which incorporate the heat from conduction and are better optimised for thin debris cover (Price, 1986; Braithwaite, 1995).

Furthermore, it has been shown that thinning of Falljökull is strongly affected by individual events which enhance or suppress surface melt production. The eruption of Grímsvötn, the growth and increased contact with the pro-glacial lake, the preservation of the winter snowpack and the presence of thick debris cover have all been shown to affect thinning rates. These individual events are difficult to incorporate into energy balance modelling. In contrast, time-lapse imagery can be used to determine the form, timing and duration of these events and their potential impact on surface energy balance. Thinning rates at Falljökull, in excess of 0.029 m d^{-1} throughout 2011-2013, are significantly higher than similar alpine glaciers (e.g. Berthier *et al.*, 2004; Paul and Haeberli, 2008). However, these data corroborate with substantial thinning at Solheimajökull (Schomacker *et al.*, 2012; James *et al.*, 2016) and

indicate the sensitivity and rapid response of these maritime glaciers to climate forcing (Sigurðsson *et al.*, 2007; Gudmundsson *et al.*, 2011)

6.2 - Controls on glaciers dynamics at Falljökull

A clear relationship between ice melt and ice dynamics is identified in these data. This is most evident at the icefall as surface velocities and melt production are generally well correlated throughout the period 2011-2013. It is likely that the icefall is well lubricated by subglacial water during the melt season which promotes sliding at the ice-bed interface (Allstadt *et al.*, 2015). In contrast, the glacier front demonstrates a variety of flow dynamics in response to surface lowering, perhaps reflecting the influence of subglacial drainage structure. These can be summarised as:

1. Events which exhibit close coupling between surface melt production and forward motion i.e. when distributed systems become over-pressurised leading to glacier uplift and basal sliding (e.g. Iken *et al.*, 1983).
2. Events which demonstrate a clear disconnection between melt and forward motion, accounted for by the process of hydrodynamic de-coupling. This can take the form of (A) the suppression of meltwater input, resulting in a return to internal deformation derived flow (e.g. Hooke *et al.*, 1989) or (B) when enhanced meltwater input to discrete systems has no impact on glacier dynamics (e.g. Mair *et al.*, 2002).
3. Events where drainage system configuration appears to hold little influence upon dynamics i.e. when discrete channelised configurations become over-pressurised due to overwhelming meltwater generation (e.g. Bartholomew *et al.*, 2011).

These models can be seen to operate variably throughout the study period and spatially across the glacier. However, the dominant trends observed include a seasonal shift in subglacial drainage structure as hydrodynamic de-coupling is representative of the transition from distributed to discrete drainage during the peak melt season (Alley, 1989). In contrast, meltwater inputs are suppressed over winter, with channel closure via creep (Hooke *et al.*, 1990) leading to deterioration of the basal drainage network (Flowers and Clarke, 2002) and reduced flow variability. Furthermore, fast glacier flow is most likely when inefficient distributed drainage is present as these configurations can be rapidly over-pressurised by meltwater inputs, leading to hydraulic jacking and forward motion. However, meltwater induced flow variability can also occur in discrete systems if meltwater inputs are rising faster than the drainage system can adjust to (Bartholomew *et al.*, 2011). Hydrologically induced

speed-up events are identified at Falljökull and may occur more readily due to substantial retreat and thinning which enhance meltwater input and instigate basal sliding, irrespective of subglacial drainage structure. However, these events are typically short-lived, as fast glacier flow is dependent on rising basal water pressures. Previous studies have shown that hydrological forcing of ice velocity can lead to limited dynamic sensitivity to inter-annual variability in surface melt (Sole *et al.*, 2013) as enhanced summer velocities condition the ice-bed interface for reduced winter motion (Van de Wal *et al.*, 2015). A similar trend is evident at Falljökull as inter-annual velocity variability is limited (Table 9), despite periods of surface meltwater-induced basal sliding.

These models may be complicated by the presence of deformable subglacial sediments, as interpreted at Falljökull (Björnsson *et al.*, 2003; Phillips *et al.*, 2013). Although fast glacier flow is dependent on high basal water pressures, a rapidly deforming sediment may be an important catalyst for enhanced velocities by providing a smooth surface to support concentrated shear stresses (Iverson *et al.*, 1995). This process may be an important control on glacier dynamics, particularly for temperate glaciers underlain by soft sediments.

6.3 - Application of time-lapse data to glacier dynamics

Time-lapse imagery has shown that Falljökull is not in equilibrium with climate, retreating ~155 m over the period 2011-2013. However, the lower reaches of the glacier are still “active” as seasonal variability in glacier flow and hydrodynamic coupling are evident. This is unlikely to be observed in stagnant ice that is wasting away in-situ (Phillips *et al.*, 2014). Forward motion is insufficient to offset retreat, which accounts for the cessation of annual push moraine formation since 2004 (Bradwell *et al.*, 2013). Slow glacier velocities ($\sim 0.01 \text{ m d}^{-1}$), as demonstrated by GNSS and time-lapse data, are not necessarily indicative of stagnant ice (Anderson *et al.*, 2004; Whitehead *et al.*, 2010). While there is some conflict with GNSS data, time-lapse velocities are in good agreement with similar mountain glaciers (Harrison *et al.*, 1996; James *et al.*, 2016).

Predicting the response of Falljökull to future climate change is particularly challenging as glacier surface conditions and subglacial hydrology exhibit significant spatio-temporal variability and strongly modulate the relationship between ice melt and ice dynamics. Ultimately, the survival of Falljökull is dependent on its connection, via the icefall, to its accumulation area on Öräfajökull. Based on these data, the icefall is still active and is feeding ice to the lower reaches of the glacier, in agreement with observations from GNSS (Phillips *et al.*, 2014). A weakened or absent

connection to Öräfajökull would lead to complete retreat of the lower reaches of Falljökull within only a few years.

6.4 - Achieving project objectives

To conclude, this study has shown that time-lapse imagery can be used to generate high spatio-temporal resolution datasets of glacier thinning and ice dynamics (Objective 1). These data were compared to high resolution meteorological datasets to determine the key controls on surface melt production (Objective 2). Finally, the degree of connectivity between ice melt and ice dynamics has been used to demonstrate the importance of subglacial drainage configuration, bed rheology and surface conditions in controlling glacier movement (Objective 3).

Many researchers establish time-lapse cameras for glacier monitoring but often don't analyse the data quantitatively (e.g. Bradwell *et al.*, 2013; Phillips *et al.*, 2014). This study has shown that these datasets are underutilised and could provide valuable long term records of glacier dynamics. Furthermore, time-lapse imagery has a number of advantages over existing techniques. Firstly, it provides a valuable record of glacier surface conditions which are difficult to incorporate into energy balance modelling. While these conditions can be captured by high resolution satellite imagery (e.g. Fugazza *et al.*, 2015), these data are generally characterised by poor temporal resolution. Furthermore, time-lapse imagery permits study of glacier dynamics at a high spatial resolution i.e. by tracking numerous glacier surface features through an image sequence. Rates of thinning and glacier surface velocities do vary significantly over small spatial scales (e.g. Allstadt *et al.*, 2015). Therefore, feature tracking reflects a natural progression from GNSS based studies (Phillips *et al.*, 2014) which are unlikely to capture this small spatial scale variability. Time-lapse imagery provides high spatio-temporal resolution data which is cost efficient to acquire, can be analysed robustly in Pointcatcher (James *et al.*, 2016) and can be compared directly to local meteorological data.

6.5 - Further work

To build on the results presented in this study, further work is necessary to address the degree of connectivity between ice melt and ice dynamics. While interpretations of subglacial drainage configuration and hydrodynamic coupling are in agreement with previous research, they have not been independently verified. Integration of time-lapse imagery with direct measurements of subglacial drainage structure (e.g. Sharp *et al.*, 1993) and bed rheology (Björnsson *et al.*, 2003) could be used to

demonstrate the importance of hydrology in controlling ice movement. Furthermore, glacier surface conditions i.e. debris thickness, snowpack extent, are simply estimated based on time-lapse images. On-site verification of surface conditions and use of EBMs which are optimised for debris cover (Reid and Brock, 2010) should result in better agreement between modelled melt data and time-lapse derived thinning rates. Collection of ablation stake data would also be useful to confirm substantial thinning at Falljökull.

For further time-lapse based studies, the use of a higher resolution camera would enable more precise tracking of surface features while more regular LiDAR acquisition would permit more robust georeferencing (e.g. James *et al.*, 2016). However, further in-depth study at the Falljökull glacier front may be challenging as the snout is increasingly covered in thick debris. As such, identifying suitable features for tracking may not be possible using the current camera set-up. However, continued monitoring and research of Falljökull may be of value although will require a new focus on the icefall and its connection to Öraefajökull. Icefalls place a key control on glacier dynamics but are poorly understood (Allstadt *et al.*, 2015) and changes in icefall structure and motion could lead to rapid and irreversible changes in glacial systems. Study of bed rheology (e.g. Hart *et al.*, 2011), subglacial drainage configuration (e.g. Hubbard *et al.*, 1995) and internal structure (e.g. Phillips *et al.*, 2014) and integration of these data with EBM and time-lapse imagery could demonstrate the key controls on icefall dynamics.

Word Count: 31,419

References

- Abbate, S., M. Avvenuti, L. Carturan, and D. Cesarini (2013), Deploying a Communicating Automatic Weather Station on an Alpine Glacier, *Procedia - Procedia Comput. Sci.*, *19*, 1190–1195, doi:10.1016/j.procs.2013.06.170.
- Aðalgeirsdóttir, G., T. Jóhannesson, H. Björnsson, F. Pálsson, and O. Sigurðsson (2006), Response of Hofsjökull and southern Vatnajökull, Iceland, to climate change, *J. Geophys. Res.*, *111*, 1–15, doi:10.1029/2005JF000388.
- Aðalgeirsdóttir, G., S. Gumundsson, H. Björnsson, F. Pálsson, H. Johannesson, H. Hannesdóttir, S. Sigurdsson, and E. Berthier (2011), Modelling the 20th and 21st century evolution of Hoffellsjökull glacier, SE-Vatnajökull, Iceland, *Cryosph.*, *5*(4), 961–976, doi:10.5194/tc-5-961-2011.
- Ahn, Y., and J. E. Box (2010), Instruments and Methods Glacier velocities from time-lapse photos: technique development and first results from the Extreme Ice Survey (EIS) in Greenland, *J. Glaciol.*, *56*(198), 723–734.
- Alley, R. B. (1989), Water-Pressure Coupling of Sliding and Bed Deformation: 1. Water System, *J. Glaciol.*, *35*, 108–118.
- Allstadt, K. E., D. E. Shean, A. Campbell, M. Fahnestock, and S. D. Malone (2015), Observations of seasonal and diurnal glacier velocities at Mount Rainier, Washington, using terrestrial radar interferometry, *Cryosph.*, *9*, 2219–2235, doi:10.5194/tc-9-2219-2015.
- Ambach, W. (1974), The influence of cloudiness on the net radiation balance of a snow surface with high albedo, *J. Glaciol.*, *13*(67), 73–84.
- Amundson, J. M., M. Truffer, M. P. Lüthi, M. Fahnestock, M. West, and R. J. Motyka (2008), Glacier, fjord, and seismic response to recent large calving events, Jakobshavn Isbræ, Greenland, *Geophys. Res. Lett.*, *35*, doi:10.1029/2008GL035281.
- Andersen, M. L., M. Nettles, P. Elosegui, T. B. Larsen, G. S. Hamilton, and L. A. Stearns (2011), Quantitative estimates of velocity sensitivity to surface melt variations at a large Greenland outlet glacier, *J. Glaciol.*, *57*(204), 609–620.
- Anderson, R. S., S. P. Anderson, K. R. Macgregor, E. D. Waddington, S. O. Neel, C. A. Riihimaki, and M. G. Loso (2004), Strong feedbacks between hydrology and sliding of a small alpine glacier, *J. Geophys. Res.*, *109*, 1–17, doi:10.1029/2004JF000120.
- Andreassen, L. M., M. R. Van den Broeke, R. H. Giesen, and J. Oerlemans (2008), A 5 year record of surface energy and mass balance from the ablation zone of Storbreen, Norway, *J. Glaciol.*, *54*(185), 245–258.
- Applegarth, L. J., M. R. James, B. V. W. De Vries, and H. Pinkerton (2010), Influence of surface clinker on the crustal structures and dynamics of “a”ā lava flows, *J. Geophys. Res.*, *115*, 1–15, doi:10.1029/2009JB006965.
- Arendt, A. A., K. A. Echelmeyer, W. D. Harrison, C. S. Lingle, and V. B. Valentine (2002), Rapid Wastage of Alaska Glaciers and Their Contribution to Rising Sea Level, *Science* (80), *297*, 382–386.
- Arnold, N., K. Richards, I. Willis, and M. Sharp (1998), Initial results from a distributed, physically based model of glacier hydrology, *Hydrol. Process.*, *12*, 191–219.
- Arnold, N. S., I. C. Willis, M. J. Sharp, K. S. Richards, and W. J. Lawson (1996), A distributed surface energy-balance model for a small valley glacier. I. Development and testing for Haut Glacier d’Arolla, Valais, Switzerland, *J. Glaciol.*, *42*(140), 77–89.
- Arnold, N. S., W. G. Rees, A. J. Hodson, and J. Kohler (2006), Topographic controls on the surface energy balance of a high Arctic valley glacier, *J. Geophys. Res.*, *111*, 1–15, doi:10.1029/2005JF000426.
- Bahr, D. B., M. Dyurgerov, and M. F. Meier (2009), Sea-level rise from glaciers and ice caps: A lower bound, *Geophys. Res. Lett.*, *36*, doi:10.1029/2008GL036309.

- Bartholomaeus, T. C., R. S. Anderson, and S. P. Anderson (2008), Response of glacier basal motion to transient water storage, *Nat. Geosci.*, *1*, 33–37, doi:10.1038/ngeo.2007.52.
- Bartholomew, I. D., P. Nienow, A. Sole, D. Mair, T. Cowton, M. A. King, and S. Palmer (2011), Seasonal variations in Greenland Ice Sheet motion: Inland extent and behaviour at higher elevations, *Earth Planet. Sci. Lett.*, *307*, 271–278, doi:10.1016/j.epsl.2011.04.014.
- Benn, D. I., and D. J. A. Evans (1998), *Glaciers & Glaciation*, Arnold, London.
- Berthier, E., and C. Vincent (2012), Relative contribution of surface mass-balance and ice-flux changes to the accelerated thinning of Mer de Glace, French Alps, over 1979 – 2008, *J. Glaciol.*, *58*(209), 501–512, doi:10.3189/2012JoG11J083.
- Berthier, E., Y. Arnaud, D. Baratoux, C. Vincent, and F. Rémy (2004), Recent rapid thinning of the “Mer de Glace” glacier derived from satellite optical images, *Geophys. Res. Lett.*, *31*, 2–5, doi:10.1029/2004GL020706.
- Bingham, R. G., P. W. Nienow, M. J. Sharp, and L. Copland (2006), Hydrology and dynamics of a polythermal (mostly cold) High Arctic glacier, *Earth Surf. Process. Landforms*, *31*, 1463–1479, doi:10.1002/esp.
- Bingham, R. G., A. L. Hubbard, P. W. Nienow, and M. J. Sharp (2008), An investigation into the mechanisms controlling seasonal speedup events at a High Arctic glacier, *J. Geophys. Res.*, *113*, 1–13, doi:10.1029/2007JF000832.
- Björnsson, H. (1979), Glaciers in Iceland, *Jökull*, *29*, 74–80.
- Björnsson, H. (1998), Hydrological characteristics of the drainage system beneath a surging glacier, *Nature*, *395*, 771–774.
- Björnsson, H. (2002), Subglacial lakes and jökulhlaups in Iceland, *Glob. Planet. Change*, *35*, 255–271.
- Björnsson, H., and P. Einarsson (1991), Volcanoes beneath Vatnajökull, Iceland: Evidence from radio echo-sounding, earthquakes and jökulhlaups, *Jökull*, *40*, 147–168.
- Björnsson, H., and F. Pálsson (2008), Icelandic glaciers, *Jökull*, *58*, 365–386.
- Björnsson, H., F. Pálsson, O. Sigurdsson, and G. E. Flowers (2003), Surges of glaciers in Iceland, *Ann. Glaciol.*, *36*, 82–90.
- Blatter, H., G. K. C. Clarke, and J. Colinge (1998), Stress and velocity fields in glaciers: Part II. Sliding and basal stress distribution, *J. Glaciol.*, *44*, 457–466.
- Boeckel, T. Van (2015), Relating Subglacial Water Flow to Surface Velocity Variations of Breiðamerkurjökull, Iceland *Published Masters Thesis*, University of Iceland
- Boon, S., and M. Sharp (2003), The role of hydrologically-driven ice fracture in drainage system evolution on an Arctic glacier, *Geophys. Res. Lett.*, *30*(18), doi:10.1029/2003GL018034.
- Boulton, G. S., and R. C. A. Hindmarsh (1987), Sediment deformation beneath glaciers: rheology and geological consequences, *J. Geophys. Res.*, *92*, 9059–9082.
- Boulton, G. S., and A. S. Jones (1979), Stability of Temperate Ice Caps and Ice Sheets Resting on Beds of Deformable Sediment, *J. Glaciol.*, *24*, 29–43.
- Boulton, G. S., K. E. Dobbie, and S. Zatsepin (2001), Sediment deformation beneath glaciers and its coupling to the subglacial hydraulic system, *Quat. Int.*, *86*, 3–28.
- Boulton, G. S., R. Lunn, P. Vidstrand, and S. Zatsepin (2007), Subglacial drainage by groundwater-channel coupling, and the origin of esker systems: Part 1 – glaciological observations, *Quat. Sci. Rev.*, *26*, 1067–1090, doi:10.1016/j.quascirev.2007.01.007.
- Bradwell, T., O. Sigurdsson, and J. Everest (2013), Recent, very rapid retreat of a temperate glacier in SE Iceland, *Boreas*, *42*, 959–973, doi:10.1111/bor.12014.
- Braithwaite, R. (1995), Aerodynamic stability and turbulent sensible-heat flux over a melting ice surface, the Greenland ice sheet, *J. Glaciol.*, *41*(139), 562–571.

- Braithwaite, R. J., and O. B. Olesen (1989), Calculation of Glacier Ablation from Air Temperature, West Greenland, in *Glacier fluctuations and climate change*, edited by J. Oerlemans, pp. 219–233, Kluwer Academic Publications.
- Braithwaite, R. J., T. Konzelmann, C. Marty, and O. B. Olesen (1998), Reconnaissance study of glacier energy balance in North Greenland, 1993–4, *J. Glaciol.*, 44(147), 239–247.
- Braun, L. N., M. Weber, and M. Schulz (2000), No Consequences of climate change for runoff from alpine regions, *Ann. Glaciol.*, 31, 19–25.
- Brock, B. W. (1997), Seasonal and spatial variations in the surface energy-balance of valley glaciers, PhD Thesis, University of Cambridge.
- Brock, B. W., and N. S. Arnold (2000), A spreadsheet-based (Microsoft Excel) point surface energy balance model for glacier and snow melt studies, *Earth Surf. Process. Landforms*, 25, 649–658.
- Brock, B. W., C. Mihalcea, M. P. Kirkbride, G. Diolaiuti, M. E. J. Cutler, and C. Smiraglia (2010), Meteorology and surface energy fluxes in the 2005–2007 ablation seasons at the Miage debris covered glacier, Mont Blanc Massif, Italian Alps, *J. Geophys. Res.*, 115, doi:10.1029/2009JD013224.
- Brown, R. J., C. Bonadonna, and A. J. Durant (2012), A review of volcanic ash aggregation, *Phys. Chem. Earth*, 45–46, 65–78, doi:10.1016/j.pce.2011.11.001.
- Carenzo, M., F. Pellicciotti, J. Mabillard, T. Reid, and B. W. Brock (2016), An enhanced temperature index model for debris-covered glaciers accounting for thickness effect, *Adv. Water Resour.*, 94, 457–469, doi:10.1016/j.advwatres.2016.05.001.
- Cerney, D. L. (2010), The Use of Repeat Photography in Contemporary Geomorphic Studies: An Evolving Approach to Understanding Landscape Change, *Geogr. Compass*, 1339–1357.
- Clark, P. U. (1994), Unstable Behavior of the Laurentide Ice Sheet over Deforming Sediment and Its Implications for Climate Change, *Quat. Res.*, 41, 19–25.
- Clark, P. U. (1995), Fast Glacier Flow Over Soft Beds, *Science (80-.)*, 267, 43–44.
- Clark, P. U., and J. Walder (1994), Subglacial drainage, eskers, and deforming beds beneath the Laurentide and Eurasian ice sheets, *Geol. Soc. Am. Bull.*, 106, 304–314, doi:10.1130/0016-7606(1994)106<0304.
- Clarke, G. K. C. (1987), Subglacial Till: A Physical Framework for Its Properties and Processes, *J. Geophys. Res.*, 92, 9023–9036.
- Cogley, J. G. (2009), Geodetic and direct mass-balance measurements: comparison and joint analysis, *Ann. Glaciol.*, 50(50), 96–100.
- Colbeck, S. C. (1973), *Theory of metamorphism of wet snow*, Cold Regions Research and Engineering Laboratory, New Hampshire, USA
- Colbeck, S. C. (1978), The physical aspects of water flow through snow, *Adv. Hydrosci.*, 11, 165–206.
- Copland, L., J. O. N. Harbor, S. Gordon, and M. Sharp (1997), The use of borehole video in investigating the hydrology of a temperate glacier, *Hydrol. Process.*, 11, 211–224.
- Copland, L., M. J. Sharp, and P. W. Nienow (2003), Links between short-term velocity variations and the subglacial hydrology of a predominantly cold polythermal glacier, *J. Glaciol.*, 49(166), 337–348.
- Copland, L., S. Pope, M. Bishop, J. Shroder, P. Clendon, A. Bush, U. Kamp, Y. Seong, and L. Owen (2009), Glacier velocities across the central Karakoram, *Ann. Glaciol.*, 50, 41–49.
- Corripio, J. G. (2004), Snow surface albedo estimation using terrestrial photography, *Int. J. Remote Sens.*, 20, 5705–5729, doi:10.1080/01431160410001709002.
- Covington, M. D., A. F. Banwell, J. Gulley, M. O. Saar, I. Willis, and C. M. Wicks (2012), Quantifying the effects of glacier conduit geometry and recharge on proglacial hydrograph form, *J. Hydrol.*, 414–415, 59–

- 71, doi:10.1016/j.jhydrol.2011.10.027.
- Cowton, T., P. Nienow, A. Sole, J. Wadham, G. Lis, I. Bartholomew, D. Mair, and D. Chandler (2013), Evolution of drainage system morphology at a land-terminating Greenlandic outlet glacier, *J. Geophys. Res. Earth Surf.*, *118*, 29–41, doi:10.1029/2012JF002540.
- Danielson, B., and M. Sharp (2013), Development and application of a time-lapse photograph analysis method to investigate the link between tidewater glacier flow variations and supraglacial lake drainage events, *J. Glaciol.*, *59*(214), 287–302, doi:10.3189/2013JG12J108.
- Delcamp, A., B. Van Wyk, D. Vries, and M. R. James (2008), The influence of edifice slope and substrata on volcano spreading, *J. Volcanol. Geotherm. Res.*, *177*, 925–943, doi:10.1016/j.jvolgeores.2008.07.014.
- Dietrich, R., H. Maas, M. Baessler, A. Rülke, A. Richter, E. Schwalbe, and P. Westfeld (2007), Jakobshavn Isbræ, West Greenland: Flow velocities and tidal interaction of the front area from 2004 field observations, *J. Geophys. Res.*, *112*, 1–16, doi:10.1029/2006JF000601.
- Duguay, C. (1993), Radiation Modeling in Mountainous Terrain Review and Status, *Mt. Res. Dev.*, *13*(4), 339–357, doi:10.2307/3673761.
- Dyurgerov, M. (2002), *Glacier Mass Balance and Regime: Data of Measurements and Analysis*, Institute of Arctic and Alpine Research, University of Colorado, 55.
- Dyurgerov, M. (2003), Mountain and subpolar glaciers show an increase in sensitivity to climate warming and intensification of the water cycle, *J. Hydrol.*, *282*, 164–176, doi:10.1016/S0022-1694(03)00254-3.
- Eiken, T., and M. Sund (2012), Photogrammetric methods applied to Svalbard glaciers: accuracies and challenges, *Polar Res.*, *31*, 1–16.
- Einarsson, M. A. (1984), Climate of Iceland, in *Climates of the Oceans*, edited by H. van Loon, pp. 673–697, Elsevier, Amsterdam.
- Elliston, G. R. (1973), Water movement through the Gornergletscher, *Symp. Hydrol. Glaciers*, *95*, 79–84.
- Engelhardt, M., T. V. Schuler, and L. M. Andreassen (2015), Sensitivities of glacier mass balance and runoff to climate perturbations in Norway, *Ann. Glaciol.*, *56*(70), 79–88, doi:10.3189/2015AoG70A004.
- Escher-Vetter, H. (1985), Energy balance calculations from five years' meteorological records at Vernagtferner, Oetztal Alps, *Zeitschrift für Gletscherkd. und Glazialgeol.*, *21*, 397–402.
- Evans, A. N. (2000), Glacier surface motion computation from digital image sequences, *IEEE Trans. Geosci. Remote Sens.*, *38*, 1064–1072.
- Evans, D. J. A., and D. R. Twigg (2002), The active temperate glacial landsystem: a model based on Breiðamerkurjökull and Fjallsjökull, Iceland, *Quat. Sci. Rev.*, *21*, 2143–2177.
- Evans, I. S. (1977), World-Wide Variations in the Direction and Concentration of Cirque and Glacier Aspects, *Geogr. Ann. Ser. A, Phys. Geogr.*, *59*, 151–175.
- Evans, I. S. (2006), Local aspect asymmetry of mountain glaciation: A global survey of consistency of favoured directions for glacier numbers and altitudes, *Geomorphology*, *73*, 166–184, doi:10.1016/j.geomorph.2005.07.009.
- Farinotti, D., J. Magnusson, M. Huss, and A. Bauder (2010), Snow accumulation distribution inferred from time-lapse photography and simple modelling, *Hydrol. Process.*, *24*, 2087–2097, doi:10.1002/hyp.7629.
- Fattahi, H., and F. Amelung (2014), InSAR uncertainty due to orbital errors, *Geophys. J. Int.*, *199*, 549–560, doi:10.1093/gji/ggu276.
- Fischer, U. H., G. K. C. Clarke, and H. Blatter (1999), Evidence for temporally varying “sticky spots” at the base of Trapridge Glacier, Yukon Territory, Canada, *J. Glaciol.*, *45*, 352–360.
- Flanner, M. G., K. M. Shell, M. Barlage, D. K. Perovich, and M. A. Tschudi (2011),

- Radiative forcing and albedo feedback from the Northern Hemisphere cryosphere between 1979 and 2008, *Nat. Geosci.*, 4, 151–155, doi:10.1038/ngeo1062.
- Flett, V., M. Kirkbride, J. Everest, A. Black, and A. MacDonald (in review), How changes in temperature and glacier hypsometry influence the short term response of a pro-glacial river, Virkisjökull, SE Iceland, *Hydrol. Res.*
- Flotron, A. (1973), Photogrammetrische Messung von Gletscherbewegungen mit automatischer Kamera, *Photogramm. Kult. Tech*, 71, 1–73.
- Flowers, G. E. (2008), Subglacial modulation of the hydrograph from glacierized basins, *Hydrol. Process.*, 22, 3903–3918, doi:10.1002/hyp.
- Flowers, G. E., and G. K. C. Clarke (2002), A multicomponent coupled model of glacier hydrology 2. Application to Trapridge Glacier, Yukon, Canada, *J. Geophys. Res.*, 107, doi:10.1029/2001JB001124.
- Fountain, A. G. (1992a), Subglacial hydraulics of South Cascade Glacier, Washington, PhD Thesis, University of Washington.
- Fountain, A. G., and W. V Tangborn (1985), The Effect of Glaciers on Streamflow Variations, *Water Resour. Res.*, 21(4), 579–586.
- Fountain, A. G., and J. S. Walder (1998), Water flow through temperate glaciers, *Rev. Geophys.*, 36(3), 299–328.
- Fountain, A. G., R. W. Jacobel, R. Schlichting, and P. Jansson (2005a), Fractures as the main pathways of water flow in temperate glaciers, *Nature*, 433, 618–621.
- Fountain, A. G., R. B. Schlichting, P. Jansson, and R. W. Jacobel (2005b), Observations of englacial water passages: a fracture-dominated system, *Ann. Glaciol.*, 40, 25–30.
- Fountain, A. G., J. L. Campbell, E. A. G. Schuur, S. E. Stammerjohn, M. W. Williams, and H. W. Ducklow (2012), The Disappearing Cryosphere: Impacts and Ecosystem Responses to Rapid Cryosphere Loss, *Bioscience*, 62(4), 405–415, doi:10.1525/bio.2012.62.4.11.
- Fugazza, D., A. Senese, R. S. Azzoni, C. Smiraglia, M. Cernuschi, D. Severi, and G. A. Diolaiuti (2015), High resolution mapping of glacier surface features. The UAV survey of the Forni Glacier (Stelvio National Park, Italy), *Geogr. Fis. e Dinamica Quat.*, 38, 25–33, doi:10.4461/GFDQ.2015.38.03.
- Funk, M., and H. Röthlisberger (1989), Forecasting the effects of a planned reservoir which will partially flood the tongue of Unteraargletscher in Switzerland, *Ann. Glaciol.*, 13, 76–81.
- Garvelmann, J., S. Pohl, and M. Weiler (2013), From observation to the quantification of snow processes with a time-lapse camera network, *Hydrol. Earth Syst. Sci.*, 17, 1415–1429, doi:10.5194/hess-17-1415-2013.
- Giesen, R. H., M. R. Van den Broeke, J. Oerlemans, and L. M. Andreassen (2008), Surface energy balance in the ablation zone of Middtdalsbreen, a glacier in southern Norway: Interannual variability and the effect of clouds, *J. Geophys. Res.*, 113, doi:10.1029/2008JD010390.
- Grainger, M. E., and H. Lister (1966), Wind speed, stability and eddy viscosity over melting ice surfaces, *J. Glaciol.*, 6, 101–127.
- Granger, R. J., and D. M. Gray (1990), A net radiation model for calculating daily snowmelt in open environments, *Nord. Hydrol.*, 21, 217–234.
- Greuell, W., and R. Böhm (1998), 2m temperatures along melting mid-latitude glaciers, and its implications for the sensitivity of the mass balance to variations in temperature, *J. Glaciol.*, 44(146), 9–20.
- Greuell, W., and J. Oerlemans (1986), Sensitivity studies with a mass balance model including temperature profile calculations inside the glacier, *Z. Gletscherkd. Glazialgeol.*, 22, 101–112.
- Gudmundsson, A. (1999), Fluid overpressure and stress drop in fault zones, *Geophys. Res. Lett.*, 26(1), 115–118.
- Gudmundsson, H. J. (1997), A review of the holocene environmental history of

- Iceland, *Quat. Sci. Rev.*, 16, 81–92.
- Guðmundsson, M. T. (2000), Mass balance and precipitation on the summit plateau of Öraefajökull, SE-Iceland, *Jökull*, 48, 49–54.
- Guðmundsson, S., H. Björnsson, E. Magnússon, E. Berthier, F. Pálsson, M. T. Guðmundsson, T. Högnadóttir, and J. Dall (2011), Response of Eyjafjallojökull, Torfajökull and Tindfjallajökull ice caps in Iceland to regional warming, deduced by remote sensing, *Polar Res.*, 1, 1–11, doi:10.3402/polar.v30i0.7282.
- Guðmundsson, M. T., T. Thordarson, A. Höskuldsson, G. Larsen, H. Björnsson, F. J. Prata, B. Oddsson, E. Magnússon, T. Högnadóttir, G. N. Petersen, C. L. Hayward, J. A. Stevenson, and I. Jónsdóttir (2012), Ash generation and distribution from the April-May 2010 eruption of Eyjafjallojökull, Iceland, *Scientific Reports.*, 2.
- Gulley, J. D., D. I. Benn, E. Screaton, and J. Martin (2009), Mechanisms of englacial conduit formation and their implications for subglacial recharge, *Quat. Sci. Rev.*, 28, 1984–1999, doi:10.1016/j.quascirev.2009.04.002.
- Haeberli, W., A. Käab, D. V. Mühll, and P. Treysseire (2001), Prevention of outburst floods from periglacial lakes at Grubengletscher, Valais, Swiss Alps, *J. Glaciol.*, 47(156), 111–122.
- Halberstam, I., and J. P. Schieldge (1981), Anomalous Behavior of the Atmospheric Surface Layer over a Melting Snowpack, *J. Appl. Meteorol.*, 20, 255–265.
- Hamilton, G. S., and I. M. Whillans (2000), Point measurements of mass balance of the Greenland Ice Sheet using precision vertical Global Positioning System (GPS) surveys, *J. Geophys. Res.*, 105, 16295–16301.
- Hannah, D. M., and A. M. Gurnell (2001), A conceptual, linear reservoir runoff model to investigate melt season changes in cirque glacier hydrology, *J. Hydrol.*, 246, 123–141.
- Harbor, J., M. Sharp, L. Copland, B. Hubbard, P. Nienow, and D. Mair (1997), Influence of subglacial drainage conditions on the velocity distribution within a glacier cross section, *Geology*, 25(8), 739–742.
- Harper, J. T., N. F. Humphrey, and W. T. Pfeffer (1998), Crevasse patterns and the strain-rate tensors: a high-resolution comparison, *J. Glaciol.*, 44(146), 68–76.
- Harrison, D., K. A. Echelmeyer, D. M. Cosgrove, and C. F. Raymond (1992), The determination of glacier speed by time-lapse photography under unfavorable conditions, *J. Glaciol.*, 38(129), 257–265.
- Harrison, W. D. (1972), Temperature measurements in a temperate glacier, *J. Glaciol.*, 14(73), 23–30.
- Harrison, W. D., C. F. Raymond, and P. MacKeith (1986), Short period motion events on Variegated Glacier as observed by automatic photography and seismic methods, *Ann. Glaciol.*, 8, 82–89.
- Hart, J. K., K. C. Rose, and K. Martinez (2011), Subglacial till behaviour derived from in situ wireless multi-sensor subglacial probes: Rheology, hydro-mechanical interactions and till formation, *Quat. Sci. Rev.*, 30, 234–247.
- Hock, R. (2005), Glacier melt: a review of processes and their modelling, *Prog. Phys. Geogr.*, 29(3), 362–391.
- Hock, R., and B. Holmgren (1996), Some Aspects of Energy Balance and Ablation of Storglaciären, Northern Sweden, *Geogr. Ann. Ser. A, Phys. Geogr.*, 78, 121–131.
- Hock, R., and P. Jansson (2005), Modelling glacier hydrology, in *Encyclopedia of Hydrological Sciences*, edited by M. G. Anderson and J. McDonnell, pp. 2647–2655, Wiley & Sons Ltd, Chichester.
- Hock, R., and C. Noetzli (1997), Areal melt and discharge modelling of Storglaciären, Sweden, *Ann. Glaciol.*, 24, 211–216.
- Hock, R., A. Iken, and A. Wangler (1999), Tracer experiments and borehole observations in the over-deepening of Aletschgletscher, Switzerland, in *Annals of Glaciology*, edited by J. Kleman, pp. 253–260, International Glaciological Society, Cambridge.

- Hock, R., P. Jansson, and L. Braun (2005), Modelling the response of mountain glacier discharge to climate warming, in *Global Change and Mountain Regions—A State of Knowledge Overview*, edited by U. M. Huber, M. A. Reasoner, and H. Bugmann, pp. 243–252, Springer, Dordrecht.
- Hock, R., V. Radic, and M. de Woul (2007), Climate sensitivity of Storglaciären, Sweden: an intercomparison of mass-balance models using ERA-40 re-analysis and regional climate model data, *Ann. Glaciol.*, 46, 342–348.
- Hock, R., M. de Woul, V. Radic, and M. Dyurgerov (2009), Mountain glaciers and ice caps around Antarctica make a large sea-level rise contribution, *Geophys. Res. Lett.*, 36, doi:10.1029/2008GL037020.
- Hodgkins, R. (1997), Glacier hydrology in Svalbard, Norwegian High Arctic, *Quat. Sci. Rev.*, 16, 957–973.
- Hoelzle, M., W. Haeberli, M. Dischl, and W. Peschke (2003), Secular glacier mass balances derived from cumulative glacier length changes, *Glob. Planet. Change*, 36, 295–306, doi:10.1016/S0921-8181(02)00223-0.
- Hooke, R. L. B. (1989), Englacial and Subglacial Hydrology: A Qualitative Review, *Arct. Alp. Res.*, 21(3), 221–233.
- Hooke, R. L. B., P. Calla, P. Holmlund, M. Nilsson, and A. Stroeven (1989), A 3 year record of seasonal variations in surface velocity, Storglaciären, Sweden, *J. Glaciol.*, 35, 235–247.
- Hooke, R. L. B., T. Laumann, and J. Kohler (1990), Subglacial water pressures and the shape of subglacial conduits, *J. Glaciol.*, 36(122), 67–71.
- Hooke, R. L. B., V. A. Pohjola, P. Jansson, and J. Kohler (1992), Intra-seasonal changes in deformation profiles revealed by borehole studies, Storglaciären, Sweden, *J. Glaciol.*, 38, 348–358.
- Howat, I. M., S. Tulaczyk, E. Waddington, and H. Björnsson (2008), Dynamic controls on glacier basal motion inferred from surface ice motion, *J. Geophys. Res.*, 113.
- Hubbard, B., and P. Nienow (1997), Alpine subglacial hydrology, *Quat. Sci. Rev.*, 16, 939–955.
- Hubbard, B. P., M. J. Sharp, I. C. Willis, M. K. Nielsen, and G. C. Smart (1995), Borehole water-level variations and the structure of the subglacial hydrological system of Haut Glacier d’Arolla, Valais, Switzerland, *J. Glaciol.*, 41(139), 572–583.
- Humphrey, N. F., C. F. Raymond, and W. D. Harrison (1986), Discharges of Turbid Water during Mini-Surges of Variegated Glacier, Alaska, U.S.A., *J. Glaciol.*, 32(111), 195–207.
- Iken, A. (1981), The effect of the subglacial water pressure on the sliding velocity of a glacier in an idealized numerical model, *J. Glaciol.*, 29, 407–421.
- Iken, A., and R. A. Binschadler (1986), Combined measurements of subglacial water pressure and surface velocity of Findelengletscher, Switzerland: conclusions about drainage system and sliding mechanism, *J. Glaciol.*, 32, 101–119.
- Iken, A., H. Röthlisberger, A. Flotron, and W. Haeberli (1983), The uplift of Unteraargletscher at the beginning of the melt season - a consequence of water storage at the bed?, *J. Glaciol.*, 29(101), 28–47.
- Illangasekare, T. H., R. J. Walter, M. F. Meier, and W. T. Pfeffer (1990), Modeling of Meltwater Infiltration in Subfreezing Snow, *Water Res.*, 26(5), 1001–1012.
- IPCC (2013), Summary for Policymakers, in *Climate Change 2013: The Physical Science Basis. Contribution of Working Group 1 to the Fifth Assessment Report of the Intergovernmental Panel on Climate Change*, edited by T. F. Stocker, D. Qin, G. Plattner, M. Tignor, S. K. Allen, J. Boschung, A. Nauels, Y. Xia, V. Bex, and P. M. Midgley, Cambridge University Press.
- Irvine-fynn, T. D. L., A. J. Hodson, B. J. Moorman, G. Vatne, and A. L. Hubbard (2011), Polythermal glacier hydrology: A review, *Rev. Geophys.*, 49, 1–37, doi:10.1029/2010RG000350.

- Irvine-fynn, T. D. L., E. Sanz-Ablanedo, N. Rutter, M. W. Smith, and J. H. Chandler (2014), Measuring glacier surface roughness using plot-scale, close-range digital photogrammetry, *J. Glaciol.*, 60(223), 957–969, doi:10.3189/2014JogG14J032.
- Iverson, N. R., B. Hanson, R. L. Hooke, and P. Jansson (1995), Flow Mechanism of Glaciers on Soft Beds, *Science.*, 80(267), 80–81.
- James, M. R., and S. Robson (2014), ISPRS Journal of Photogrammetry and Remote Sensing Sequential digital elevation models of active lava flows from ground-based stereo time-lapse imagery, *ISPRS J. Photogramm. Remote Sens.*, 97, 160–170, doi:10.1016/j.isprsjprs.2014.08.011.
- James, M. R., P. How, and P. M. Wynn (2016), Pointcatcher software: analysis of glacial time-lapse photography and integration with multitemporal digital elevation models, *J. Glaciol.*, 1–11, doi:10.1017/jog.2016.27.
- Jansson, P., and R. L. B. Hooke (1989), Short-term variations in strain and surface tilt on Storglaciären, Kebnekaise, Northern Sweden, *J. Glaciol.*, 35, 201–208.
- Jansson, P., R. Hock, and T. Schneider (2003), The concept of glacier storage: a review, *J. Hydrol.*, 282, 116–129, doi:10.1016/S0022-1694(03)00258-0.
- Jóhannesson, T., and O. Sigurðsson (1998), Interpretation of glacier variations in Iceland 1930-1995, *Jökull*, 45, 27–34.
- Kamb, B. (1970), Sliding Motion of Glaciers: Theory and Observation, *Rev. Geophys. Sp. Phys.*, 8(4), 673–728.
- Kamb, B. (1987), Glacier Surge Mechanism Based on Linked Cavity Configuration of the Basal Water Conduit System, *J. Geophys. Res.*, 92, 9083–9100.
- Kamb, B. (1991), Rheological Nonlinearity and Flow Instability in the Deforming Bed Mechanism of Ice Stream Motion, *J. Geophys. Res.*, 96, 16585–16595.
- Kamb, B., H. Engelhardt, M. A. Fahnestock, N. Humphrey, M. Meier, and D. Stone (1994), Mechanical and hydrologic basis for the rapid motion of a large tidewater glacier: 2. Interpretation, *J. Geophys. Res.*, 99, 15231–15244.
- Kayastha, R. B., Y. Takeuchi, M. Nakawo, and Y. Ageta (2000), Practical prediction of ice melting beneath various thickness of debris cover on Khumbu Glacier, Nepal, using a positive degree-day factor, in *Debris-Covered Glaciers*, pp. 71–81, IAHS, Seattle, Washington.
- Kehrl, L. M., H. J. Horgan, B. M. Anderson, R. Dadić, and A. N. Mackintosh (2015), Glacier velocity and water input variability in a maritime environment: Franz Josef Glacier, New Zealand, *J. Glaciol.*, 61(228), 663–674.
- Khan, S. A., J. Wahr, E. Leuliette, T. Van Dam, K. M. Larson, and O. Francis (2008), Geodetic measurements of postglacial adjustments in Greenland, *J. Geophys. Res.*, 113, doi:10.1029/2007JB004956.
- King, M. (2004), Rigorous GPS data-processing strategies for glaciological applications, *J. Glaciol.*, 50, 601–607.
- Kirkbride, M. P., and S. Winkler (2012), Correlation of Late Quaternary moraines: impact of climate variability, glacier response, and chronological resolution, *Quat. Sci. Rev.*, 46, 1–29, doi:10.1016/j.quascirev.2012.04.002.
- Kjær, K. H., and J. Krüger (2001), The final phase of dead-ice moraine development: processes and sediment architecture, Kötlujökull, Iceland, *Sedimentology*, 48, 935–952.
- Kjær, K. H., N. J. Korsgaard, and A. Schomacker (2008), Impact of multiple glacier surges — a geomorphological map from Brúarjökull, East Iceland, *J. Maps*, 4(1), 5–20, doi:10.4113/jom.2008.91.
- Klok, E. J., and J. Oerlemans (2002), Model study of the spatial distribution of the energy and mass balance of Morteratschgletscher, Switzerland, *J. Glaciol.*, 48(163), 505–518.
- Klok, E. J., and J. Oerlemans (2004), Modelled climate sensitivity of the mass balance of Morteratschgletscher and its dependence on albedo parameterization, *Int. J. Climatol.*, 24, 231–245, doi:10.1002/joc.994.

- Kuhn, M. (1989), The response of the equilibrium line altitude to climate fluctuations: theory and observations, in *Glacier Fluctuations and Climate Change*, edited by J. Oerlemans, pp. 407–417, Kluwer.
- Lang, H. (1967), Über den Tagesgang im Gletscherabfluss, *Schweizerischen Meteorol. Zentralanstalt*, 4, 32–38.
- Laumann, T., and N. Reeh (1993), Sensitivity to climate change of the mass balance of glaciers in southern Norway, *J. Glaciol.*, 39(133), 656–665.
- Leprince, S., F. Ayoub, Y. Klinger, and J.-P. Avouac (2007), Co-Registration of Optically Sensed Images and Correlation (COSI-Corr): an Operational Methodology for Ground Deformation Measurements, pp. 1943–1946, IEEE International Geoscience and Remote Sensing Symposium, Barcelona.
- Lüthi, M. P., and M. Funk (2001), Modelling heat flow in a cold, high-altitude glacier: interpretation of measurements from Colle Gnifetti, Swiss Alps, *J. Glaciol.*, 47(157), 314–324.
- Maas, H.-G., D. Schneider, E. Schwalbe, G. Cassasa, and A. Wendt (2010), Photogrammetric determination of spatio-temporal velocity fields at Glacier San Rafael in the Northern Patagonian Icefield, *Int. Arch. Photogramm. Remote Sens. Spat. Inf. Sci.*, 48(5), 417–421.
- Mair, D., I. Willis, U. H. Fischer, B. Hubbard, P. Nienow, and A. Hubbard (2003), Hydrological controls on patterns of surface, internal and basal motion during three spring events: Haut Glacier d’Arolla, Switzerland, *J. Glaciol.*, 49, 555–567.
- Mair, D., B. Hubbard, P. Nienow, I. Willis, and U. H. Fischer (2008), Diurnal fluctuations in glacier ice deformation: Haut Glacier d’Arolla, Switzerland, *Earth Surf. Process. Landforms*, 33, 1272–1284, doi:10.1002/esp.
- Male, D. (1980), The seasonal snowcover, in *Dynamics of Snow and Ice Masses*, edited by S. C. Colbeck, pp. 305–395, Academic, San Diego.
- Manson, R., R. Coleman, P. Morgan, and M. King (2000), Ice velocities of the Lambert Glacier from static GPS observations, *Earth Planets Sp.*, 52, 1031–1036.
- Maohuan, H. (1990), On the temperature distribution of glaciers in China, *J. Glaciol.*, 36(123), 210–216.
- Marcus, M. G., R. D. Moore, and I. F. Owens (1985), Short-term estimates of surface energy transfers and ablation on the lower Franz Josef Glacier, South Westland, New Zealand, *New Zeal. J. Geol. Geophys.*, 28(3), 559–567, doi:10.1080/00288306.1985.10421208.
- Mattson, L. E., J. S. Gardner, and G. J. Young (1993), Ablation on Debris Covered Glaciers: an Example from the Rakhiot Glacier, Punjab, Himalaya, in *Snow and Glacier Hydrology*, pp. 289–296, IAHS, Kathmandu.
- Meier, M. F., M. B. Dyurgerov, U. K. Rick, S. O’Neel, W. T. Pfeffer, R. S. Anderson, S. P. Anderson, and A. F. Glazovsky (2007), Glaciers Dominate Eustatic Sea-Level Rise in the 21st Century, *Science.*, 80(317), 1064–1068.
- Messerli, A., and A. Grinsted (2015), Image georectification and feature tracking toolbox: ImGRAFT, *Geosci. Instrum. Methods Data Syst.*, 4, 23–34, doi:10.5194/gi-4-23-2015.
- Miles, B. W. J., C. R. Stokes, A. Vieli, and N. J. Cox (2013), Rapid, climate-driven changes in outlet glaciers on the Pacific coast of East Antarctica, *Nature*, 500, 563–566, doi:10.1038/nature12382.
- Miller, R. D., and D. R. Crandell (1959), Time-lapse motion picture technique applied to the study of geological processes, *Science.*, 80(130), 795–796.
- Minchew, B., M. Simons, S. Hensley, H. Björnsson, and F. Pálsson (2016), Early melt season velocity fields of Langjökull and Hofsjökull, central Iceland, *J. Glaciol.*, 61(226), 253–266, doi:10.3189/2015JG14J023.
- Möller, R., M. Möller, H. Björnsson, S. Gudmundsson, F. Pálsson, B. Oddsson, P. A. Kukla, and C. Schneider (2014), MODIS-derived albedo changes of Vatnajökull (Iceland) due to tephra

- deposition from the 2004 Grímsvötn eruption, *Int. J. Appl. Earth Obs. Geoinf.*, 26, 256–269, doi:10.1016/j.jag.2013.08.005.
- Möller, R., M. Möller, P. A. Kukla, and C. Schneider (2016), Impact of supraglacial deposits of tephra from Grímsvötn volcano, Iceland, on glacier ablation, *J. Glaciol.*, 1–11, doi:10.1017/jog.2016.82.
- Mouginot, J., E. Rignot, and B. Scheuchl (2014), Sustained increase in ice discharge from the Amundsen Sea Embayment, West Antarctica, from 1973 to 2013, *Geophys. Res. Lett.*, 41, 1–9, doi:10.1002/2013GL059069.1.
- Munro, D. S. (1989), Surface roughness and bulk heat transfer on a glacier: comparison with eddy correlation, *J. Glaciol.*, 35, 153–162.
- Munro, D. S. (1990), Comparison of Melt Energy Computations and Ablatometer Measurements on Melting Ice and Snow, *Arct. Alp. Res.*, 22(2), 153–162.
- Munro, D. S. (1991), A surface energy exchange model of glacier melt and net mass balance, *Int. J. Climatol.*, 11, 689–700.
- Munro, D. S. (2010), Runoff response time of a loosely defined supraglacial microbasin, *Hydrol. Earth Syst. Sci. Discuss.*, 7, 1569–1587.
- Munro, D. S., and J. A. Davies (1977), An experimental study of the glacier boundary layer over melting ice, *J. Glaciol.*, 18(80), 425–436.
- Munro, D. S., and G. J. Young (1982), An Operational Net Shortwave Radiation Model for Glacier Basins, *Water Resour. Res.*, 18(2), 220–230.
- Murray, T. (1994), Glacial Deformation, in *The Geological Deformation of Sediment*, edited by A. J. Maltman, pp. 73–93, Chapman and Hall, London.
- Murray, T. (1997), Assessing the paradigm shift: deformable glacier beds, *Quat. Sci. Rev.*, 16, 995–1016.
- Naruse, R., and P. Skvarca (2000), Dynamic Features of Thinning and Retreating Glacier Upsala, a Lacustrine Calving Glacier in Southern Patagonia, *Arctic, Antarct. Alp. Res.*, 32(4), 485–491.
- Nicholson, L., and D. I. Benn (2006), Calculating ice melt beneath a debris layer using meteorological data, *J. Glaciol.*, 52(178), 463–470.
- Nienow, P., M. Sharp, and I. Willis (1998), Seasonal changes in the morphology of the subglacial drainage system, Haut Glacier d’Arolla, Switzerland, *Earth Surf. Process. Landforms*, 23, 825–843.
- Nienow, P. W., A. L. Hubbard, B. P. Hubbard, D. M. Chandler, D. W. F. Mair, M. J. Sharp, and I. C. Willis (2005), Hydrological controls on diurnal ice flow variability in valley glaciers, *J. Geophys. Res.*, 110, doi:10.1029/2003JF000112.
- Nuth, C., and A. Kääb (2011), Co-registration and bias corrections of satellite elevation data sets for quantifying glacier thickness change, *Cryosph.*, 5, 271–290, doi:10.5194/tc-5-271-2011.
- Oerlemans, J. (1992), Climate sensitivity of glaciers in southern Norway: application of an energy-balance model to Nigardsbreen, Hellstugubreen and Alftobreen, *J. Glaciol.*, 38(129), 223–232.
- Oerlemans, J. (1993), A model for the surface balance of ice masses: Part 1, Alpine glaciers, *Z. Gletscherkd. Glazialgeol.*, 27–28, 63–83.
- Oerlemans, J., and N. C. Hoogendoorn (1989), Mass-balance gradients and climatic change, *J. Glaciol.*, 35(121), 399–405.
- Oerlemans, J., and E. J. Klok (2002), Energy Balance of a Glacier Surface: Analysis of Automatic Weather Station Data from the Morteratschgletscher, Switzerland, *Arctic, Antarct. Alp. Res.*, 34(4), 477–485.
- Oerlemans, J., M. Dyurgerov, and R. S. W. Van de Wal (2007), Reconstructing the glacier contribution to sea-level rise back to 1850, *Cryosph.*, 1, 59–65.
- Olyphant, G. A. (1986a), Longwave Radiation in Mountainous Areas and Its Influence on the Energy Balance of Alpine Snowfields, *Water Resour. Res.*, 22(1), 62–66.
- Olyphant, G. A. (1986b), The Components of

- Incoming Radiation within a Mid-Latitude Alpine Watershed during the Snowmelt Season, *Arct. Alp. Res.*, 18(2), 163–169.
- Østrem, G. (1959), Ice Melting under a Thin Layer of Moraine and the Existence of Ice Cores in Moraine Ridges, *Geogr. Ann.*, 41, 228–230.
- Pagli, C., F. Sigmundsson, B. Lund, E. Sturkell, H. Geirsson, P. Einarsson, T. Árnadóttir, and S. Hreinsdóttir (2007), Glacio-isostatic deformation around the Vatnajökull ice cap, Iceland, induced by recent climate warming: GPS observations and finite element modeling, *J. Geophys. Res.*, 112, doi:10.1029/2006JB004421.
- Paterson, W. S. B. (1994), *The Physics of Glaciers*, Elsevier, Oxford.
- Patton, H., A. Hubbard, T. Bradwell, N. F. Glasser, M. J. Hambrey, and C. D. Clark (2013), Rapid marine deglaciation: asynchronous retreat dynamics between the Irish Sea Ice Stream and terrestrial outlet glaciers, *Earth Surf. Dyn.*, 1, 53–65, doi:10.5194/esurf-1-53-2013.
- Paul, F., and W. Haeberli (2008), Spatial variability of glacier elevation changes in the Swiss Alps obtained from two digital elevation models, *Geophys. Res. Lett.*, 35, 1–5, doi:10.1029/2008GL034718.
- van Pelt, W. J. J., J. Oerlemans, C. H. Reijmer, V. A. Pohjola, R. Pettersson, and J. H. Van Angelen (2012), Simulating melt, runoff and refreezing on Nordenskiöldbreen, Svalbard, using a coupled snow and energy balance model, *Cryosph.*, 6, 641–659, doi:10.5194/tc-6-641-2012.
- Petersen, G. N., H. Björnsson, P. Arason, and S. von Löwis (2012), Two weather radar time series of the altitude of the volcanic plume during the May 2011 eruption of Grímsvötn, Iceland, *Earth Syst. Sci. Data*, 4, 121–127, doi:10.5194/essd-4-121-2012.
- Phillips, E., A. Finlayson, and L. Jones (2013), Fracturing, block faulting, and moulin development associated with progressive collapse and retreat of a maritime glacier: Falljökull, SE Iceland, *J. Geophys. Res. Earth Surf.*, 118, 1545–1561, doi:10.1002/jgrf.20116.
- Phillips, E., A. Finlayson, T. Bradwell, J. Everest, and L. Jones (2014), Structural evolution triggers a dynamic reduction in active glacier length during rapid retreat: Evidence from Falljökull, SE Iceland, *J. Geophys. Res. Earth Surf.*, 119, 2194–2208, doi:10.1002/2014JF003165. Received.
- Pimentel, S., and G. E. Flowers (2010), A numerical study of hydrologically driven glacier dynamics and subglacial flooding, *Proc. R. Soc. A*, 467, 537–558, doi:10.1098/rspa.2010.0211.
- Plüss, C., and A. Ohmura (1997), Longwave Radiation on Snow-Covered Mountainous Surfaces, *J. Appl. Meteorology*, 36, 818–824.
- Pohjola, V. A. (1993), TV-video observations of bed and basal sliding on Storglaciären, Sweden, *J. Glaciol.*, 39, 111–118.
- Quincey, D. J., and N. F. Glasser (2009), Morphological and ice-dynamical changes on the Tasman Glacier, New Zealand, 1990–2007, *Glob. Planet. Change*, 68(3), 185–197, doi:10.1016/j.gloplacha.2009.05.003.
- Quincey, D. J., and A. Luckman (2009), Progress in satellite remote sensing of ice sheets, *Prog. Phys. Geogr.*, 33(4), 547–567, doi:10.1177/0309133309346883.
- Radic, V., and R. Hock (2011), Regionally differentiated contribution of mountain glaciers and ice caps to future sea-level rise, *Nat. Geosci.*, 4, 91–94, doi:10.1038/ngeo1052.
- Raper, S. C. B., and R. J. Braithwaite (2006), Low sea level rise projections from mountain glaciers and icecaps under global warming, *Nature*, 439, 311–313, doi:10.1038/nature04448.
- Raper, S. C. B., and R. J. Braithwaite (2009), Glacier volume response time and its links to climate and topography based on a conceptual model of glacier hypsometry, *Cryosph.*, 3, 183–194.
- Raymond, C. F., R. J. Benedict, W. D. Harrison, K. A. Echelmeyer, and M. Sturm (1995), Hydrological discharges and motion of Fels and Black Rapids Glaciers, Alaska, U.S.A.: implications for the structure of their drainage systems, *J. Glaciol.*, 41(138),

- 290–304.
- Reid, T. D., and B. W. Brock (2010), An energy-balance model for debris-covered glaciers including heat conduction through the debris layer, *J. Glaciol.*, *56*(199), 903–916.
- Rignot, E., J. Mouginot, and B. Scheuchl (2011), Ice Flow of the Antarctic Ice Sheet, *Science.*, *80*(33), 1427–1430, doi:10.1126/science.1208336.
- Robertson, C. M., M. S. Brook, K. A. Holt, I. C. Fuller, and D. I. Benn (2013), Calving retreat and proglacial lake growth at Hooker Glacier, Southern Alps, New Zealand, *N. Z. Geog.*, *69*, 14–25, doi:10.1111/nzg.12001.
- Rosen, P. A., S. Hensley, G. Peltzer, and M. Simons (2004), Updated Repeat Orbit Interferometry Package Released, *Eos (Washington. DC.)*, *85*, 47.
- Röthlisberger, H. (1972), Water pressure in intra- and subglacial channels, *J. Glaciol.*, *11*, 177–203.
- Röthlisberger, H., and H. Lang (1987), Glacial hydrology, in *Glacio fluvial sediment transfer: an alpine perspective*, edited by A. M. Gurnell and M. J. Clark, pp. 207–284, John Wiley and Sons.
- Salinger, J., T. Chinn, A. Willsman, and B. Fitzharris (2008), Glacier response to climate change, *Water Atmos.*, *16*(3), 16–17.
- Scambos, T. A., M. J. Dutkiewicz, J. C. Wilson, and R. A. Bindshadler (1992), Application of Image Cross-Correlation to the Measurement of Glacier Velocity Using Satellite Image Data, *Remote Sens. Environ.*, *42*, 177–186.
- Schomacker, A., Í. Ö. Benediktsson, Ó. Ingólfsson, B. Friis, N. J. Korsgaard, K. H. Kjær, and J. K. Keiding (2012), Late Holocene and modern glacier changes in the marginal zone of Sólheimajökull, South Iceland, *Jökull*, *62*, 111–130.
- Schomacker, A., I. O. Benediktsson, and Ó. Ingólfsson (2014), The Eyjabakkajökull glacial landsystem, Iceland: Geomorphic impact of multiple surges, *Geomorphology*, *218*, 98–107, doi:10.1016/j.geomorph.2013.07.005.
- Schubert, A., A. Faes, A. Käab, and E. Meier (2013), Glacier surface velocity estimation using repeat TerraSAR-X images: Wavelet- vs. correlation-based image matching, *ISPRS J. Photogramm. Remote Sens.*, *82*, 49–62, doi:10.1016/j.isprsjprs.2013.04.010.
- Schuler, T., U. H. Fischer, and G. H. Gudmundsson (2004), Diurnal variability of subglacial drainage conditions as revealed by tracer experiments, *J. Geophys. Res.*, *109*, doi:10.1029/2003JF000082.
- Schwalbe, E., H.-G. Maas, R. Dietrich, and H. Ewert (2008), Glacier velocity determination from multi temporal terrestrial long range laser scanner point clouds, *Int. Arch. Photogramm. Remote Sens. Spat. Inf. Sci.*, *36*(B5), 457–462.
- Schwalbe, E., R. Koschitzki, and H.-G. Maas (2016), Recognition of drainage tunnels during glacier lake outburst events from terrestrial image sequences, vol. XLI, pp. 537–543, The International Archives of the Photogrammetry, Remote Sensing and Spatial Information Sciences, Prague, Czech Republic.
- Sevestre, H., and D. I. Benn (2015), Climatic and geometric controls on the global distribution of surge-type glaciers: implications for a unifying model of surging, *J. Glaciol.*, *61*(228), 646–662, doi:10.3189/2015JG14J136.
- Sharp, M. J., J. C. Gemmell, and J.-L. Tison (1989), Structure and stability of the former subglacial drainage system of the glacier de Tsanfleuron, Switzerland, *Earth Surf. Process. Landforms*, *14*, 119–134.
- Sharp, M. J., K. Richards, I. Willis, N. Arnold, P. Nienow, W. Lawson, and J.-L. Tison (1993), Geometry, bed topography and drainage system structure of the Haut Glacier d’Arolla, Switzerland, *Earth Surf. Process. Landforms*, *18*, 557–572.
- Shi, Y., and S. Liu (2000), Estimation on the response of glaciers in China to the global warming in the 21st century, *Chinese Sci. Bull.*, *45*(7), 668–672.
- Shreve, R. L. (1972), Movement of water in glaciers, *J. Glaciol.*, *11*(62), 205–214.

- Shreve, R. L. (1985), Esker characteristics in terms of glacier physics, Katahdin esker system, Maine, *Geol. Soc. Am. Bull.*, 96, 639–646.
- Sicart, J. E., J. W. Pomeroy, R. L. H. Essery, and D. Bewley (2006), Incoming longwave radiation to melting snow: observations, sensitivity and estimation in northern environments, *Hydrol. Process.*, 20, 3697–3708, doi:10.1002/hyp.
- Sicart, J. E., R. Hock, P. Ribstein, M. Litt, and E. Ramirez (2011), Analysis of seasonal variations in mass balance and meltwater discharge of the tropical Zongo Glacier by application of a distributed energy balance model, *J. Geophys. Res.*, 116, doi:10.1029/2010JD015105.
- Sigurðsson, O. (1998), Glacier variations in Iceland 1930–1995: from the database of the Iceland Glaciological Society, *Jökull*, 45, 3–25.
- Sigurðsson, O. (2005), Variations of termini of glaciers in Iceland in recent centuries and their connection with climate, in *Iceland – Modern Processes and Past Environments*, edited by C. Caseldine, A. Russell, J. Hardardottir, and O. Knudsen, pp. 241–255, Elsevier, Amsterdam.
- Sigurðsson, O., and R. S. Williams (2008), *Geographic names of Icelandic glaciers: historic and modern*, US Geological Survey Professional Paper, 1746, 225.
- Sigurðsson, O., T. Jonsson, and T. Jóhannesson (2007), Relation between glacier-termini variations and summer temperatures in Iceland since 1930, *Ann. Glaciol.*, 42, 395–401.
- Singh, P., G. Spitzbart, H. Hübl, and H. W. Weinmeister (1997), Hydrological response of snowpack under rain-on-snow events: a field study, *J. Hydrol.*, 202.
- Sole, A., P. Nienow, I. Bartholomew, D. Mair, T. Cowton, A. Tedstone, and M. A. King (2013), Winter motion mediates dynamic response of the Greenland Ice Sheet to warmer summers, *Geophys. Res. Lett.*, 40, 3940–3944, doi:10.1002/grl.50764.
- Sole, A. J., D. W. F. Mair, P. W. Nienow, I. D. Bartholomew, M. A. King, M. J. Burke, and I. Joughin (2011), Seasonal speedup of a Greenland marine-terminating outlet glacier forced by surface melt-induced changes in subglacial hydrology, *J. Geophys. Res.*, 116, doi:10.1029/2010JF001948.
- Sorg, A., A. Kääb, A. Roesch, C. Bigler, and M. Stoffel (2015), Contrasting responses of Central Asian rock glaciers to global warming, *Sci. Rep.*, 5, doi:10.1038/srep08228.
- Stenborg, T. (1970), Delay of Run-Off from a Glacier Basin, *Geogr. Ann. Ser. A, Phys. Geogr.*, 52(1), 1–30.
- Stenborg, T. (1973), Some viewpoints on the internal drainage of glaciers, *IAHS Publ.*, 95, 117–129.
- Sugiyama, S., and G. H. Gudmundsson (2003), Diurnal variations in vertical strain observed in a temperate valley glacier, *Geophys. Res. Lett.*, 30(2), doi:10.1029/2002GL016160.
- Sugiyama, S., K. Fukui, K. Fujita, K. Tone, and S. Yamaguchi (2013), Changes in ice thickness and flow velocity of Yala Glacier, Langtang Himal, Nepal, from 1982 to 2009, *Ann. Glaciol.*, 54(64), 157–162, doi:10.3189/2013AoG64A111.
- Sundal, A. V., A. Shepherd, P. Nienow, E. Hanna, S. Palmer, and P. Huybrechts (2011), Melt-induced speed-up of Greenland ice sheet offset by efficient subglacial drainage, *Nature*, 469, 521–524, doi:10.1038/nature09740.
- Tangborn, W. V., R. M. Krimmel, and M. F. Meier (1975), *A comparison of glacier mass balance by glacier hydrology and mapping methods*, South Cascade Glacier, Snow and Ice - Symposium -- Neiges et Glaces, 185–196.
- Tedstone, A. J., P. W. Nienow, A. J. Sole, D. W. F. Mair, T. R. Cowton, I. D. Bartholomew, and M. A. King (2013), Greenland ice sheet motion insensitive to exceptional meltwater forcing, *Proc. Natl. Acad. Sci. U.S.A.*, 110(49), 19719–24.
- Thomas, R., B. Scheuchl, E. Frederick, R. Harpold, C. Martin, and E. Rignot (2013), Continued slowing of the Ross Ice Shelf and thickening of West Antarctic ice streams, *J. Glaciol.*, 59(217), 838–844.

- doi:10.3189/2013JoG12J122.
- Thompson, C. (2016), Identifying the Drivers of Glacier Melt in Southern Iceland, Unpublished Masters Thesis, Lancaster University.
- Thompson, S. S., D. I. Benn, K. Dennis, and A. Luckman (2012), A rapidly growing moraine-dammed glacial lake on Ngozumpa Glacier, Nepal, *Geomorphology*, 145-146, 1-11, doi:10.1016/j.geomorph.2011.08.015.
- Tranter, M., G. Brown, R. Raiswell, M. Sharp, and A. Gurnell (1993), A conceptual model of solute acquisition by Alpine glacial meltwater, *J. Glaciol.*, 39, 573-581.
- Tsutaki, S., D. Nishimura, T. Yoshizawa, and S. Sugiyama (2011), Changes in glacier dynamics under the influence of proglacial lake formation in Rhonegletscher, Switzerland, *Ann. Glaciol.*, 52(58), 31-36.
- Tsutaki, S., S. Sugiyama, D. Nishimura, and M. Funk (2013), Acceleration and flotation of a glacier terminus during formation of a proglacial lake in Rhonegletscher, Switzerland, *J. Glaciol.*, 59(215), 559-570, doi:10.3189/2013JoG12J107.
- Van der Veen, C. J. (2007), Fracture propagation as means of rapidly transferring surface meltwater to the base of glaciers, *Geophys. Res. Lett.*, 34, doi:10.1029/2006GL028385.
- Vernier, F., R. Fallourd, J. M. Friedt, Y. Yan, E. Trouvé, J. Nicolas, and L. Moreau (2011), Fast correlation technique for glacier flow monitoring by digital camera and space-borne SAR images, *EURASIP J. Image Video Process.*, 11.
- Vernier, F., R. Fallourd, J. Friedt, Y. Yan, E. Trouvé, J. Nicolas, and L. Moreau (2012), Glacier flow monitoring by digital camera and space-borne SAR images, *Image Process. Theory, Tools Appl.*, 25-30.
- Wagnon, P., P. Ribstein, G. Kaser, and P. Berton (1999), Energy balance and runoff seasonality of a Bolivian glacier, *Glob. Planet. Change*, 22, 49-58.
- Van de Wal, R. S. W., J. Oerlemans, and J. C. Van der Hage (1992), A study of ablation variations on the tongue of Hintereisferner, Austrian Alps, *J. Glaciol.*, 38(130), 319-324.
- Van de Wal, R. S. W., W. Greuell, M. R. Van den Broeke, C. H. Reijmer, and J. Oerlemans (2005), Surface mass-balance observations and automatic weather station data along a transect near Kangerlussuaq, West Greenland, *Ann. Glaciol.*, 42, 311-316.
- Van de Wal, R. S. W., W. Boot, M. R. Van den Broeke, C. J. P. P. Smeets, C. H. Reijmer, J. J. A. Donker, and J. Oerlemans (2008), Large and Rapid Melt-Induced Velocity Changes in the Ablation Zone of the Greenland Ice Sheet, *Science.*, 80(321), 111-113, doi:10.1126/science.1158540.
- Van de Wal, R. S. W., C. J. P. P. Smeets, W. Boot, M. Stoffelen, R. van Kampen, S. H. Doyle, F. Wilhelms, M. R. Van den Broeke, C. Reijmer, J. Oerlemans, and A. Hubbard (2015), Self-regulation of ice flow varies across the ablation area in south-west Greenland, *Cryosph.*, 9, 603-611, doi:10.5194/tc-9-603-2015.
- Warren, C., and M. Aniya (1999), The calving glaciers of southern South America, *Glob. Planet. Change*, 22, 59-77.
- Warren, S. G. (1984), Impurities in snow: effects on albedo and snowmelt, *Ann. Glaciol.*, 5, 177-179.
- Weertman, J. (1957), On the sliding of glaciers, *J. Glaciol.*, 3, 33-38.
- Weertman, J. (1964), The theory of glacier sliding, *J. Glaciol.*, 287-303.
- Weertman, J. (1972), General theory of water flow at the base of a glacier or ice sheet, *Rev. Geophys. Sp. Phys.*, 10, 287-333.
- Whitehead, K., B. Moorman, and P. Wainstein (2010), The Use of Ground-Based Photogrammetry and SAR Interferometry to Characterize the Surface Motion of an Arctic Glacier, in *Proceedings 63rd Canadian Geotechnical Conference & 6th Canadian Permafrost Conference*, pp. 1298-1306, Calgary, Alberta.
- Whitehead, K., B. J. Moorman, and C. H. Hugenholtz (2013), Low-cost, on-demand

- aerial photogrammetry for glaciological measurement, *Cryosph.*, 7, 1879–1884, doi:10.5194/tc-7-1879-2013.
- Whitehead, K., B. Moorman, and P. Wainstein (2014), Measuring daily surface elevation and velocity variations across a polythermal arctic glacier using ground-based photogrammetry, *J. Glaciol.*, 60(224), 1208–1220, doi:10.3189/2014JG14J080.
- Willis, I. C., M. J. Sharp, and K. S. Richards (1990), Configuration of the drainage system of Middtdalsbreen, Norway, as indicated by dye-tracing experiments, *J. Glaciol.*, 36(122), 89–101.
- Willis, I. C., N. S. Arnold, and B. W. Brock (2002), Effect of snowpack removal on energy balance, melt and runoff in a small supraglacial catchment, *Hydrol. Process.*, 16, 2721–2749, doi:10.1002/hyp.1067.
- Willis, I. C., C. D. Fitzsimmons, K. Melvold, L. M. Andreassen, and R. H. Giesen (2012), Structur , morphology and water flux of a subglacial drainage system, Middtdalsbreen, Norward, *Hydrol. Process.*, 26, 3810–3829, doi:10.1002/hyp.8431.
- de Woul, M., R. Hock, M. Braun, T. Thorsteinsson, T. Jóhannesson, and S. Halldórsdóttir (2006), Firn layer impact on glacial runoff: a case study at Hofsjökull, Iceland, *Hydrol. Process.*, 20, 2171–2185, doi:10.1002/hyp.6201.
- Zitová, B., and J. Flusser (2003), Image registration methods: a survey, *Image Vis. Comput.*, 21, 977–1000, doi:10.1016/S0262-8856(03)00137-9.
- Zwally, H. J., M. B. Giovinetto, J. Li, H. G. Cornejo, M. A. Beckley, A. C. Brenner, J. L. Saba, and D. Yi (2005), Mass changes of the Greenland and Antarctic ice sheets and shelves and contributions to sea-level rise: 1992–2002, *J. Glaciol.*, 51(175), 509–527.